An Electrochemical Investigation of Electroless Deposition: the Copper-DMAB System

A thesis submitted to the University of Manchester for the degree of

Doctor of Philosophy

in the Faculty of Engineering and Physical Sciences

2010

Daniela Plana

School of Chemistry

TABLE OF CONTENTS

Word count: 59,623

List of Figures

List of Tables

The University of Manchester

Daniela Plana

Doctor of Philosophy Thesis: "An Electrochemical Investigation of Electroless Deposition: the Copper-DMAB System"

Submission Date: 29/06/2010

Abstract

An electrochemical study of the copper electroless deposition process, using dimethylamine borane as a reducing agent, has been performed, in order to gain further understanding of the mechanism and kinetics of electroless deposition. An in-depth study of the electro-oxidation of dimethylamine borane (DMAB) was additionally carried out, due to its increasing relevance, not only in electroless deposition, but also in fuel cell technology.

DMAB oxidation was studied using different experimental techniques such as voltammetry, chronoamperometry, single-crystal electrochemistry and *in-situ* Fourier Transform infrared spectroscopy, which demonstrated that adsorption of the DMAB molecule, and its intermediates, plays an important role in the oxidation mechanism and kinetics. The initial dissociation process is catalysed by the presence of metallic surfaces and the applied potential. On gold surfaces, DMAB undergoes a three-electron transfer at low overpotentials, with a further oxidation process of up to six electrons occurring at high overpotentials. Chemical interactions with gold oxide produce further oxidation of the DMAB molecule. In the potential region of gold oxide formation, in highly alkaline media, the dimethylamine is also oxidised.

The voltammetric behaviour of bipolar cells was studied using model reversible and quasi-reversible redox couples, in conjunction with numerical simulations of the system. DMAB oxidation and copper electrodeposition were studied separately and together using the bipolar cell, providing useful information of the "coupling" effects between the cathodic and anodic processes of electroless deposition. The ability to quantify side reactions associated with electroless plating, namely hydrogen evolution in the copper-DMAB system, was also demonstrated.

The kinetics of the copper-DMAB electroless system was studied in detail, using the electroless bath and a galvanic cell configuration. The fact that the rate of deposition decreased upon the physical separation of the two half-reactions, as well as the observed catalysis of the oxidation of DMAB by copper surfaces, lead to the conclusion that the mixed potential theory (MPT) does not apply to this system. Faradaic efficiencies never reached 100% due to the parasitic side reactions mentioned above; the latter were especially prominent in the early stages of deposition. Crystalline copper films were obtained, with a higher fraction of Cu (111) than expected for polycrystalline copper, while the roughness of the deposits was found to increase with deposition time.

Declaration

The author declares that no portion of the work referred to in this thesis has been submitted in support of an application for another degree, or qualification, in this, or any other university or institute of learning.

Copyright

Acknowledgements

I would first like to thank my supervisor, Rob Dryfe, for all he has taught me throughout these four years; for his guidance and support, and specially for not killing me after one of my many rants. I'd like to thank everyone in the electrochemistry group, past and present, for their help, as well as their ever needed distractions, *i.e.* coffee, chocolate and/or cigarette breaks! I'd particularly like to acknowledge Fran Jones for all I learnt from her and her invaluable help in getting this project started. I'd like to thank Huong, Dan, Jeff, Matej and Briony… I'm not sure I'd have been able to finish this without you guys!!!

I want to acknowledge everyone in the electrochemistry group at the Leiden Institute of Chemistry. I particularly want to thank Marc Koper, for the opportunity of working with them, and Paramaconi Rodríguez, for all he taught me while I was there. I would also like to acknowledge everyone in the School of Chemistry, here in Manchester, who contributed with my project, especially Chris and everyone in the workshop!

I'd like to acknowledge Carlos Borrás and everyone in the electrochemistry group at the Universidad Simón Bolívar, for starting me on this path…

Last but certainly not least I'd like to thank my parents and family, for their unconditional support and for always pushing me to do my best. I want to acknowledge Aloha, Fabianna, Gilberto, Julia, Rhea and Suzanne for being there when I needed them and for keeping me somewhat sane during my PhD.

… a mis abuelos Luis y Jaime

Abbreviations and Symbols

α	transfer coefficient
δ	diffusion or Nernst layer
ΔE^0	difference in standard potentials between two redox couples
η	overpotential ($E - E^0$)
ν	scan rate
χ	dimensionless current function
ω	angular velocity
AFM	atomic force microscopy, atomic force microscope
Ag/AgCl	silver / silver chloride reference electrode
C	concentration
CE	chemical-electrochemical counter electrode(s)
CV	cyclic voltammetry, cyclic voltammogram
D	diffusion coefficient
DBFC	direct borohydride fuel cell
DEMS	differential electrochemical mass spectroscopy
DFT	density functional theory
DMAB	dimethylamine borane
E^0	redox potential
ECE	electrochemical-chemical-electrochemical
E_i	start potential
E_{MP}	mixed potential
E_p	peak potential
EQCM	electrochemical quartz crystal microbalance
E_s	set potential during chronoamperometry
F	Faraday's constant (96485 C)
f	frequency
FTIR	Fourier transform infrared
GC	glassy carbon
I_0	exchange current
i_l	limiting current
I_p	peak current
IR	infrared
Irrev	irreversible
I_{ss}	steady-state current
j	current density
J	flux
k	rate constant
k^0	standard heterogeneous rate constant
k_f	electron transfer rate constant

L/L	liquid/liquid
M	multimeter
MPT	mixed potential theory
n	number of electrons
N	number of moles
n_a	number of electrons in the rate-determining step
OCP	open circuit potential
O_i	oxidised species
Q	charge
QCM	quartz crystal microbalance
Q_{od}	overall deposition charge
Q_s	stripping charge
R	gas constant
r	radius
RDE	rotating disk electrode
RE	reference electrode(s)
Rev	reversible
RHE	reversible hydrogen electrode
R_i	reduced species
RPM	revolutions per minute
S	surface, substrate
	switch
SAM	self-assembled monolayer
T	temperature
t	time
TEA	triethanolamine
ULSI	ultra-large scale integration
UME	ultramicroelectrodes
WE	working electrode(s)
XRD	x-ray diffraction

1 Introduction

1.1 Electroless Deposition

Electroless deposition is a heterogeneous electrochemical process through which a metal ion in solution is reduced to its metallic state, on a catalytic surface, by a reducing agent. The reductant acts as an electron donor, so no external power supply is necessary in order to reduce the metal ions. This last point means that the process can occur on nonconductive surfaces, as well as on metals and semiconductors. A schematic of the electroless deposition reaction can be seen in Figure 1, where the reducing agent goes from its reduced (red) to its oxidised (ox) form, providing the electrons needed to reduce the metal ion (M^{n+}) to its metallic state (M). The process is initially catalysed by the substrate (S); in many cases, metal nanoparticles are used to start the reaction. As the plating proceeds, the deposited metal can also be autocatalytic for the deposition process, as seen in the lower part of Figure 1.[1-7] This metallization method was first studied and used in a “controlled” fashion in the 1940s. Before this, metal films were produced from unstable solutions; these baths frequently decomposed due to the preference of homogeneous reactions over heterogeneous electron transfer.[8,9]

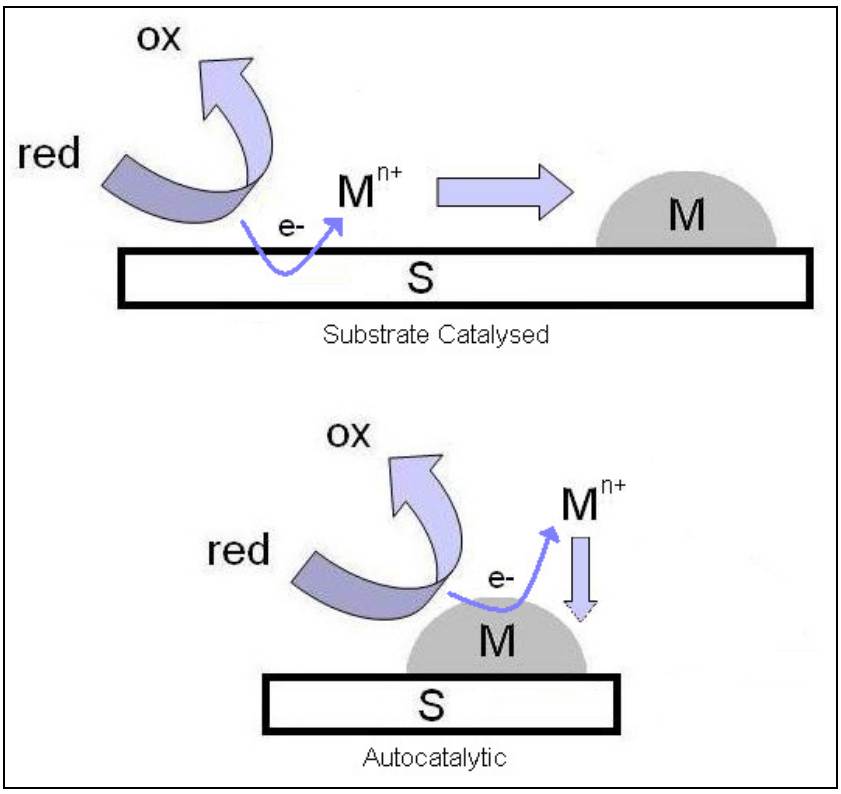

Figure 1. Schematic of the electroless deposition process.

A wide range of applications has been found for electroless plating, including the preparation of chip interconnects and other devices in electronics (and microelectronics), in metallurgy, and in the production of medical devices and batteries. It is used to produce thermic and electric conductors, as well as anticorrosion and decorative coatings. More recently, electroless deposition has been used in the metallization of carbon nanotubes and the formation of metal nanoparticles and nanowires.[4,6,9-17]

There are several advantages to using electroless deposition methods over other metallization processes such as physical and chemical vapour deposition or electrodeposition techniques; it is a low cost technique which produces high quality films and can be easily incorporated into large scale processes, while not requiring excessively high temperatures of operation. Electroless plating is also a highly selective process, which plates well on complex-shaped substrates and nonconductive surfaces, such as glass, ceramics and polymers.[8,10,11,16,18-22]

Electroless plating baths have very complex chemistry; other than the source of the metal ions and the reducing agent, already mentioned, they also include complexing agents and additives, which can be stabilizers or inhibitors.[16,23] The

complexing agents can act as buffers and prevent precipitation of the metal as hydroxides or other salts, as well as allowing some control over the stability of the bath and rate of reaction; this is achieved by changing the driving force for the reduction, through the formation of the metal complex, and thus the potential difference between the anodic and cathodic reactions. Although the potential difference between the redox couples (ΔE^0) must allow a spontaneous process, it cannot be too large in order to avoid homogeneous decomposition of the solution. ΔE^0 can also be regulated by controlling the pH, upon which the potential of the reducing agent is generally dependent.[16,20,24]

Different types of additives are used in electroless baths. Stabilizers are used in order to inhibit homogeneous decomposition and deposition on small particles, such as dust, by strongly adsorbing on them. Buffers are needed as many of the reactions consume or produce protons and hydroxide ions, changing the pH of bulk solution, or locally close to the plating surface. Other additives are used to control the surface tension, to remove hydrogen from the deposits, or to suppress hydrogen evolution, and in order to improve the quality of the metallic films obtained.[8,24,25]

Physical properties of the metal deposits produced through electroless plating, such as resistivity, thickness, morphology, purity, adherence or ductility, depend on many factors, other than simply the identity of the metal being deposited.[26-28] Bath composition, temperature, reaction rate and the catalytic substrate are amongst the variables that can influence the characteristics of the deposits, which often also include the co-production of hydrogen (or other gases) during the process. Additives to the plating baths also have significant consequences, yet their effects are not well understood. Most of the knowledge on the effect of bath chemistry on the physical properties of the deposits is empirical, and is thus of little use in the improvement of process' efficiency and applicability.[19,25,29-31] Some headway has been made, however, and it has been proved recently, for example, that the morphology of the deposit can be controlled to fill trenches effectively, by addition of a combination of additives with retarding and accelerating effects; the filling of nanometre-scale trenches is of upmost importance in the ultra-large scale integration (ULSI) interconnect technology.[18,32]

The plating rate and its efficiency have generally been found to be dependent on a number of factors, such as the nature of the catalytic surface, pH, temperature and bath composition, with the initial stages of the process being critical.[22,23,33] As can be seen from the quantity of factors involved in the chemistry of an electroless deposition bath, it is a highly complex process; in spite of decades of research, this has resulted in the lack of establishment of an adequate model for this process.[16,34]

1.1.1 Mixed Potential Theory (MPT)

Traditionally, electroless deposition has been studied using the corrosion derived concepts of mixed potential theory. This theory is applied to electrochemical systems that include two, or more, redox couples with different standard potentials that, when in contact, will try to reach equilibrium by the more electropositive couple being reduced, while the more electronegative one is oxidised. MPT has been extensively used to explain diverse electron transfer processes such as corrosion, mineral extraction, photographic development, as well as in electroless deposition.[8,25,35]

According to the mixed potential theory, when equilibrium is established, the rate of the anodic and cathodic reactions is equal, and no net current will flow. The electroless plating rate is then proportional to the exchange current (either the cathodic or anodic current, as they are equal) and will depend on the surface potential. This potential, called the mixed potential (E_{MP}), will fall between the redox potentials of the two half-reactions, as seen in Figure 2. The principal condition for the MPT is that the individual anodic and cathodic reactions are not affected by the occurrence of the other at the E_{MP}.[35,36]

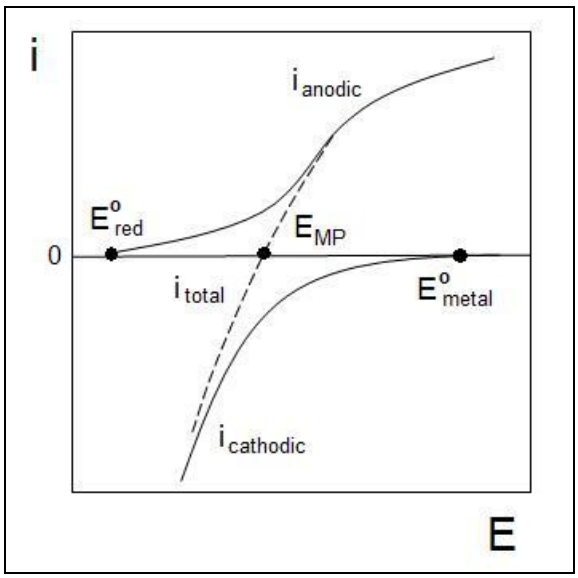

Figure 2. Schematic of the current-potential curves according to the MPT.

The mixed potential theory indicates that the deposition rate will be proportional to the concentrations of the reducing agent and the metal ion raised to fractional powers, if both reactions follow Tafel behaviour. In the most simple of cases, it will simply be proportional to both concentrations. In some cases, however, the limiting step of one of the half-reactions is the diffusion of the reactant; in such cases, the overall deposition rate will only be proportional the concentration of the reactant in question.[8]

The mixed potential theory only completely explains the process when both anodic and cathodic reactions are viable at the mixed potential. While some electroless systems have proven to follow the electrochemical mechanism explained above, others follow what could be called a chemical mechanism when direct interactions occur between the different species involved.[36]

Although the MPT has been widely used to study electroless deposition, it does not fully explain all electroless systems. Changes to the electrode surface, or the rate-determining step of the process, throughout the potential ranges covered by each half-reaction can limit the use of this theory. Further limitations arise from the possible interdependence of the individual reactions, as well as from effects produced by the adsorption of one component on the other component's reaction.[25,35-37] The mixed potential theory has been proven not to hold for specific cases of Ni-P and copper deposition, for example. The MPT is not able to explain the mechanism of nickel deposition, using hypophosphite as a reducing agent,

mainly due to considerable direct reaction between the Ni ions and the reducing radicals formed from the hypophosphite molecule.[22] The mechanism of copper deposition, using formaldehyde as a reducing agent, on the other hand, has proven to be electrochemical, with no homogeneous electron transfer; however, the combination of rapid solution exchange and electrochemical quartz crystal microbalance have proven that the mixed potential theory does not hold for this system either, as the copper reduction reaction catalyses the oxidation of formaldehyde.[37]

1.1.2 Kinetics

An electroless plating bath produces metallization of a catalytic substrate through the decomposition of the solution; a well prepared bath is thermodynamically unstable, yet has kinetic stability.[17] The study of the kinetics of these systems is complicated by the effect each of the components of the solution has on the plating rates. Some attempts have been made to express the deposition rate as a function of the concentrations of the main components (the metal ions and the reducing and complexing agents) raised to fractional powers; these rate laws are not entirely accurate and as they are mainly empirical, they vary across the literature for similar systems.[16,25] Different electrochemical methods have been used in studying the kinetics of electroless deposition, such as impedance, polarization curves and electric resistance; additional techniques used include gravimetric and spectroscopic methods.[16,38]

The kinetics of electroless deposition systems, as in most heterogeneous reactions, can be dependant on the rates of different processes, including mass transport through solution, adsorption on the catalytic surface, mass transport on the surface and desorption, as well as on the actual electron transfer.[10,39] An important parameter is the temperature at which the plating reaction proceeds; for most electroless systems the rate is found to increase strongly with temperature.[19,28,40]

The fact that only a selected group of compounds have been found useful as reducing agents in electroless plating, added to the specific substrates and metal

complexes on which each of them work, and the induction times observed in the process, indicate that catalysis of the anodic reaction is a key factor of the deposition process.[38] In many cases, the rate-determining step has been found to be a part of the kinetically-controlled anodic reaction.[8,25] The deposition rate of copper, using formaldehyde as reducing agent, for example, has been found to decrease considerably on the substitution of hydrogen with deuterium, indicating that the rate-limiting step is part of the oxidation of formaldehyde.[39] In addition, higher plating rates are observed in different baths that use reducing agents with greater interaction with the surface through adsorption, such as electroless gold deposition with dimethylamine borane (DMAB).[31] A good knowledge of the reducing agent's oxidation mechanism is consequently useful in any electroless system, as the selection of the reducing agent leads to the possible control of the plating rate, bath stability and the catalytic activity required to start the metallization.[17,26]

Most commonly used reducing agents in electroless plating baths have complex electrochemical oxidation mechanisms and the catalytic effect of the substrates is unique to each. No universal catalyst has been found; palladium, however, seems to be a good catalyst for the most common reductants. Palladium's catalytic effects and nobility have made it a popular choice as an initiator on inactive surfaces.[8,17] A reducing agent that works adequately on all significant substrates has not been found either; in order to remedy these issues, work done on the use of baths containing a mixture of reducing agents has been described.[11,41]

1.1.3 Reaction Mechanisms

An important element of most electroless plating systems, not fully described above, is the parallel evolution of hydrogen. Although different attempts have been made to explain the mechanism of formation of hydrogen, it is still a subject of debate in the literature. Four mechanisms for hydrogen evolution have traditionally been proposed in electroless deposition; although they adequately explain some systems, none is capable, in itself, to characterise all systems.[1,36,42]

The first mechanism proposes that each molecule of the reducing agent produces a hydride anion (H^-). This species then acts as a reductant or reacts with a proton to form a hydrogen molecule. The formation of H^-, however, is unlikely and such a mechanism would lead to at least equal amounts of hydrogen being formed to the metal being deposited, which has proven not to be the case.[8,42]

Another suggested path is the “metal hydroxide mechanism”, which was proposed for nickel deposition; according to this theory, nickel hydroxide rather than free nickel ion is reactive. The metal hydroxides can react several times, with water or the reductant molecules, to produce adsorbed hydrogen, which can consequently recombine, producing H_2. This mechanism is not likely as hypophosphite oxidation does not occur on hydrated nickel oxide, a reaction that would be expected if this mechanism took place. Additionally this process would not occur in electrochemical cells that separate the anodic and cathodic reactions, while experiments of that nature have been successfully carried out.[8,42]

The third attempt at explaining the production of hydrogen implies that the reducing agent is actually adsorbed atomic hydrogen. This adsorbed species is produced through the oxidation of the reductant and can recombine to produce molecular hydrogen. As in the first case, the amount of hydrogen evolved would be proportional to the metal deposition; this proportionality has not been observed. Furthermore, experiments performed with the addition of different organic molecules in attempts to suppress the evolution of hydrogen have not been successful.[8,42]

The last mechanism proposed is an entirely electrochemical one, in which hydrogen is produced from the reduction of protons formed from water during the oxidation of the reducing agent. Although this mechanism still holds some popularity, it does not take into account the catalytic effect of the substrate, nor does it allow for the fact that most of the hydrogen evolved has been shown to originate from the reducing agent.[42]

Many authors believe that the main step in electroless deposition reactions is the dissociative chemical adsorption of the reducing agent. This reaction would

likely produce a radical anion and a hydrogen atom.[1] Almost thirty years ago, Van den Meerakker proposed one mechanism for all reductants in electroless plating.[42] This approach has not been universally accepted, but appears to be quite comprehensive and a good starting point in any further study.[8]

Van den Meerakker's mechanism is reproduced below. It proposes dehydrogenation of the reducing agent as the first step of the anodic reaction. The atomic hydrogen formed can consequently recombine or be oxidised, while the resultant radical is always oxidised. The cathodic reaction is simply the reduction of the metal ions by the electrons produced in the anodic reactions, accompanied in some cases by hydrogen evolution.

Anodic Reaction:

Dehydrogenation: $RH_{ad} \xrightarrow{S} \dot{R}_{ad} + \dot{H}_{ad}$

Oxidation of the radical: $\dot{R}_{ad} + OH^- \rightarrow ROH + e^-$

Recombination: $2\dot{H}_{ad} \rightarrow H_2\uparrow$

Oxidation in alkali medium: $\dot{H}_{ad} + OH^- \rightarrow H_2O + e^-$

Oxidation in acidic medium: $\dot{H}_{ad} \rightarrow H^+ + e^-$

Cathodic Reaction:

Metal deposition: $M^{n+} + ne^- \rightarrow M_\downarrow$

Hydrogen evolution in alkali medium: $2H_2O + 2e^- \rightarrow 2OH^- + H_2\uparrow$

Hydrogen evolution in acidic medium: $2H^+ + 2e^- \rightarrow H_2\uparrow$

Although a unified mechanism, it must be adapted to each reducing agent - substrate pair. For alkylamine boranes, for example, a dissociation step frees the amine from the borane radical, prior to the dehydrogenation reaction.[17] Additionally, in the case of some reducing agents the oxidation of the radical produces compounds that can be further dehydrogenated.[42] The nature of the catalytic substrate can lead to the recombination or the oxidation of the atomic hydrogen, depending on plating conditions, explaining the wide range of efficiencies for hydrogen evolution.[8]

1.2 Dimethylamine Borane (DMAB) Oxidation

With some variations depending on the active surface used and the metal being deposited, the most common reducing agents in electroless deposition are formaldehyde and hypophosphite. The high toxicity of formaldehyde and the need for highly alkaline media are major drawbacks in the use of this compound for electroless plating.[8] On the other hand, the use of hypophosphite as a reducing agent is limited by the co-deposition of phosphorus when used with some metals, such as nickel and cobalt, and the fact that its oxidation is not catalysed by some industrially significant substrates.[8,42] These issues have led to the search for other possible reducing agents for electroless deposition baths. Only a small number of compounds are generally used; hydrazine, borohydride and alkylamine boranes are the most common, after formaldehyde and hypophosphite. The proper choice of reducing agent can lead to the control of the rate and stability of the electroless bath, as well as the determination of the catalytic activity needed from the substrate to start the plating reaction.[8,17,42]

Amine boranes have been used in a wide range of systems, as reducing and stabilizing agents, antioxidants and catalysts for polymerisation, both in aqueous and non-aqueous solvents.[17] The oxidation of these compounds, and particularly that of dimethylamine borane, has attracted increasing interest due to their use in electroless deposition not only on metals and alloys, but also on semiconductors and insulators. In common with the borohydride ion, amine boranes have low toxicity in comparison to other reducing agents, and are catalytically oxidised on surfaces such as copper, nickel and iron without the need of palladium activation layers, making them excellent choices for plating baths. Although their reduction power is lower than that of borohydride, they are less prone to hydrolysis reactions. A number of studies have been carried out in order to investigate the oxidation mechanism of amine boranes, and DMAB in particular; however, the multi-electron reactions involved have led to a lack of consensus regarding the operative mechanism.[17,31,43-46] After initial dissociation steps, the main intermediate in the oxidation process is similar, if not identical, to that of borohydride; unfortunately, this does not significantly help in clarifying the mechanism, as the mechanism of borohydride oxidation is still under investigation and debate, as discussed below.

1.2.1 Borohydride Oxidation

Borohydride has traditionally been used in a wide range of homogeneous reactions, as a powerful reducing agent.[47,48] It has more recently attracted attention as a reductant in electroless deposition, and additionally as a possible alternative for hydrogen in fuel cells; in the direct borohydride fuel cell (DBFC),[49,50] the anodic reaction is the oxidation of borohydride, while oxygen reduction, for example, can occur on the cathode. The interest arises from the fast kinetics, as well as the high theoretical voltage, capacity, energy density and hydrogen storage density of the DBFC. The stability and safe storage of the borohydride, with the added possibility of recycling side products, makes it an ideal candidate for fuel cells.[49-53]

Although generally stable in alkali, borohydride hydrolyses at low pH, evolving hydrogen. The hydrolysis, with its associated hydrogen production, can be catalysed not only by acidic media, but also by certain metals. This reaction is the main drawback in the development of the DBFC and the understanding of the electroless deposition mechanism, as it reduces the faradaic efficiencies obtained and complicates the study of the electrochemical oxidation of the tetrahydroborate ion.[52,54-58]

In view of the importance of borohydride in aqueous reactions, its hydrolysis has been extensively studied; its mechanism and kinetics, however, are not completely understood. The influence hydrolysis has on the electro-oxidation of borohydride is particularly complex and continues to be of interest.[53,59]

Borohydride hydrolysis can be generally expressed through Equation 1.[58]

$$BH_4^-{}_{(aq)} + 2H_2O_{(l)} \rightleftarrows BO_2^-{}_{(aq)} + 4H_2\nearrow \qquad \text{Equation 1}$$

As mentioned above, this reaction is highly dependent on the pH of the solution; the final product might vary slightly, with $B(OH)_4^-$ likely to be produced in

alkaline media, while boric acid is usually formed at low pH.[43,56,60] The process has at least one known intermediate; a negatively charged $-BH_3$ containing species was identified through ^{11}B NMR and salt effects on reaction kinetics.[58,61]

Numerous researchers postulate BH_3OH^- as a stable intermediate, while others believe borine, or $(BH_3)_{aq}$, is produced. Due to the instability of borine, it is thought to react quickly in a number of ways; the formation of diborane or subsequent hydrolysis, through intermediaries of the form $BH_{4-n}(OH)_n^-$, are some examples.[43,60,62] The overall process can be consequently summarised by Equation 2, where *n* is a number between 1 and 4.[63]

$$BH_4^-{}_{(aq)} + nH_2O_{(l)} \rightleftarrows BH_{4-n}(OH)_n^-{}_{(aq)} + nH_2\nearrow \qquad \text{Equation 2}$$

The protonated form of these intermediates has also been proposed, particularly for very acidic media and low temperatures.[43]

Borohydride is usually stable in aqueous alkaline solutions; it can hydrolyse when in contact with some transition metals (Pt, Pd, Ru, Co or Ni), whether they are in the metallic state, or present as alloys or salts. Metals with high hydrogen evolution overpotential such as gold, on the other hand, are very efficient electrodes for the electro-oxidation of BH_4^-, while not catalytic for the hydrolysis reaction.[52,57,64,65]

The only mechanisms proposed for the metal-catalysed hydrolysis are similar to those of the acid-catalysed reaction, though it appears to proceed at much slower rates in the former case and no intermediates have been identified. The heterogeneous reaction has proven to be dependent on potential, possibly indicating a pair of coupled reactions, perhaps involving the reduction of water (Equation 3 and Equation 4).[50] In Equation 3, the reactants and products could be free in solution or adsorbed on the metal surface.

Equation 3

$$BH_4^- + 2OH^- \rightarrow BH_3OH^- + H_2O + 2e^-$$
$$2H_2O_{(l)} + 2e^- \rightarrow 2OH^-_{(aq)} + H_{2(g)}$$

Equation 4

The interest in borohydride, both as fuel in the DBFC and as a reducing agent in electroless plating, revolves around its electro-oxidation mechanism. As stated above, the hydrolysis reaction can complicate the electrochemical studies; even when hydrolysis is completely avoided, however, the oxidation mechanism is a complex irreversible, multi-electron reaction.[52,66,67]

Though the theoretical voltage is normally not achieved due to kinetic limitations, amongst other factors, Equation 5 is generally accepted to be the overall electrochemical reaction in alkaline media; in terms of the DBFC, however, the operative potentials are still more negative than those from hydrogen or other common fuels.[68] As with the case of the hydrolysis, different end products can be obtained, depending on reaction conditions; either boric acid or $B(OH)_4^-$, for example, can be expected.[55]

$$BH_4^-{}_{(aq)} + 8OH^-{}_{(aq)} \rightarrow BO_2^-{}_{(aq)} + 6H_2O_{(l)} + 8e^-$$

Equation 5

The complete oxidation of borohydride, expressed in Equation 5, is generally only achieved on electrode materials that are catalytic towards the reaction, have a high overpotential for hydrogen evolution or are non-catalytic towards the hydrolysis reaction. Gold is generally considered the best example, with 7 to 8 electrons being easily obtained,[52,54,64,67] although values as low as 4.5 have occasionally been reported at low overpotentials.[57,59] Anywhere between 4 and 8 electrons can be obtained on surfaces that catalyse hydrogen evolution and hydrolysis. On nickel only 4 electrons are usually produced; palladium also produces a low number of electrons, while platinum can yield between 4 and 8 electrons.[50,57,59,64] Recent research, however, has suggested that hydrolysis can occur on gold surfaces, and that platinum might prove to be a better catalyst for borohydride oxidation, thus a better option as anode material in the DBFC.[59]

As stated above, the oxidation process might yield less than eight electrons due to the parallel reaction of partial hydrolysis of borohydride to BH_3OH^-, which can be oxidised at lower potentials and with faster kinetics than its predecessor; this last reaction produces only three electrons, as seen in Equation 6.[52,60,61] As mentioned above for the metal-catalysed hydrolysis, the species involved in this reaction might be free in solution or adsorbed on the electrode surface.

$$BH_3OH^- + 3OH^- \rightarrow BO_2^- + \tfrac{3}{2}H_2 + 2H_2O + 3e^- \qquad \text{Equation 6}$$

Although many different techniques have been used to probe the mechanism of borohydride electro-oxidation, the area needs further investigation, as conflicting results have been reported in the literature. Polarography, cyclic voltammetry, chronoamperometry, and chronopotentiometry are the most commonly used electrochemical techniques; methods such as NMR, MS, electrochemical impedance, rotating disk electrode (RDE) voltammetry and Fourier transform infrared (FTIR) spectroscopy have more recently been applied.[53,60,61,69,70] Some points of almost universal agreement do exist, such as coupled chemical reactions being involved in the process and the fact that adsorption plays a mayor role in both mechanism and kinetics.[57,63,66,71]

It is widely believed that the first intermediate is BH_3OH^-, with this species consequently undergoing further oxidation. Whether this first step is considered to occur through adsorbed species, or in solution, varies within the literature.[55,63] Equation 7 is believed, by some research groups, to be the result of a heterogeneous CE mechanism, better described by Equation 8 and Equation 9, where S is the catalytic surface.

$$BH_4^- + OH^- \rightarrow BH_3OH^- + H + e^- \qquad \text{Equation 7}$$

$$BH_4^- + H_2O \xrightarrow{S} BH_3OH^- + H_2 \qquad \text{Equation 8}$$

$$\tfrac{1}{2}H_2 + OH^- \rightarrow H_2O + e^- \qquad \text{Equation 9}$$

The hydrogen atom removed from borohydride in Equation 7, which is most likely adsorbed on the electrode surface, can further react in two different ways; recombining to evolve hydrogen (Equation 10) or oxidising to form water (Equation 11); the reaction pathway depends on the active surface and other experimental conditions.[50]

$$2H \rightarrow H_2\uparrow$$ Equation 10

$$H + OH^- \rightarrow H_2O_{(l)} + e^-$$ Equation 11

Some authors postulate that the first intermediate species in borohydride oxidation is actually adsorbed monoborane, BH_3; the high irreversibility of the process could be explained by the instability of such a compound. The electrochemical-chemical-electrochemical (ECE) mechanism, through which monoborane is formed, is represented by Equation 12 to Equation 14, where the chemical step (Equation 13) is very fast.[50,66]

$$BH_4^-{}_{(ads)} \rightleftarrows BH_4^{\bullet}{}_{(ads)} + e^-$$ Equation 12

$$BH_4^{\bullet}{}_{(ads)} + OH^- \rightleftarrows BH_3^-{}_{(ads)} + H_2O_{(l)}$$ Equation 13

$$BH_3^-{}_{(ads)} \rightleftarrows BH_{3(ads)} + e^-$$ Equation 14

Monoborane is very unstable, so if formed it would quickly react with water or hydroxide to form BH_3OH^-, or a similar species, or simply dimerise to diborane.[52]

A recent study, combining FTIR and electrochemical techniques, proposes a slightly different mechanism, as seen in Equation 15 to Equation 17.[69]

$$BH_4^- + OH^- \overset{S}{\rightleftharpoons} BH_{3(ads)} + H_2O_{(l)} + 2e^- \quad \text{Equation 15}$$

$$BH_{3(ads)} + OH^- \rightleftarrows BH_3OH^-_{(ads)} \quad \text{Equation 16}$$

$$BH_3OH^-_{(ads)} + 6OH^- \rightleftarrows BO_2^-{}_{(aq)} + 5H_2O_{(l)} + 6e^- \quad \text{Equation 17}$$

Although there is no clear consensus about the rest of the mechanism, most researchers seem to accept a stepwise electrochemical reaction, coupled with chemical reactions, with boron hydroxides as intermediates. A recent first-principles mechanistic study of borohydride electro-oxidation on gold suggest $B(OH)_2$* and BOOH* as adsorbed intermediates, while RDE studies have led to the proposal of $BH_2(OH)_2^-$ and $BH(OH)_3^-$ as intermediate species.[59,70,72]

The stepwise mechanism mentioned could involve the dissociative adsorption of hydrogen with subsequent oxidative electrochemical steps, as described by Equation 18 and Equation 19, where *n* is a number between 1 and 4.[50]

$$BH_n(OH)_{4-n}^- \rightarrow BH_{n-1}(OH)_{4-n}^- + H_{(ads)} \quad \text{Equation 18}$$

$$BH_{n-1}(OH)_{4-n}^- + OH^- \rightarrow BH_{n-1}(OH)_{5-n}^- + e^- \quad \text{Equation 19}$$

Similarly, a mechanism involving a series of electrochemical steps with ensuing intake of hydroxide ions has been proposed and is presented in Equation 20 and Equation 21.[55] In both of these mechanisms, the boron-containing species might or might not be adsorbed on the electrode surface.

$$BH_n(OH)_{4-n}^- \rightarrow BH_{n-1}(OH)_{4-n} + \tfrac{1}{2}H_2 + e^- \quad \text{Equation 20}$$

$$BH_{n-1}(OH)_{4-n} + OH^- \rightarrow BH_{n-1}(OH)_{5-n}^- \quad \text{Equation 21}$$

The determination of the diffusion coefficient, D, of borohydride in aqueous media is complicated by the uncertainty in the number of electrons involved in its electro-oxidation, as well as the possible coverage of part of the electrode surface by hydrogen gas and/or adsorbed atoms. The value of D has been reported to increase with both pH and temperature.[64]

One of the first reported values of D, 2.1 x 10^{-5} cm^2 s^{-1}, was obtained through polarographic methods in alkaline media.[60,61] Later studies, using chronoamperometric techniques performed at gold microelectrodes, report a D value of 1.68 x 10^{-5} cm^2 s^{-1}.[67] More recently ring-disk rotating gold electrodes and electrochemical impedance have been used to determine the diffusion coefficient, yielding values of 2.24 and 2.8 x 10^{-5} cm^2 s^{-1}, respectively.[70,73]

Further complications in the study of the electrochemical behaviour of BH_4^- derive from the fact that the production and stability of the BH_3OH^- species is heavily dependent on the pH, and more particularly on the ratio of concentrations between borohydride and hydroxide anions.[58] The history of the electrode used also has an important effect on the voltammetric behaviour of solutions containing borohydride.[73] It has been claimed, for example, that Au^+/Au^{3+} species formed on gold electrodes in the oxidation region can act as mediators, catalysing the electro-oxidation of borohydride.[74]

Evidence that borohydride oxidation does not occur under simple diffusion control is seen in RDE studies, which have shown deviations from the diffusion-controlled Levich behaviour.[57] Likewise, chronoamperograms do not show the Cottrell response expected for diffusion-controlled systems,[51] while voltammetric studies present mixed kinetic and diffusion control.[49] Recently, electrochemical impedance techniques have shown that the electrochemical behaviour of borohydride is dominated by irreversible and adsorption processes.[70]

1.2.2 DMAB Oxidation

The electro-oxidation mechanism of dimethylamine borane has been studied mainly through cyclic voltammetry and polarization curves.[1,28,41,75,76] A number of more specialized techniques have been employed to unravel the complex behaviour of DMAB; microelectrodes, chronoamperometry, RDE, as well as electrochemical impedance and quartz crystal microbalances (EQCM) have all been used.[26,31,33,44,59,77] Density functional theory (DFT) and ab-initio molecular orbital studies of DMAB oxidation have also been reported.[34,78,79]

DMAB, much like borohydride, is unstable in acidic media, hydrolyzing quickly to produce significant amounts of gas, thought to be hydrogen and/or BH_3 decomposition products. These reactions are especially violent at pH values lower than 4, while tend to a minimum above pH 5. It is reported that DMAB hydrolysis is negligible above pH 12.[16,44,76] As a reducing agent, dimethylamine borane works best in alkaline media, showing an increase in activity with increasing pH and no activity reported below pH 7.[80]

As described previously for the case of borohydride oxidation, the debate about the oxidation mechanism of DMAB is still not resolved; there are contrasting reports on whether it is the boron or hydrogen that is actually oxidised in the process. There is, however, some agreement on the initial stages of the mechanism: it is generally assumed that dimethylamine borane dissociates in aqueous media, at least partially. This process forms the free amine and either BH_3 or a $–BH_3$ containing species, such as BH_3OH^-, according to Equation 22. Although a value for the dissociation constant was not found in the literature, it has been suggested that this chemical process can be the rate-determining step in the oxidation of DMAB. Surface catalysis, particularly by metallic substrates, of the B-N cleavage has also been reported.[17,26,41]

$$(CH_3)_2NHBH_{3(aq)} + H_2O_{(l)} \rightleftarrows (CH_3)_2NH_2{}^+{}_{(aq)} + BH_3OH^-{}_{(aq)} \quad \text{Equation 22}$$

Due to the increasing reduction activity of DMAB at higher pH, most of the electroless deposition and electro-oxidation studies have been carried out in alkaline media. In such cases, Equation 22 can be re-written as Equation 23.

$$(CH_3)_2NHBH_{3(aq)} + OH^-_{(aq)} \rightarrow (CH_3)_2NH_{(g)} + BH_3OH^-_{(aq)} \quad \text{Equation 23}$$

If this is indeed the first step, the actual reducing agent would be BH_3OH^-, which would imply that the electrochemical behaviour of DMAB would be quite similar to that of borohydride. Some authors, however, have clearly stated that the mechanisms, although similar are not the same, as the potentials at which intermediates are oxidised varies.[59]

The final product of DMAB oxidation varies with the reaction conditions; similar products to those reported for BH_4^- are obtained in some cases: BO_2^-, $B(OH)_4^-$, borate and boric acid.[19,31,33,40,41,76] Other end products, such as $HB_4O_7^-$, boron or boron oxide, have been proposed. The co-deposition of boron or boron oxide has been reported with certain metals like nickel and cobalt, while their presence has never been detected on other metals, such as copper.[4,9,40,46,81]

The number of electrons transferred during DMAB electro-oxidation is yet another point of controversy, with three or six electrons being reported, or expected, by different research groups. These differences might be due, as in the case of borohydride, to the production of hydrogen during oxidation and/or hydrolysis. Both of these side processes can be catalysed by the reaction conditions and the electrode material used. A number of materials have been used as working electrodes in the study of DMAB oxidation: glassy carbon, Ag, Au, Cu, Co, Ni, Pd and Pt.[1,75]

The overall three-electron oxidation of DMAB can be described by Equation 24.[40]

$$(CH_3)_2NHBH_{3(aq)} + 4H_2O_{(l)} \rightarrow B(OH)_4^-{}_{(aq)} + 3H^+_{(aq)} + 3H_{(ads)} + (CH_3)_2NH_2^+{}_{(aq)} + 3e^- \quad \text{Equation 24}$$

As most authors assume that the dissociation takes place as a prior chemical reaction (see Equation 22 and Equation 23), the electrochemical process can be more accurately described by the electro-oxidation of BH_3OH^-; an example of such a reaction can be seen in Equation 6. Possible mechanisms leading from the dissociation process involve consecutive one-electron steps, as described by Equation 25 through Equation 27. As in the case of borohydride oxidation, whether these species are adsorbed or in solution is not known.

$$BH_3OH^- + OH^- \rightarrow BH_2(OH)_2^- + \tfrac{1}{2}H_2 + e^- \quad \text{Equation 25}$$

$$BH_2(OH)_2^- + OH^- \rightarrow BH(OH)_3^- + \tfrac{1}{2}H_2 + e^- \quad \text{Equation 26}$$

$$BH(OH)_3^- + OH^- \rightarrow B(OH)_4^- + \tfrac{1}{2}H_2 + e^- \quad \text{Equation 27}$$

Alternative reactions involving a six electron transfer per DMAB molecule are suggested, depending on the final product obtained. Two examples can be seen in Equation 28 and Equation 29.[4,76]

$$4(CH_3)_2NHBH_{3(aq)} + 21OH^-_{(aq)} \rightarrow HB_4O_7^-{}_{(aq)} + 4(CH_3)_2NH_2^+{}_{(aq)} + 14H_2O_{(l)} + 24e^- \quad \text{Equation 28}$$

$$BH_3OH^-_{(aq)} + 8OH^-_{(aq)} \rightarrow BO_3^{-3}{}_{(aq)} + 6H_2O_{(l)} + 6e^- \quad \text{Equation 29}$$

It has been suggested that DMAB electro-oxidation is a six-electron transfer which proceeds via Equation 30, after the dissociation step; the lower number of electrons sometimes obtained is accounted for by a decrease in BH_3OH^- concentration, through a competing hydrolysis reaction (Equation 31).[45]

$$BH_3OH^-_{(aq)} + 6OH^-_{(aq)} \rightarrow B(OH)_4^-{}_{(aq)} + 3H_2O_{(l)} + 6e^- \quad \text{Equation 30}$$

$$BH_3OH^-_{(aq)} + 3H_2O_{(l)} \rightleftarrows B(OH)_4^-{}_{(aq)} + 3H_2\nearrow \quad \text{Equation 31}$$

Such a scheme would also involve a series of one-electron transfers, which in some cases would be coupled with chemical reactions (see Equation 32 to Equation 37). The five-coordinated boron species are based on ab-initio molecular orbital studies of DMAB oxidation, and should be viewed as transition states rather than reaction intermediates.[44,78] The intermediates described below are likely adsorbed, but might be found in solution.

$$BH_3(OH)^- + OH^- \rightarrow BH_3(OH)_2^- + e^- \quad \text{Equation 32}$$

$$BH_3(OH)_2^- \rightarrow BH_2(OH)_2^- + \tfrac{1}{2} H_2 \quad \text{Equation 33a}$$

$$BH_3(OH)_2^- + OH^- \rightarrow BH_2(OH)_2^- + H_2O + e^- \quad \text{Equation 33b}$$

$$BH_2(OH)_2^- + OH^- \rightarrow BH_2(OH)_3^- + e^- \quad \text{Equation 34}$$

$$BH_2(OH)_3^- \rightarrow BH(OH)_3^- + \tfrac{1}{2} H_2 \quad \text{Equation 35a}$$

$$BH_2(OH)_3^- + OH^- \rightarrow BH(OH)_3^- + H_2O + e^- \quad \text{Equation 35b}$$

$$BH(OH)_3^- + OH^- \rightarrow BH(OH)_4^- + e^- \quad \text{Equation 36}$$

$$BH(OH)_4^- \rightarrow B(OH)_4^- + \tfrac{1}{2} H_2 \quad \text{Equation 37a}$$

$$BH(OH)_4^- + OH^- \rightarrow B(OH)_4^- + H_2O + e^- \quad \text{Equation 37b}$$

The maximum amount of electrons, six, is transferred if mechanism “b” is followed, *i.e.* if the processes described in Equation 33a, Equation 35a and Equation 37a fail to occur; in this case, water is produced in addition to the boron-containing products. If any of the reactions denoted “a” occur, a lower number of electrons, down to three, is obtained and hydrogen gas evolves. A summary of the mechanism can be seen in Equation 38, where *n* varies from 3 to 6.

$$BH_3(OH)^-_{(aq)} + nOH^- \rightarrow$$
$$B(OH)_4{}^-_{(aq)} + (3 - n/2)H_{2(g)} + (n-3)H_2O_{(l)} + ne^- \quad \text{Equation 38}$$

The majority of electrochemical studies on DMAB oxidation have used gold as the electrode surface, as this metal appears not to catalyse the hydrolysis reaction, while it has low hydrogen adsorption and background currents in the potential window of interest.[44] Some recent studies, however, suggest that hydrolysis and hydrogen oxidation indeed occur on gold.[59] Mechanisms involving a series of individual steps are supported by voltammetric studies, where two or three oxidation waves are observed. The second voltammetric wave is partly obscured by the metallic hydroxide or oxide formation on the electrode surface. In this potential region, competition between the adsorption of hydroxide, boron-containing molecules and even dimethylamine, occurs, further complicating the voltammetric analysis. On the other hand, it has been suggested that the low coverage of hydrous oxide formed on gold surfaces catalyses the electro-oxidation reaction.[33,45,76,82] DFT calculations suggest that the inclusion of hydroxide into the molecule is rate-determining, thus the behaviour of hydroxides on the electrode surface is thought to play a major role on the overall reaction.[79]

As discussed for borohydride oxidation, adsorption of reagents and/or intermediates appears to be an important element of DMAB oxidation. Although mixed diffusion and kinetic control has been reported for the reaction, other reports have suggested that the overall kinetics depend on the rate of adsorption.[11,26,76] EQCM and electrochemical impedance studies seem to confirm that chemisorption occurs during the second voltammetric wave; these adsorbates have been assumed to be boron-containing. Ab-initio molecular orbital studies indicate that DMAB oxidation is enhanced at the interface, through a lowering of the activation energy and by the metal accepting the electrons produced in the reaction; the number of electrons transferred was found to be directly related to the adsorption energy.[26,31,34]

Only two diffusion coefficient values have been reported for DMAB: 7.48 x 10^{-6} and 8.55 x 10^{-6} cm^2 s^{-1}. The first was obtained through chronoamperometric techniques using microelectrodes, where two three-electron processes are

evident, while the second was found through hydrodynamic voltammetric methods, assuming three two-electron steps.[44,77] These small inconsistencies, as well as the assumption of a full six-electron transfer in both cases, have recently led to the use of the borohydride diffusion coefficient as an estimated value to allow the evaluation of the voltammetric behaviour of dimethylamine borane.[59]

In an electroless bath, the overall process encompasses not only the anodic oxidation of the reducing agent, but also the cathodic reduction of the metal ion. Dimethylamine borane has been mainly used for gold and copper deposition, although metals such as cobalt and nickel have also been plated using DMAB.[19,81] The complete bath chemistry of gold and copper electroless systems can be expressed by Equation 39, Equation 40 and Equation 41, depending on reaction conditions. The rate of this type of process has generally been found to increase with DMAB concentration, pH and temperature, in agreement with the effect of these factors on DMAB electro-oxidation.[19,81]

$$(CH_3)_2NHBH_{3(aq)} + 4OH^-_{(aq)} + 3Au(CN)_2^-_{(aq)} \rightarrow (CH_3)_2NH_{(g)} + BO_2^-_{(aq)} + \tfrac{3}{2}H_2\uparrow + 2H_2O_{(l)} + 3Au\downarrow + 6CN^-_{(aq)} \quad \text{Equation 39}$$

$$4(CH_3)_2NHBH_{3(aq)} + 9OH^-_{(aq)} + 12CuEDTA^{-2}_{(aq)} \rightarrow 12Cu\downarrow + 4(CH_3)_2NH_2^+_{(aq)} + HB_4O_7^-_{(aq)} + 2H_2O_{(l)} + 12HEDTA^{-3}_{(aq)} \quad \text{Equation 40}$$

$$2(CH_3)_2NHBH_{3(aq)} + 6H_2O_{(l)} + 3Cu^{+2}_{(aq)} \rightarrow 2(CH_3)_2NH_{(g)} + 2H_3BO_{3(aq)} + 6H^+_{(aq)} + 3Cu\downarrow + 3H_2\uparrow \quad \text{Equation 41}$$

1.3 Electroless Copper Deposition

Electroless deposition can be used to plate a limited number of metals. Copper is one of the few metals within that group that produces pure deposits; it is

quite common for electroless deposits to incorporate additives or form alloys with boron or phosphorus from the reducing agent.[8]

1.3.1 Mechanism and Kinetics

Although considerable effort has gone into investigating the mechanism and kinetics of the electroless copper deposition process, most of the work is empirical and there is considerable disagreement throughout the literature on how the process actually occurs and what rate laws govern it. A good understanding of the mechanism is important in the development of any good industrial process and there are still many questions to be answered in this case.[24,39,83]

The electroless copper deposition system is thermodynamically favourable, with a negative Gibbs energy change, but kinetically hindered. The surface properties are very important to the kinetics of the system, which has autocatalytic properties; generally, the rate is initially slow, but increases as the fresh copper surface catalyses the deposition.[4,19,37,84,85] Induction times are frequently observed, due to the change of properties and nature of the substrate as the plating reaction proceeds; through combined Raman and impedance spectroscopy, for example, it has been noted that the morphology of the deposited copper has an important effect on the rate of oxidation of the reducing agent, in baths containing formaldehyde.[86,87] The morphology of the substrate also has an effect on the kinetics, with some studies reporting that on flat surfaces the process is controlled by charge transfer kinetics, while deposition into deep or narrow features is mass transport dependent.[20]

Electroless copper deposition is a complex multi-step redox mechanism which involves the diffusion of the metal complex and the reducing agent to the catalytic surface and their subsequent reaction on it; each of these steps could limit the reaction.[20,39] The accompanying evolution of hydrogen further complicates kinetic and mechanistic studies, by producing microconvection which influences the mass transport phenomena and thus the overall rate of the electroless copper deposition process.[88]

A number of experimental and analytical techniques have been employed to measure or estimate electroless copper rates. Traditionally gravimetric techniques have been used to determine the weight change during deposition; as this is an *ex-situ* technique, in many cases a limited number of time points are evaluated or averages over long ranges of time, such as one hour, are used.[9,83,89-91] *In-situ* weight measurements are also common, through the use of quartz-crystal microbalances.[20,37,39,92,93] Surface techniques, such as the use of roughness step testers[85] or profilometers,[19,29] have been employed in a number of occasions as a means of measuring the thickness of the copper deposits. Copper deposition rates have also been estimated using MPT derived concepts, through the use of plating currents, individual polarization curves and Evans diagrams.[25,91,94] Another electrochemical approach is the use of impedance techniques, as the plating rate has been found to be inversely proportional to the polarization resistance.[30,38,83]

The kinetics of the system depend heavily on the bath chemistry and operating conditions, with the limiting step possibly changing from the anodic to the cathodic reaction, and even mixed control found in certain cases.[83] The concentration of the copper complex and the reducing agent, as well as the pH and the temperature of the bath all influence the reaction kinetics.[19] The reducing agent has a great effect on the system's kinetics, particularly if adsorptive processes are involved, whilst the rate of deposition has been found to be independent of the copper concentration at relatively high copper concentrations.[9,39] Increases in bath temperature generally lead to higher deposition rates, whereas the effect of pH on the rate is highly complex and depends heavily on the reducing agent used.[19,25,39]

The most widely used reducing agent in copper electroless deposition systems is formaldehyde, and thus much of the knowledge of the mechanism is based on the anodic oxidation of this compound. Environmental and safety concerns, as well as the need for less alkaline conditions in certain applications, have led to the use of other reducing agents such as glyoxylic acid and alkylamine boranes. Although they have shown promising results, further investigation of their particular mechanisms and their effect on the deposition process of copper is needed.[8,19,23]

Generally, one of two approaches is used to investigate the kinetics of copper electroless systems: the MPT (see Section 1.1.1) or classical chemical kinetic theory.[25,39] Each one has its advantages and drawbacks; for example only a limited concentration range can be studied with the classical kinetic approach, due to bath instability, copper colloid formation or precipitation of copper hydroxides.[93]

Following the classical chemical kinetic approach, many authors have arrived at rate laws that depend on the concentration of the different components (C) of the plating bath generalised as Equation 42; the deposition rate (r) is then proportional to the concentration of the copper ions, the ligand, the hydroxyl ions and the reducing agent raised to different powers.

$$r = kC_{Cu^{2+}}^{\alpha} C_{lig}^{\beta} C_{OH^-}^{\gamma} C_{reductant}^{\delta} \qquad \text{Equation 42}$$

Different values of α, β, γ, and δ have been reported for different baths, even when conditions appear very similar.[20,24,25,94] While some studies have shown the concentration of copper to have little effect on the system's kinetics[39], others report high values of α and low δ magnitudes.[95] It has been suggested that the differences found are mainly due to the great variations between the copper concentrations at the interface and in bulk solution; if the interfacial concentrations are used, rather than the bulk values, the values of α across the literature grow closer together.[88]

The effect of the hydroxide concentration is complex, with optimum values found to vary according to the nature of the substrate. Even at high pH values, where the bulk concentration remains fairly stable, the surface concentration of hydroxide can change dramatically as the plating progresses; this can lead to mass transport of hydroxide being a key factor of the system's kinetics.[39,86,95]

The dependence of the rate constant, k, on the temperature can be expressed most simply by the Arrhenius equation (Equation 43). For formaldehyde-containing baths, activation energies (E_a) of 60.9 kJ mol^{-1}[39] and 170 – 260 kJ mol^{-1} (depending on different additives used)[89] have been reported.

$$k = Ae^{\frac{-E_a}{RT}}$$ Equation 43

The individual polarization curves and their intersection have been traditionally thought useful in the investigation of the mechanism and kinetics of electroless deposition, according to the MPT.[96] Some authors, however, indicate that while it shows the electrochemical character of the process, the MPT is not particularly helpful in the determination of the rate limiting step or the kinetic laws.[94]

Although it has been widely used in the investigation of the mechanism and kinetics of electroless copper deposition, the validity of the MPT on this particular process has been questioned by several research groups. On a number of occasions, the individual polarization curves have been found not to coincide with the bath plating rates.[38,83,93] In some cases this has been attributed to local changes of pH or the activity of the copper complex.[38] The combination of EQCM and current measurements determined that the copper reduction is catalysed by formaldehyde, showing that the two half-reactions are not independent.[93]

The interdependence of the two half-reactions has also been suggested by studies which show that the polarization curves obtained through two-compartment cells, with both reactions coupled, are closer to mimicking the bath than those obtained individually. Although the potential was particularly close to that of the plating bath, the currents drawn from the two-compartment cell were always lower than expected from the rate of deposition of the bath.[83]

The use of fast solution exchange and EQCM in formaldehyde-containing baths, has determined that no direct homogeneous reaction between copper and formaldehyde occurs and an electrochemical mechanism, with electrons being transferred through a catalytic surface, is suggested; an interdependence between the anodic and cathodic reaction, through mutual catalysis, was detected, however.[37]

1.3.2 Additional Considerations

In some cases an initial step must be taken in order to start the copper deposition process. This process involves the incorporation of small amounts of noble metals such as Pt or Pd to the surface where deposition is going to occur.[4,23] For certain applications, such as ultra-large scale integration (ULSI), diffusion barriers, between the substrate and the copper deposit, and capping layers, above the copper to protect it from oxidation, are needed. Different materials have been used to form these layers; NiB, for example, has been used for both, while TiN or TiW work well as diffusion barriers and Co-based films are good capping layers.[18,29,46]

Adsorbed hydrogen produced during the anodic oxidation of the reducing agents is not oxidised on the copper surfaces, thus it is either incorporated into the deposits or evolved from the surface. Hydrogen evolution can be an important factor in mass transport and thus on the overall plating rate, by producing microconvection in unstirred baths.[8,25,88]

The use of additives is fairly common in electroless copper deposition; they are used for different reasons such as improving the stability of the bath, the quality of deposits or increasing the deposition rate. Common additives in copper deposition are 2,2-dipyridyl and the surfactant known as triton X-100, which reduce violent hydrogen evolution, thus producing smother and brighter deposits.[32,85,90] Oxygen (or air) is sometimes bubbled through the plating solution, in order to avoid homogeneous decomposition and disproportionation reactions involving Cu(I); in some cases oxidising agents, such as hydrogen peroxide, chromates and iodates, are included in copper baths in order to oxidise any Cu(I) to Cu(II).[9,24,25] Nitrogen gas is also used in order to remove the hydrogen formed at the surface, improving the morphology of the deposits obtained while avoiding the incorporation of hydrogen, which can leave voids in the copper structure and influence its properties.[19,85]

The morphology of the copper deposits is heavily influenced by the substrate, but, as mentioned above, plating conditions and hydrogen evolution can have important effects. The uniformity of the deposits seems to decrease with

increasing temperature, for example. The ductility of copper, on the other hand, has been found to increase with temperature, while decreasing with plating rate.[19,25]

1.3.3 Applications

An ample range of applications has been found for electroless copper deposition due to advantages over other plating techniques, such as low cost and fast yet selective deposition, with good uniformity and reproducibility.[20,29,85,97]

Electroless copper has been used in ULSI applications, due to its high capability for step coverage and via/trench filling. Copper deposits have been shown to exhibit lower bulk resistivity and to be more resistive to electromigration than the traditionally used aluminium, while being less susceptible to stress induced voiding.[18,20,29,32]

As well as being used for printed and integrated circuit manufacturing, electroless copper deposition is widely used as a starting point for the plating of other metals, due to its high selectivity and its ability to plate not only on conductive surfaces, but on plastics and other non-conductive or semiconductor substrates;[23,90] biomolecules, such as the tobacco mosaic virus, have been used as templates for nano-scale deposits, for example.[4]

1.4 Scope of the Present Work

The present work is an electrochemical study of copper electroless deposition, using dimethylamine borane as a reducing agent. The main aim of the investigation was to gain further understanding of the electroless deposition process as a whole using the Copper-DMAB system as a model, by employing relevant *in-situ* electrochemical techniques. A secondary purpose was an in-depth study of the electro-oxidation of DMAB, due to its increasing relevance, not only in electroless deposition but also in fuel cell technology.

The mechanism and kinetics of the Copper-DMAB system are investigated using mainly voltammetric techniques, in combination with a number of other electrochemical and spectroscopic methods. The present work contains five results chapters, preceded by a methods chapter and an experimental section. The first (Chapter 2) explains in some detail the techniques used throughout this investigation, in order to understand the copper-DMAB electroless system. The experimental section (Chapter 3), on the other hand, describes the equipment, cells and conditions used when carrying out the work.

The first two results chapters (Chapters 4 and 5) describe the investigation of the electro-oxidation of dimethylamine borane, which, as stated in Section 1.2, is not completely understood despite the fact that DMAB is a commonly used reducing agent. Different techniques were used in order to gain further understanding of the mechanism of DMAB oxidation, such as voltammetry, microelectrodes, chronoamperometry, single-crystal electrochemistry and FTIR; the results from the last two are described in detail in Chapter 5. It was found that adsorptive processes of not only the DMAB molecule, but its intermediates, play an important role on the oxidation mechanism and kinetics, with the initial dissociation process being catalysed by the presence of the metallic surface and the applied potential. Interactions with the gold oxide, formed at a certain potential window, provide further oxidation of the molecule and produce interesting voltammetric behaviour. At these potentials, in highly alkaline media, the dimethylamine is also oxidised on the electrode surface. It was established that on gold surfaces, DMAB can undergo a three-electron transfer at low overpotentials, while at higher potentials, further oxidation provides a total of up to six electrons. Borohydride oxidation was also studied, albeit in less detail, in order to establish whether the reducing agents share the same oxidation pathway, as discussed in Section 1.2.

A small section of the work, Chapter 6, is dedicated to the voltammetric study of the reduction of the copper complex. Copper(II) ions were complexed using 1,5,8,12-tetraazadodecane, in order to avoid the precipitation of copper hydroxides and oxides which form spontaneously in the alkaline media used in the electroless baths.[9] The voltammetric behaviour of the complex was studied on

different substrates and at different pH values, in the presence and absence of other bath components, such as triethanolamine.

A bipolar cell was used throughout Chapter 7. The voltammetric behaviour of this type of cell was studied using model reversible and quasi-reversible redox couples, in conjunction with numerical simulation of the system. A thorough understanding of the system led to its use in the investigation of electroless deposition. DMAB oxidation and copper electrodeposition were studied separately and then together using the bipolar cell configuration. It proved useful in studying the “coupling” effects between the two processes and the effect of the surface on each. The possibility of identifying side reactions was also shown, the importance of which lies in the fact that they might influence the efficiency of the electroless deposition process.

The last results chapter (Chapter 8) presents a detailed investigation of the kinetics of the copper-DMAB electroless system, using the typical electroless bath and a galvanic cell configuration. Rates of 0.05 $\mu m\ min^{-1}$ were obtained, with an induction time of 30 seconds, for the electroless bath, while the galvanic cell deposition rate is 0.03 $\mu m\ min^{-1}$. It was concluded that the MPT does not apply to this system, as the anodic and cathodic reactions are interdependent; in particular it was found that the copper substrates are more catalytic towards DMAB oxidation than gold surfaces. Faradaic efficiencies never reached 100%, indicating the presence of parasitic side reactions, especially prominent in the early stages of deposition. Characterization of the copper deposits was carried out and is also presented in this chapter: crystalline films were obtained, with a higher fraction of Cu(111) than that expected for polycrystalline copper, while the roughness of the deposits increased with deposition time.

Finally overall conclusions are presented in Chapter 9, where a brief description of further work that could, and should, be carried out is also included. Appendix A contains a list of publications and other scientific communications (talks and poster presentations) that have resulted from the work included here, while Appendix B provides a small explanation on the treatment of errors.

2 Electrochemical Methods

This chapter describes in some detail the theory behind the main electrochemical techniques employed throughout the present work.

2.1 Chronoamperometry

Chronoamperometry is a commonly used electrochemical technique which consists of applying a set potential to a stationary electrode in a non-stirred solution; as the name suggests the current produced is recorded as a function of time. This method is generally used in systems where there is a small area (of the electrode) to volume (of bulk electrolyte solution) ratio and mass transport is controlled by diffusion; migration should be avoided by addition of enough supporting electrolyte. A potentiostat is normally employed to record the current generated between the WE and CE, while controlling the voltage between the reference and working electrodes according to a function generator.[98,99]

A potential step method, chronoamperometry has a square-wave voltage signal (see Figure 3); the potential generally goes from an initial value, E_i, at which no reaction occurs, hence no current flows, to a set potential, E_s, where either an oxidation or a reduction takes place. If the overpotential applied, or the potential difference between the set potential and the standard reduction potential, is high enough the reaction is fast and only limited by mass transfer; all the electro-active species near the surface react immediately.[98,99]

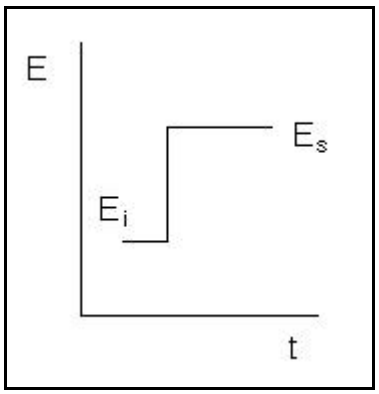

Figure 3. Potential scheme for chronoamperometry.

The concentration at the electrode surface is consequently zero and a depletion zone or diffusion layer, δ, is created, generating a concentration gradient. This layer produces diffusion from the bulk solution towards the electrode surface. The replenished electro-active species instantly reacts when it reaches the electrode and the process continues. As more of the reactant is consumed, δ grows with time. Diffusion away from the electrode also occurs, as the product of the electrochemical reaction, initially absent in solution, accumulates near the surface and eventually diffuses in the opposite direction to the original electro-active species.[99,100]

A concentration profile of a chronoamperometric experiment can be seen in Figure 4. This is a schematic of how the concentration changes with the distance from the electrode surface (x) at different times (t_i); the change of the diffusion layer thickness with time is also depicted (δ_i).

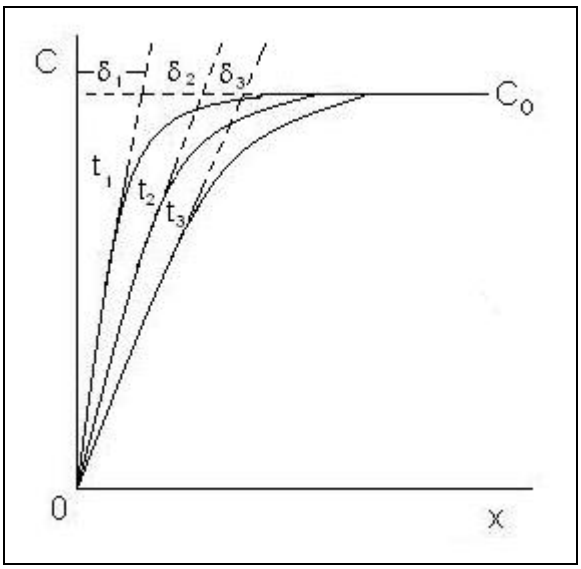

Figure 4. Concentration profile in chronoamperometry, where x represents the distance from the electrode surface and C_o is the bulk concentration.

The plots produced in chronoamperometry, depicting the current as a function of time, are called current transients. At very short times, very high currents are usually produced, although a finite rise time might be observed due to instrumental limitations or charging of the double layer.[100] After this the current drops as the electrolysis occurs, as shown in Figure 5. Although ideally the current should eventually decay to zero, at long times convection will play a role in mass transport and thus non-zero currents are often observed. Usually electrolysis times of no more than 20 seconds are employed in this method, although ranges from 10 μs to 300 s have been reported, as the appropriate time scale changes with the system studied.[98]

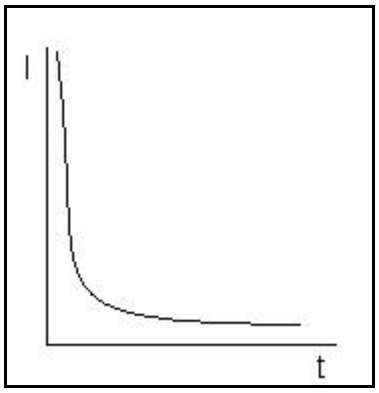

Figure 5. Current transient for chronoamperometry.

The shape of the current transients is a direct result of the effect of the concentration gradients and Faraday's law (Equation 44), which states that the

electric charge transferred, Q, is proportional to the moles of reactant, N, and the number of electrons transferred per molecule, n.

$$Q = nFN \qquad \text{Equation 44}$$

As the charge is the integral of the current with time, the instantaneous current is then proportional to the flux of the electro-active species, J, using Fick's diffusion laws (see Equation 45). On a planar electrode, the instantaneous current follows the Cottrell equation, Equation 46, where A is the area of the electrode, C is the concentration in the bulk of the solution, D is the solute diffusion coefficient and F is the Faraday constant.[99]

$$I = nFAJ = nFAD\left(\frac{\partial C}{\partial x}\right)_{x=0} \qquad \text{Equation 45}$$

$$I = \frac{nFACD^{1/2}}{\pi^{1/2}} t^{-1/2} \qquad \text{Equation 46}$$

The Cottrell equation provides a quantitative description of the currents produced in chronoamperometry at high overpotentials, where planar diffusion is the limiting mode of mass transport. A linear form of the data, depicting the current as a function of $t^{-1/2}$, is generally known as a Cottrell plot; deviations from linearity will sometimes occur at short and long times. As mentioned above, at short times deviations will mainly be due to instrumental error and/or charging currents, while at long times, convection might interfere.[98,100] The linear portion of Cottrell plots consequently marks the time frame over which there is a diffusive control on the rate of the electrochemical reaction.

2.2 Cyclic Voltammetry (CV)

Cyclic voltammetry is one of the most effective and versatile electrochemical methods, especially in the study of reaction pathways. Also known as sweep

voltammetry or potential sweep chronoamperometry, this technique has been used in a wide range of applications; from studying enzymatic catalysis and free radicals generated electrochemically, in organic chemistry, to the study of the ligand effect on the redox behaviour of metallic centres in complexes, in inorganic chemistry, CVs have also been used in more simple applications such as measuring effective electrode areas and the evaluation of new experimental configurations.[101,102]

This technique consists of measuring the current as the applied potential is varied linearly with time, at a constant rate, ν. At a certain point, the sweep direction is reversed and the potential is scanned back to the starting point, at the same rate.[99,100] Figure 6 shows the potential waveform used in a typical CV.

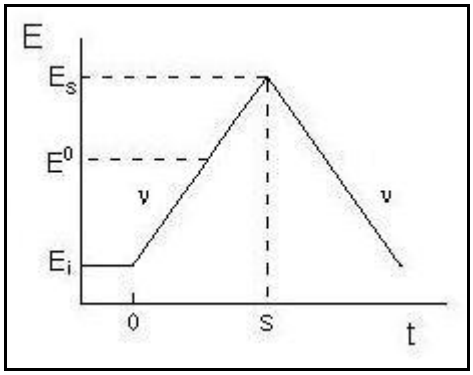

Figure 6. Potential scheme as a function of time for cyclic voltammetry.

In order to avoid altering the composition of the solution close to the electrode, the starting potential, E_i, is usually chosen so no reaction occurs on the surface, and thus no current is produced. The potential is then scanned up to a high enough overpotential that the concentration of the redox-active solute at the electrode surface is close to zero, passing through the standard reduction potential of the redox couple studied, E^0.[99,103]

As stated above, the current is recorded as the potential is swept; the graphs produced, for example the one seen in Figure 7, are called voltammograms. Initially no current flows, but as the potential gets close to the standard potential, the electrochemical reaction (in Figure 7, an oxidation) begins and a current is produced. Cyclic voltammetry depends basically on two processes: mass transport and electron transfer; as the solutions are normally unstirred and

migration is avoided, the main form of mass transport is diffusion. Diffusion is generally a slow process, so once high enough overpotentials are reached and the concentration at the electrode drops to zero, diffusion becomes the limiting step and the current decays as the depletion layer grows. This occurs at x,y = I_{pa},E_{pa} in the figure, after that point, the current drops with the square root of time as in chronoamperometry.[98,102]

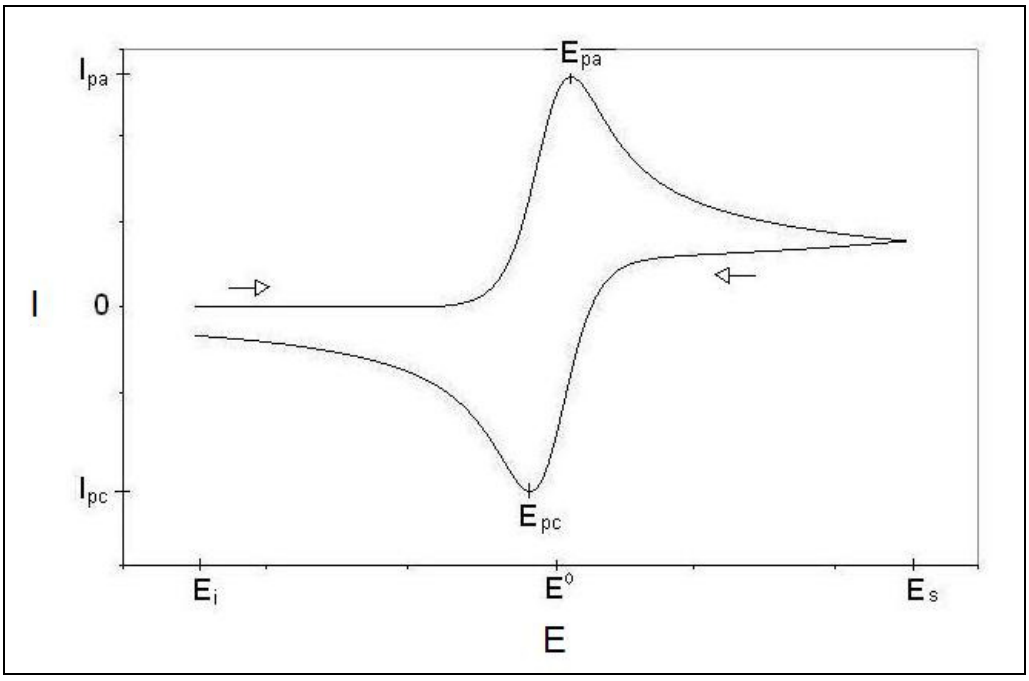

Figure 7. Cyclic voltammogram; the arrows indicate the direction of the sweep.

The way the current increases before the diffusion limitation sets in can be understood through the Nernst equation. For reversible reactions, this relationship (Equation 47) describes the concentration changes near the electrode; the applied potential, E, dictates the concentration ratio of the reduced (C_R) and oxidised species (C_O). The logarithmic relationship, giving an exponential relation between current and potential, determines the initially rapid growth of the current.[103]

$$E = E^0 + \frac{RT}{nF}\ln\left(\frac{C_O}{C_R}\right) \qquad \text{Equation 47}$$

Once the scan is reversed, the opposite process occurs, with the product of oxidation on the forward scan being reduced as E^0 is reached and exceeded. The

shape of the backward scan is similar to that of the forward, and the explanation for it is analogous.

The rate of the electron transfer, k_f, is also dependent on the potential, as can be seen in Equation 48, the simplest equation to describe the potential dependence of electron transfer rates, known as the Butler-Volmer relation. In Equation 48, k^0 is the standard heterogeneous rate constant and α is the transfer coefficient. The latter factor represents the symmetry of the transition state and takes values from 0 to 1, usually being approximately 0.5.[104]

$$k_f = k^0 e^{\left[-\frac{\alpha F}{RT}\left(E-E^0\right)\right]} \qquad \text{Equation 48}$$

In a completely reversible system, the oxidation and reduction peaks of the voltammogram have similar shape and size; the ratio of the anodic (I_{pa}) and cathodic (I_{pc}) peak currents should be one. Any deviation from unity might have mechanistic implications, such as for example chemical reactions involving the product of the forward scan.[99,100] The peak current for a reversible system is dependent on a number of factors, as can be seen in Equation 49, known as the Randles-Ševčik equation.

$$I_p = 0.4463\left(\frac{F^3}{RT}\right)^{1/2} n^{3/2} A D^{1/2} C \upsilon^{1/2} \qquad \text{Equation 49}$$

A more common form of the Randles-Ševčik equation can be seen in Equation 50, which results from using the usual electrochemical units (A for the current, cm^2 for the area, $cm^2\ s^{-1}$ for D, mol cm^{-3} for the solute concentration and V s^{-1} for the scan rate), at 25 ºC.

$$I_p = 2.69\times10^5 n^{3/2} A D^{1/2} C \upsilon^{1/2} \qquad \text{Equation 50}$$

For this relationship to hold, diffusion must be the only form of mass transport; high scan rates are avoided in order to ensure no kinetic effects are observed, as well as the increasing influence of charging currents and ohmic

drop. Although slower and faster scan rates are sometimes performed for particular systems, the usual experimental scan rate range is from 0.01 to 100 V s^{-1}.[98,99] Deviations from the Randles-Ševčik equation might also occur at extremely low concentrations, as the non-faradaic currents due to the charging of the double layer will have an important effect on the measured peak current.[100]

The standard reduction potential of a given redox couple is found somewhere between the anodic and cathodic peak potentials, E_{pa} and E_{pc} respectively; for a reversible system, E^0 is exactly halfway between them. Equation 51 shows that the separation between the peak potentials in a reversible system, at room temperature, is dependent on the number of electrons transferred.[99]

$$\Delta E_p = E_{pa} - E_{pc} \approx \frac{59}{n} mV \qquad \text{Equation 51}$$

The distance between the peak potential, E_p, and the half-peak potential, ($E_{p/2}$, the potential at which the current is half of the peak current) is also dependant on the number of electrons transferred; for a reversible system, Equation 52 describes the relationship.[98]

$$\left| E_p - E_{p/2} \right| = \frac{56.5}{n} mV \qquad \text{Equation 52}$$

Voltammograms with increasing peak separation with the scan rate indicate quasi reversible kinetics. When the peaks shift so far apart that no portion of them overlap on the potential axis, they are irreversible; this includes those systems that present no back peak, as in the case of chemical irreversibility, where the reverse reaction does not occur due to a chemical process consuming the species formed in the initial scan.[102]

Some relationships have been established for completely irreversible systems, although they are more complex than the reversible cases. The peak current is also dependent on the square root of the scan rate, as can be seen in Equation 53, which describes the case for room temperature and the usual

electrochemical units (noted above). The irreversible equation involves a few additional parameters to that of the reversible counterpart, with n_a being the number of electrons in the rate-determining step of the process.[99]

$$I_p = 2.99\times10^5 n(\alpha n_a)^{1/2} AD^{1/2}C\upsilon^{1/2}$$ Equation 53

The shape of the wave produced in totally irreversible systems is different from the reversible case; though the separation between the peak potential and the half-peak potential is also dependant on the number of electrons, it is smaller (see Equation 54).[98]

$$\left|E_p - E_{p/2}\right| = \frac{47.7}{n} mV$$ Equation 54

Quasi-reversible systems are harder to describe; the peak current, for example, is not proportional to $\nu^{1/2}$ in these cases.[102] Some simple numerical methods have been described in order to obtain the kinetic parameters of quasi-reversible systems, k^0 and α, using experimentally obtained values such as the peak separation as a function of scan rate or $E_{1/4}$, $E_{1/2}$ and $E_{3/4}$; $E_{1/4}$ and $E_{3/4}$ are the potentials at which the current is ¼ and ¾ of the peak current, respectively. Fitting experimental voltammograms to those obtained through numerical simulation has also been used for this purpose.[105,106]

There are a number of practical issues that must be addressed when using voltammetric techniques, besides those already mentioned above. The presence of oxygen, for example, can interfere with the results even if it does not chemically interact with the electro-active species. Oxygen is electrochemically active and can be reduced (to water, superoxide or peroxide); it must therefore be removed from the system, especially if its reduction potential lies within potential window of interest. The solvent must not only dissolve the electro-active species, but it must be stable at the conditions at which it is to be studied. The use of water, for example, is limited by its reduction and oxidation reactions, restricting the useful potential window between the evolution of hydrogen at the negative end and oxygen at the more positive potentials. The potential window also depends on the

nature of the working electrode and the supporting electrolyte. The electrolyte must provide sufficient ionic strength (usually a concentration 100 times larger than that of the species of interest is sufficient) and be compatible with the system.[101]

2.3 Electron Transfer Kinetics

In a simple chemical reaction, the rate constant is generally seen to be exponentially dependant on the temperature, following the Arrhenius equation (see Equation 43). For electrochemical reactions, the driving force is the applied potential, so for a constant temperature, the current, which is proportional to the rate of reaction, is exponentially dependant on the overpotential, η.[100]

When experimental conditions are such that mass transport effects can be neglected so the surface concentration is not appreciably different from the bulk, the Butler-Volmer equation (Equation 55, where $I_0 = nFAk_0 C_{surface}$) can be used to describe the behaviour of the current as a function of overpotential. This equation will hold true when the current is less than 10% of the limiting current, either cathodic or anodic.[98] In it, I_0 is the exchange current, which is proportional to the rate constant of electron transfer at zero overpotential (k^0 in Equation 48).

$$I = I_0 \left[e^{\frac{-\alpha F}{RT}\eta} - e^{\frac{(1-\alpha)F}{RT}\eta} \right] \qquad \text{Equation 55}$$

For large overpotentials, where one of the two reactions (reduction or oxidation) is practically negligible, the Tafel approach may be applied. This description, which described the magnitude of the currents, has slightly different expression for the cathodic and anodic reactions, as seen in Equation 56 and Equation 57.

$$I_a = I_0 e^{\frac{(1-\alpha)F}{RT}\eta} \qquad \text{Equation 56}$$

$$I_c = I_0 e^{\frac{-\alpha F}{RT}\eta}$$ Equation 57

Kinetic parameters of an electrochemical reaction can be obtained through analysis of the logarithm of the current as a function of the overpotential, known as Tafel plots. Although they should be linear, Tafel plots can have deviations at low overpotentials, due to the influence of both anodic and cathodic reactions occurring at appreciable rates. Deviations from linearity can also be found at very large values of η, due to mass transport limitations. Reaction with fast kinetics do not follow Tafel behaviour, as they are limited by mass transport, which is not taken into account in the Tafel equation; consequently Tafel behaviour can be considered a measure of irreversibility in a system.[98,100]

2.4 Four-Electrode Voltammetry

This technique is similar to the cyclic voltammetry described above, but it is designed to study charge transfer across an interface, rather than simply electronic transfer from/to an electrode. Although it has found other applications, this method is mainly used to probe charge transfer across liquid/liquid (L/L) interfaces and has been largely developed for this purpose.

In liquid/liquid voltammetry two immiscible liquids, usually an aqueous and an organic phase, are placed in contact with each other, while a counter electrode and reference electrode immersed in each phase allow the potential to be swept in a similar manner to that described in Section 2.2. The polarization of the interface can produce a current due to ionic or electronic transfer through the interface. In the first case, charged species transfer from one phase to the other; in the second, opposite reactions occur on each side of the interface: the electrons produced through an oxidation in one phase go through to the second phase causing a reduction process. In both cases, the process depends on the mass transport to and from the interface, on both sides, as well as the interfacial reaction itself.[107,108]

The current produced in a liquid/liquid system flows through the counter electrodes placed in each phase; they are connected through a potentiostat allowing the measurement of the current magnitude. The applied potential, on the other hand, is controlled through the reference electrodes placed within each phase, near the interface through luggin capillaries; the potential difference between them (ΔE) controls the polarization of the interface, according to Equation 58, where $\Delta_B^A\varphi$ is the Galvani potential difference at the interface between phases A and B. The other two terms are due to the reference electrode used in each phase; an additional term might be needed if an aqueous reference is used in the organic phase.[109,110]

$$\Delta E = \Delta_B^A\varphi + \Delta\varphi_{RE_A} - \Delta\varphi_{RE_B} \qquad \text{Equation 58}$$

In the bimolecular electron transfer reactions that occur at L/L interfaces, the equilibrium potential also follows the Nernstian behaviour. In these cases, the potential is related to the concentration of the four species involved: reduced (R) and oxidised (O) forms in each phase, as seen in Equation 59.[111]

$$E = E^0 + \frac{RT}{nF}\ln\left(\frac{R_A O_B}{O_A R_B}\right) \qquad \text{Equation 59}$$

The voltammetric behaviour observed might at first glance indicate that the kinetics of the liquid/liquid system depends not only on the electron transfer rate, but also on the concentrations of all the species involved. It has been proven, however, that the behaviour observed is not necessarily indicative of slow electron transfer kinetics, as might be initially assumed: although the potentials at which the transfer occurs change with concentration, the peak potentials do not always shift with scan rate, indicating diffusive rather than kinetic control.[111-113]

Equation 59 reduces to Equation 47, if a large excess of reactants is present in one phase, leading to the process being mainly dependent on the concentration of reactants in the other phase. As this simplifies the understanding of a particular system, it is consequently usual for L/L electron transfer to be studied with a high

relative excess of reagents in one phase. It has been shown, however, that even at high relative concentrations in one phase the diffusion of all species has an effect on the voltammetric behaviour.[111,114]

Only when the concentrations of both species in one phase (oxidised and reduced) are high and equal does the voltammetry become dependent on the other reactant and the behaviour of a three electrode system can be obtained; a peak separation of ~60 mV can be seen and the equations given in Section 2.2 apply. This allows for the transfer potentials to be predicted from the corresponding three electrode cell behaviour.[113,114]

2.4.1 Bipolar Voltammetry

Although less common than liquid/liquid systems, bipolar voltammetry is another form of four-electrode voltammetry. The approaches are very similar, with the main difference being that an electronic conductor is placed between the two phases, in the bipolar case. This allows electronic transfer between the two phases, while inhibiting molecular transport completely.[115]

As described for electron transfer in liquid/liquid voltammetry, the bipolar configuration potential is controlled through the reference electrodes. The potential difference between the two half-cells (each side of the electronic conductor) can be swept in one direction and then the other to produce voltammograms. A schematic of the bipolar voltammetric process can be seen in Figure 8, where EC is the electronic conductor placed between phases A and B. On the forward scan, the reduced species in phase B is oxidised, producing the electrons needed for the oxidised species of phase A to be reduced; when the scan is reversed, the opposite reactions occur: the reduced species in phase A is oxidised, reducing the oxidised form in phase B.

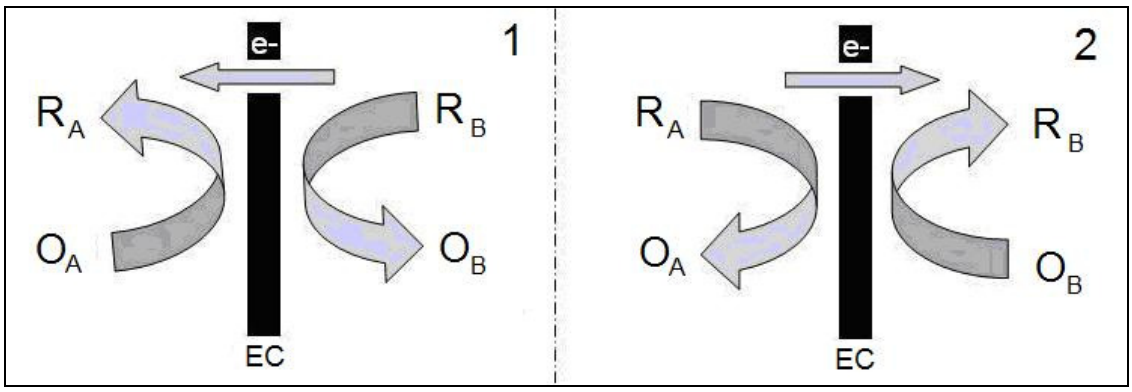

Figure 8. Schematic of the reactions that occur during four-electrode voltammetry in a bipolar cell. 1 – forward scan, 2 – reverse scan.

This type of system has been used in order to distinguish between electronic and ionic transfer in liquid/liquid systems by Hotta *et al.* They have found that although the thermodynamics of the conductor-separated system is equal to that of the L/L equivalent, the kinetics and concentration effects may vary due to the influence of ionic transfer in the latter. They have also established that numerical simulations are very useful in further understanding these systems and extracting parameters such as the standard potentials, rate constants and transfer coefficients.[115-117]

Bipolar cells have also been used successfully to process and characterise semiconductors, by using the semiconductor to separate the two solution phases; in some cases, the same electrolytic solution is actually used on both sides of the semiconductor. In this case, in addition to the control of the electrochemistry through the four electrode configuration, one side of the semiconductor can be illuminated, while the other remains in the dark, in order to create equal and opposite currents on each side of the electrode.[118] More recently, a variation of these cells has been used in the splitting of water to produce hydrogen and oxygen; in that particular case, the energy input came solely from illumination and not through the applied voltage, while the photocurrent produced was measured. A series of semiconductors has been used recently as bipolar electrodes, within the cell, in order to improve the voltage generated and thus the hydrogen production.[119]

The introduction of an electronic conductor to separate the two phases has several advantages. For example, it allows the study of wider potential windows

as it eliminates transfer of supporting electrolyte and other components, which is a recurring problem in L/L systems.[114,120] The separation of the phases also implies that not only immiscible liquids can be used; as they are not in contact miscible and even identical solvents can be used on either side of the conducting phase.

2.5 Microelectrodes

Microelectrodes, sometimes called ultramicroelectrodes (UME), have become very useful tools in electrochemistry, as they allow the study of electrode kinetics under steady-state conditions.[121] Though it is generally accepted that any electrode with at least one dimension in the range of 10 nm to 50 μm constitutes a microelectrode, there is no real agreement on their actual definition; any electrode smaller than the diffusion layer formed during an electrochemical experiment can be termed an UME.[98]

Fabricating UMEs is not technically easy, however, many different types, such as disks, spheres, hemispheres, cylinders and bands have been successfully made and applied. Using microelectrodes can result in mass transport limited by 2-dimensional or 3-dimensional diffusion; the current density increases with respect to macroelectrodes and the small currents produced are not proportional to the area of the UME. There are many advantages to the use of microelectrodes, in spite of the complicated mass transport and the possible decrease in the signal to (electrical) noise ratio.[121]

A steep concentration gradient is produced with the use of microelectrodes, as the mass transport increases due to small depletion layers. The faradaic currents are consequently increased, while the non-faradaic remain small and unchanged as they are proportional to the electrode area. This enhances the ratio between these currents and improves the sensitivity of the technique.[100]

The currents obtained are steady-state or quasi steady-state, facilitating kinetic measurements. Highly accurate measurements have been reported in resistive solutions and the use of large amounts of supporting electrolyte can be

avoided, as the low absolute currents mean that Ohmic drop is less significant. Fast evaluations can be made, which allow the determination, for example, of local concentration profiles.[100,121]

The steady-state response of voltammograms at disk microelectrodes, encapsulated in relatively large insulating materials, is described by Equation 60, where r is the radius of the disk; this relation is valid for infinitely large volume (of solution) to area (of electrode) ratios. The equation shows that the current at a disk UME is independent of scan rate; this is true as long as the scan rate is significantly smaller than RTD/nFr^2.[121]

$$I_{ss} = 4nFDCr \qquad \text{Equation 60}$$

In chronoamperometry, the current initially follows the Cottrell equation (Equation 46), but at longer times a steady-state current is produced, which is also described by Equation 60; a transition period between the initial time-dependent linear diffusion (Cottrell) and the final time-dependent radial diffusion (steady-state condition) is observed in the current transients.[98,121]

2.6 Rotating Disk Electrode (RDE)

Hydrodynamic techniques in electrochemistry consist of methods in which either the solution or the working electrode are set in motion, in order to create a convective flow. Convection, a form of mass transport which implies the movement of the solution, is much more efficient than diffusion, thus the effects of diffusion are reduced. The control of convective flow improves reproducibility and sensitivity in electrochemical methods, while in some cases it also allows the measurement of kinetic parameters. Although different types of electrochemical hydrodynamic methods have been developed, such as channel electrodes and wall-jet electrodes, the rotating disk electrode is by far the most commonly used.[100]

The RDE consists of a conductive disk encapsulated in a rod of insulating material, with an internal electrical connection. The rod rotates about its own axis at a specific frequency, f (revolutions per second). The angular velocity, ω, is a more useful term in describing the RDE; it is equivalent to 2πf.[98] The convective flow produced by the rotation of the electrode can be seen in Figure 9.

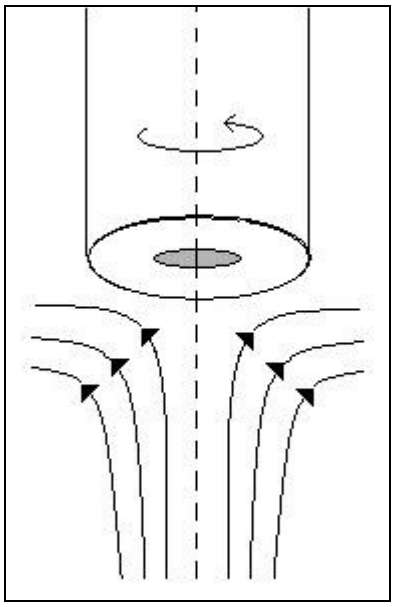

Figure 9. Schematic of the convective flow at a rotating disk electrode.

The hydrodynamic equations have been rigorously solved for the rotating disk electrode in the steady state; when ω is fixed and a steady velocity profile is reached, a steady-state limiting current is produced. When the concentration of the electro-active species at the surface is zero, the limiting current can be expressed through the Levich equation (Equation 61, where υ is the kinematic viscosity of the solution).[98,100]

$$i_l = 0.62nFAD^{2/3}\upsilon^{-1/6}C\omega^{1/2} \qquad \text{Equation 61}$$

Although convection is the main form of mass transport in these systems, there is a thin layer of solution, δ, adjacent to the electrode surface in which diffusion plays a significant part in the mass transport of the electroactive species; this explains why the diffusion coefficient appears in the Levich equation. The thickness of the diffusion layer depends on the rotation speed, kinematic viscosity

of the solution and the diffusion coefficient of the electro-active species, as seen in Equation 62.[100]

$$\delta = \frac{1.61 \upsilon^{1/6} D^{1/3}}{\omega^{1/2}} \qquad \text{Equation 62}$$

The Levich equation describes the limiting current of a voltammogram or chronoamperometry; for a reversible redox couple, however, the current at any point of voltammogram is dependent on $\omega^{1/2}$. Deviations from this relationship consequently indicate a kinetic effect on the electron transfer. The Koutecký-Levich equation, Equation 63, describes the current at a RDE when a kinetically hindered redox reaction occurs.[98]

$$\frac{1}{i} = \frac{1}{i_K} + \frac{1}{i_l} = \frac{1}{nFAk_f C} + \frac{1}{0.62nFAD^{2/3}\upsilon^{-1/6}C\omega^{1/2}} \qquad \text{Equation 63}$$

In Equation 63, k_f represents the kinetic limitation to the electron transfer reaction and as mentioned in Section 2.2, it is related to the standard heterogeneous rate constant through Equation 48. Koutecký-Levich plots, depicting i^{-1} as a function of $\omega^{-1/2}$, are useful tools in determining values of k^0 and α; the intercept of these graphs, i_K, at different potentials allows the calculation of the kinetic parameters.[98]

2.7 Spectroelectrochemistry: *In-Situ* Fourier Transform Infrared Spectroscopy (FTIR)

Spectroelectrochemical techniques consist, as the name implies, of combined spectroscopic and electrochemical methods; electrochemical processes are followed through the absorption or emission of some form of electromagnetic radiation. Spectroelectrochemistry can be *in-situ*, when electrochemical and spectroscopic techniques are used simultaneously, or *ex-situ*, by taking aliquots of solution as the electrochemical experiment is carried out or by comparison of

spectra taken before and after an electrochemical reaction has taken place, for example.[100]

Infrared (IR) spectroscopy allows the study of chemical systems through the use of electromagnetic radiation with lower frequencies than those of red light. The frequencies of infrared light (approximately 10^{13} – 10^{14} Hz) correspond to the frequencies of molecular vibration, and thus absorption of the infrared light can induce vibrational excitation of molecules. Molecular vibrations can be resolved into different normal modes, namely stretching, where atoms move towards and away from each other, and bending, when the bond angles periodically change. The frequencies at which the molecular bonds vibrate depend on the mass of the atoms involved and the rigidity of the bonds, consequently different bonds or functional groups will vibrate and absorb radiation at different frequencies. A full IR spectrum will show bands, which are signals associated with the absorption due to a particular functional group and relatively independent of other groups in the molecule, at characteristic frequencies.[98,122]

Species at the electrode surface and in a thin layer of solution close to the electrode can be studied through infrared spectroelectrochemistry. This technique has been used to study the electrical double layer and reactants, intermediates and products of electrochemical systems, both adsorbed on the electrode or in solution near to the surface. Although there are several configurations, *in-situ* IR is generally performed through an external reflection mode. Figure 10 shows how the infrared light goes through an optically transparent window and through the solution, before being reflected at the electrode surface; the reflected radiation goes back through solution and window towards the detector. Most solvents have strong IR absorption, so the layer of solution through which the radiation passes must be thin (below 100 μm). Even with these precautions, the absorbance of the species of interest at/near the electrode is usually very small in comparison to those of the bulk. Modulation or difference techniques are generally used in order to improve the signals obtained; both the applied potential and the light polarization can be modulated.[98] The polarization of the light also distinguishes between solution and surface-bound species, as polarization perpendicular to the plane of reflection (s) is only active towards molecules in solution, while p-

polarised light (parallel to the plane of reflection) is active for both solution and surface-bound species.[123]

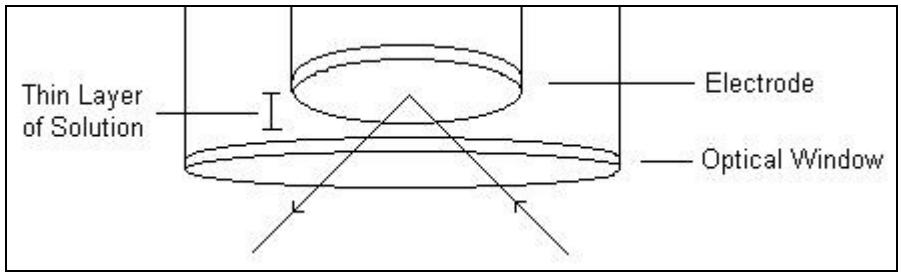

Figure 10. Schematic of an external reflectance configuration, where the arrows indicate the radiation pathway.

Fourier transform methods are used to obtain many interferograms, or recordings of intensity as a function of mirror position, in short amounts of time. These are averaged and converted back to conventional IR spectra by inverse Fourier transform. The spectra are obtained at separate potentials, usually one where no electrochemical reaction occurs and one where it does, and the absorbances at corresponding wavelengths are subtracted. Due to the subtraction, the background contributes with a negative sign, and consequently positive and negative peaks appear in the spectra obtained.[98]

In the last few decades, FTIR spectroelectrochemistry has been used in a wide range of applications, starting with the oxidation of methanol and ethanol, due to their interest for fuel cells, to the study of anion adsorption on different metals, such as Pt and Au; the effect of sulfates, phosphates, carbonates and cyanide on the electrochemical double-layer has been studied, for example.[123] The oxidation of other organic molecules, particularly water contaminants, has been investigated using *in-situ* FTIR: the oxidation kinetics of p-chlorophenol and p-nitrophenol has been followed through the measurement of the reaction products; the complete mineralization to CO_2 has been particularly characterised through this method.[124] The adsorption of amino acids and their electrochemical behaviour, for example, has been studied using this technique; it has been found that on Pt the reversible adsorption of glycinate occurs, alongside the strong adsorption of cyanide produced from the oxidation of glycine.[125] Self-assembled monolayers (SAMs) have been also probed using FTIR, with the structural reorientation of ferrocenyl alkyl thiols observed on gold when the ferrocene group

undergoes a redox reaction; the *in-situ* spectroelectrochemical method also helped to determine that longer alkyl chains produce more ordered SAMs on the surface.[126] In yet a different study, the adsorption sites of CO on Pt, as well as its oxidation intermediates and products have been investigated as a function of applied potential and electrode surface treatment.[127] FTIR spectroelectrochemistry has been widely used in the investigation of the adsorption and redox reactions of carbon monoxide and carbon dioxide, the electrochemistry of small organic molecules and the characterization of the double layer in the presence of species such as water, hydrogen and different anions.[123]

3 Experimental

In this chapter the experimental conditions used, including reagents, materials and equipment, are described. The different experimental set-ups are also depicted and explained in detail.

3.1 Chemicals

The reagents used throughout this work are presented in Table 1. All solutions were prepared using deionised water (of 18 MΩ cm resistivity) prepared using a reverse osmosis unit (Millipore) coupled to an Elga “Purelab Ultra” purification system (Veolia Water Systems). Unless otherwise stated, when used for electrochemical measurements, solutions were deoxygenated by bubbling argon through the cell for no less than 20 minutes. If the same solution was used for more than one experiment, the solution was bubbled for at least 2 minutes between runs, in order to remove any oxygen re-dissolved during the preceding measurement.

Table 1. Specification of the reagents used.

Name	Purity	Supplier
Acetone	99+%	Fisher
Agar	-	Sigma-Aldrich
Ammonium Hydroxide	ACS	Sigma-Aldrich
Argon	99.998%	BOC
Boric Acid	>98.5%	Sigma-Aldrich
Cerium(III) Sulfate, octahydrate	-	Fisher
Cerium(IV) Sulfate	98%	Alfa Aesar
Copper(II) Sulfate, pentahydrate	99.9%	Sigma-Aldrich
Diamond Suspension	1.0, 0.25, 0.10 μm	Kemet
Dimethylamine Borane (DMAB)	97%	Sigma-Aldrich
Dimethylamine Solution	40% in water	Sigma-Aldrich
Ethanol	99.99%	Fisher
Hexaammineruthenium(II) Chloride	>99.9%	Sigma-Aldrich
Hexaammineruthenium(III) Chloride	98%	Sigma-Aldrich
Hydrochloric Acid	37%	Sigma-Aldrich
Hydrogen	-	BOC
Hydrogen Peroxide	30%	Sigma-Aldrich
Nitric Acid	69%	BDH Chemicals
Potassium Chloride	99.5%	Sigma-Aldrich
Potassium Ferricyanide	>99%	Sigma-Aldrich
Potassium Ferrocyanide	>99%	Sigma-Aldrich
Potassium Hydroxide	99.99%	Sigma-Aldrich
Potassium Perchlorate	>99%	Sigma-Aldrich
Potassium Permanganate	-	Sigma-Aldrich
Sodium Borohydride	99%	Sigma-Aldrich
Sodium Sulfate	99%	Sigma-Aldrich
Sulfuric Acid	95+%	Fisher
1,5,8,12-Tetraazadodecane	94%	Sigma-Aldrich
Triethanolamine (TEA)	98%	Alfa Aesar

3.2 Electrodes

Different electrodes were used throughout this work; some were obtained from commercial suppliers and others were made in-house. A list of all electrodes and electrode material employed is presented in Table 2.

Table 2. Electrodes and electrode material.

Electrode / Material	Specifications	Supplier
Carbon Graphite Rod	6.3 mm diameter	Alfa
Glass Tubes	4 mm diameter, ~5.5 cm long (with Porous Tips)	CH Instruments, Inc.
Glassy Carbon Disk	3 mm diameter, enclosed in Kel-F	CH Instruments, Inc.
Gold Bead Single-Crystals	Au(111), Au(100) and Au(110)	icryst
Gold Disk	2 mm diameter, enclosed in Kel-F	CH Instruments, Inc.
Gold Foil	1 cm^2 (0.25 and 0.50 mm thickness)	Goodfellow Cambridge Limited
Gold Microdisk	10 μm, encapsulated in glass	CH Instruments, Inc.
Gold Single-Crystal Disks	Au(111), Au(100) and Au(110)	MaTeck GmbH
Heat-Shrinkable Tubing	with adhesive inner liner	Maplin Electronics Ltd.
Parafilm M	-	Pechiney Plastic Packaging Company
Platinum Disk	2 mm diameter, enclosed in Kel-F	CH Instruments, Inc.
Platinum Gauze	82x82 wires/in, 65% open area	Goodfellow Cambridge Limited
Platinum Wire	0.5 mm diameter	Advent Research Materials, Ltd.
Silver Paint	-	SPI Supplies
Silver Wire	0.75 mm diameter	Advent Research Materials, Ltd.

3.2.1 Reference Electrodes (RE)

Most of the work was done using Ag/AgCl reference electrodes. These were prepared by immersing a silver wire and a graphite rod in a 0.1 M KCl solution and connecting them to the anode and cathode, respectively, of a 9 V battery. After fifteen minutes, the silver wire was disconnected and removed from solution. It was then placed inside a small glass tube filled with 3.0 M KCl; one end of which was sealed with a porous tip. Parafilm was wrapped around the top of the tube, with the silver wire protruding from it. The electrode was stored at all times in 3.0 M KCl.

The Ag/AgCl reference electrode was frequently renewed by stripping the silver chloride from the wire, through immersion in concentrated ammonium hydroxide. The wire and the glass tube were cleaned by placing them in concentrated nitric acid and agitating them using an ultrasound bath. The preparation procedure was then repeated using fresh KCl solutions.

For single-crystal electrochemical experiments, the reversible hydrogen electrode (RHE) was used as reference. This electrode consists of a platinum mesh electrode immersed in the electrolyte solution used in a particular experiment. The electrode sits in a separate compartment of the electrochemical cell, through which hydrogen gas is bubbled continuously, and is connected to the rest of the cell through a glass valve. The electrode was freshly made for each set of experiments and the platinum gauze was flame-cleaned before being immersed in solution. The electrodes were left to stabilise for at least 20 minutes before use.

3.2.2 Counter Electrodes (CE)

In general, platinum counter electrodes were used; in cases where the use of platinum should be avoided, however, gold foils and graphite rods were employed. The platinum counter electrodes were prepared by spot-welding a rolled platinum gauze to a platinum wire; they were flame-cleaned with a Bunsen burner. The graphite rods were used as bought, and rinsed with de-ionised water before use. The gold foils were connected to platinum wires using silver paint and

the connection was insulated using heat-shrinkable tubing. These electrodes were cleaned following the procedure described below for gold disk working electrodes. Gold counter electrodes were also used in single-crystal experiments, these consisted of gold foils attached to gold wires; they were flame-cleaned and immediately rinsed with de-ionised water before being introduced in the electrochemical cell.

3.2.3 Working Electrodes (WE)

The working disk electrodes were cleaned before experiments using the following procedure for each surface. They were all polished with diamond suspensions of varying sizes (1 and 0.25 μm for macroelectrodes, and 0.25 and 0.1 μm for microelectrodes) on a polishing cloth. They were thoroughly rinsed with deionised water after each suspension was used. The glassy carbon disk electrodes were then immersed in a 1:1 mix of ethanol and water and placed for one minute in an ultrasound bath; acetone and water were used in place of the ethanol/water mix for the gold and platinum electrodes, respectively.

The gold and platinum disk electrodes and the gold microelectrode were placed in 0.1 M H_2SO_4 in the electrochemical cell for further cleaning. Voltammetric scans were performed between 0.00 and 1.60 V vs. Ag/AgCl for the gold electrodes and -0.25 and 1.30 V for the platinum electrode, until reproducible voltammograms were obtained; typically no less than 15 cycles were performed. Thorough electrochemical cleaning was completed, whenever necessary, by consecutive potential steps at 1.80 and 0.00 V for the gold electrodes and 1.60 and -0.30 V for the platinum electrodes.

3.2.4 Single-Crystal Electrodes

Two types of gold single-crystal electrodes were used; the first, bead single-crystals, for voltammetric analysis and the other, disk single-crystals, for *in-situ*

FTIR measurements.[i] Both types of electrodes were connected to the potentiostat and an initial potential was applied, at which no reactions occur, before they were introduced in solution.

Bead-type electrodes were attached to copper wires, which were then introduced in glass tubes. These electrodes were flame-annealed with a Bunsen burner, "quenched" with de-ionised water and dried in an Argon environment, before being immersed in solution. They were used in a "meniscus" configuration, which is achieved by immersing the electrode in the solution and pulling it out to create the meniscus (see Figure 11). This is done in order to have only the flat desired phase in contact with the electrolyte solution, and assure a constant area.

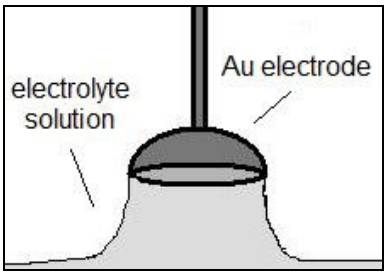

Figure 11. Meniscus configuration of the bead single-crystal electrodes.

The single-crystal disks used for the spectroscopic experiments were initially treated in a similar manner to the bead electrodes: they were attached to platinum wires and introduced in glass tubes. Flame-annealing, quenching and drying of the electrodes was done, as described above for the beads, prior to their introduction to the spectroelectrochemical cell. These electrodes were not used in the meniscus configuration described above, however. They were, on the contrary, completely submerged in solution and pressed into the optical window at the bottom of the cell (see Section 3.3.2), in order to obtain a thin layer of solution as the optical pathway.

[i] Single-crystal electrochemical experiments were carried out with Marc Koper's group in the Leiden Institue of Chemistry, at Leiden University. Training in these techniques was received from Dr Paramaconi Rodriguez, Postdoctoral Reasearcher at Leiden University.

3.3 Electrochemical Configurations

A variety of experimental configurations were used throughout this work. In particular, three electrode, spectroelectrochemical, galvanic and bipolar cells were employed; these are described in detail in this section. A simple set-up, also described in this section, was used to carry out the traditional electroless deposition process.

3.3.1 Three Electrode Cell

Conventional three electrode, one compartment, cells were used for a number of traditional electrochemical techniques such as voltammetry and chronoamperometry. The cells were made in-house[ii] and a schematic can be seen in Figure 12.

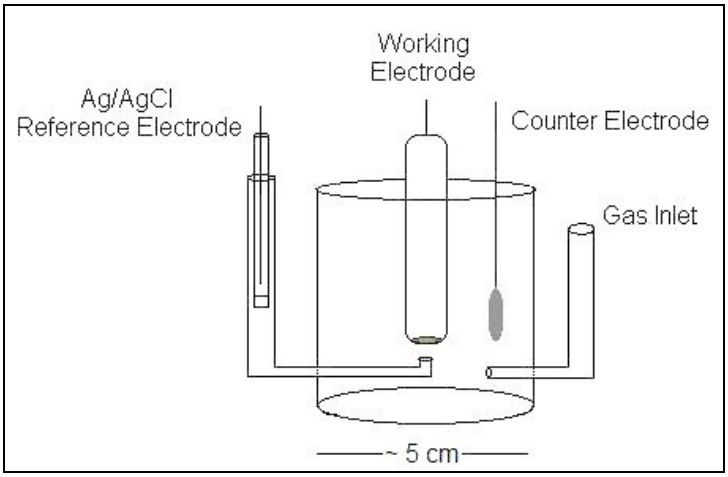

Figure 12. Schematics of the three electrode cell.

The cells are made entirely out of glass, with a Teflon lid; a perfect fit is achieved thanks to an O-ring placed around the lid. The reference electrode, on the left hand side of the figure, is connected to the solution adjacent to the working electrode through a Luggin capillary tube, located as close as possible to the working electrode surface. The working and counter electrodes are introduced

[ii] All the cells, except those used in single-crystal electrochemistry, were made by the glassblower (Mr David Gordon) and the mechanical workshop (Mr Christopher Slann) of the School of Chemistry at the University of Manchester.

to the cell, through holes in the lid. Opposite the reference electrode is a gas inlet, used to bubble argon through the solution, for degassing purposes; the lid possesses an additional small hole to liberate any gasses and avoid the build-up of pressure.

The cells were cleaned using deionised water and acetone before each experiment, with more thorough cleaning regularly carried out with sulfuric and nitric acid.

A very similar three electrode cell was used for single-crystal electrochemical experiments; the main difference consisted of air-tight fits of the electrodes to the glass cell through glass holders, without the need for Teflon lids. More thorough cleaning was done for this cell and all glassware used in experiments in which it was employed. The cell was boiled in concentrated nitric and sulfuric acid and then rinsed with de-ionized water. Fresh de-ionized water was then boiled in the cell three consecutive times.

3.3.2 Spectroelectrochemical Cell

A spectroelectrochemical cell was used when carrying out *in-situ* FTIR and voltammetric experiments. It is similar to the three electrode cell described in the previous section, as can be seen in Figure 13. The main difference is that the bottom of the cell consists of a flat CaF_2 window, *in lieu* of the glass that constitutes the rest of the cell. This optical window is screwed onto the rest of the cell immediately before use and is otherwise kept in an air-tight container. The cell is made to fit exactly into the FTIR spectrometer, with the light coming through the optical window, up to the electrode surface where it is reflected and sent to the detector.

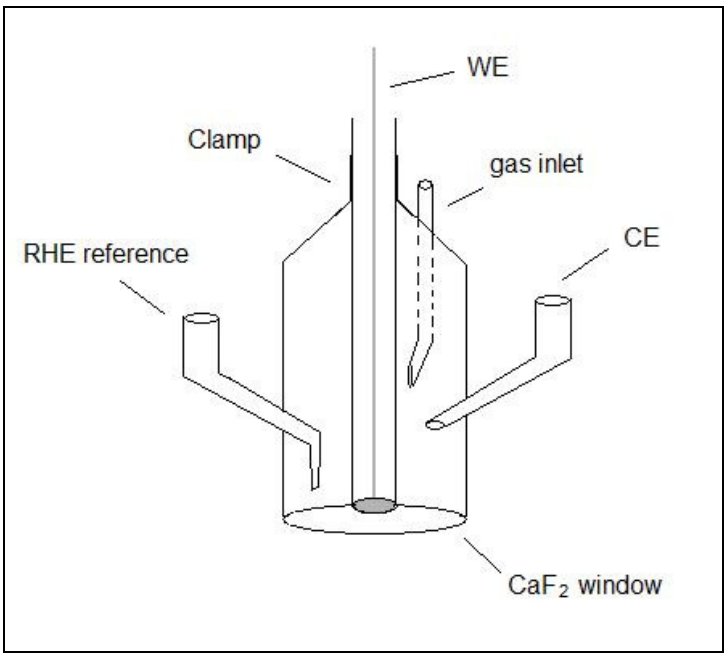

Figure 13. Schematic of the spectroelectrochemical cell.

The working electrode, once fitted into its glass tube and cleaned (see Section 3.2.4), is introduced through the top of the cell and pressed onto the optical window, until a high enough light intensity is obtained with the spectrometer. The electrode is then clamped into place and the reference spectrum is taken.

The spectroelectrochemical cell, as well as any glassware used in experiments in which it was employed, was cleaned by immersing overnight in a solution of potassium permanganate. Traces of this solution were removed with a dilute mix of hydrogen peroxide and sulfuric acid; the cell was finally rinsed with de-ionised water and left to dry before use.

3.3.3 Electroless Bath

The electroless baths simply consisted of 50 mL Pyrex beakers, fitted with Teflon lids (with O-rings as described above). The lids had holes drilled into them in order to introduce the gold disks used as the plating surfaces. These containers were placed in a metallic stand immersed in a thermostatic water bath set at 55 ºC (see Figure 14).

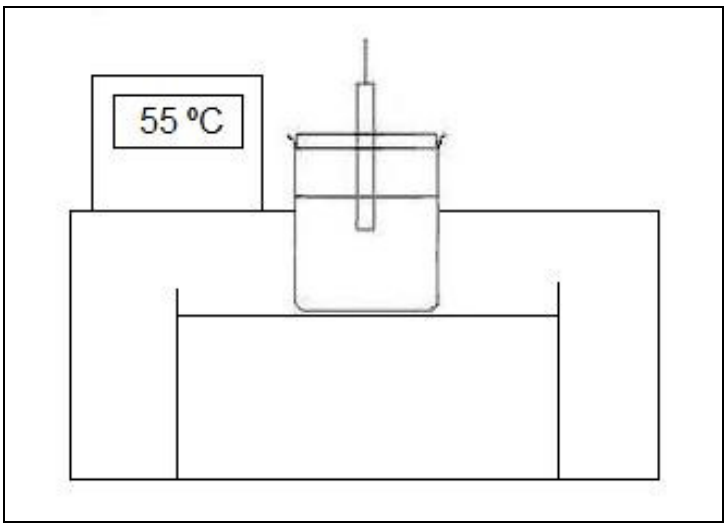

Figure 14. Electroless Bath.

When samples for AFM, XRD or elemental analysis were made, where gold disk electrodes were not used, the plating surfaces were simply dropped into solution and at the appropriate time the solution was decanted from the beaker.

Due to the highly unstable nature of the electroless process,[8,16] cleanliness was of upmost importance; any active nuclei, such as dust or metal particles, could trigger homogenous decomposition of the solution over time.[25] The beakers used for electroless bath were immersed in nitric acid for no less than 12 hours before use. They were then rinsed with deionised water and allowed to dry before being filled with the solution of choice.

3.3.4 Galvanic Cell Configuration

A galvanic cell was used in order to study the interdependence of the anodic and cathodic reactions of the electroless process, as well as to gain *in-situ* information from the process, such as potentials and currents. A schematic of the cell can be seen in Figure 15, where again the cells are made of glass and are fitted with Teflon lids with the appropriate holes.

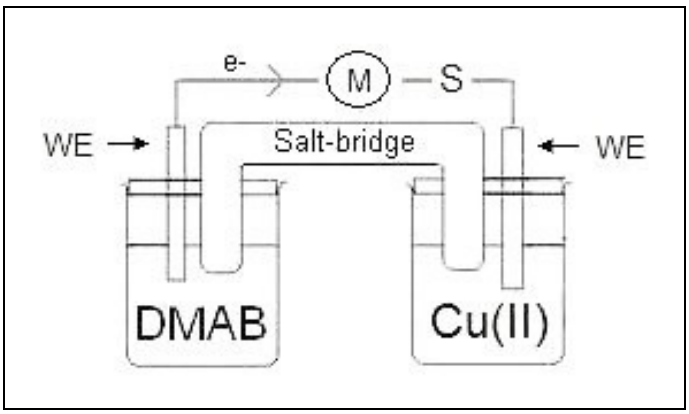

Figure 15. Schematic of the galvanic cell.

The galvanic cell configuration separates the two half-reactions, but allows electronic and ionic transfer between them. The anodic oxidation (left) produces electrons which are transferred to the cathodic half-cell (right) in order to produce the reduction reaction. A digital multimeter (described in detail in Section 3.4.2) was used to measure the open circuit potential (OCP) before the reaction, as well as the current produced by the transfer of electrons from the anodic to the cathodic half-cells. The measurements were made by simply connecting the working electrodes through the multimeter (M in the figure), by attaching one lead from the multimeter to each of the working electrodes in the galvanic cell. A switch (S) was placed between the multimeter and one of the WEs, in order to initiate or stop the spontaneous reactions at any time. A salt-bridge was used to complete the circuit, by allowing ionic transfer. The salt-bridge consisted of a glass U-tube filled with a 1 M KCl, 3% aqueous agar gel. The gel was made by heating the 1 M KCl solution to 70 – 80 ºC, in a water bath, and then dissolving the agar powder in it, with constant stirring. Once the solution was clear (complete dissolution), it was poured into the glass U-tube and left to set at room temperature. Salt-bridges were stored dipped into 1 M KCl solutions and were regularly re-made.

The galvanic cell was immersed in a thermostatic water bath in order to control the temperature of the solution, as described in Section 3.3.3 for the electroless bath. The cleaning procedure used for the electroless bath was followed for these cells.

3.3.5 The Bipolar Cell

While the galvanic cell configuration described above allows the measurement of spontaneous currents and potentials, it cannot control either one. In order to have potentiostatic control, a bipolar cell was used (see Figure 16).

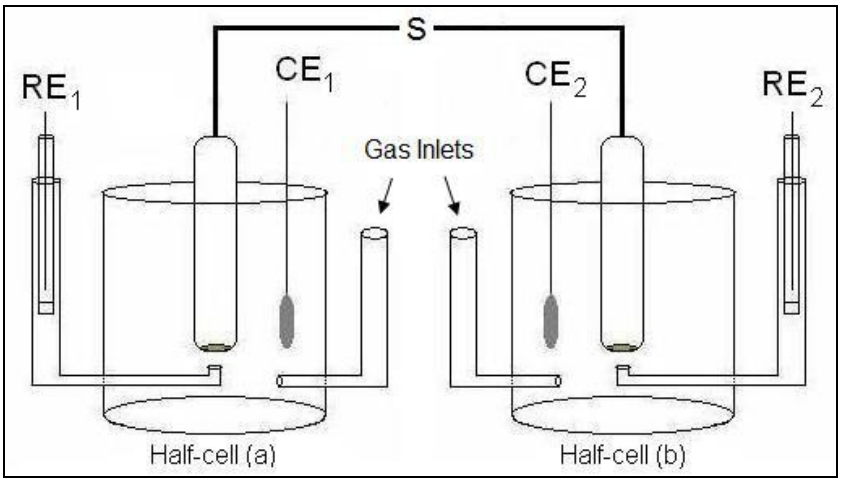

Figure 16. Schematic of the bipolar cell.

As with the cells described before, each half-cell of the bipolar cell is made of glass and is fitted with a Teflon lid. As can be seen in the figure, each half-cell possesses a Luggin capillary for the reference electrode and a gas inlet, which allows de-oxygenation of the solution. The cleaning procedure for the three electrode cell was followed, except when the bipolar cell was used to study the electroless system. In this latter case, cleaning was done as for the electroless bath.

The bipolar cell consists of a four electrode system, similar to that used in electrochemical studies at liquid/liquid interfaces, as discussed in Section 2.4.[109,128] Two counter electrodes (CE_1 and CE_2) and two reference electrodes (RE_1 and RE_2) were connected to a four-electrode potentiostat; RE_1 and CE_1 were connected to the RE and CE terminal, while RE_2 and CE_2 were attached to the sense and WE lead, respectively.

The circuit was completed by connecting the two working electrodes through a switch, each functioning as one face of a bipolar electrode. As in the galvanic cell, the electrons produced in one half-cell are transferred from one working

electrode to the other. In this case, however, the completion of the circuit is also electronic (through the counter electrodes), rather than ionic (through a salt-bridge). The use of the RE and the potentiostat consequently allow the potential difference between the individual half-cells to be controlled.

3.4 Equipment and Software

Standard laboratory glassware and other materials were used. The specialized equipment is summarised in Table 3. Detailed experimental conditions of some of the equipment and computer software employed are also described in this section.

Table 3. Equipment specifications.

Equipment	Model	Company
Analytical Balance	Explorer	Ohaus
Atomic Force Microscope	Quesant 250	Windsor Scientific Limited
Autolab Potentiostat	PGSTAT 100	Eco-Chemie
Battery	Silver (9 V)	Eveready
Digital Multimeter Card	PCI-4065	National Instruments
FTIR Spectrometer	Vertex 80v	Bruker
Micropipettes	10-100 μL 100-1000 mL	Eppendorf Research Fisherbrand
pH Meter	HI 991300	Hanna
Purelab Ultra Purification Unit	-	Elga Labwater
Rotating Disk Motor	EG&G PAR model 616	Princeton Applied Research
Ultrasound Bath	-	Clifton
Thermostatic Water Bath	GD100	Grant Scientific
X-Ray Diffraction System	X'Pert Powder with X'Celerator detector	Philips

3.4.1 Atomic Force Microscopy (AFM)

All AFM measurements were performed in contact mode in air with a Quesant 250 AFM.[iii] This technique was used to characterize electroless copper deposits on gold foils, by measuring the deposit thickness as well as the average roughness. Film thicknesses were measured across the gold/copper interface using a three point tilt removing filter. The roughness values were obtained from the root mean square values of surface height measurements using the image analysis software supplied with the instrument. The roughness was measured over an area of 3 μm × 3 μm, avoiding edge effects by taking all measurements from the central areas of the image.

3.4.2 Digital Multimeter

A National Instruments digital multimeter card was used in order to measure spontaneous currents and potentials, using the galvanic cell configuration described above (Section 3.3.4). The current transients and open circuit potentials (OCP) were recorded using a custom-written LabView program.[iv] At its highest accuracy setting of 22-bits, the PCI-4065 can probe the reaction at a maximum rate of 10 Hz, with an accuracy of ± 0.15 μA and ± 26 μV when measuring DC current and voltage, respectively.

3.4.3 Fourier Transform Infrared Spectroscopy (FTIR)

The *in-situ* FTIR experiments were carried out using the spectroelectrochemical cell described in Section 3.3.2 and a Bruker Vertex80 V IR spectrophotometer, with a CaF_2 prism bevelled at 60°. Spectra were recorded every 80 mV, in a range from 4000 to 800 cm^{-1}. All spectra reported are difference

---

[iii] AFM measurements were made by Dr Samson N. Patole, former Postdoctoral Research Associate of the Manchester Electrochemistry Group.

[iv] The multimeter was installed and the program written by Dr Andrew I. Campbell, former Postdoctoral Research Associate of the Manchester Electrochemistry Group.

spectra, with the reference spectrum acquired at the initial potential of each voltammogram, using either p- or s-polarised light.[v]

3.4.4 Numerical Simulations of Bipolar Cell Voltammetry

In order to gain further understanding of the bipolar cell, numerical simulation of its voltammetric response was performed. A custom-written C program[vi] was used to solve the coupled mass-transport equation via time-dependent backwards implicit finite-difference simulations; the Thomas Algorithm was used to determine the concentration profiles at each time increment, *i.e.* the concentration of each redox active species was calculated at different distances from the electrode surface for each time point.[129] In the program, the transport of each of the four redox-active species involved is treated using Fick's second law, Equation 64.

$$\frac{\partial C}{\partial t} = D\frac{\partial^2 C}{\partial x^2} \qquad \text{Equation 64}$$

The time-dependent concentration profiles of the four redox species are related through the boundary conditions describing the potential dependent redox equilibrium, as stated in Equation 65. This equation relates the concentration of each of the oxidised, O, and reduced, R, species of both half-cells (a and b) of Figure 16 to the potential difference between the cells.

$$\frac{O_a R_b}{R_a O_b} = e^{\left[\frac{nF(\Delta E - \Delta E^0)}{RT}\right]} \qquad \text{Equation 65}$$

[v] FTIR measurements were performed with training and help from Dr Paramaconi Rodríguez, Postdoctoral Reasearcher of the Leiden Institute of Chemistry at Leiden University.

[vi] The program was written by Dr Fran G.E. Jones, former Postdoctoral Research Associate of the Manchester Electrochemistry Group.

The coupled mass-transport equations are initially solved to find the concentrations of one of the redox couples, for example both forms of the species in half-cell (a), at a given time, t. The order of the calculation is determined by the initial concentrations: the limiting species are identified and their concentrations are simulated first. Since the concentrations of the other redox couple (half-cell (b)) are necessary to calculate the concentration profile in half-cell (a), the previous concentrations (at t-1) of the former are used to approximate the values at time t. Subsequently, the new concentrations of species in half-cell (b) are found, using the interfacial concentrations of half-cell (a). This alternating calculation is repeated until the entire voltammogram is simulated. The current is then determined from the concentration gradients close to the electrode surface. This approach is analogous to the alternating-direction implicit finite-difference (ADI) method, which has previously been employed in the numerical solution of electrochemical mass-transport problems; in the case of the ADI approach, however, it is the spatial direction of the numerical calculation, rather than the identity of the species calculated, which is alternated.[129]

3.4.5 X-Ray Diffraction (XRD)

X-ray diffraction patterns were obtained on an X'Pert Powder system, with an X'Celerator detector.[vii] A generator voltage of 40 kV and a tube current of 30 mA were used to study a range of diffraction angles from 5 to 120°. Continuous scans were done, with a step size of 0.033° every 60 seconds. Slit widths of 1/8 and 1/4 degrees were used for the ray and the sample, respectively.

[vii] XRD patterns were obtained with training and help from Dr Christopher Muryn of the University of Manchester.

4 DMAB Oxidation

This chapter describes the investigation of the mechanism of DMAB oxidation, which, as discussed in the introduction, is not well understood at present, despite dimethylamine borane being a widely-used reducing agent. Borohydride oxidation was also studied in order to determine whether these molecules share the same oxidation mechanism, as reviewed in Section 1.2. Different electrochemical techniques, such as voltammetry and chronoamperometry (at both macro- and micro electrodes) were used, along with some complementary techniques such as NMR spectroscopy. The effect of important parameters in electroless deposition systems, such as concentration, pH and the catalytic effect of the substrate, were examined.

4.1 Stability

The stability of aqueous DMAB solutions was studied, through voltammetry, at different pH values. Figure 17 shows the changes observed in the voltammetry of the same solution over a week; the results indicate that the solutions are not stable over that period, as the shape of the voltammetry changes, showing oxidation peaks at less positive potentials than those observed initially. The total charge transferred during oxidation does not greatly vary in a week, however; for pH 12.3, for example, it is first 1.8 x 10^{-3} C (blue line) and 1.9 x 10^{-3} C (green line) a week later.

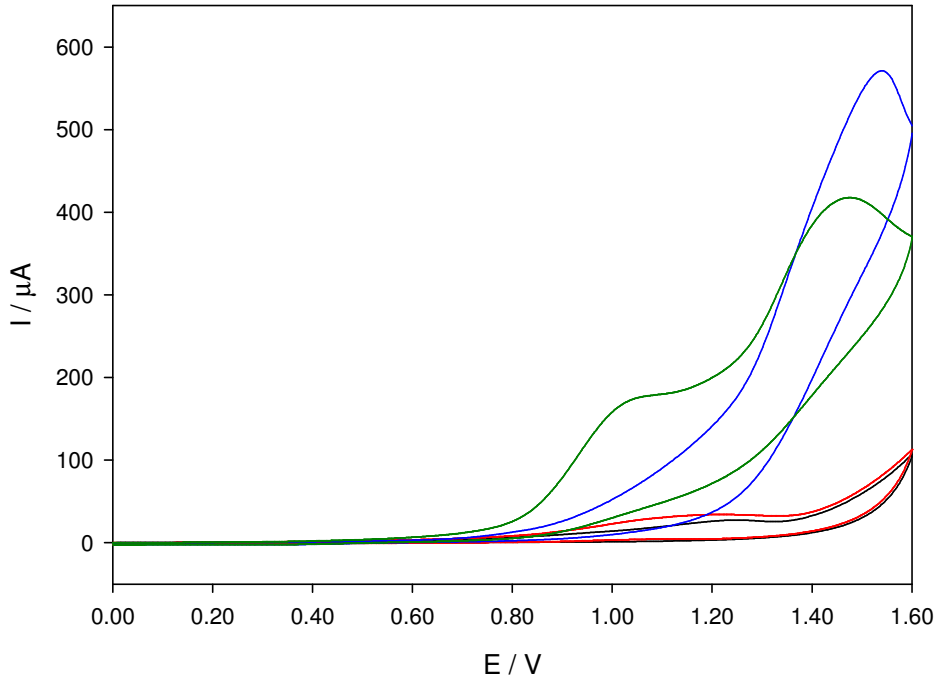

Figure 17. Cyclic voltammetry, at 100 mV/s, of 6.1 mM DMAB solution, on a glassy carbon disk, at pH 11.0 (black) and 12.3 (blue). Voltammetry performed one week later on the same samples is also shown; pH 11.0 (red) and 12.3 (green).

The stability of the DMAB solutions was also studied at higher pH, on gold surfaces. As discussed in the introduction, both the highly alkaline media and the gold substrate should help avoid the hydrolysis reaction.[26,45,76] Figure 18 shows voltammograms performed at different times after solution preparation.

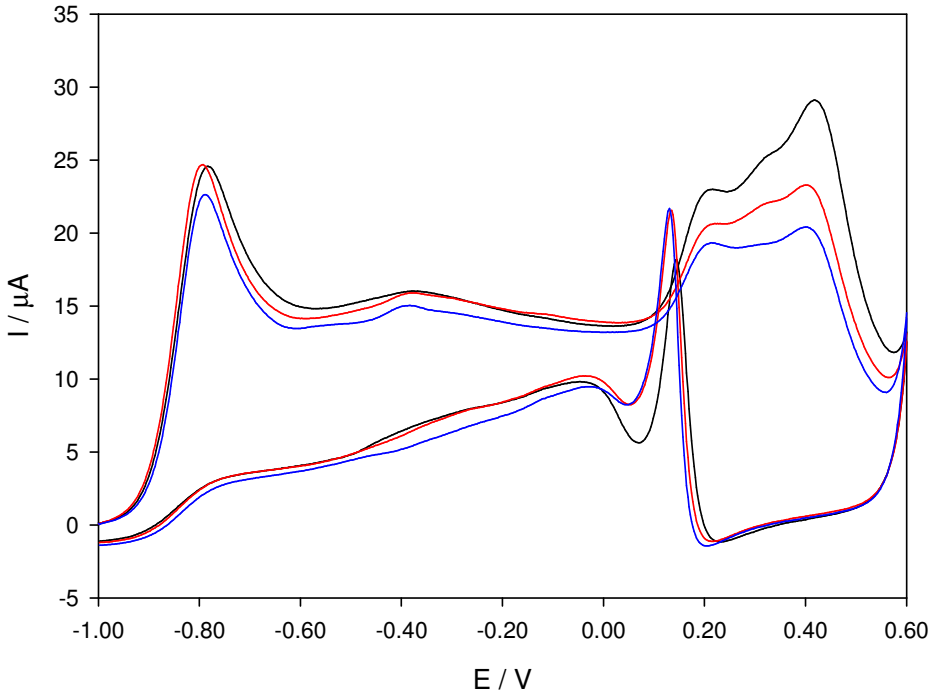

Figure 18. Stability study of a 1.0 mM DMAB solution at pH 13.6, through cyclic voltammetry on a gold disk, at 100 mV/s. Voltammograms of the fresh solution (black), a day-old solution (red) and a five-day solution (blue) are shown.

The variations in the voltammograms with time are less noticeable than in Figure 17. Since the electrode was only used during the recording of the voltammograms and was not stored with the solution, the difference in behaviour is most likely due to the higher pH used in Figure 18; the higher concentration of hydroxide stabilises the BH_3OH^- species assumed to form from the dissociation of DMAB in aqueous solution.[26,45,76] Another important difference is the potential range studied; as discussed below (Section 4.2.1) the oxidation observed on the glassy carbon is probably that of the amine, a gas at room temperature,[130] while the process on gold is that of the boron-containing species. These results indicate that at highly alkaline pH, the homogeneous hydrolysis reaction is slow enough, if it occurs at all, not to interfere with the studies of the electro-oxidation reaction.

4.2 Electrode Surface

The voltammetric behaviour of DMAB was studied on different electrode surfaces, as the catalytic properties of the substrate is a key aspect of the

electroless deposition process. Figure 19 shows the typical linear voltammograms obtained on gold, platinum, copper and glassy carbon. It is clear from the graph that the metallic surfaces are more catalytic towards DMAB oxidation than the carbon substrate, which presents no oxidation signals in the potential range studied.

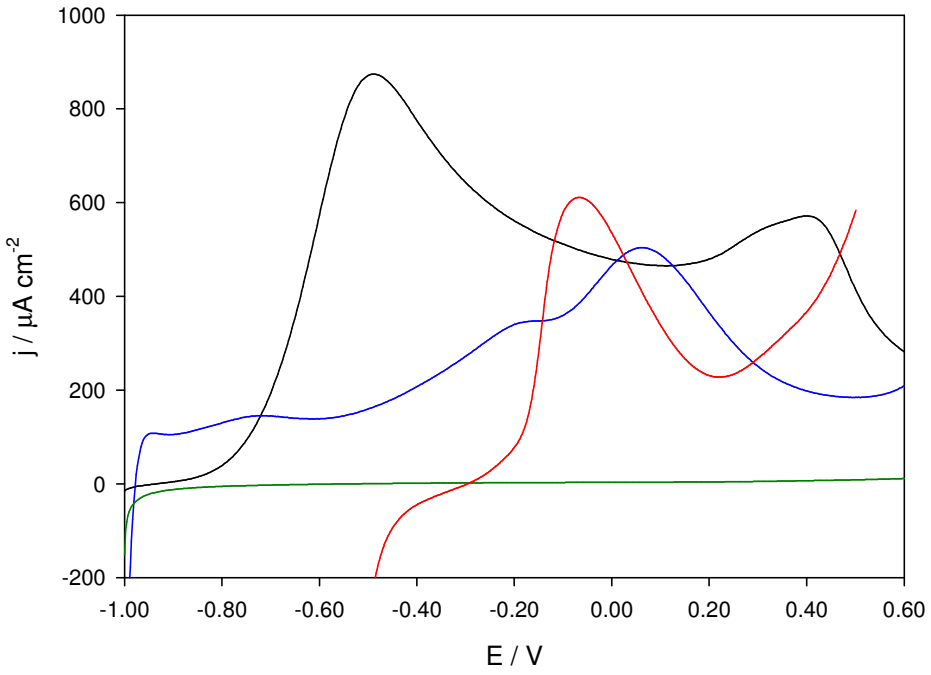

Figure 19. 50 mV s^{-1} linear voltammograms of 1.2 mM DMAB solutions, at pH 13.6, on gold (black), copper (red), platinum (blue) and glassy carbon (green) disk electrodes.

The three metals produce distinctly different voltammograms; the copper electrode in particular could only be studied over a smaller potential window, as it was not particularly stable in such alkaline media at very negative potentials. The reduction currents at the negative end of the voltammograms on copper and platinum are also present in the corresponding blank voltammograms, as seen for example in Figure 24 for Pt; these signals are likely due to hydrogen evolution. Both platinum and copper present DMAB-related signals around 0.00 V vs. Ag/AgCl, with the gold favouring the oxidation, as it occurs at more negative potentials, while also producing the highest current densities. As this behaviour agrees with that reported in the literature, *i.e.* gold is catalytic for DMAB oxidation while inhibiting loss due to hydrolysis,[44] most of the present work was done using gold electrodes. Small sections are dedicated to the use of non-catalytic surfaces (GC) and less catalytic metals (platinum), for comparative purposes.

4.2.1 Glassy Carbon (GC) Electrode

At higher potentials than those shown in Figure 19, glassy carbon electrodes do produce oxidation peaks, as seen in Figure 20; this surface was consequently used to investigate the electro-oxidation of DMAB on a non-catalytic substrate. As both the efficiency and stability of DMAB have proven to be dependent on pH,[80] its voltammetric behaviour on a GC electrode was studied as a function of pH; Figure 20 shows the results through a series of cyclic voltammograms of DMAB solutions on a GC electrode. The increase in pH produces a significant rise in current, while changing the potential at which peaks are observed.

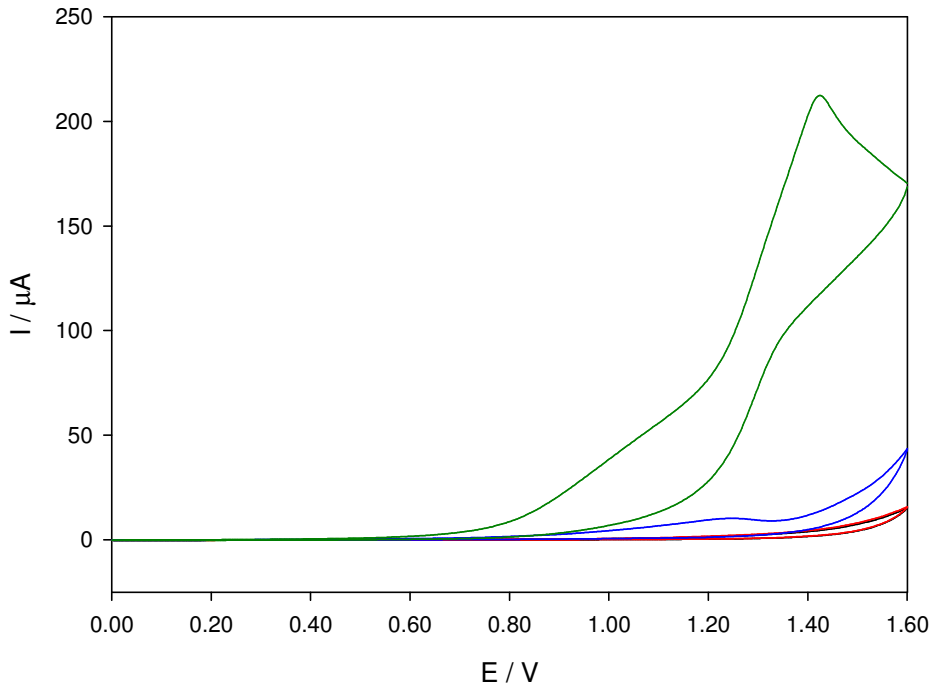

Figure 20. Cyclic voltammograms of 6.1 mM DMAB, at 10 mV/s, at pH: 7.5 (black), 9.8 (red), 11.0 (blue) and 12.3 (green).

The increase of current is partly due to the higher concentration of the hydroxide ions, but is also a consequence of the DMAB reaction on the electrode surface. The effect of solution concentration was studied, as seen in Figure 21, where the pH and scan rate are kept constant. Although a trend was not found, it is reasonable to state that at the lower concentrations, the voltammograms are similar, but they change once the DMAB concentration becomes higher than that

of the hydroxide ions. The second type of behaviour can be seen through the increase of the first peak, which eventually produces a shoulder that might indicate a second step or a different reaction altogether. The more defined peak, around 1.50 V, is probably associated with hydroxide reactions as it is present in the blank (purple curve in Figure 21); further confirmation is in the fact that it disappears at high concentrations of DMAB.

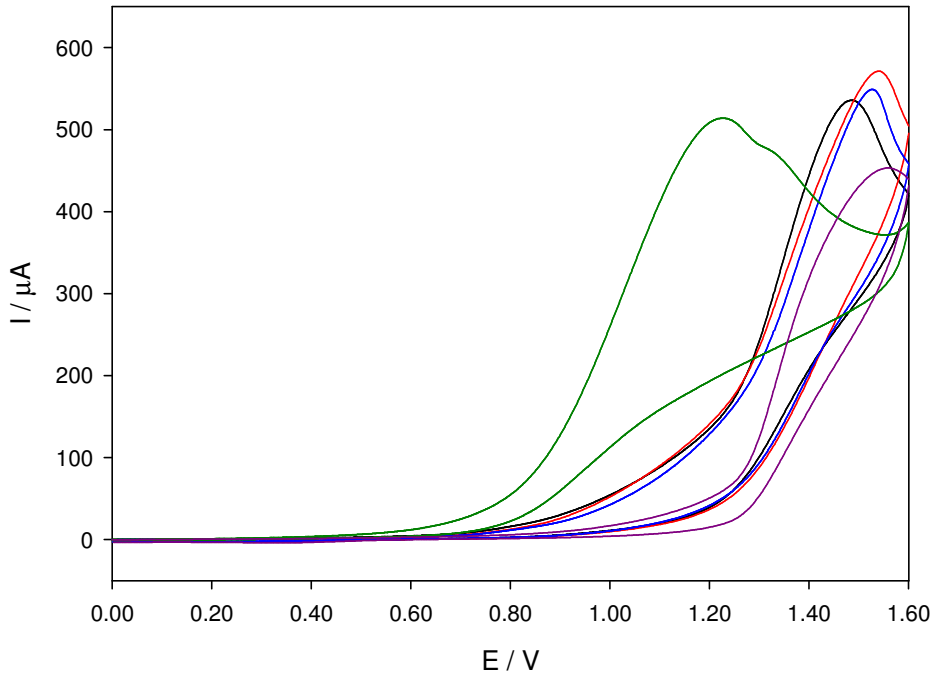

Figure 21. Cyclic voltammetry as a function of DMAB concentration at 100 mV/s (pH = 12.3). Purple: 0.0 mM (blank), black: 3.0 mM, red: 6.1 mM, blue: 10.0 mM, green: 139.0 mM.

In order to gain further information on the oxidation of DMAB, the effect of scan rate was studied, varying both pH and concentration. Scan rates of 5, 10, 25, 50 and 100 mV s^{-1} were used. Voltammograms performed under identical conditions, with the exception of the scan rate, were recorded consecutively, stirring the solution lightly between scans; each set took under 20 minutes to complete. Figure 22 is an example, at pH 12.3, with a concentration of 3.0 mM.

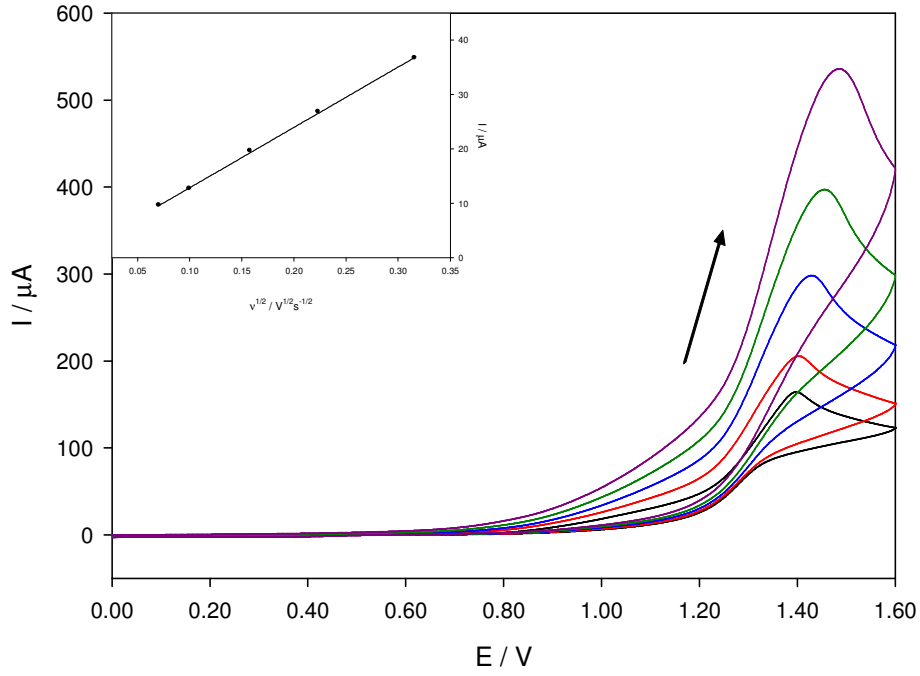

Figure 22. CVs of 3.0 mM DMAB at pH 12.3 on a GC electrode. The arrow indicates increasing scan rate. The inset shows the Randles-Ševčik plot for a 6.1 mM DMAB solution at pH 9.8.

The inset of Figure 22 shows a linear relationship between the peak current and the square root of the scan rate. This type of relationship was found for all values of pH and concentrations investigated. From the linear regressions, either the number of electrons transferred or the diffusion coefficient could be calculated, according to Equation 53, assuming irreversible behaviour (assuming $\alpha = 0.5$ and $n_a = 1$), or Equation 50, for the reversible case (for the relevant error analysis see Appendix B). Table 4 summarises the results obtained using D values reported in the literature.[44,77] D and n values were not calculated for pH 12.3, as the DMAB related peaks appear as shoulders to the hydroxide related peaks and could not be easily separated.

Table 4. Number of electrons transferred and diffusion coefficient obtained through voltammetric techniques for DMAB oxidation on glassy carbon electrodes.

		D / cm^2 s^{-1}			**n**	
pH	**E / V**	**Irreversible (n = 1)**	**Reversible (n = 1)**	**Reversible (n = 2)**	**D = 8.55 x 10^{-6} [77]**	**D = 7.48 x 10^{-6} [44]**
7.5	~1.0	1.2 x 10^{-6}	9.3 x 10^{-8}	7.4 x 10^{-7}	0.4	0.5
9.8	~1.1	5.9 x 10^{-5}	4.5 x 10^{-6}	3.6 x 10^{-5}	1.6	1.7
11.0	~1.2	2.3 x 10^{-5}	1.8 x 10^{-6}	1.4 x 10^{-5}	1.1	1.2

Dimethylamine oxidation in aqueous solutions has been reported to occur on carbon electrodes at potentials just positive of 1.0 V vs. SCE, with rising peak currents as the pH is increased;[131] it is likely that the oxidation observed is that of the free amine once it dissociates from the borane complex. The increase in currents with pH, observed clearly in Figure 20, is most likely linked to the protonation of the amine at lower pH values, hindering its oxidation process; the relevant pKa has a value of between 10.77 and 10.94, according to previous work, coinciding with the sudden increase in current observed at pH 11 (blue curve in Figure 20).[132,133] If that were the case, calculations of the number of electrons would have to be revised, using the diffusion coefficient of the amine rather than the DMAB molecule.

In order to determine whether or not the amine oxidation is being observed, experiments with dimethylamine in alkaline aqueous solution and mixtures of dimethylamine and DMAB were performed. Figure 23 shows a comparison of cyclic voltammograms at similar concentrations of DMAB, dimethylamine and a mixture of the two, at equal pH and scan rate.

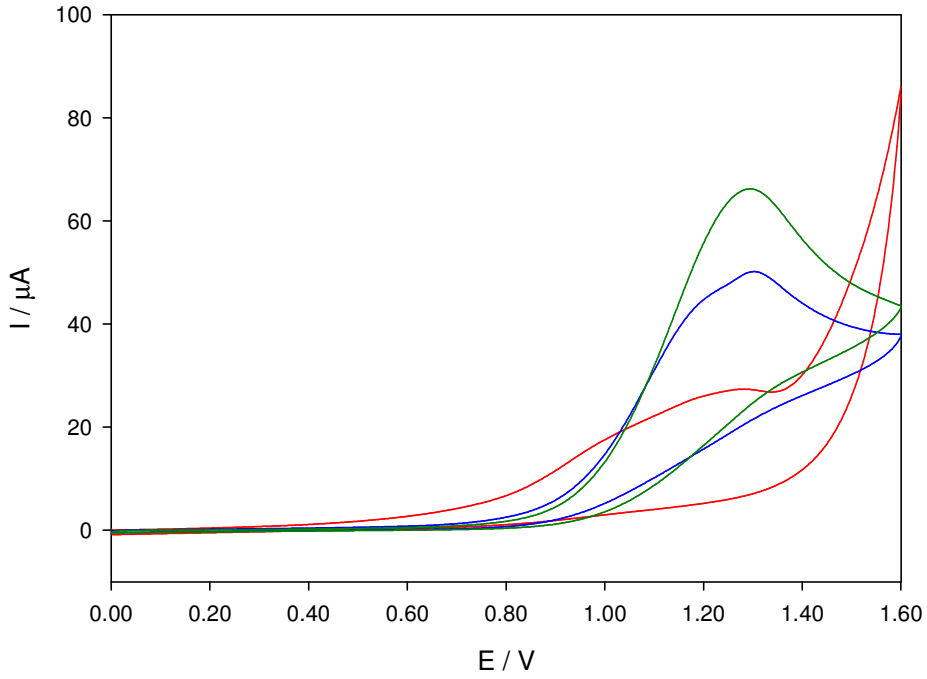

Figure 23. Cyclic voltammograms of a 6.1 mM DMAB solution (red), a ~6.0 mM dimethylamine solution (green) and a mixture of ~3.0 mM in both DMAB and dimethylamine (blue), at 50 mV/s and pH 11.5.

The DMAB signal in the graph is noticeably smaller than that of the free amine, although a peak is observed at the same potential. Both the DMAB and the mixed solutions present a broad peak, as though two distinct but overlapping signals are observed. It is possible that DMAB does not fully dissociate in alkaline solution as was previously thought; the free amine and the complexed amine might oxidise at close but not identical potentials. Additionally the dissociation might be aided by the presence of hydroxide adsorbed on the electrode surface, complicating the electrochemical behaviour. In either case, it appears that the oxidation signals observed on the glassy carbon electrode, at highly positive potentials, arise from the dimethylamine and not the boron-related species.

4.2.2 Platinum Electrode

In order to understand better the “catalytic” effect of gold on DMAB oxidation, some voltammetry was performed on a platinum electrode. Figure 24 shows the different voltammetric behaviour of gold and platinum in aqueous alkaline solution. Both have a marked oxide layer formation region on the anodic scan, with its subsequent reduction on the cathodic sweep; on platinum, however, both signals appear at less positive potentials. Platinum also displays signals potentials below -0.60 V vs. Ag/AgCl due to hydrogen adsorption/desorption and oxidation/reduction processes.[134,135]

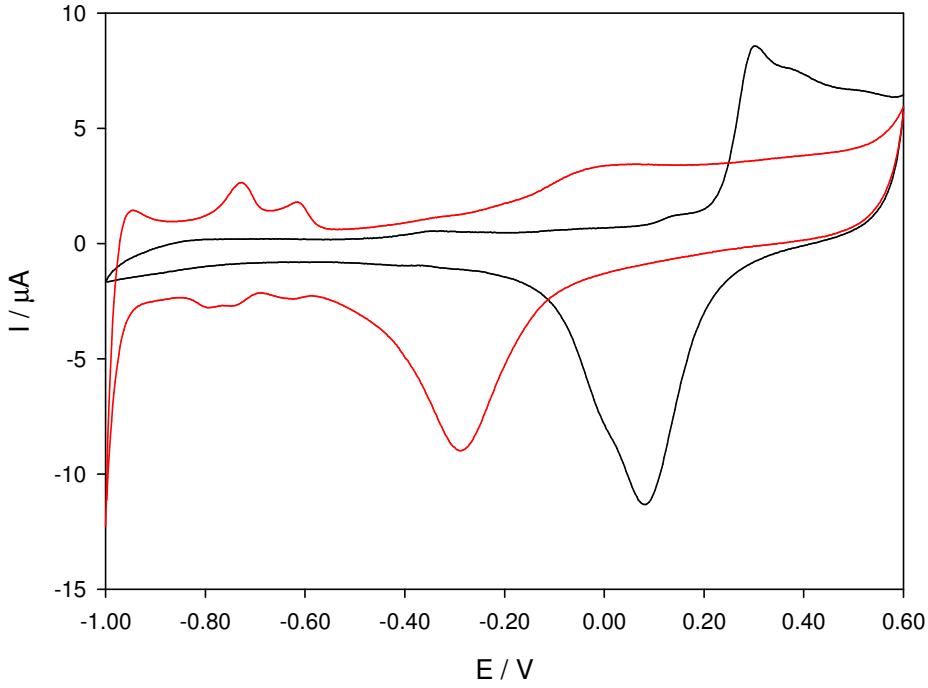

Figure 24. Cyclic voltammograms of gold (black) and platinum (red) electrodes in aqueous alkaline solution; electrode areas are equal.

As shown in Figure 19, the behaviour of gold and platinum is also different in the presence of DMAB; the currents are lower and the oxidation potential is more positive on platinum. Figure 25 shows that the reactivation signal on the cathodic scan appears at more negative potentials on platinum, agreeing with the shift in potential observed for the reduction of the metal oxide in the blanks (Figure 24). The reactivation peak on Au appears at the potential at which the reduction of the gold oxide would be seen, in the absence of DMAB; on platinum, on the other hand, the reactivation occurs at more negative potentials than those of the platinum oxide reduction: a small reduction current is observed even in the presence of DMAB, after which reactivation occurs. This behaviour indicates a greater interaction between the surface and DMAB in the case of gold electrodes, as the platinum oxide is not completely removed by the reducing agent, leading to electrochemical reduction of the oxide.

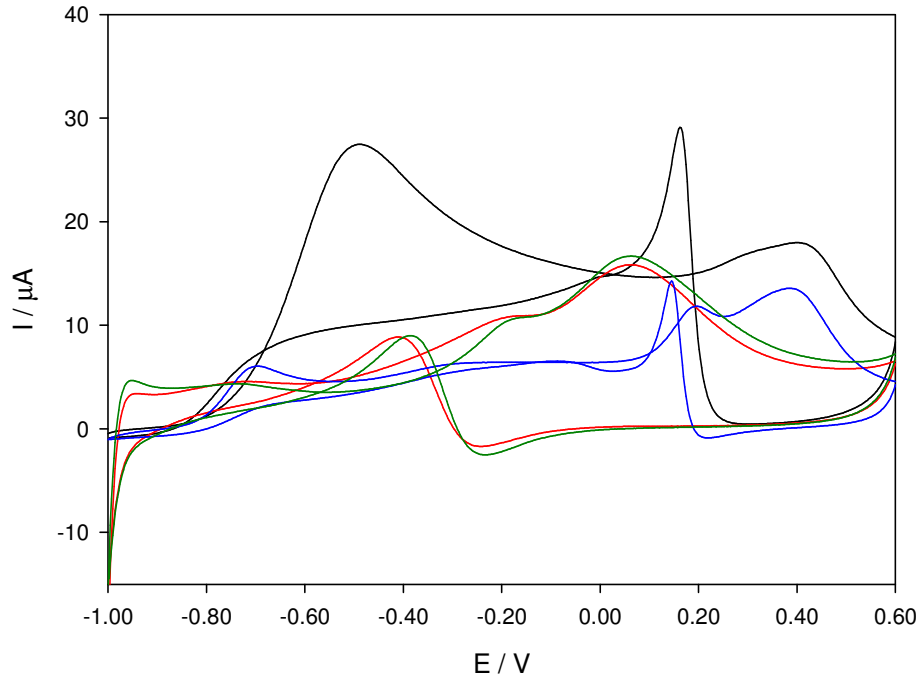

Figure 25. CVs of 1.2 mM DMAB aqueous alkaline solution at gold (black) and platinum (red) electrodes, at pH 13.6. The tenth cycle in each case is also shown: blue – gold; green – platinum.

As will be discussed later on (Section 4.3), consecutive scans show a decrease in current and a shift in the potential of the first peak. Figure 25 shows the first and tenth cycles of consecutive scans on platinum and gold. It is clear that while the gold behaviour changes dramatically, on platinum consecutive scans are very similar.

Figure 26 shows the same CV presented in Figure 25 for the gold electrode and a voltammogram recorded on platinum after immersing the electrode in solution for 20 minutes, without an applied potential. A first peak, absent in the previous figure, is now observed on platinum. This, along with the behaviour observed with consecutive scans in Figure 25, indicates that an adsorption process is associated with the first electrochemical signal. The results also imply that the adsorption is facilitated by the gold surface; in comparison, platinum requires much longer times in order to adsorb comparable amounts of DMAB and thus produce similar currents.

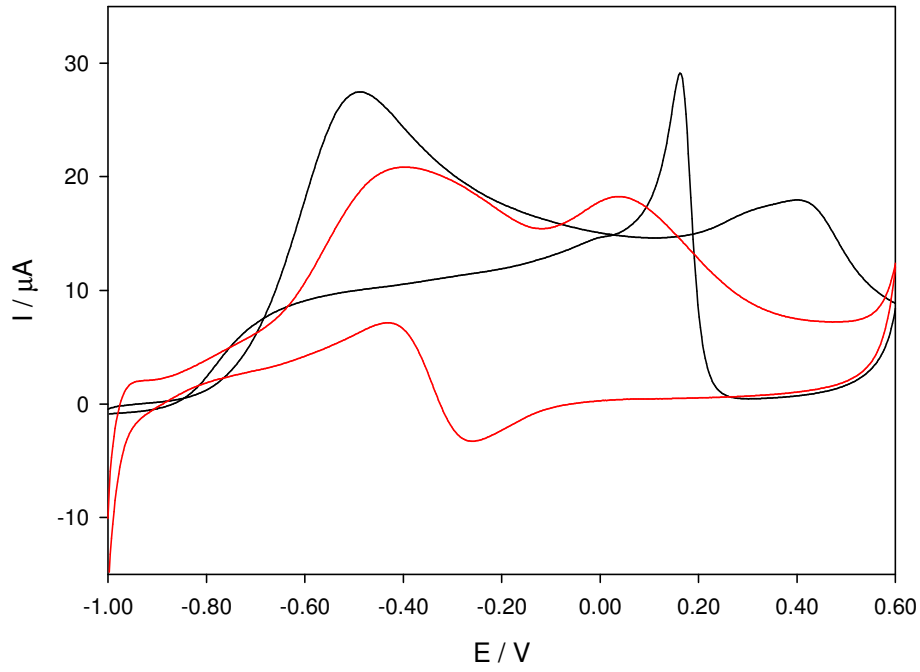

Figure 26. CVs of 1.2 mM DMAB aqueous alkaline solution at gold (black) and platinum (red) electrodes; the platinum electrode was introduced in solution 20 minutes prior to the scan shown.

Potential steps performed on platinum, with applied potentials just positive of each oxidation peak in Figure 25, produced three and 1.5 electrons; as will be seen later (Section 4.3.6), the number of electrons transferred overall is less than on gold.

4.3 DMAB Oxidation on a Gold Disk Electrode

The electro-oxidation of DMAB on gold was studied, through cyclic voltammetry, in aqueous alkaline solution as presented in Figure 27. As noted above, the potential range studied is more negative than that needed on glassy carbon surfaces; this suggests that while only the amine is oxidised on the GC, the boron-containing species reacts on the gold surface. The voltammograms have three distinct oxidation peaks on the forward scan (at approximately -0.80, 0.20 and 0.41 V vs. Ag/AgCl), possibly some additional processes occur between the first and second peaks. A reactivation peak occurs on the backward scan (near 0.15 V).

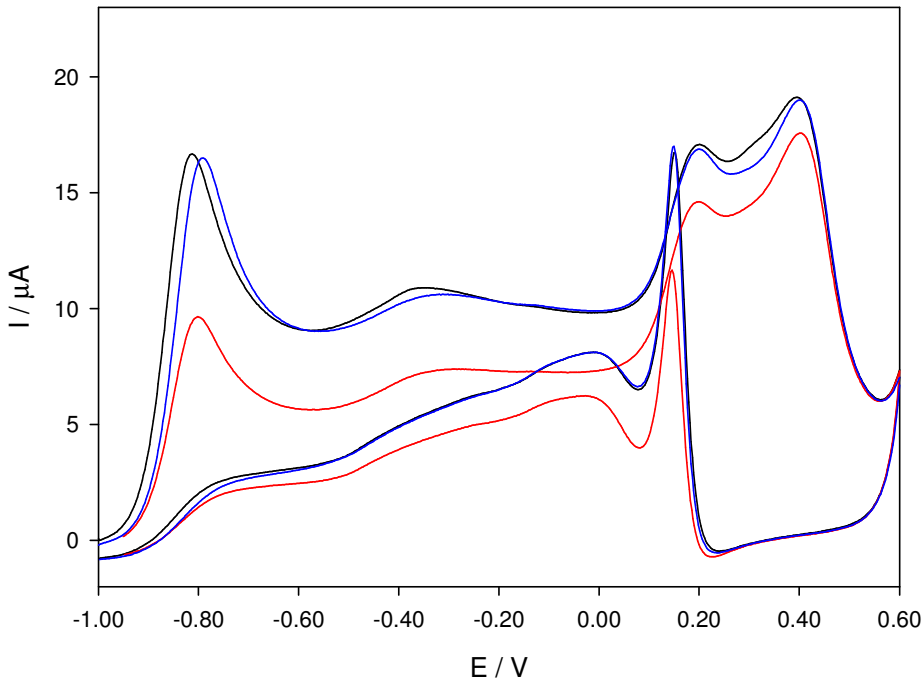

Figure 27. CVs of a 1.0 mM DMAB solution at pH 13.6, on a gold disk electrode at 50 mV s^{-1}. The first cycle was recorded after 20 minutes of degassing with Ar (black), the second was immediately after the first (red), and the third, stirring the solution after the second (blue).

Figure 27 shows a series of consecutive voltammograms; it is clear that when the solution is not stirred between each scan the current drops, possibly due to local changes in concentration or pH. Figure 28 shows CVs at different DMAB concentrations, while comparing them with a cycle in the absence of DMAB under equivalent conditions.

The first DMAB oxidation peak appears in a region where no signals are observed in the blank. On the forward scan, additional signals are observed in the positive potential region; although they are present in all the voltammograms, the current increases with DMAB concentration and the shape of the voltammograms changes.

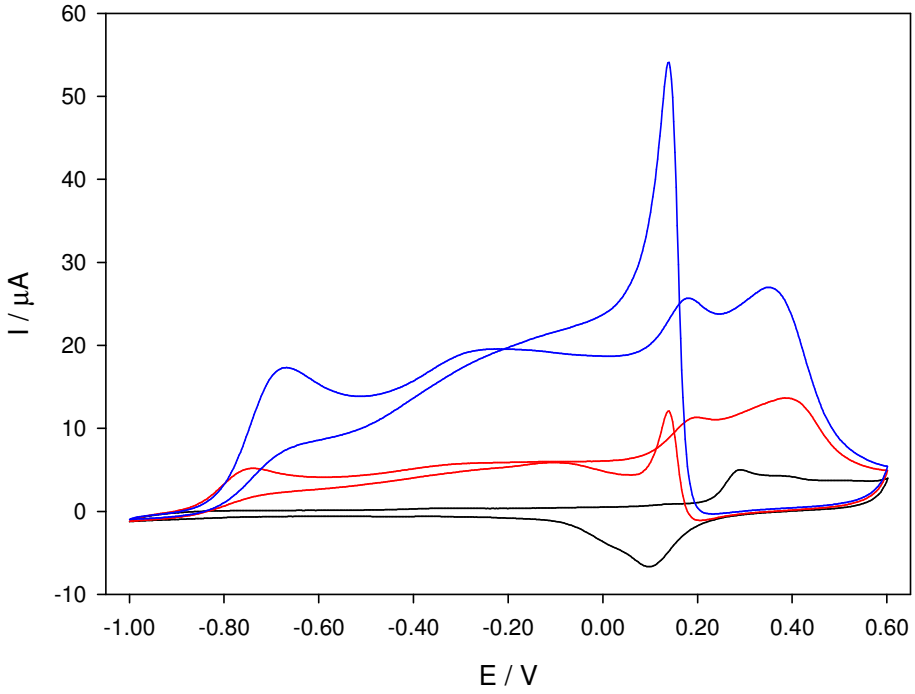

Figure 28. Cyclic voltammograms, at 50 mV s^{-1}, of alkaline aqueous solution on a gold electrode, in the presence (red – 1.1 mM, blue – 3.5 mM) and absence (black) of DMAB.

The most striking difference between the behaviour of the blank solution and the ones that contain DMAB appears on the cathodic scan. Between 0.00 and 0.20 V, a cathodic current is produced in the absence of DMAB, due to the reduction of the gold oxide formed on the forward scan; on the other two cycles shown in Figure 28, a "reactivation" anodic signal can be seen.

4.3.1 Consecutive Voltammetry

Due to the behaviour observed in Figure 27, with successive cycles, ten consecutive CVs of a DMAB solution were recorded and are presented in Figure 29. There is a distinctive decreasing trend in the current with subsequent scans (the first scan is marked in red); the change lessens with consecutive scans, however, and eventually the voltammograms are essentially reproducible. A shift in the position of the first oxidation peak is also observed with each scan.

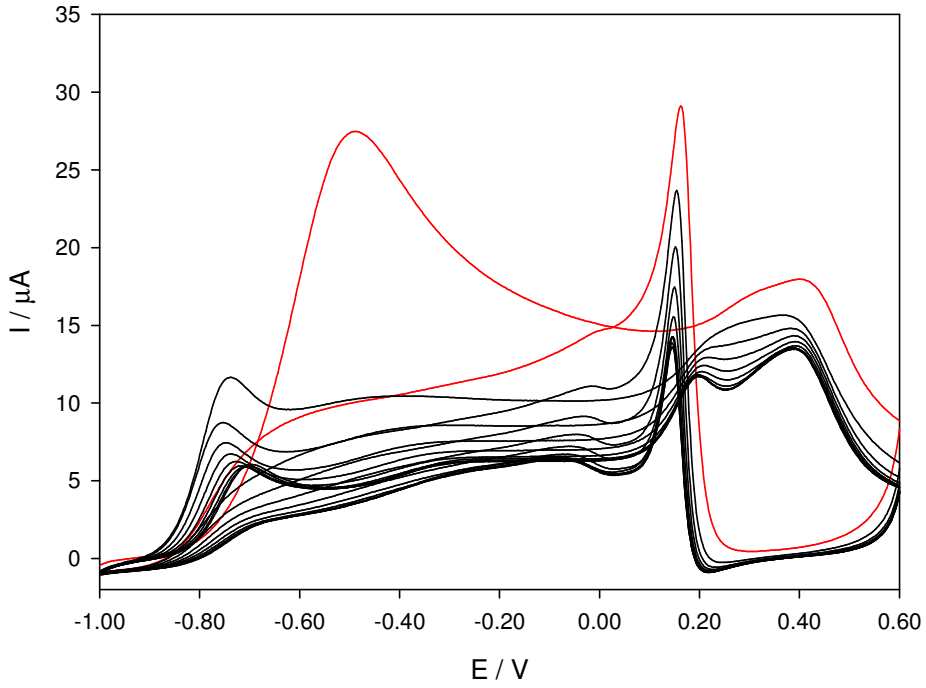

Figure 29. Consecutive cyclic voltammograms, at 50 mV s^{-1}, of 1.2 mM DMAB alkaline solution on a gold electrode. The first scan is marked red.

Figure 30 through Figure 33 show similar experiments, where the turning point of the scans is shifted toward less positive potentials in each case. Both the current and the potential shift with successive scans, in each set of experiments; at more positive turning points, however, they seem to stabilise more quickly, reaching lower values of current. This indicates that the current is strongly dependant on a process occurring at the electrode surface, which is either time or potential dependent.

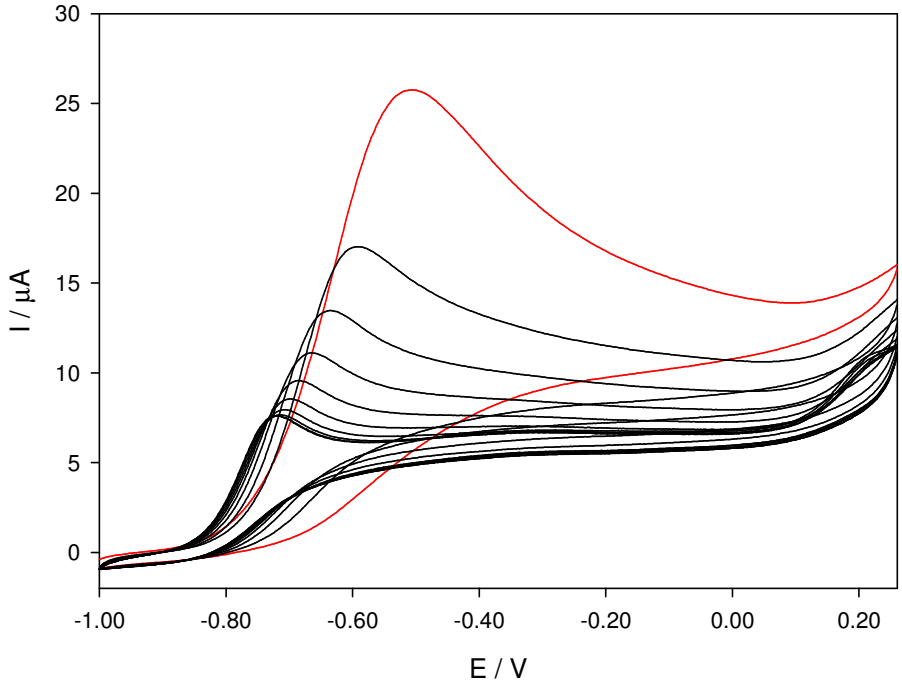

Figure 30. Conditions as in Figure 29; turning point: 0.26 V vs. Ag/AgCl.

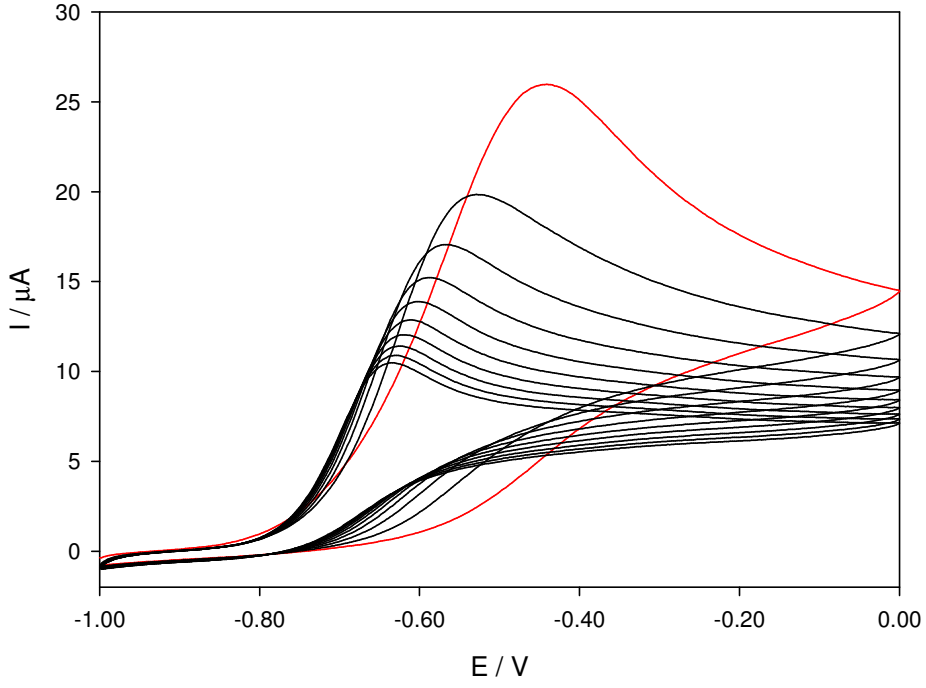

Figure 31. Conditions as in Figure 29; turning point: 0.00 V vs. Ag/AgCl.

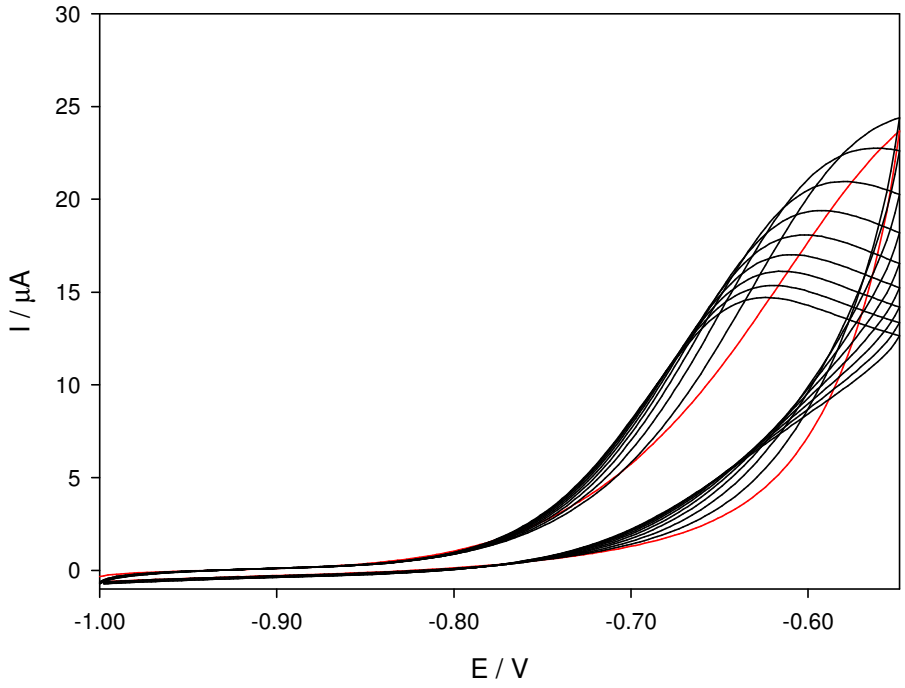

Figure 32. Conditions as in Figure 29; turning point: -0.55 V vs. Ag/AgCl.

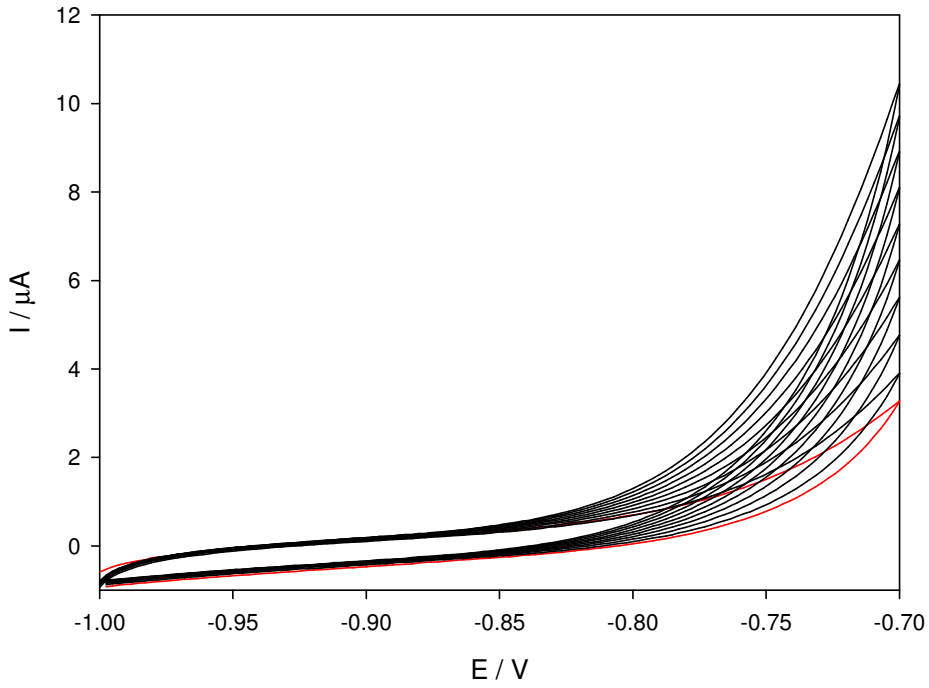

Figure 33. Conditions as in Figure 29; turning point: -0.70 V vs. Ag/AgCl.

In order to investigate the possible potential dependence of the decrease in current, cyclic voltammetry was performed, in which the turning point was set at 0.00 V vs. Ag/AgCl, and the potential was held there for ten seconds; Figure 34 shows the results obtained. The current decreases and stabilises more rapidly than when the potential was not held at 0.00 V (see Figure 31), showing that time

(not potential) is the crucial factor, once the potential has passed a critical value. The large drop in current between the first two scans could indicate a chemical interaction between the species generated at the peak potential and at 0.00 V, or the adsorption of species at potentials close to 0.00 V which inhibits the oxidation process at lower potentials.

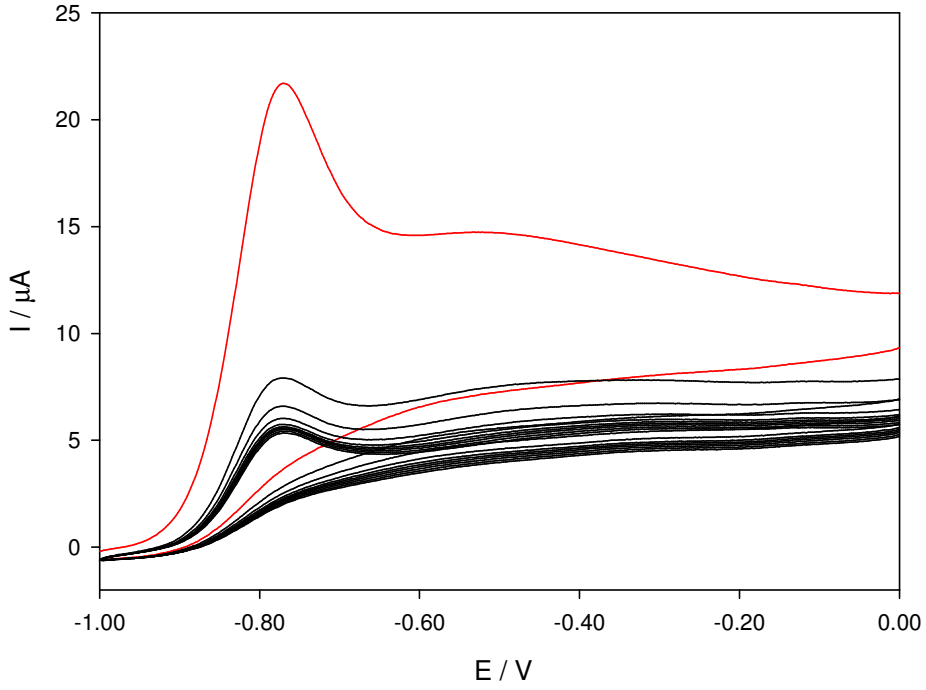

Figure 34. Consecutive CVs at 50 mV s^{-1} of 1.1 mM DMAB solution; turning point: 0.00 V vs. Ag/AgCl, holding the potential at 0.00 V for ten seconds. The first cycle is marked red.

4.3.2 Effect of Scan Rate and pH

The effect of scan rate on the oxidation process was studied; the results are presented in Figure 35. The peak currents rise with increasing scan rate, having a linear relationship with the square root of the scan rate, as in the case of the GC electrodes. Again, D and n were calculated, assuming reversible and irreversible behaviour; for the irreversible case, n_a was set as 1 and α as 0.5; these values were used as a first approximation, as multi-electronic transfers are usually limited by a single electron transfer, and the D values obtained are within the range reported for borohydride, which is expected to have a similar diffusion coefficient.[59] The results of these calculations for each oxidation peak, at two

different pH values are summarised in Table 5 (the corresponding treatment of errors can be seen in Appendix B).

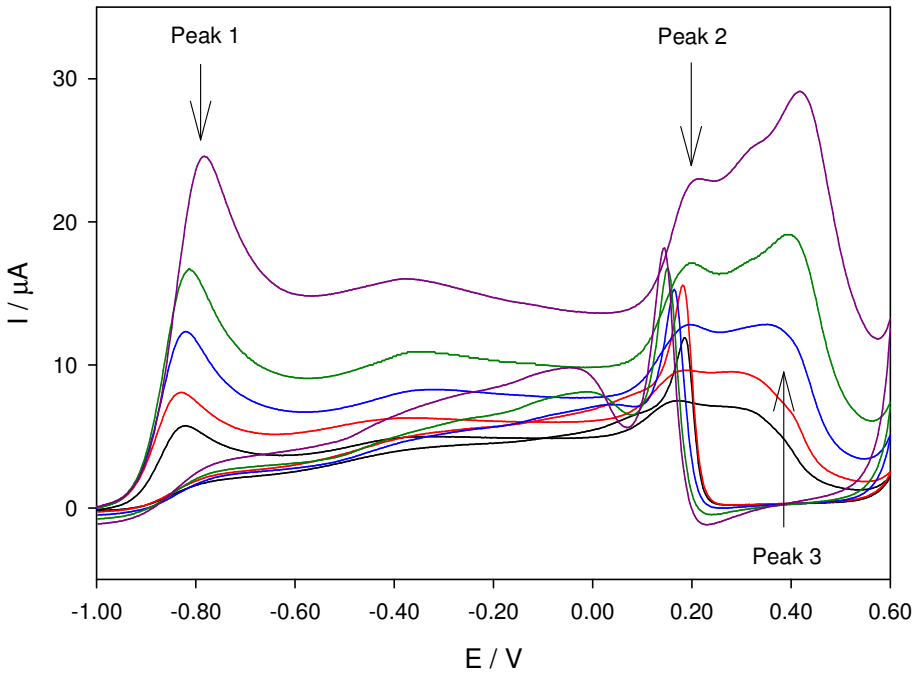

Figure 35. CVs of a 1.0 mM DMAB solution at pH 13.6; scan rates: 5 (black), 10 (red), 25 (blue), 50 (green) and 100 (purple) mV s^{-1}.

Table 5. Number of electrons transferred and diffusion coefficient obtained for DMAB oxidation through voltammetric techniques on gold electrodes.

		D / cm^2 s^{-1}			**n**	
		Irreversible	**Reversible**			
pH	**Peak**	**n = 3**	**n = 3**	**n = 2**	**D = 8.55 x 10^{-6} [77]**	**D = 7.48 x 10^{-6} [44]**
12.6	1	1.9 x 10^{-5}	4.0 x 10^{-6}	1.4 x 10^{-5}	2.3	2.4
	2	1.3 x 10^{-5}	2.7 x 10^{-6}	9.0 x 10^{-6}	2.0	2.1
	3	1.2 x 10^{-5}	2.5 x 10^{-6}	8.4 x 10^{-6}	2.0	2.1
13.6	1	1.7 x 10^{-5}	3.4 x 10^{-6}	1.2 x 10^{-5}	2.2	2.3
	2	8.9 x 10^{-6}	1.8 x 10^{-6}	6.2 x 10^{-6}	1.8	1.9
	3	1.5 x 10^{-5}	3.1 x 10^{-6}	1.0 x 10^{-5}	2.1	2.2

If the scan rate is increased further, the shapes of the voltammograms change, particularly in the reverse scan (see Figure 36). A small reactivation peak is still present, but it appears to be overlaid on a cathodic process. It is possible that the gold oxide is reduced electrochemically in that potential region, with the

fast scan not allowing DMAB sufficient time to chemically interact with it. It has been suggested in previous work that DMAB, or more likely some of its intermediates, react with the gold oxide before desorbing from the surface in this region of the voltammogram; the behaviour observed in Figure 36 is consistent with this scheme.[77]

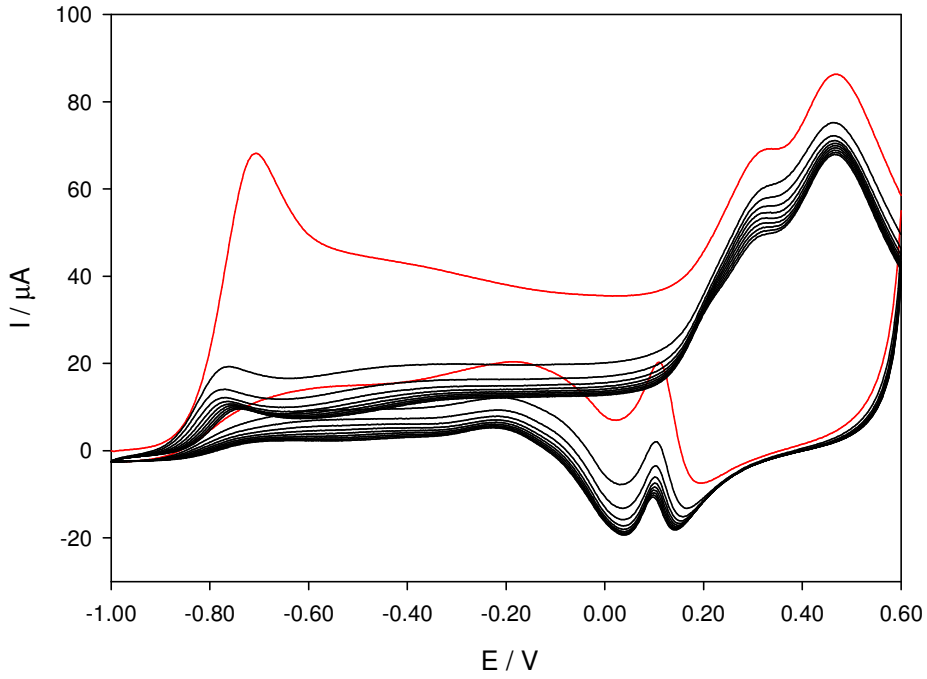

Figure 36. Consecutive voltammograms of a 1.1 mM DMAB solution, at pH 13.6 and 500 mV s^{-1}. The first cycle is marked in red.

Although essentially the same number of electrons is transferred at the two pH values presented in Table 5, the potentials at which the oxidation signals appear on the voltammograms shift with hydroxide concentration. Table 6 shows the shifts observed between pH 12.6 and 13.6 for each peak. Increasing pH facilitates the oxidation process, as the peak potentials move to more negative values.

Table 6. Peak shift with a unit of pH.

Peak	Δ E / V	stdev
1	-0.14	0.02
2	-0.07	0.01
3	-0.11	0.01

4.3.3 Effect of Concentration

The effect of solution concentration on DMAB oxidation was studied and the results can be seen in Figure 37 and Figure 38. The first figure shows the initial scan of a series of ten cycles for each concentration, while the second shows the tenth. The currents increase with DMAB concentration, and in Figure 38 a perfect trend can be seen.

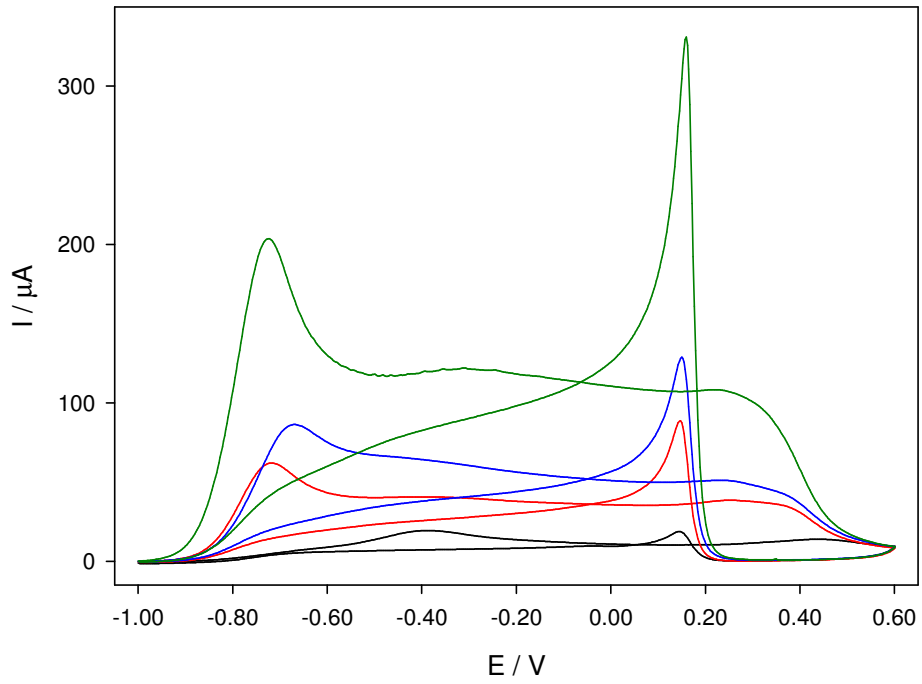

Figure 37. Cyclic voltammograms of DMAB on gold, at 50 mV s^{-1}. Concentrations: 1.1 (black), 3.4 (red), 6.2 (blue) and 11.3 (green) mM; the initial scan is shown in each case.

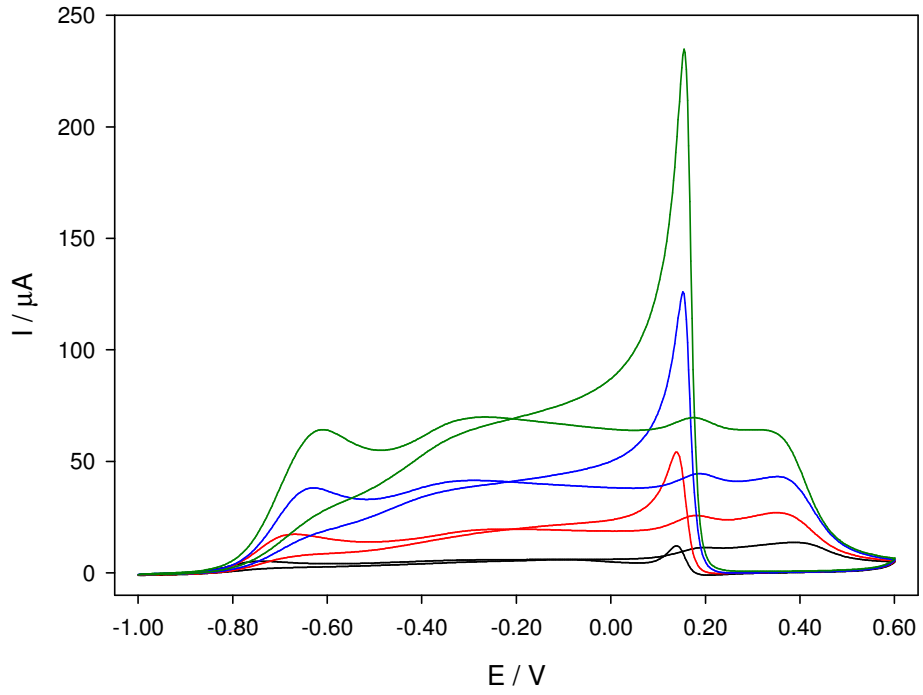

Figure 38. Conditions as in Figure 37, with the tenth scan shown in this case.

The position of the first peak in Figure 37 varies; the peak current, however, was found to be proportional of the concentration. As in the previous section, the number of electrons transferred and the diffusion coefficients were determined and are presented in Table 7. Only values for the first oxidation peak are given, as the peaks at positive potentials were not clearly defined at higher concentrations.

Table 7. Number of electrons transferred and diffusion coefficient obtained for DMAB oxidation, from the peak current dependence on the concentration, on the first scans.

D / cm^2 s^{-1}			**n**	
Irreversible	**Reversible**		**D = 8.55 x 10^{-6} cm^2 s^{-1} [77]**	**D = 7.48 x 10^{-6} cm^2 s^{-1} [44]**
n = 3	**n = 3**	**n = 2**		
1.6 x 10^{-5}	3.3 x 10^{-6}	1.1 x 10^{-5}	2.2	2.3

4.3.4 Time-dependent Voltammetry

The change in the position and height of the first peak is thought to be related to adsorption. In order to confirm this, the working electrode was immersed in a DMAB solution, while bubbling argon, for varying amounts of time

prior to the first voltammetric cycle. Figure 39 and Figure 40 show the first and tenth scan, respectively, of each series.

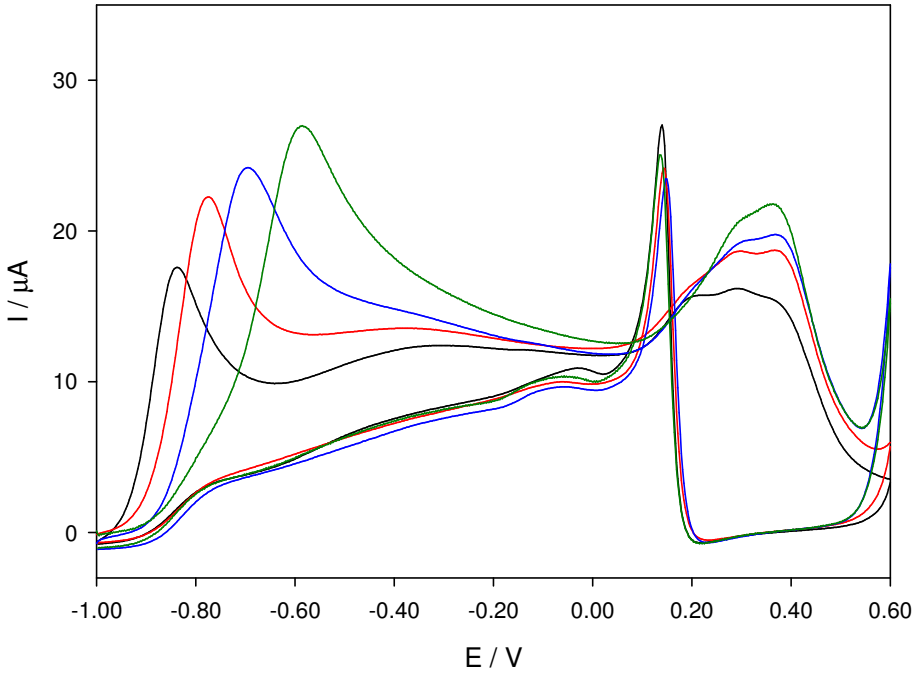

Figure 39. Voltammograms of a 1.2 mM DMAB alkaline solution, at 50 mV s^{-1}, with varying times of electrode immersion in solution prior to the first scan; black: t = 0, red: t = 5 min, blue: t = 10 min and green: t = 20 min.

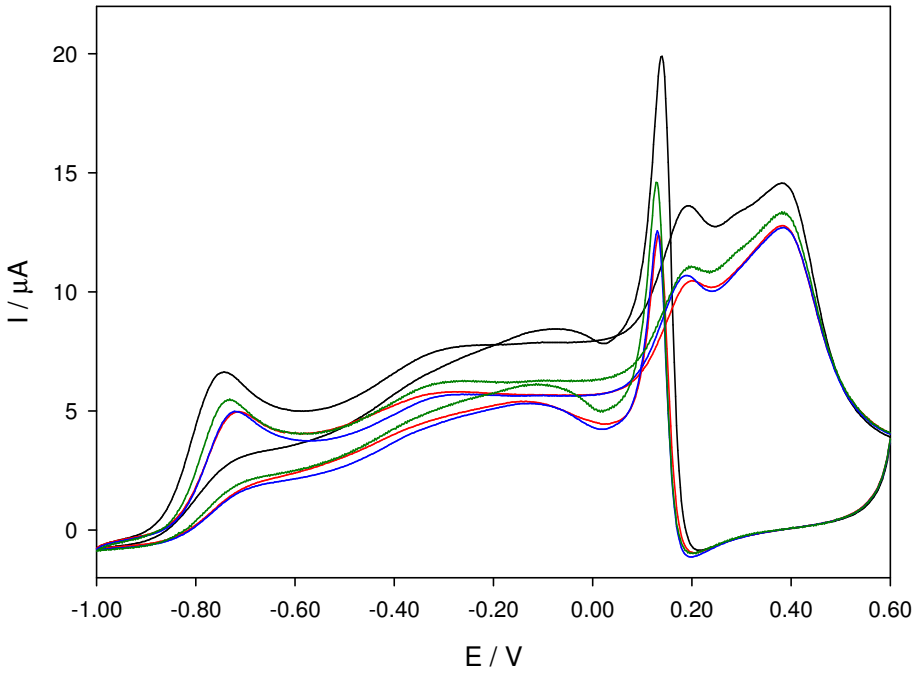

Figure 40. Conditions as in Figure 39, with the tenth scan shown in each case.

The peak current, and corresponding charge transferred, increase with immersion time; they are, however, practically constant by the tenth cycle. This behaviour is consistent with a strong influence of adsorption processes on the first scan, while the latter is driven basically by the diffusion from the bulk.

The potential at which the first oxidation peak appears shifts toward more positive potentials with immersion time on the first scan, while settling at a constant value by the tenth cycle. This could be due to the adsorbed species requiring a different oxidation potential or, more likely, to dimethylamine adsorption on the electrode surface hindering the oxidation of the boron-containing part of the DMAB molecule. The blocking effect of DMA on DMAB oxidation on gold surfaces has been previously suggested, though its effect has only been mentioned for the potential range of gold oxide formation.[45]

4.3.5 Dimethylamine Oxidation

Tests were performed in order to confirm that the oxidation signals observed are due to the boron-containing part of the DMAB molecule, and not the amine, as was the case on GC substrates. Figure 41 shows voltammograms performed in the presence of DMAB, dimethylamine, and the corresponding potassium hydroxide blank. It is clear that at negative potentials, the amine produces no signals above the blank; in the potential region between 0.10 and 0.60 V vs. Ag/AgCl, however, currents significantly higher than those due to the oxidation of the electrode surface can be seen, indicating oxidation of the dimethylamine molecule. This process is catalysed by the Au surface, as it occurs at much lower potentials than on GC (see Section 4.2.1). The possible catalysing effects of hydrous oxide formation of gold surface on the oxidation of small organic molecules, including DMAB, has been suggested in the literature;[76,82] the behaviour observed here would be consistent with this theory as the dimethylamine oxidation is seen at potentials just prior to and during gold oxide signals in the corresponding blank.

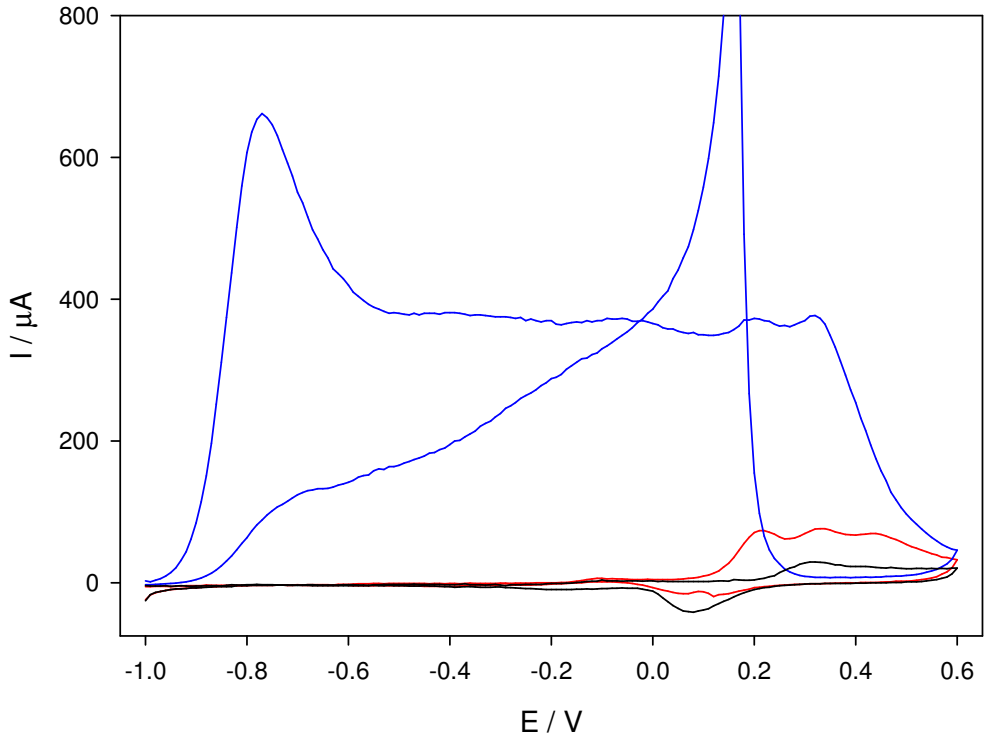

Figure 41. CVs on a gold electrode, at 100 mV s^{-1}, in alkaline aqueous solutions; black: blank, red: ~5.0 mM dimethylamine, and blue: 5.1 mM DMAB.

Although the currents due to the amine are considerably smaller than those in the presence of DMAB, at similar concentrations, the wave shape obtained is similar; a distinct peak is observed at approximately 0.20 V in both the dimethylamine and DMAB voltammograms, for example. This suggests that while the oxidation of dimethylamine contributes to the current in the positive potential region of the CV, other processes also occur, including the oxidation of the boron-related species and the gold surface. The multiple reactions render the study of that specific potential region particularly difficult, as the contributions from each process cannot be easily separated.

4.3.6 Choronoamperometric Studies

The electro-oxidation process of DMAB on gold electrodes was also studied through chronoamperometry. Figure 42 shows a series of consecutive potential steps at potentials slightly more positive than each of the three oxidation peaks.

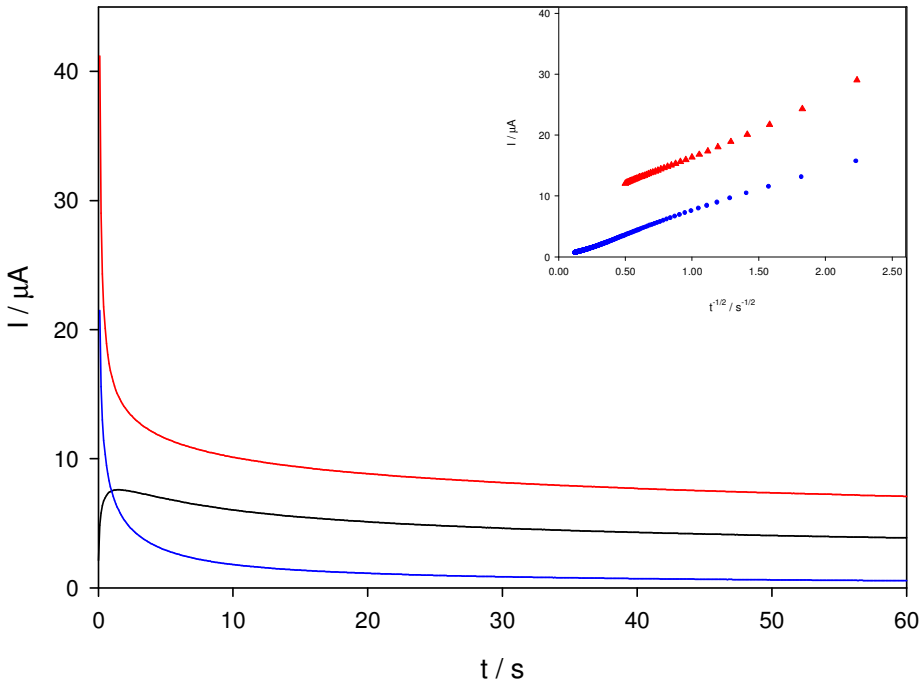

Figure 42. Consecutive potential steps in a 1.3 mM DMAB solution, at pH 13.6. Starting potential: -1.00 V vs. Ag/AgCl; successive applied potentials: -0.75 (black), 0.28 (red) and 0.42 (blue) V. Inset: corresponding Cottrell plots.

The data from these experiments was used to construct Cottrell plots (inset of Figure 42). A linear relationship between the current and $t^{-1/2}$ was found, in a certain time range. The number of electrons transferred in each step was calculated, using the Cottrell equation and reported diffusion coefficients; the results obtained are presented in Table 8.

Table 8. Number of electrons transferred in DMAB oxidation, obtained through consecutive potential steps.

	n	
E / V	**D = 8.55 x 10^{-6} cm^2 s^{-1} [77]**	**D = 7.48 x 10^{-6} cm^2 s^{-1} [44]**
-0.75	3.3	3.5
0.28	2.9	3.1
0.42	2.1	2.3

4.4 Microelectrode Electrochemistry

4.4.1 Voltammetric Studies

DMAB oxidation was studied on gold microelectrodes, through cyclic voltammetry; Figure 43 shows a series of representative voltammograms, at different scan rates. Two distinct oxidation signals can be seen on the forward scan and a sudden drop in current occurs around 0.40 V vs. Ag/AgCl; a sharp reactivation signal appears close to 0.18 V on the backward scan.

Although most voltammograms showed similar shape and current values, the lower scan rates display completely different behaviour (see inset of Figure 43). A change in mechanism has been reported at and below 5 mV s^{-1} on gold macroelectrodes; the behaviour observed here would be consistent with such a scheme.[77] This change in behaviour could be linked to the adsorption process of the dimethylamine; the slower scan rate would allow more time for the process to occur, leading to the partial blocking of the surface and lowering of the currents.

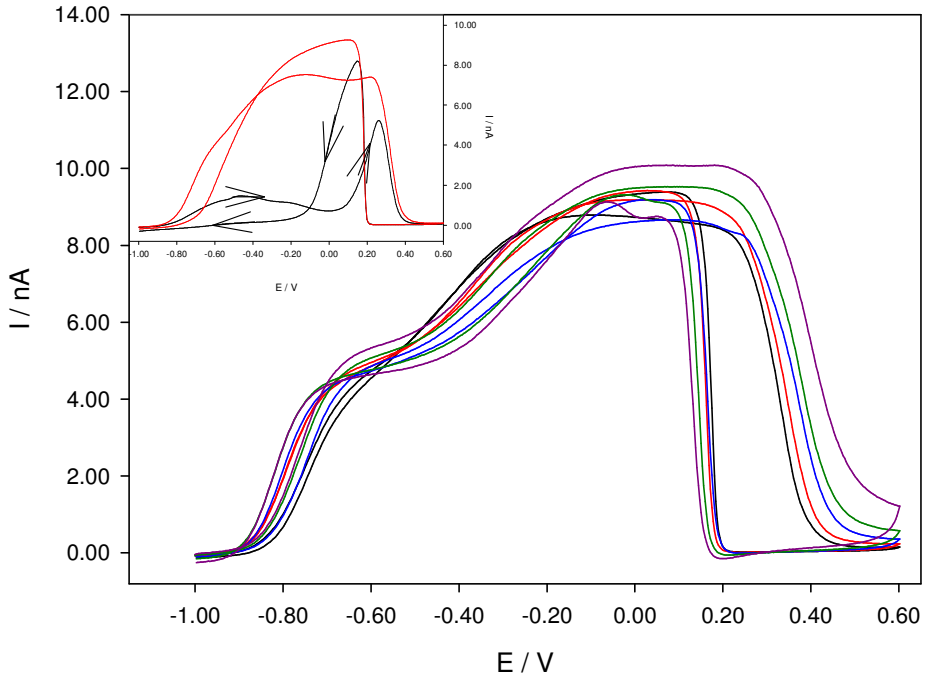

Figure 43. Voltammograms of a 0.9 mM DMAB solution at pH 13.6, on a gold microelectrode. Scan rates shown are 10 (black), 25 (red), 50 (blue), 100 (green) and 250 (purple) mV s^{-1}. The inset shows the behaviour at slower scan rates: 2 (black) and 5 (red) mV s^{-1}.

Equation 60 was used to determine the number of electrons transferred at each oxidation signal, using the values of the diffusion coefficient reported in the literature.[44,77] The value of D was also calculated, assuming a three-electron transfer for each oxidative wave. The average values obtained through different experiments, at scan rates that presented steady-state behaviour (*i.e.* > 5 mV s^{-1}), are displayed in Table 9.

Table 9. Number of electrons transferred and diffusion coefficient obtained for DMAB oxidation through voltammetric techniques on gold microelectrodes.

	n		**D / cm^2 s^{-1}**
E / V	**D = 7.48 x 10^{-6} cm^2 s^{-1} [44]**	**D = 8.55 x 10^{-6} cm^2 s^{-1} [77]**	**n = 3**
-0.60	3.6	3.2	9.1 x 10^{-6}
0.00	3.4	3.0	8.4 x 10^{-6}

Consecutive voltammograms of a DMAB solution were recorded and are presented in Figure 44 to Figure 47; each figure has different turning points, progressively going towards more positive potentials. In all cases, the first scan, marked in red, is different from the subsequent cycles, which tend towards similar behaviour.

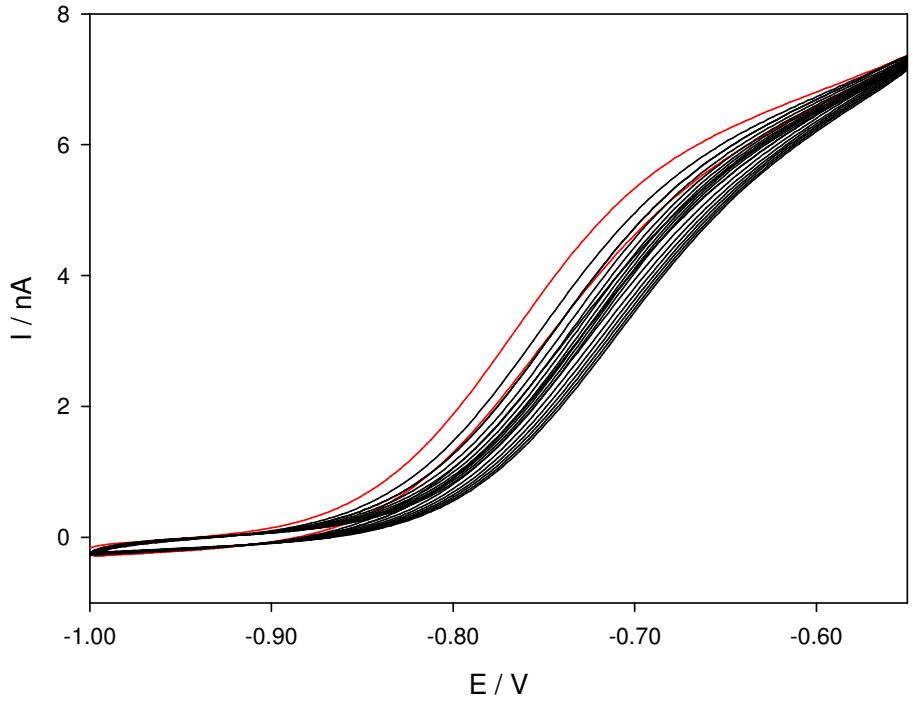

Figure 44. Consecutive cyclic voltammetries at 50 mV s^{-1} of 1.2 mM DMAB solution at pH 13.6 on a gold microelectrode; turning point: -0.55 V vs. Ag/AgCl. The first cycle is marked red.

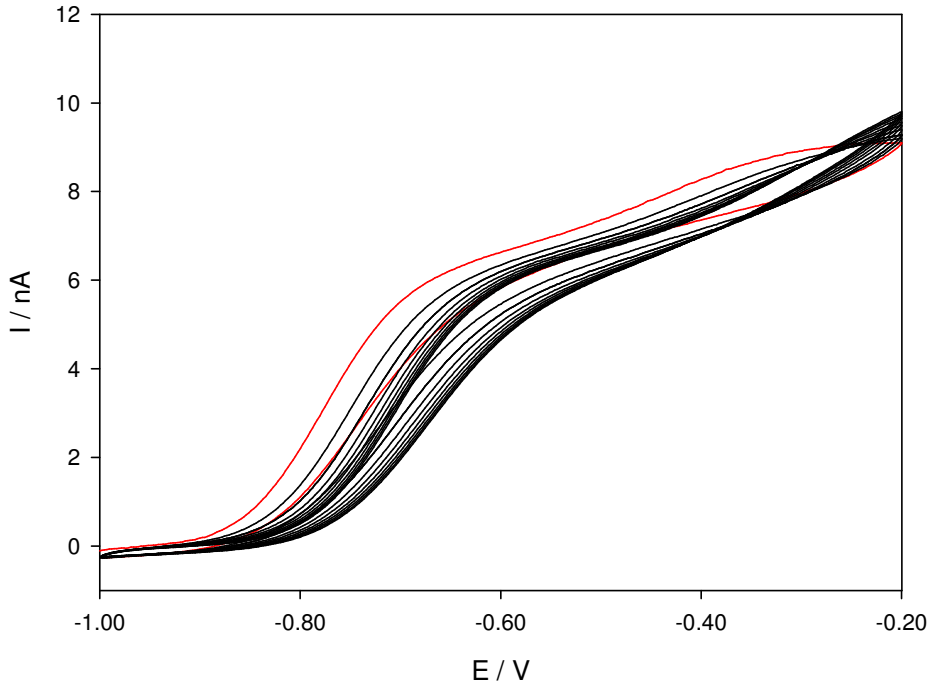

Figure 45. Conditions as in Figure 44; turning point: -0.20 V vs. Ag/AgCl.

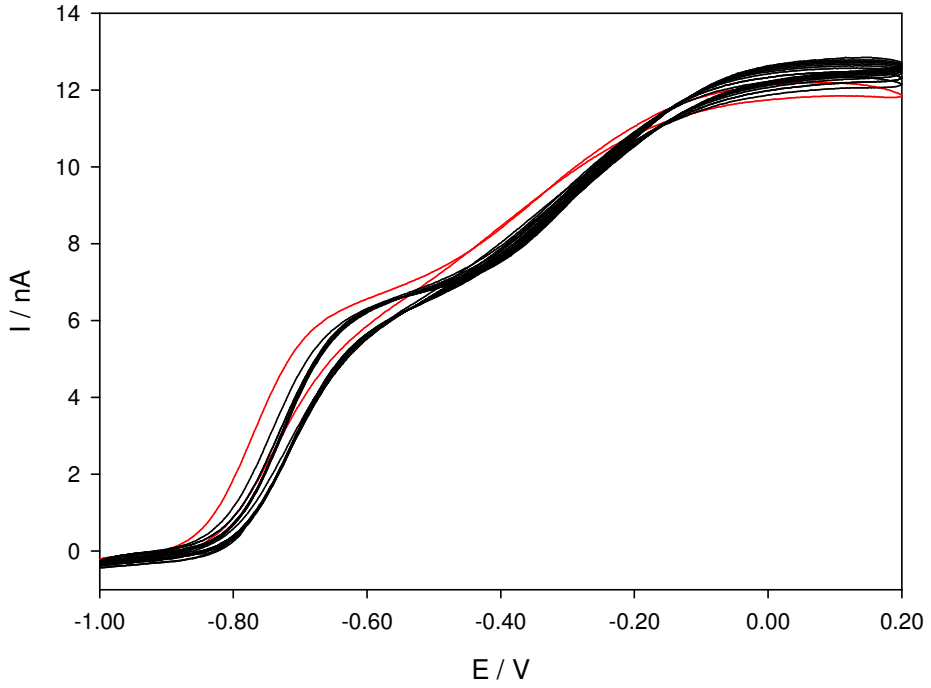

Figure 46. Conditions as in Figure 44; turning point: 0.20 V vs. Ag/AgCl.

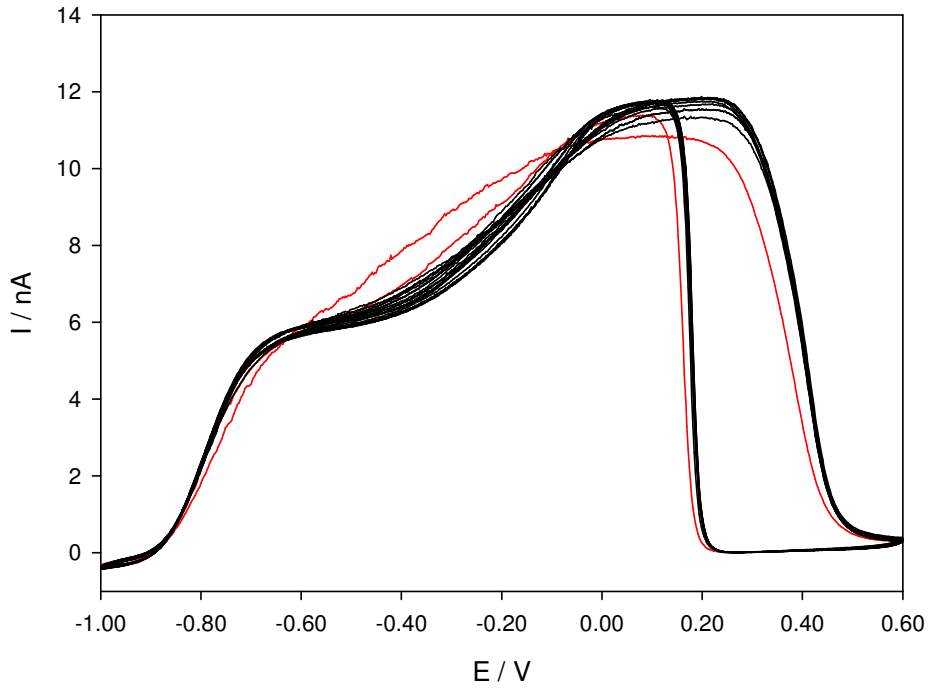

Figure 47. Conditions as in Figure 44; turning point: 0.60 V vs. Ag/AgCl.

It can be seen in the series of graphs that as the turning point was set to more positive potentials, the change between the first scan and subsequent scans is less pronounced. A small negative shift in the steady-state current value and the $E_{p/2}$ potential can also be observed, as the turning point is raised. This behaviour implies that a potential (or time) dependant adsorption process occurs.

4.4.2 Chronoamperometric Approach

Consecutive potential steps were applied, resulting in plots like the one presented in Figure 48. Although sweep voltammetries displayed steady-state behaviour, the chronoamperograms at different potentials displayed a continuous (and parallel) decay rather than a steady-state current; it was therefore not possible to calculate D and n.

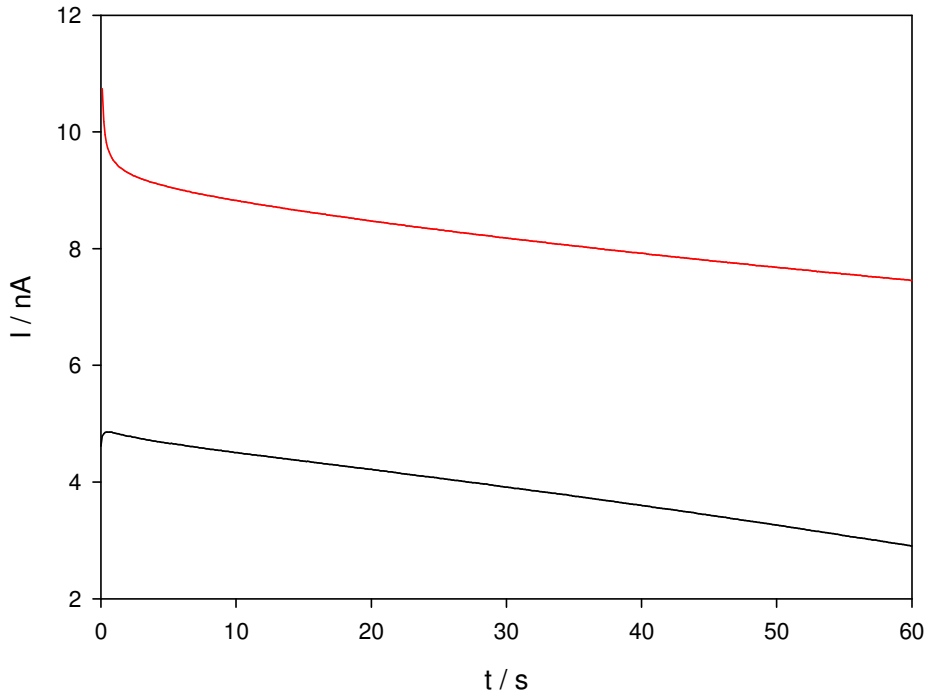

Figure 48. Chronoamperograms of a 0.9 mM DMAB solution at pH 13.6 at a gold microelectrode. Applied potentials: -0.60 (black) and 0.00 (red) V.

The current response from the first potential step, at -0.60 V, initially rises, probably due to an adsorption process, as seen for macroelectrodes at the first potential step. This, along with the possibility of an irreversible change of the electrode surface process observed through the voltammetric analysis, led to the application of potential steps after a series of voltammograms had been performed. Figure 49 shows two chronoamperograms at -0.55 V vs. Ag/AgCl: one performed after ten cycles (from -1.00 to 0.60 V, at 50 mV s^{-1}) and the other without the previous voltammetry. Although a rise in current is still observed after the voltammetric treatment, the shape of the transient changes; the potential cycling has conditioned the electrode surface, possibly by allowing adsorption phenomena to occur.

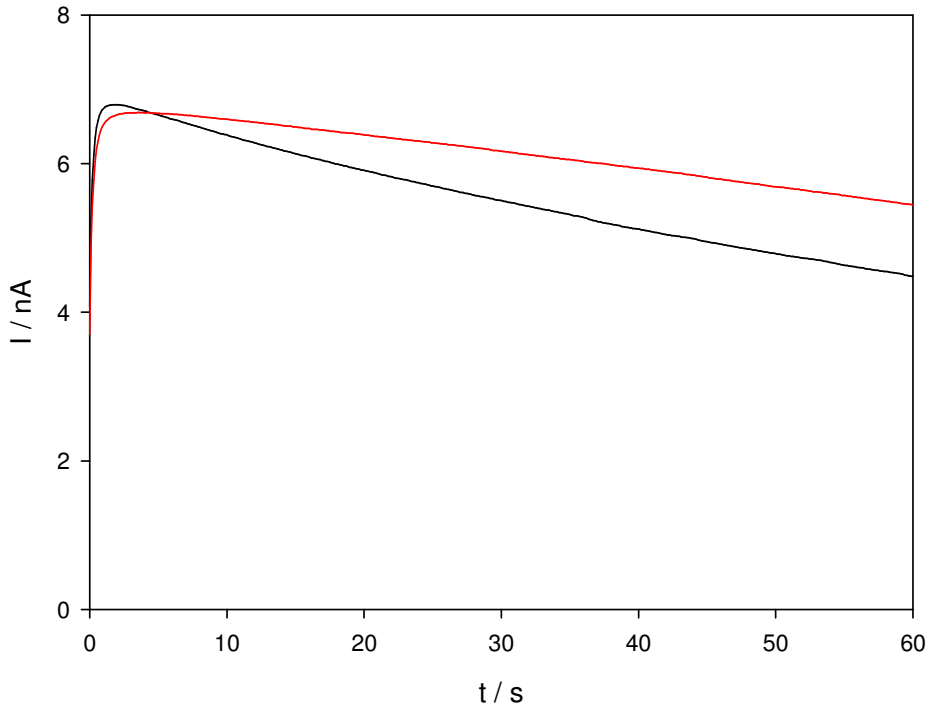

Figure 49. Chronoamperograms, at -0.55 V, of a 1.2 mM DMAB solution, with and without a series of ten cyclic voltammograms from -1.00 to 0.60 V at 50 mV s^{-1} (red and black lines, respectively).

A series of consecutive potential steps was then performed, alternating between a sixty seconds step at -0.55 V and a ten seconds step at -1.00 V; the corresponding transient is presented in Figure 50.

Although the first step shows the rising current in the first few seconds, mentioned above, the four subsequent steps appear almost identical, with the more conventional drop from the initial current. The current at longer times, however, seems to have similar behaviour in all five potential steps. The behaviour observed indicates a slow time-dependant adsorption process; it can be appreciated more clearly when the five potentials steps are overlaid (see Figure 51).

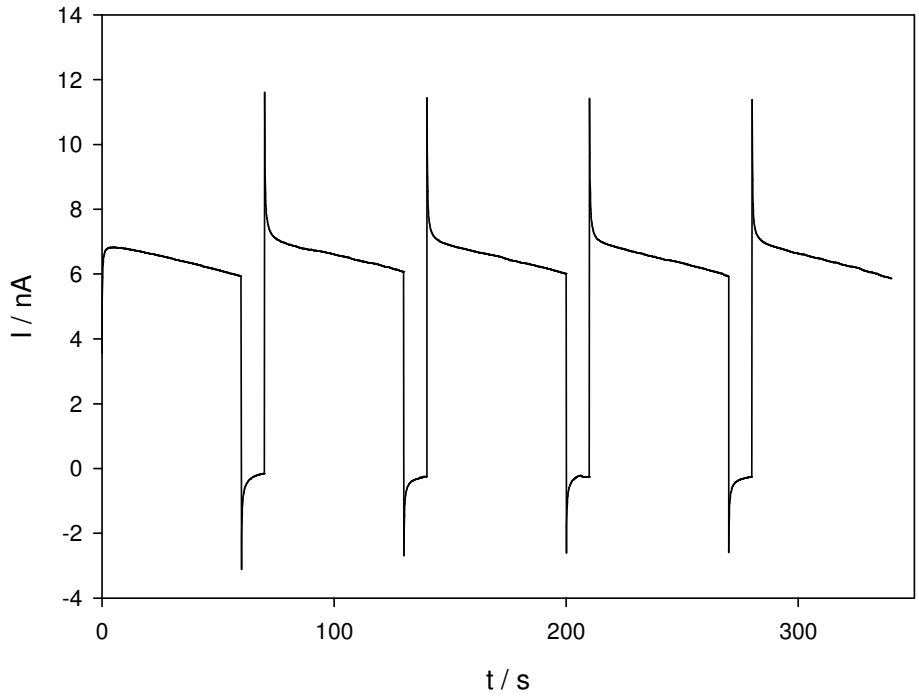

Figure 50. Chronoamperogram of a 1.2 mM DMAB solution at a gold microelectrode; alternating the applied potential between -0.55 and -1.00 V (60 and 10 seconds respectively).

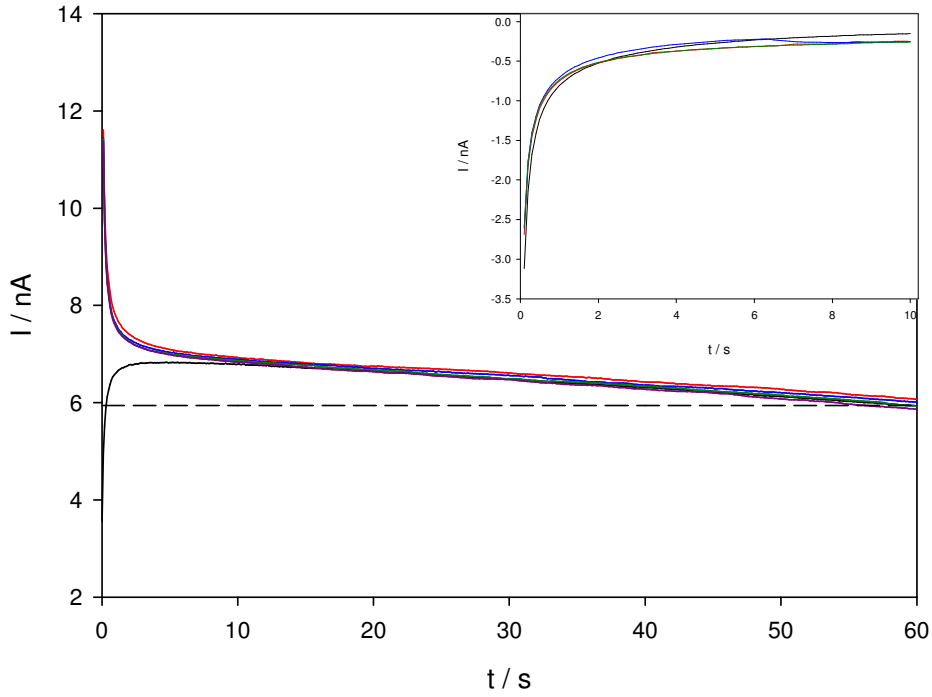

Figure 51. Overlay of the potential steps at -0.55 V vs. Ag/AgCl in Figure 50; the first one is marked in black. The inset shows the overlay of the potentials steps at -1.00 V. The dashed line represents the theoretical value of the current for a three-electron transfer.

As mentioned above, all chronoamperograms in Figure 51 reach similar currents, though they have quite different behaviour in the first ten seconds. The

current reached after a minute of applied potential agrees with that theoretically calculated for a three-electron transfer in the experimental conditions, assuming the reported diffusion coefficient for DMAB (dashed line in Figure 51). The inset of Figure 51 shows the overlay of the potential steps at -1.00 V. In that case, the current practically drops to zero after the first couple of seconds.

4.5 Complementary Techniques

4.5.1 Nuclear Magnetic Resonance (^{11}B NMR)

^{11}B NMR was employed in an attempt to identify the B-containing species found in aqueous DMAB solutions.[viii] Four different systems were studied, with both proton-coupled and decoupled spectra recorded. All the systems studied consisted of solutions of approximately the same concentration of DMAB in deuterated water; in addition, solutions b, c and d contained ~0.7M KOH. Samples c and d were in contact with a platinum gauze and a gold disk, respectively, before the spectra were taken. Table 10 shows that the results obtained in all cases are very similar.

Table 10. ^{11}B NMR signals and coupling constants for DMAB in D_2O (a), in alkaline solution (b), in contact with a platinum electrode (c), and with a gold electrode (d).

	H-decoupled / ppm	**H-coupled / ppm**				**j / Hz**
		1	**2**	**3**	**4**	
a	-15.1	-13.7	-14.6	-15.6	-16.6	92.7
b	-15.2	-13.7	-14.7	-15.6	-16.6	92.4
c	-15.2	-13.7	-14.7	-15.7	-16.6	92.4
d	-15.2	-13.7	-14.7	-15.7	-16.6	92.9

The 1:3:3:1 quartets obtained for the coupled spectra indicate that a tetrahedral species containing $-BH_3$ is present in solution. From the results

[viii] ^{11}B NMR spectroscopic measurements were made by Dr Barabara E. Gore of the NMR Laboratory of the School of Chemistry.

observed in Table 10, the same species is probably present in all the conditions studied. Unfortunately, the experiments performed do not allow the differentiation between the DMAB molecule and its likely dissociation product, BH_3OH^-. Comparison to literature values, however, would indicate that DMAB, and not BH_3OH^-, is predominant in solution. The spectra obtained for all the DMAB solutions are somewhat different from that reported for the intermediate of borohydride hydrolysis, thought to be BH_3OH^-; in that case the coupling constant was found to be 60 Hz, centred around 13.9 ppm.[60] Previous ^{11}B NMR spectra of DMAB in aqueous solution were not found in the literature. Reported spectra in other media, however, are similar to the results presented here; in deuterated chloroform , for example, δ = 15.12 and j = 95.6 Hz.[136,137]

4.5.2 EQCM and X-Ray Photoelectron Spectroscopy (XPS)

Other techniques were used in order to obtain further understanding of the adsorption process involved in the electro-oxidation of DMAB, such as XPS and EQCM. The former gave negative results, as no traces of boron were found on the gold surfaces, either after immersion in DMAB solutions or after extended electrolysis. EQCM did not provide any relevant information, as the weight changes of the gold electrodes in the KOH blank, in the potential region of interest, were very large; it was therefore not possible to extract any reliable DMAB-related information.

4.6 Borohydride Oxidation

As discussed in the introduction (Section 1.2), borohydride and DMAB oxidation are closely related, as the most commonly accepted intermediates and mechanisms are the same for both. Borohydride oxidation was studied in a similar manner to DMAB; its behaviour in alkaline aqueous solution through cyclic voltammetry, on gold electrodes, can be seen in Figure 52.

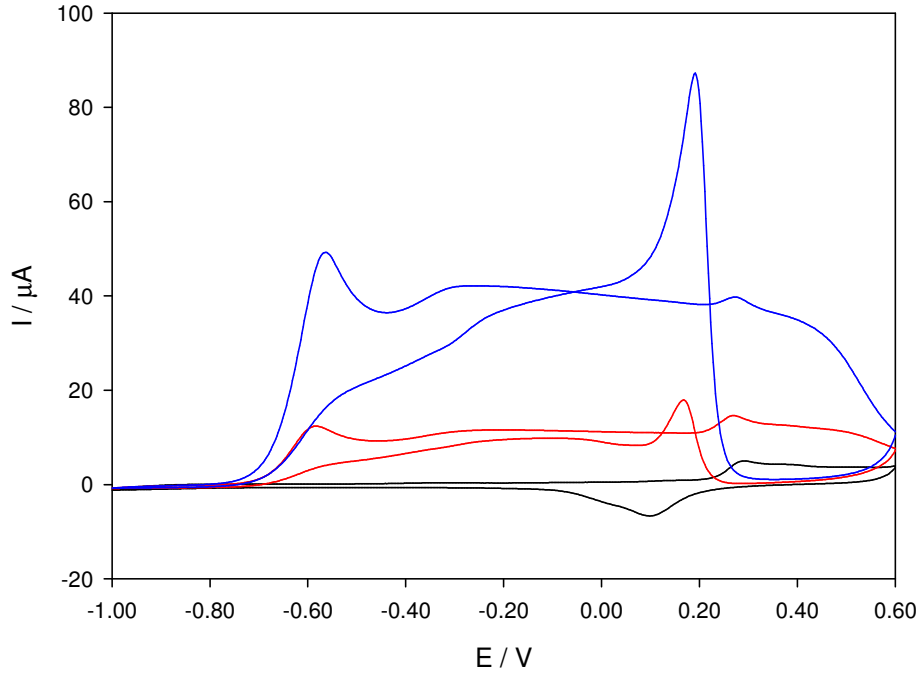

Figure 52. Cyclic voltammograms at 50 mV s^{-1} of alkaline aqueous solution on a gold electrode, in the presence (red: 1.0 mM, blue: 3.4 mM) and absence of Borohydride (black).

Figure 52 shows two cyclic voltammograms at different borohydride concentrations and one in the absence of borohydride at equal pH and scan rate. The borohydride voltammograms present two clear oxidation signals on the forward scan, in addition to those in the gold oxide potential region, and a reactivation peak on the backward scan (at around 0.15 V vs. Ag/AgCl). The reactivation peak appears at similar potentials in both scans, while its position is also close to that found in DMAB voltammetry.

The most marked difference between the blank and the scans in the presence of borohydride appears in the reverse scan, between 0.00 and 0.20 V; in the former a cathodic peak is observed, while in the presence of borohydride the reactivation signal is seen. On the forward scan, in the positive potential region, similar peaks are observed in all three voltammograms, though the current increases in proportion to the concentration of borohydride. There are no signals in the negative potential region of the blank, while defined peaks close to -0.60 V appear in the presence of borohydride, with a shoulder between -0.40 and -0.20 V vs. Ag/AgCl.

4.6.1 Consecutive Voltammetry

Fifteen consecutive scans were recorded (see Figure 53), demonstrating a trend of decreasing current and potential shifts for the forward scans. The graph shows a series of consecutive voltammograms where the potential of the oxidation peaks clearly shifts to more negative values from the first scan, marked red, to subsequent scans; for the first oxidation peak, for example, the potential shifts approximately from -0.35 to -0.55 V. A small shoulder can be seen on subsequent cycles, where the first oxidation peak appears on the initial scan. After the tenth cycle the voltammograms seem to be reproducible, the largest difference being between the first and second scan.

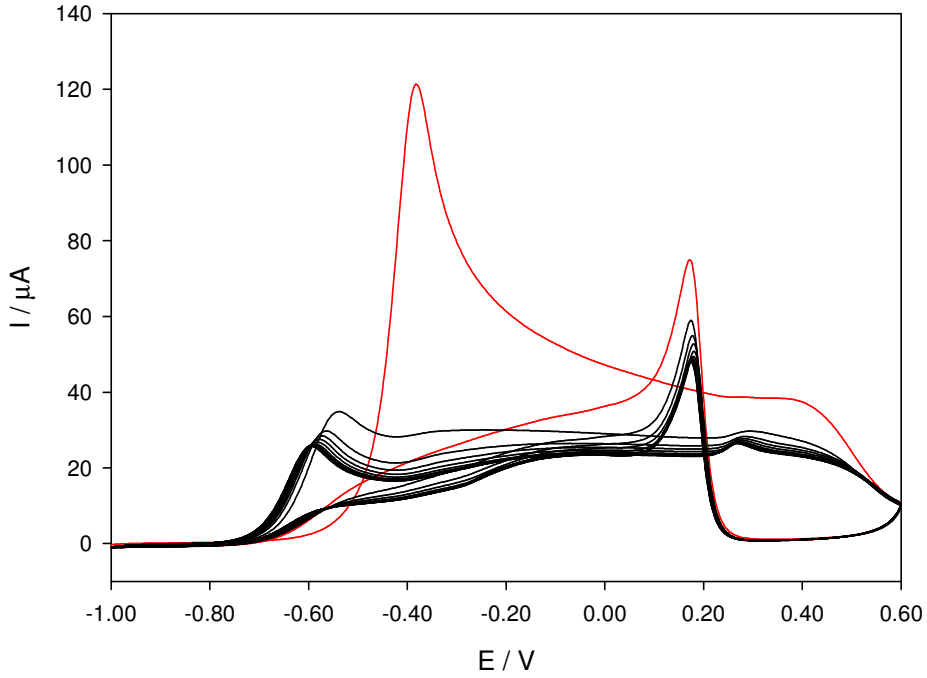

Figure 53. Consecutive cyclic voltammograms of a 1.9 mM Sodium Borohydride solution at a pH value of 13.6, on a gold disk electrode at 50 mV s^{-1}. The first scan is in red.

As the biggest changes were observed for the first oxidation peak, consecutive voltammograms of that potential region were also performed, and are presented in Figure 54. Although the current decreases with each cycle, the drop is not as marked as it was in Figure 53. The peak potential, on the other hand, appears to be relatively stable throughout the experiment.

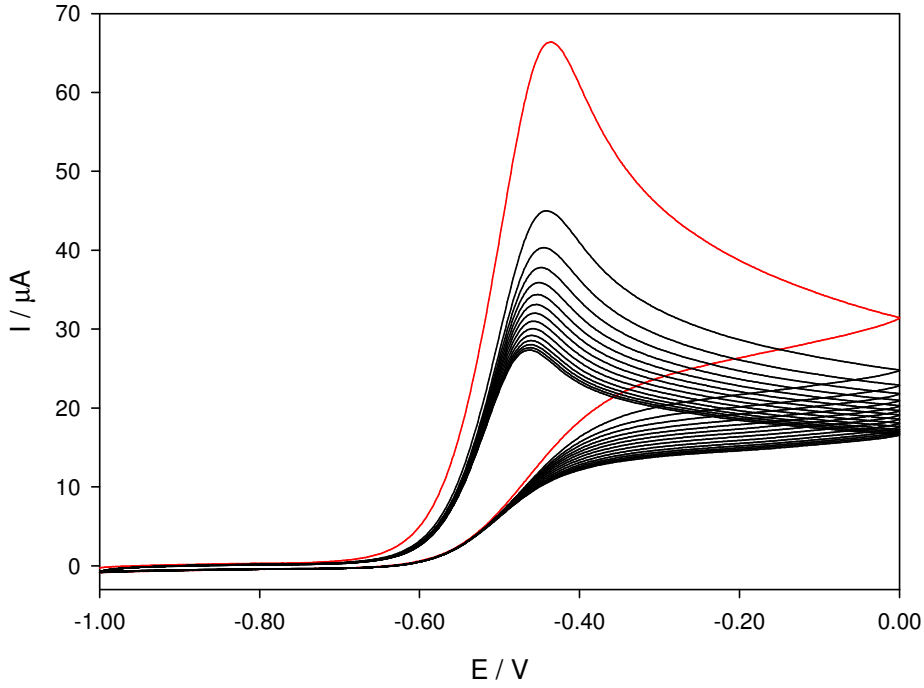

Figure 54. Consecutive CVs of a pH 13.6, 1.3 mM Sodium Borohydride solution at 50 mV s^{-1} with a turning potential between the first and second peak (0.00 V). The first cycle is in red.

Consecutive voltammograms of a borohydride solution, with different positive turning potentials, were recorded and are presented in Figure 55 through Figure 59. In each case, the first scan is marked in red and the subsequent scans have a consistent trend. As was the case for DMAB, the change between the first scan and subsequent scans is more pronounced as the turning point is set more positive. A small negative shift in the peak potential is also observed as the turning point is raised.

The last few scans of Figure 59 (and also Figure 53), where the whole potential range is covered, overlay. This does not occur for voltammograms with other turning points; in those cases, the scans continuously change, following a trend. The difference between consecutive cycles decreases with the number of scans in Figure 55 through Figure 58, however. It is possible that the generation of an adsorbed species on the electrode surface causes the suppression of subsequent voltammograms, as the turning points is more positive.

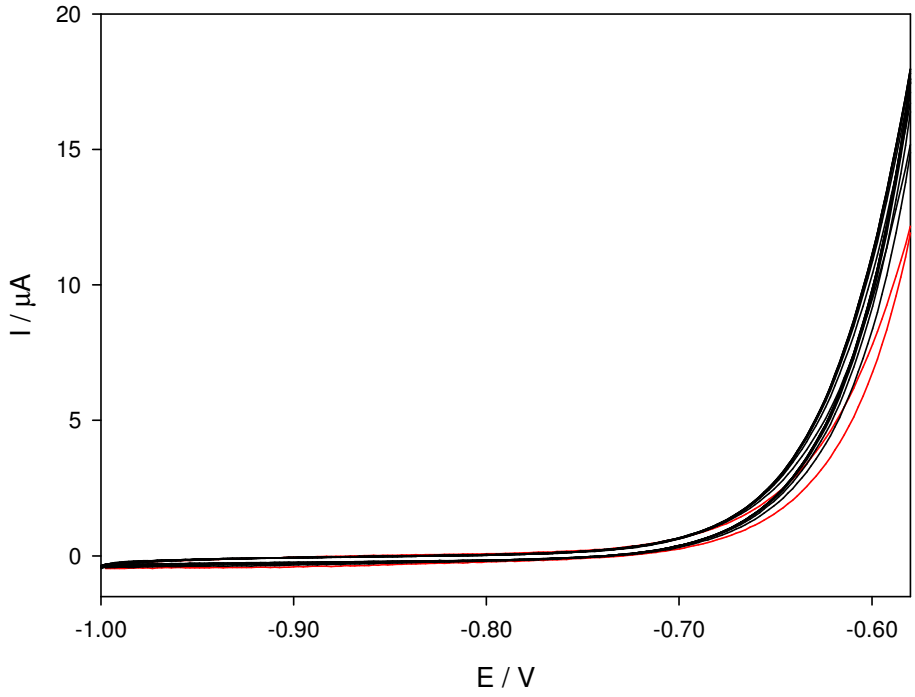

Figure 55. Consecutive CVs at 50 mV s^{-1} of 1.0 mM Borohydride solution on a gold electrode; the first scan is marked red. Turning point: -0.58 V vs. Ag/AgCl.

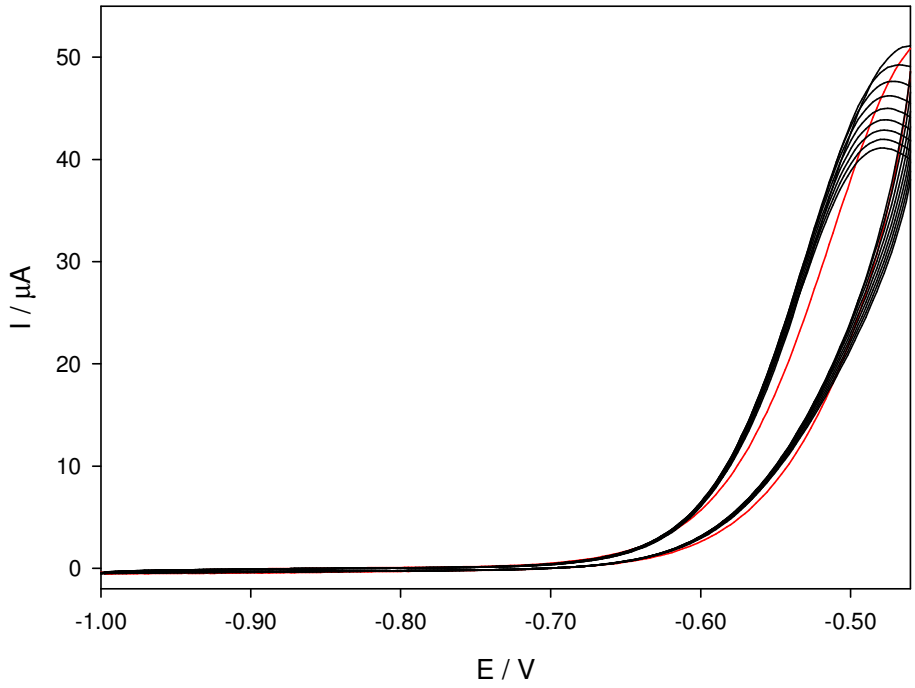

Figure 56. Conditions as in Figure 55; turning point: -0.46 V vs. Ag/AgCl.

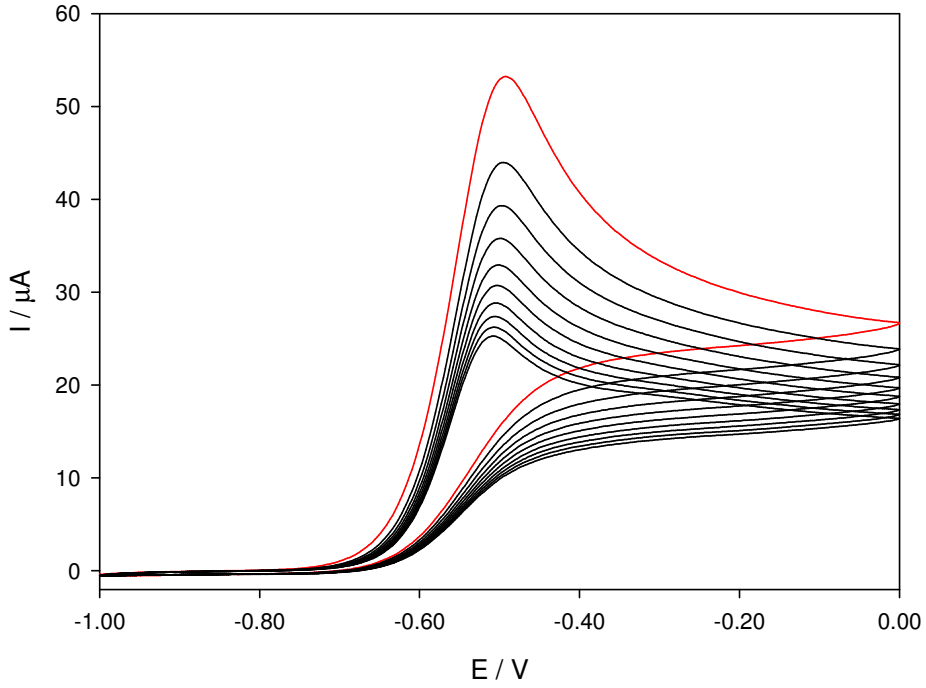

Figure 57. Conditions as in Figure 55; turning point: 0.00 V vs. Ag/AgCl.

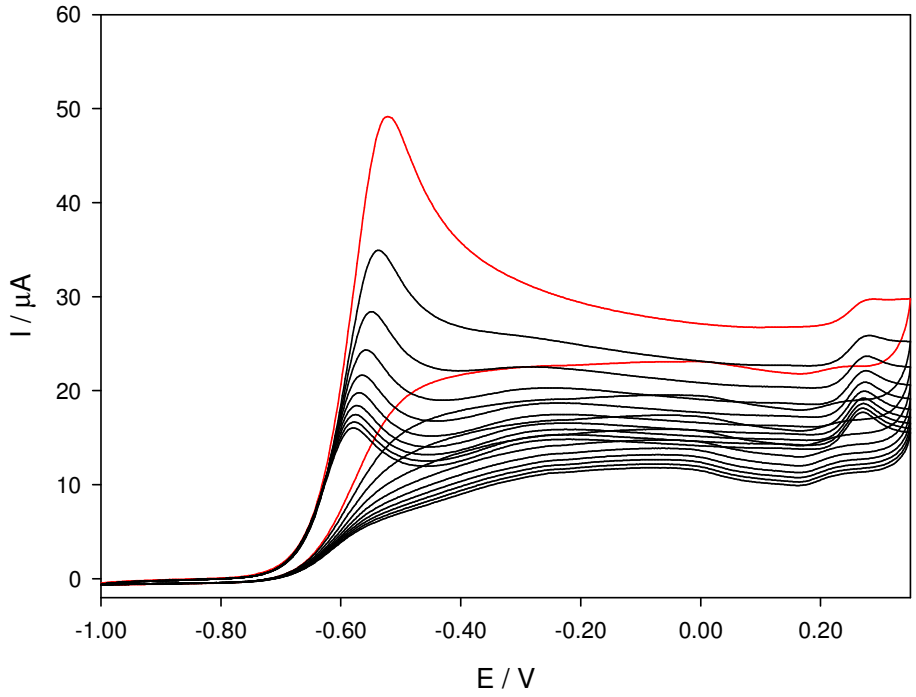

Figure 58. Conditions as in Figure 55; turning point: 0.35 V vs. Ag/AgCl.

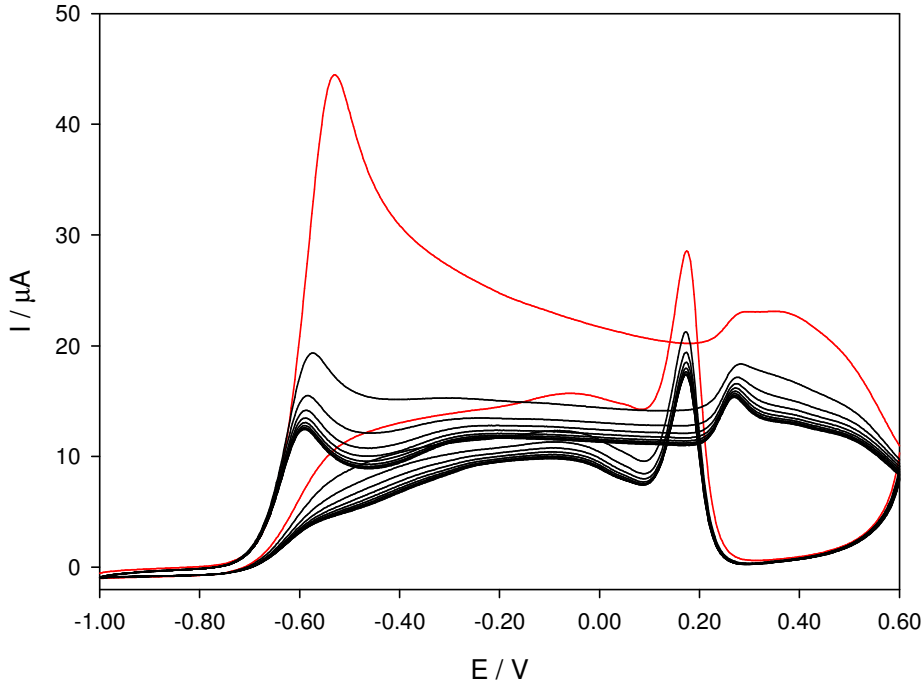

Figure 59. Conditions as in Figure 55; turning point: 0.60 V vs. Ag/AgCl.

The peak currents of the first oxidation signal from Figure 57 to Figure 59 are presented as a function of scan number in Figure 60; the trends obtained demonstrate that the higher turning potential promotes the decrease in current and stabilization of the voltammograms. It is particularly clear that once the full potential range is covered, reproducibility is achieved within the first three or four cycles. This could indicate an effect of the oxide formation and removal from the surface; the renewal of the electrode surface removes the adsorbed borohydride (or intermediates) and thus the consecutive cycles are mainly diffusion controlled, with little effect of the pre-adsorbed species. The chemical interaction between the gold oxide and the borohydride (or intermediate) molecules would lead to the complete oxidation of all molecules at the surface, providing a “fresh” surface for the next voltammogram. The inset of Figure 60 shows the charge associated to the borohydride oxidation (up to 0.00 V); the results show that less charge is transferred with each consecutive scan, settling sooner with increasing turning potential. This confirms that more molecules of borohydride are oxidised initially, likely due to the adsorbed molecules adding to those diffusing from solution, while as the process progresses it is more diffusion controlled, as the adsorbed species are removed from the surface.

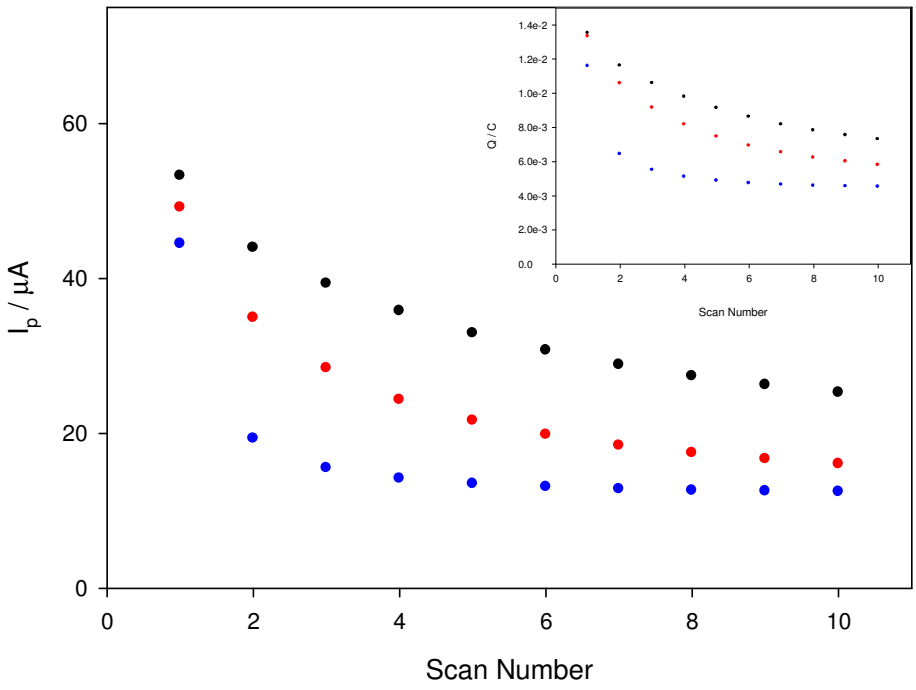

Figure 60. Peak current as a function of the number of cycles; data extracted from Figure 57 (black), Figure 58 (red) and Figure 59 (blue). The inset shows the corresponding charges transferred up to 0.00 V.

Similar behaviour was observed for DMAB (see Section 4.3.1), and it can be attributed to the same effects of the oxidative removal of adsorbed species with increasing turning potential. The CVs become reproducible sooner for borohydride, however, and the potential of the first oxidation peak does not change as noticeably in this case. The large potential shifts observed in the DMAB case, as well as the additional cycling needed to obtain reproducible voltammograms, are likely due to the strong adsorption of dimethylamine on the gold surface; dimethylamine adsorption has been reported to affect the oxidation process of the boron-containing part of the molecule.[45]

4.6.2 Time and Potential Dependence

The trends observed in the previous section do not reveal whether the decrease in current, from one scan to the next, is due to simple concentration depletion near the electrode surface, or if it is due to other potential-dependant or time-dependant phenomena. For further clarification, a series of experiments was carried out in which several scans were performed, either in direct succession or waiting some time at open circuit potential, with and without bubbling argon in the

meantime. One minute was left between the first two scans, as well as between the second and the third scans; five minutes were left between the third and the fourth cycle, on the other hand. The results obtained are presented in Figure 61.

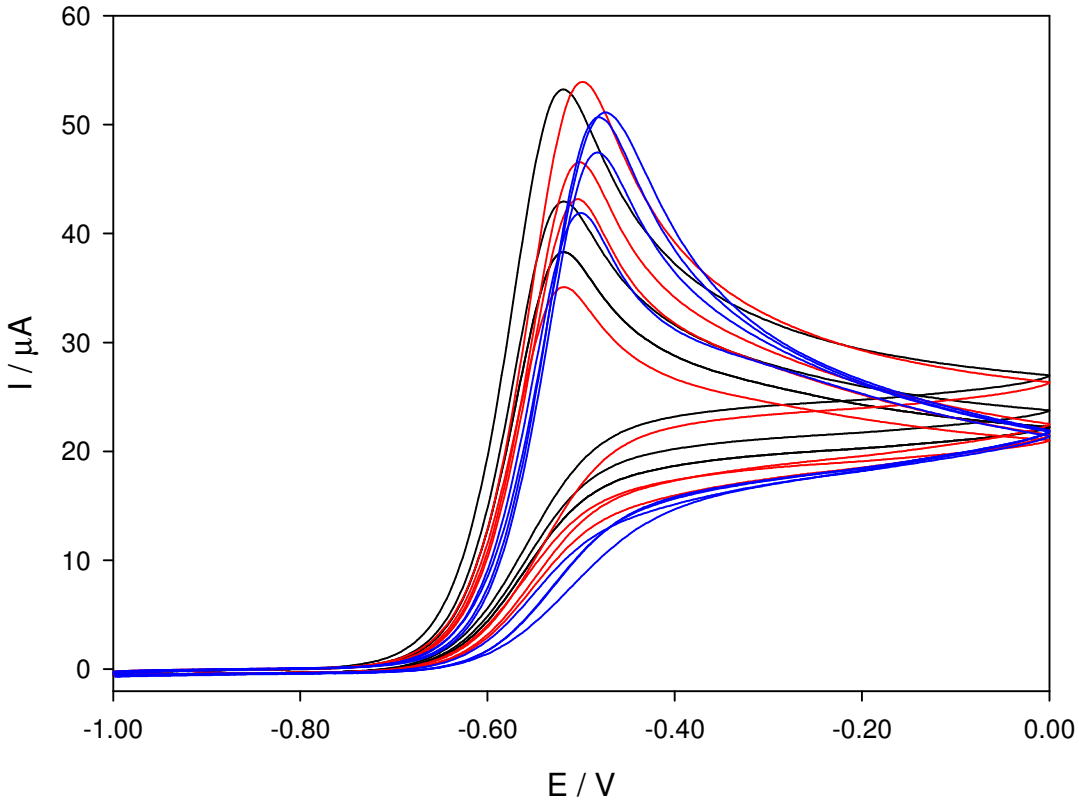

Figure 61. Successive voltammograms at 50 mV s^{-1} of a 1.0 mM borohydride solution; the black curves are consecutive scans, the red curves were recorded with set waiting times between scans, and the blue curves were recorded bubbling argon during the waiting times.

The decrease in current is more pronounced in the scans that were performed in direct succession. The difference between bubbling argon or not is less striking, although the current decreases slightly more slowly when argon is used. The drop in current with successive scans appears to be strongly linked to a potential-dependant phenomenon, as well as concentration depletion near the surface. It is possible that an irreversible process takes places on the electrode, that the borohydride molecule is further oxidised at higher potentials or even that □□□□□□□□□□□□□□w□□□□□□□□□□□□□□□□□□□□□□□□□□□□□□□□□ he first step; waiting between scans might allow the removal of the adsorbed species, accounting for the behaviour observed.

4.6.3 Effect of Scan Rate

The effect of scan rate on the oxidation process was studied: the results are presented in Figure 62, where the scan rates used were 2, 5, 10, 25, and 50 mV s^{-1}. As expected, the currents rise with increasing scan rate; this trend is not followed on the first peak above 50 mV s^{-1}, however. It is possible that at higher scan rates the adsorption process does not have enough time to occur.

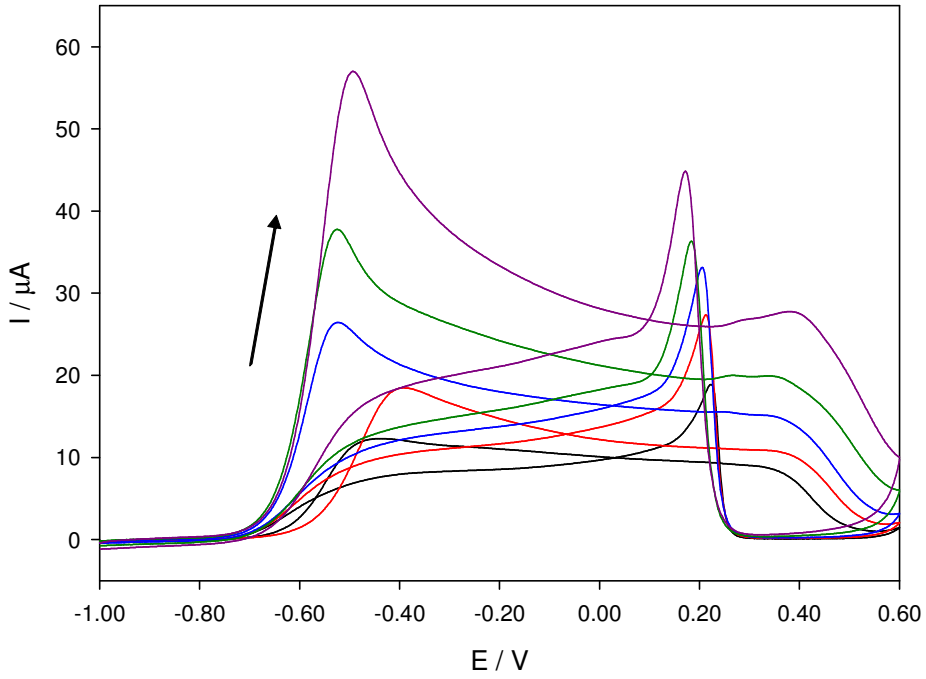

Figure 62. Cyclic voltammetries of a 1.3 mM solution of sodium borohydride at pH 13.6 on a gold disk electrode. The arrow indicates increasing scan rate: 2, 5, 10, 25 and 50 mV s^{-1} are shown.

The diffusion coefficient and the number of electrons transferred were calculated and are presented in Table 11. Both reversible (Rev) and irreversible (Irrev) cases were assumed, with 3 and 4 electrons used in the determination of D; as in the case of DMAB, α was assumed to be 0.5, while n_a was set as 1, for the irreversible analysis.

Table 11. Number of electrons transferred and diffusion coefficient obtained for the first peak of borohydride oxidation, through the effect of scan rate, on a gold electrode.

D / cm^2 s^{-1}			
Irrev (n = 3)	**Irrev (n = 4)**	**Rev (n = 3)**	**Rev (n = 4)**
2.9 x 10^{-5}	1.2 x 10^{-5}	1.8 x 10^{-5}	7.7 x 10^{-6}
n			
D = 2.24 x 10^{-5} cm^2 s^{-1} [73]		**D = 1.68 x 10^{-5} cm^2 s^{-1} [67]**	
2.9		3.1	

4.6.4 Effect of Concentration

The effect of solution concentration was also studied. The results obtained can be seen in Figure 63 and Figure 64, where the first and tenth cycles, respectively, are shown for each concentration studied. As expected, the currents increase with borohydride concentration, and in Figure 64 a perfect trend is observed.

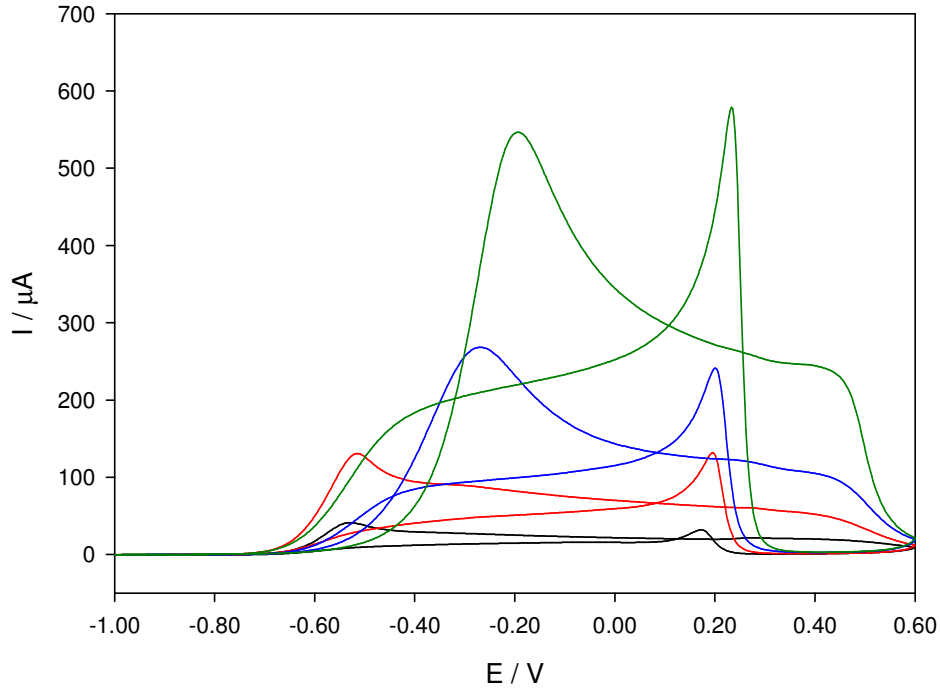

Figure 63. CVs of borohydride on gold, at 50mV s^{-1}. Concentrations: 1.0 mM (black), 3.4 mM (red), 5.8 mM (blue) and 12.5 mM (green).

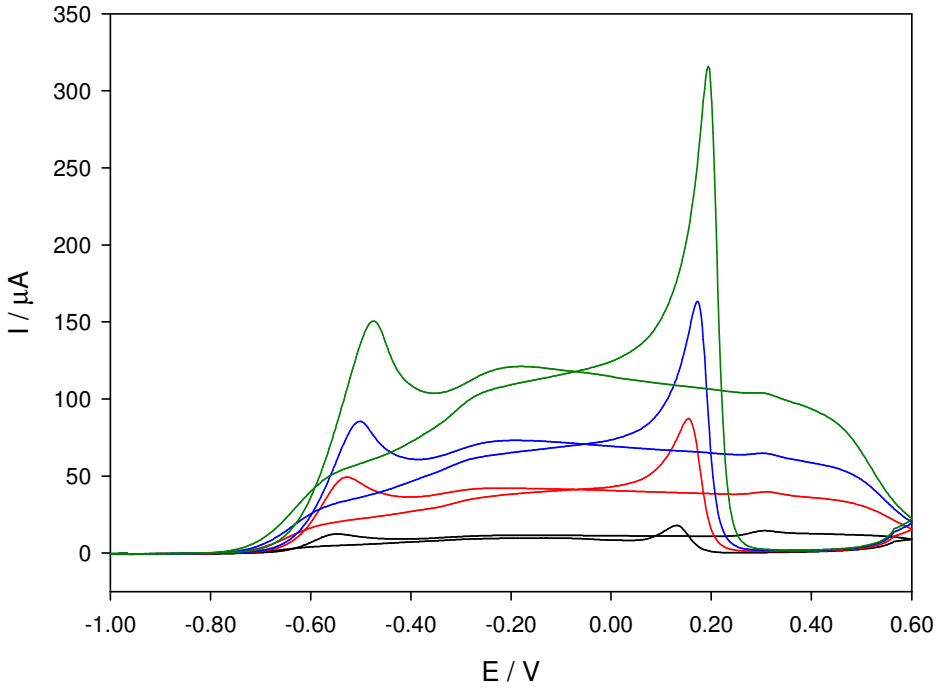

Figure 64. CVs of borohydride on gold, at 50mV s^{-1}; the tenth cycle is shown in each case. Concentrations: 1.0 mM (black), 3.4 mM (red), 5.8 mM (blue) and 12.5 mM (green).

Although the position of the first peak in Figure 63 varies, the peak current is directly proportional to the concentration. This allowed the determination of the values of n and D shown in Table 12. The conditions used for the calculations are as discussed in Section 4.6.3, for the scan rate.

Table 12. Number of electrons transferred and diffusion coefficient obtained for borohydride oxidation, through the effect of concentration, on a gold electrode (based on the first cycle).

D / cm^2 s^{-1}			
Irrev (n = 3)	**Irrev (n = 4)**	**Rev (n = 3)**	**Rev (n = 4)**
4.2 x 10^{-5}	1.8 x 10^{-5}	2.6 x 10^{-5}	1.1 x 10^{-5}
n			
D = 2.24 x 10^{-5} cm^2 s^{-1} [73]		**D = 1.68 x 10^{-5} cm^2 s^{-1} [67]**	
3.1		3.5	

4.6.5 Chronoamperometric Studies

Chronoamperometric measurements were carried out: with the consecutive application of potentials more positive than those at which each oxidation peak

occurs on the CVs (0.00 and 0.50 V vs. Ag/AgCl). An example of such experiments is shown in Figure 65.

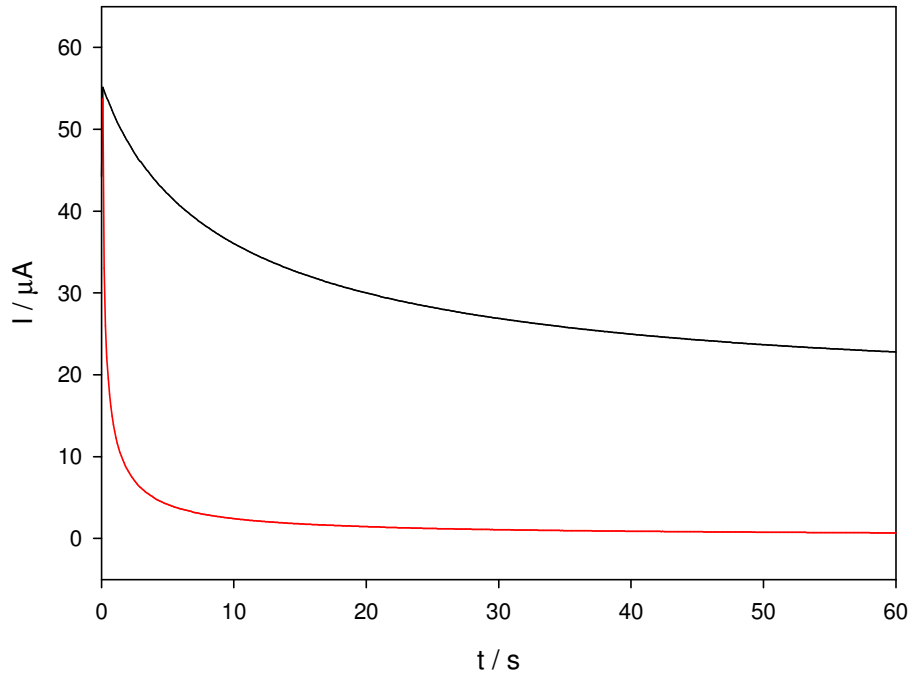

Figure 65. Chronoamperograms at 0.00 V (black) and 0.50 V (red) in a 1.9 mM sodium borohydride solution, at pH 13.6 (starting potential: -1.00 V vs. Ag/AgCl).

A peak in the current is not observed at the first applied potential, in contrast to the DMAB case; the transients for the two applied potentials, however, do not have the same type of behaviour. Using the Cottrell equation, and taking diffusion coefficient values from the literature,[67,73] the number of electrons transferred at each potential step was obtained. The results are presented in Table 13.

Table 13. Number of electrons transferred in borohydride oxidation at gold electrodes, obtained through chronoamperometric studies.

	n	
E	**D = 1.68 x 10^{-5} cm^2 s^{-1} [67]**	**D = 2.24 x 10^{-5} cm^2 s^{-1} [73]**
0.00	8.7	7.5
0.50	2.4	2.1

Complete direct oxidation of borohydride is achieved at an applied potential of 0.00 V vs. Ag/AgCl, as evidenced by the calculated eight-electron transfer, which is consistent with earlier literature.[52,57,64] The voltammetric response

between -0.60 and -0.40 V apparently produces only three electrons, indicating that one or more additional processes occur between those potentials and 0.00 V. The second oxidation signal observed would consequently be linked to a different process, or another oxidation mechanism, possibly coupled to the formation of surface oxides and/or hydroxides.

4.6.6 DMAB and Borohydride Mixtures

A plot showing voltammograms, recorded on the same Au electrode, of separate DMAB and Borohydride solutions, normalised by the concentration, is presented in Figure 66, for comparative purposes. Although they have somewhat similar features, the potential at which the first oxidation peak appears is noticeably different (-0.80 and -0.35 V vs. Ag/AgCl for DMAB and borohydride, respectively) and its corresponding current is much higher in the case of borohydride. In view of the differences apparent in the voltammograms in Figure 66, voltammetric studies of a mixed solution of DMAB and borohydride were carried out. Figure 67 presents ten consecutive voltammograms recorded at 50 mV s^{-1}.

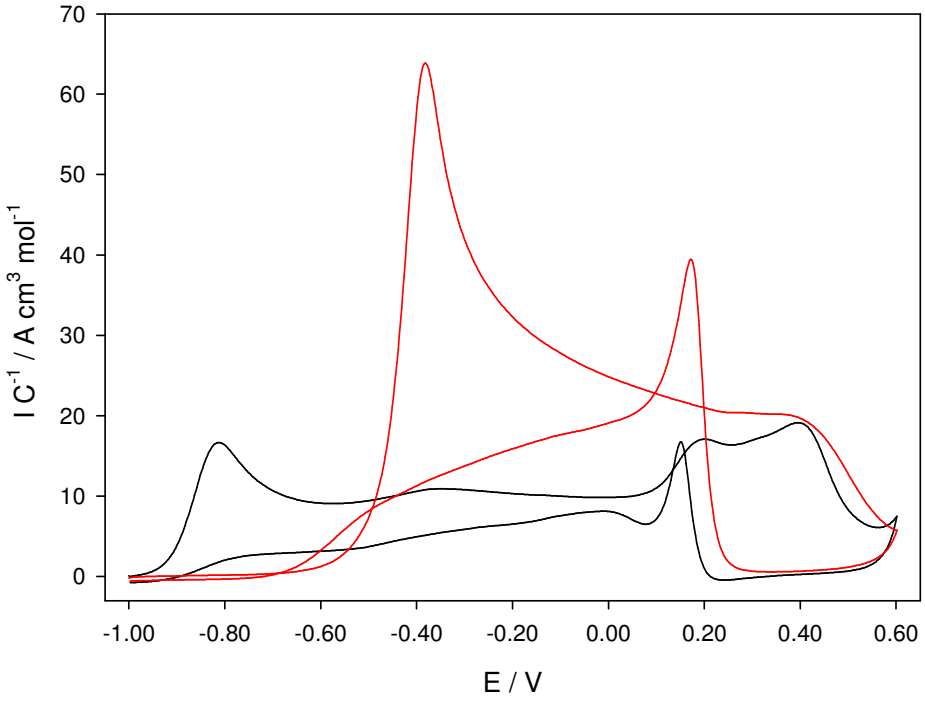

Figure 66. Concentration-normalised CVs of a 1.0 mM DMAB solution (black) and a 1.9 mM borohydride solution (red), at pH 13.6 and 50 mV s^{-1}.

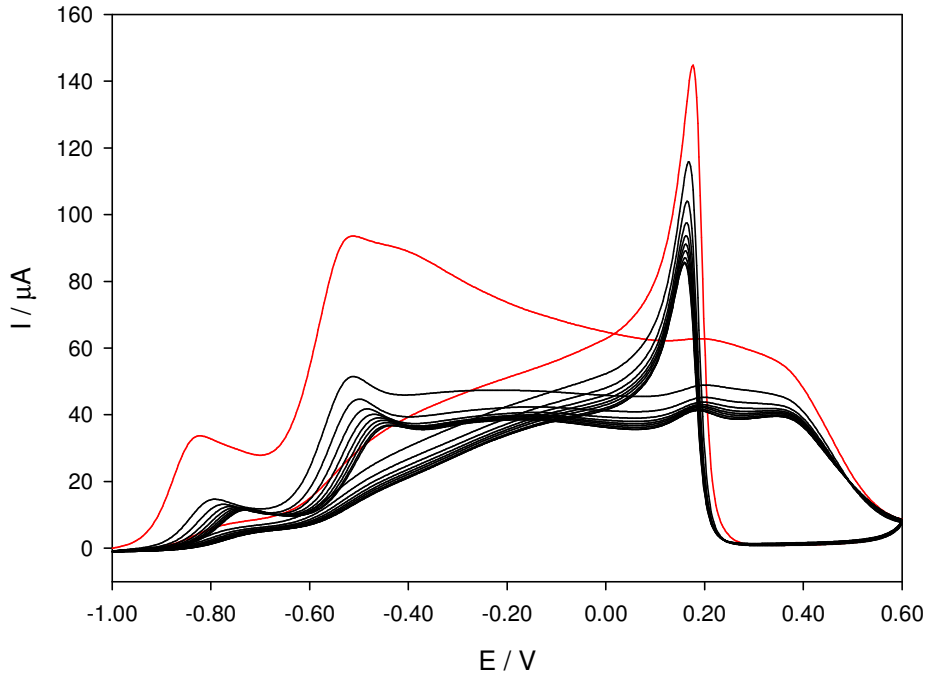

Figure 67. Consecutive voltammograms of a mixed 1.9 mM Borohydride and 2.2 mM DMAB solution, at 50 mV s^{-1}. The first cycle is marked in red.

From the results obtained it appears that there are two processes occurring in the potential region between -1.00 and -0.30 V vs. Ag/AgCl, presumably the first steps of DMAB and borohydride oxidation. The same experiment was carried out at different scan rates, as was seen for both borohydride and DMAB, the peak positions vary noticeably in the first cycle of each set, but start to settle as the scans go on. The peak currents at approximately -0.8 and -0.5 V show a linear relation with the square root of the scan rate, for the first scan, as can be seen in Figure 68.

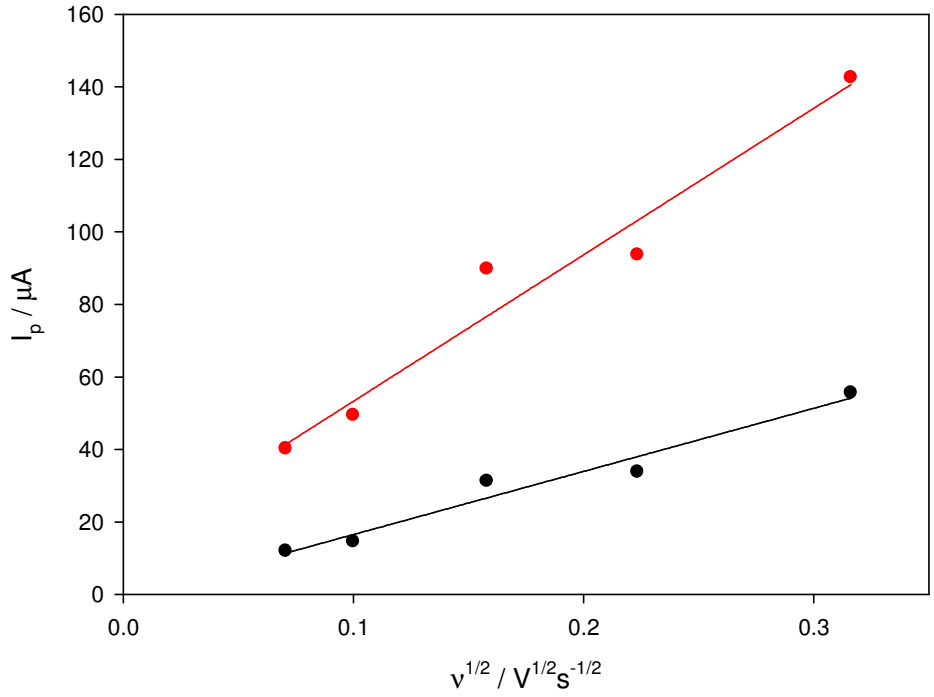

Figure 68. Peak current versus the square root of the scan rate for a mixed 1.9 mM Borohydride and 2.2 mM DMAB solution; the first (red: ~ -0.8V) and second (black: ~ -0.5V) signals in Figure 67 are shown.

As was done for each species in separate solutions, values of the number of electrons transferred were calculated from the linear regressions of Figure 68; the diffusion coefficients were assumed to be those of DMAB,[44,77] for the first signal, and borohydride,[67,73] for the second. Table 14 presents the results obtained.

Table 14. Number of electrons transferred obtained through voltammetric techniques for a mixture of DMAB and borohydride.

	n (D / cm^2 s^{-1})	
First	2.2 (8.55 x 10^{-6})	2.3 (7.48 x 10^{-6})
Second	3.0 (2.24 x 10^{-5})	3.3 (1.68 x 10^{-5})

The fact that the number of electrons obtained for the mixed solution is identical to that for each species on its own, indicates that the oxidation mechanisms are independent of each other; the presence of one compound does not affect the oxidation of the other, therefore they do not involve the same intermediates.

4.7 Conclusions

Although complete understanding of the oxidation mechanism of dimethylamine borane has not been reached at present, several interesting conclusions can be drawn. In the first place, the mixed borohydride and DMAB experiments suggest that their oxidation processes, while similar, are not identical. Each compound follows a different, independent oxidation pathway, which produces the same number of electrons whether alone in solution or in a mixture, apparently unaffected by the presence of the other species.

The dissociation process assumed to be the first step of DMAB oxidation is catalysed by the presence of metallic surfaces; possibly not taking place at all in their absence. The use of non-catalytic electrodes, such as glassy carbon, only produced oxidation at high positive potentials. This anodic process is linked with the amine oxidation rather than the boron-containing fragment of the complex.

Both borohydride and DMAB have a complicated, multiple step oxidation mechanism. The first step of the process, at least, is greatly influenced by adsorption phenomena, which have a greater effect on DMAB than on borohydride, as evidenced by the transients measured. Adsorption is a function of time and applied potential, as well as being catalysed by the gold surface when compared to other surfaces, such as glassy carbon or platinum.

The formation of gold oxide catalyses DMAB oxidation, allowing some of the solution species to be oxidised by a chemical reaction with the surface hydroxide and/or oxide, in addition to the electrochemical oxidation process. In this potential region, the amine is also oxidised on the gold surface; dimethylamine reactions have been largely ignored in previous studies of DMAB oxidation, with only some studies on the effect of its adsorption reported.[45]

The number of electrons obtained during DMAB and borohydride oxidation on gold, assuming literature values for their diffusion coefficients, using the techniques employed in this chapter, are summarised in Table 15. A six-electron and an eight-electron oxidation are obtained for DMAB and Borohydride, respectively.

Table 15. Number of electrons transferred during DMAB and borohydride electro-oxidation.

	DMAB	**Borohydride**
Cyclic Voltammetry	6	3 (first peak)
Chronoamperometry	6-8	8 (at 0.0 V)
Microelectrodes	6	-

Whether three two-electron steps or two three-electron steps are involved in the electro-oxidation of DMAB remains unclear, although two three-electron steps appears a more likely mechanism; this scheme results from two different techniques at different types of electrode and is in better agreement with the results obtained for borohydride. Three electrons could be obtained from the first voltammetric signal if irreversibility is assumed; this assumption is fairly safe as no reduction signals are ever observed. The additional electrons obtained through chronoamperometry could be due to the effect of dimethylamine and/or gold oxidation.

Other techniques are needed in order to yield further insight on the adsorption processes and the identification of intermediate species and products. The following chapter presents results obtained using single-crystal electrochemistry coupled with FTIR spectroscopy.

5 Single-Crystal Electrochemistry: DMAB Oxidation

This chapter continues the investigation of the mechanism of DMAB oxidation described in Chapter 4. In the work contained here, single-crystal gold electrodes were employed in order to confirm the effect of the surface on the oxidation mechanism; three model gold structures were used: Au (111), Au (110) and Au (100). Additionally, the different species produced during the process were studied through *in-situ* FTIR spectroscopy; this technique also proved helpful in the clarification of the initial steps of the DMAB oxidation reaction.

The DMAB oxidation process was studied at two different pH values: a highly alkaline media (pH 13) and at a slightly lower value of pH 11. This comparison allowed the determination of the influence of the hydroxide concentration on the mechanism, particularly on the influence of the dimethylamine fragment of the molecule.

5.1 DMAB Voltammetry at pH 13

The voltammetric behaviour of DMAB was studied on three model gold surfaces (Au (111), Au (110) and Au (100)); representative voltammograms on each surface can be seen in Figure 69. The most prominent feature observed is the reactivation peak on the reverse scan. As mentioned in Chapter 4, this peak arises from oxidation being possible on the electrode surface, once the oxide layer on the surface is removed.[33,44] This peak has very different magnitudes on each gold surface and, due to the very high currents reached, other features of the voltammograms are difficult to observe. In order to better study the electrochemical behaviour, the data was magnified and is presented in the inset of Figure 69.

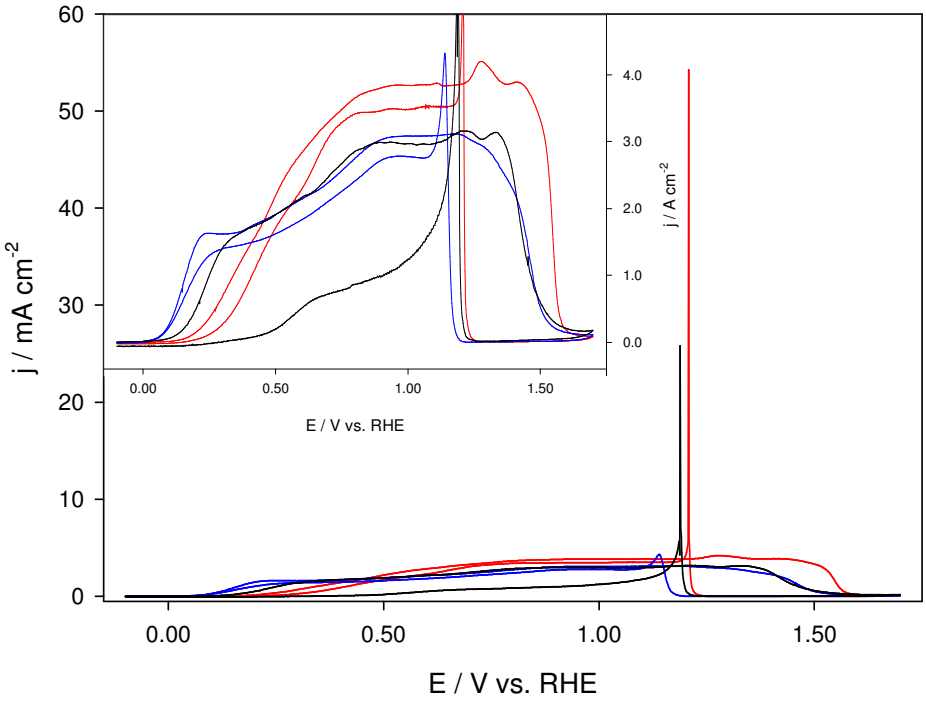

Figure 69. Cyclic voltammograms of 2.0 mM DMAB in 0.1 M KOH, at 50 mV s^{-1}, on Au (111) (black), Au (110) (blue) and Au (100) (red) surfaces.

All three voltammograms present, roughly, the same basic features: an irreversible oxidation, with cathodic currents in the reverse scan as well as the forward scan (the initial potential is -0.10 V vs. RHE), plateaus rather than diffusion limited peaks and a sudden drop in current after a specific highly positive potential. There are also some very marked differences, however, between the voltammograms obtained on each surface. The potential onset for the oxidation, for example, increases in the following manner: Au (110) < Au (111) < Au (100); the drop in current, due to passivation of the electrode surface, follows a similar trend, though the current on Au (110) and Au (111) actually decrease at essentially the same potential.

Although the voltammograms are similar to those obtained in Chapter 4, some marked differences are evident. Figure 70 compares the voltammetric behaviour of DMAB on single crystal gold electrodes with that on polycrystalline gold surfaces. The voltammograms on polycrystalline gold appear compressed, with the first oxidation signal much closer to the gold oxide region than on the three model surfaces. On the polycrystalline electrode, the first anodic signal shows a peak, and not a steady-state current, although the current does drop to a distinctly non-zero current. The currents after the initial oxidation peak are always

distinctly lower than the peak, whereas on all the single crystal electrodes, the currents increase with increasing potential, up to the formation of the oxide layer. The voltammetric behaviour of the Au (110) is more closely related to that observed throughout Chapter 4, than that of the other two single-crystal surfaces.

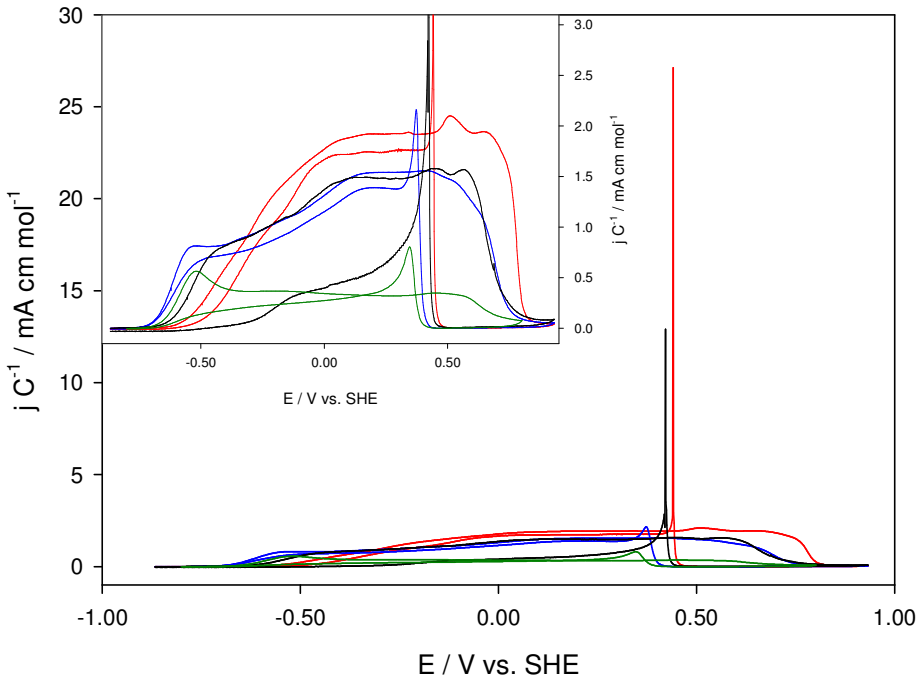

Figure 70. DMAB CVs, at 50 mV s^{-1}, on Au (111) (black), Au (110) (blue), Au (100) (red) and polycrystalline gold (green) surfaces; 2.0 and 3.5 mM DMAB solutions were used on single crystal and polycrystalline electrodes, respectively.

Further inspection of the voltammograms on the single crystal surfaces reveals that the wave shape is fairly similar for Au (110) and Au (111), with two processes visible, while on Au (100) the oxidation begins at more positive potentials and contains only one distinct plateau. Although the oxidation on Au (100) starts at higher potentials, Figure 69 shows that the limiting current reached is significantly higher than that of the other two surfaces. The charge transferred in each case was consequently studied (see Table 16); the total charge transferred on the forward scan (Q_f) is similar on the Au (111) and Au (110) surfaces, while it is higher on the Au (100). As this might be due to the higher potential at which passivation of this last surface is attained, the charge transferred before the oxidation of the gold surfaces, up to 1.0 V vs. RHE (Q_{+1}), was studied. In this case the values are relatively similar for all three gold surfaces. These results indicate that although the DMAB molecule has a more

favourable interaction with the Au (110) surface, the oxidation kinetics are largely improved on Au (100).

Table 16. Charges associated with the forward scans in Figure 69.

	Q_f / C cm^{-2}	Q_{+1} / C cm^{-2}
Au (100)	8.2 x 10^{-2}	4.0 x 10^{-2}
Au (111)	6.3 x 10^{-2}	3.5 x 10^{-2}
Au (110)	6.5 x 10^{-2}	3.8 x 10^{-2}

5.1.1 Reverse Scans

The study of the backward scan shows that the reactivation peak follows the opposite trend to that seen for the onset of the oxidation; the signal appears first on the Au (100) surface, followed by the Au (111) substrate, emerging last on the Au (110) electrode. The order in which the reactivation peaks occur corresponds to that observed for the gold oxide reduction peaks in 0.1 M KOH (see Figure 71), indicating a link to the readiness with which the gold oxide is removed from each of the surfaces. This agrees with previous works which suggest that the DMAB reactivation peak is seen only after the gold oxide is completely removed from the surface.[33]

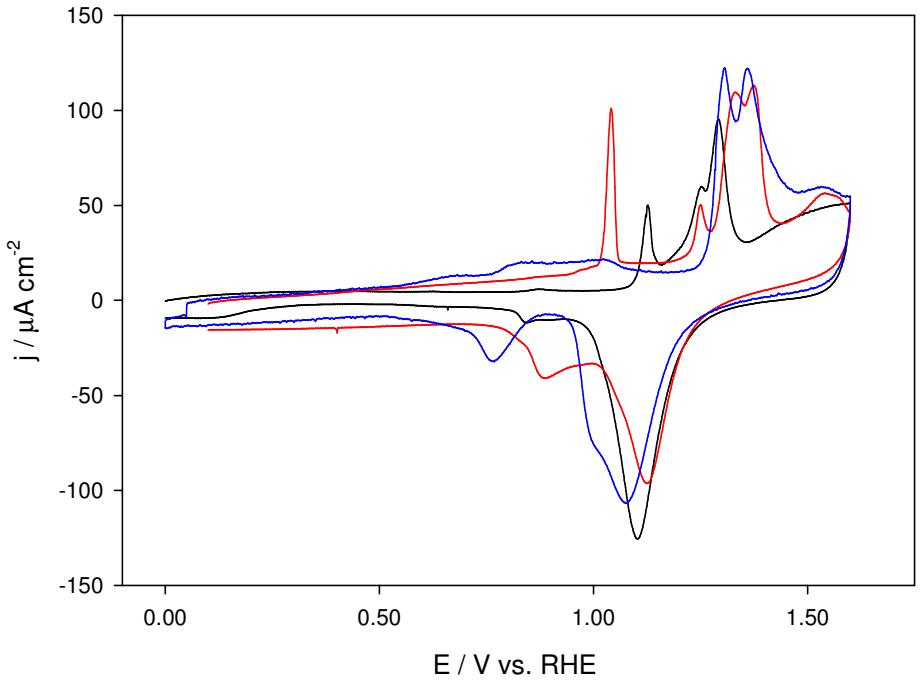

Figure 71. Cyclic voltammograms of 0.1 M KOH, at 50 mV s^{-1}, on Au (111) (black), Au (110) (blue) and Au (100) (red) surfaces.

The height of the reactivation peaks also varies with the surface, somewhat following the potential trend mentioned above: Au (100) > Au (111) >> Au (110). The charge transferred in these peaks (above the steady-state current of the corresponding forward scan) was calculated; Table 17 shows that the charges on Au (111) and Au (100) are comparable, being approximately a third of that obtained on Au (110). As with the general wave shape, the charge obtained on a polycrystalline surface is similar to that of Au (110). On the polycrystalline electrode a range of concentrations was studied (see Section 4.3.3); the reactivation charges were calculated as a function of concentration, and a linear relationship was found (see Table 18).

Table 17. Charges of the reactivation peaks in Figure 69. The equivalent number of DMAB molecules oxidised, assuming complete oxidation, is given along with the number of gold atoms on the surface.[138]

	Q / C cm^{-2}	**DMAB / molecules cm^{-2}**	**Au / n cm^{-2}**
Au (100)	1.98 x 10^{-3}	2.06 x 10^{+15}	1.20 x 10^{+15}
Au (111)	1.76 x 10^{-3}	1.83 x 10^{+15}	1.39 x 10^{+15}
Au (110)	5.00 x 10^{-3}	5.20 x 10^{+15}	1.70 x 10^{+15}

Table 18. Charges of the reactivation peak, on polycrystalline gold, as a function of DMAB concentration (data from voltammograms in Figure 37).

C / mM	Q / C cm^{-2}
1.1	2.80×10^{-4}
3.5	2.15×10^{-3}
6.2	3.63×10^{-3}
11.3	9.65×10^{-3}

Table 17 also illustrates that if the number of DMAB molecules oxidised during the reactivation peak is calculated, assuming a six electron transfer as for example in Equation 29 or Equation 30, more than a complete coverage of the surface would be needed to produce the reactivation peaks. This fact, added to the proportionality of the reactivation charges to the concentration, appears to indicate that the oxidation process that occurs once the clean gold surface is recuperated is due not only to adsorbed but also solution species; whether DMAB or an intermediate is oxidised cannot be determined through these experiments. The removal of the gold oxide appears to be aided by the chemical interaction with DMAB or an intermediate species, in agreement with Section 4.3.2; this will be discussed in more detail in 5.2.

5.1.2 Consecutive Voltammetry

Consecutive scans on the same surface were studied, with the second cycles of the experiments shown in Figure 69 presented in Figure 72. Lower currents are observed on the second scan on all three surfaces; the decrease is most significant on Au (111). Although the general wave shapes are maintained some marked differences can be observed. On the Au (110) and Au (111) electrodes, the first signal shows an initial diffusion-limited peak above the steady-state current, with an additional shoulder peak can be seen in the plateau. The onset of the oxidation on the Au (111) surface shifts to match that of the Au (100) surface. The voltammetric behaviour on Au (100) remains unchanged, with only lower currents observed on the second scan; this is consistent with a weaker interaction between DMAB and this surface.

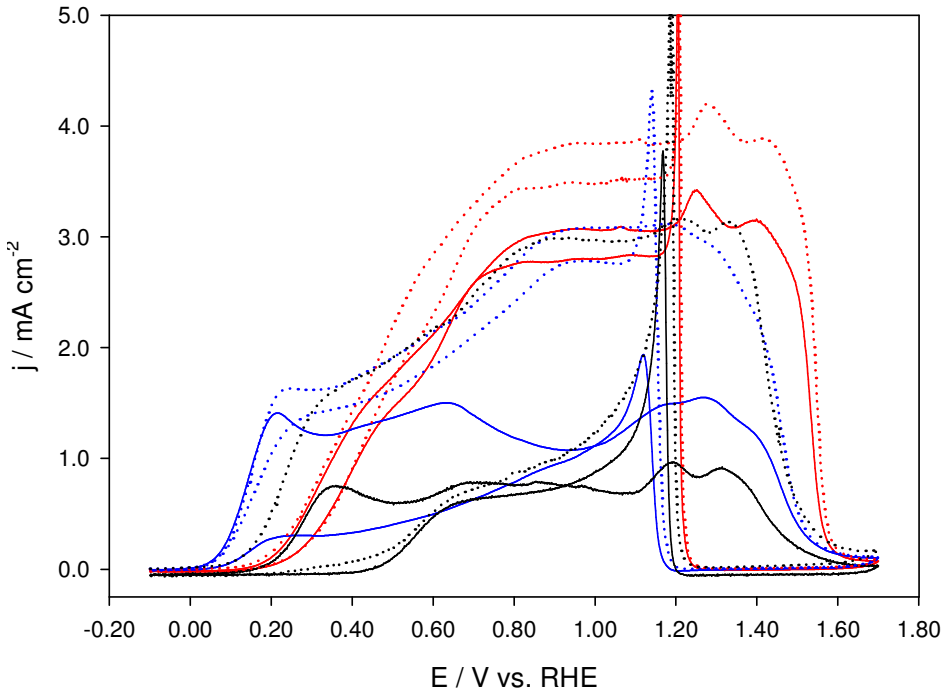

Figure 72. Second cycles corresponding to those shown in Figure 69; the first scans are shown as dotted lines for comparison. Au (111) - black, Au (110) - blue, and Au (100) – red.

5.1.3 Rotating Disk Electrode

Rotating disk electrode voltammetry was employed on the Au (111) surface, in order to determine the number of electrons transferred in each oxidation wave, as well the diffusion coefficient of DMAB. Figure 73 shows the effect of rotation on DMAB voltammetry, using a Au (111) electrode; the currents increase, while the general wave shape is maintained. The only marked difference between static and hydrodynamic conditions is observed on the reactivation peak: it essentially disappears at higher rotation speeds; under rotation the current increases towards a steady-state value, without the characteristic spike previously seen.

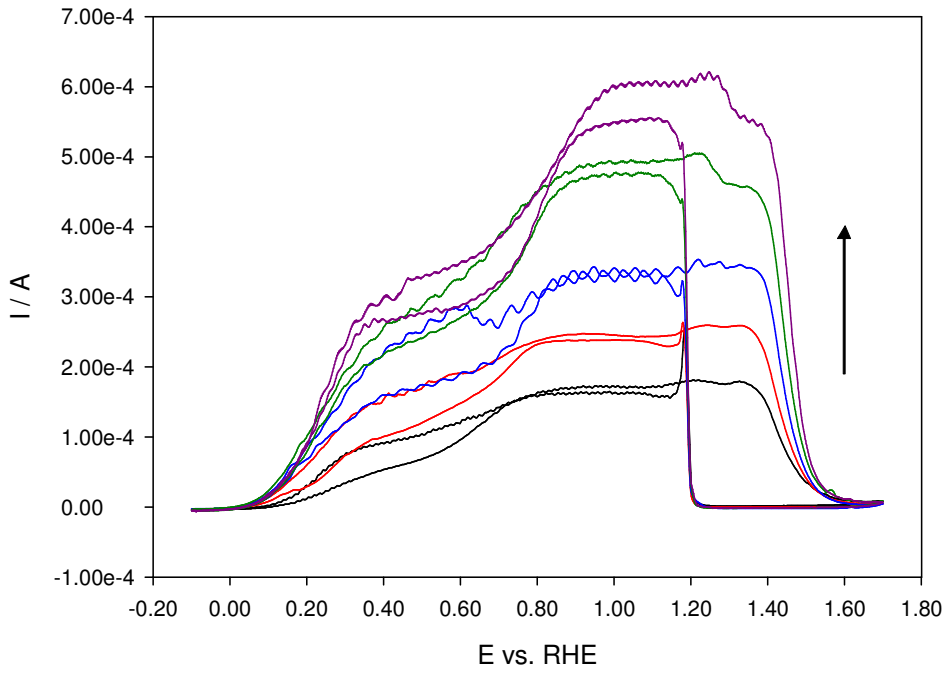

Figure 73. Cyclic voltammograms of 2.0 mM DMAB in 0.1 M KOH, at 50 mV s^{-1}, on a rotating Au (111) disk. The arrow indicates increasing rotation rates: 200, 400, 800, 1000 and 1300 RPM are shown.

Levich plots (see Figure 74) yield a diffusion coefficient value of 2.3 x 10^{-5} cm^2 s^{-1} for DMAB, assuming a three electron transfer on the first wave; this value would also yield a further three electron process on the second wave. Koutecký-Levich, which takes into account possible kinetic influences, provide a slightly better fit (as shown in Figure 74 and corroborated in Appendix B); the diffusion coefficient in that case has a value of 1.6 x 10^{-5} cm^2 s^{-1}, again with two three-electron transfers. Although both of these values are larger than those reported for DMAB (7.48 x 10^{-6} and 8.55 x 10^{-6} cm^2 s^{-1}),[44,77] they are more in line with the literature values for borohydride.[67,73] The latter's diffusion coefficient has recently been used as an approximation to that of DMAB, as it has been suggested that they should be fairly similar.[59] These values are also consistent with those obtained through voltammetric methods on polycrystalline gold, assuming a kinetically-hindered three-electron transfer on the first oxidation step (see Chapter 4, Table 5 and Table 7, for example).

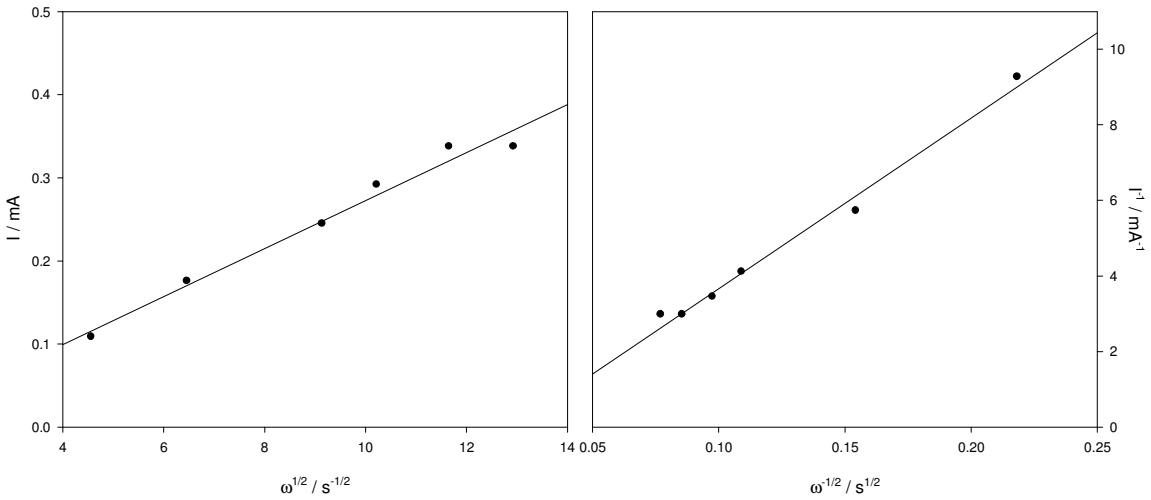

Figure 74. Levich (right) and Koutecký-Levich (left) plots corresponding to the data shown in Figure 73; the lines represent the linear regressions obtained.

5.2 *In-situ* FTIR Spectroscopy at pH 13

In-situ FTIR was employed in order to study the different species produced during DMAB oxidation. The three model gold surfaces were studied through both p- and s-polarised light, in order to probe solution and surface-bound species. A higher concentration of DMAB was required for the FTIR measurements than for the CVs performed in the previous section, so 50 mM DMAB solutions were used; the voltammetric behaviour remained unchanged at higher concentrations, though slightly noisier CVs were obtained, due to more vigorous gas evolution, while the spectroscopic signals greatly improved. Figure 75 shows the spectra obtained every 80 mV during a cyclic voltammogram on a Au (111) surface, using p-polarized light; the reference was taken prior to the start of the scan, at -0.20 V vs. RHE. The same signals and behaviour were observed on Au (110) and Au (100), differing only on the potentials at which each of the bands first appear.

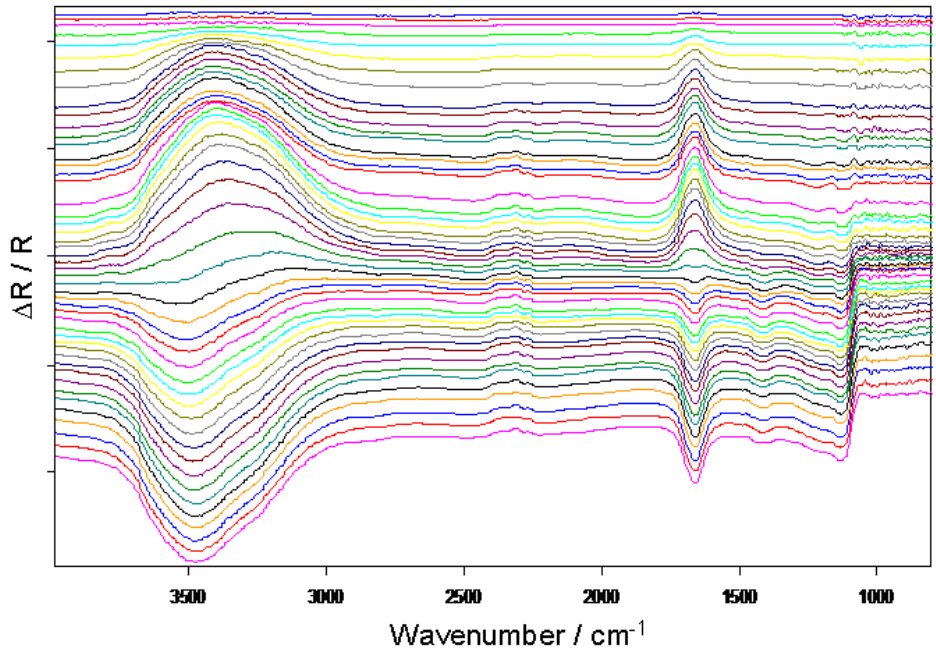

Figure 75. Consecutive spectra obtained, using p-polarised light, every 80 mV during a CV at 10 mV s^{-1}, from -0.20 to 1.80 V (and back to 0.00 V) on a Au (111) electrode. Reference: -0.20 V.

The main features of the spectra are in the regions where signals due to O-H and N-H bonds appear; between 1700 and 1600 cm^{-1} and at wavenumbers above 3000 cm^{-1}. The changes in the thin solution layer and on the electrode surface throughout the voltammetry due to water and hydroxide are predominant due to the wide potential range employed and the highly alkaline media used. Upon closer inspection, however, smaller bands associated with boron-containing molecules can be seen. These signals are amplified in Figure 76.

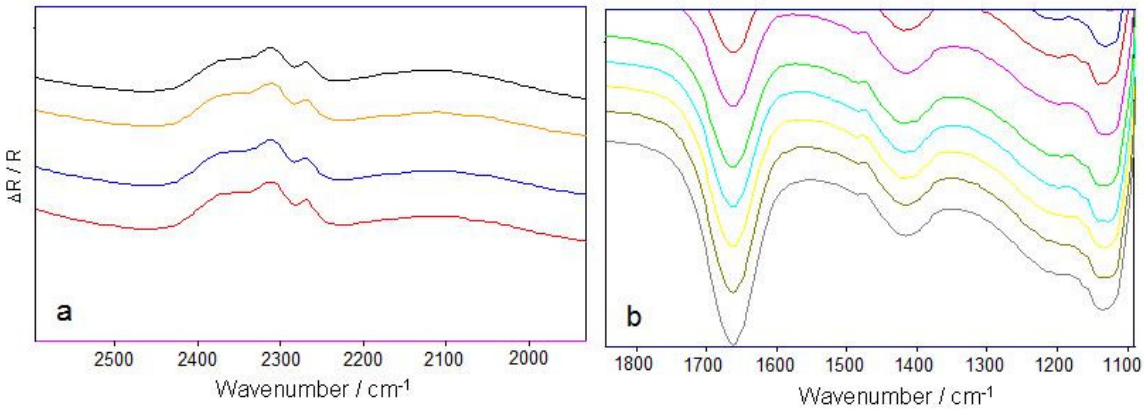

Figure 76. Magnification of signals from Figure 75.

The three up-going bands seen in Figure 76a, at 2368, 2313 and 2270 cm^{-1}, are associated with the disappearance of molecules containing B-H bonds from

the system, as they are associated with the stretching of B-H bonds.[139,140] The first of these bands starts to appear after the other two signals in all cases and it shifts to 2379 cm^{-1} in s-polarized light. All three bands in Figure 76a are first observed between 0.10 and 0.30 V (see Figure 77), and they somewhat follow the trend of the oxidation onset; they appear at lower potentials on the Au (110) surface.

Another upwards band, assigned to the breaking of the B-N bond of the DMAB molecule, can be seen at 1477 cm^{-1} (p-polarized light) or 1474 cm^{-1} (s-polarized light); see Figure 76b.[139,140] This signal first appears at approximately the same potentials as the B-H related bands. The fact that this band is observed only above a certain potential, which varies according to the surface (see Figure 77), indicates that the dissociation of the DMAB molecule is potential dependant. Although partial dissociation spontaneously occurs in solution, a significant amount only takes place after a certain electrode potential is achieved. It has generally been assumed that BH_3OH^- is the only electro-active species present in alkaline DMAB solutions, although previous work has suggested that B-N cleavage is a metal-catalysed process.[17,33,44]

The results obtained here indicate that the bands at 2313 and 2270 cm^{-1} could belong to the BH_3OH^- species, while the other B-H signal might be due to the DMAB molecule itself. Initially a mix of both species can be found in solution, at certain potentials, however, the break-up of the B-N bond is catalysed and the DMAB molecule dissociates, producing more BH_3OH^-.

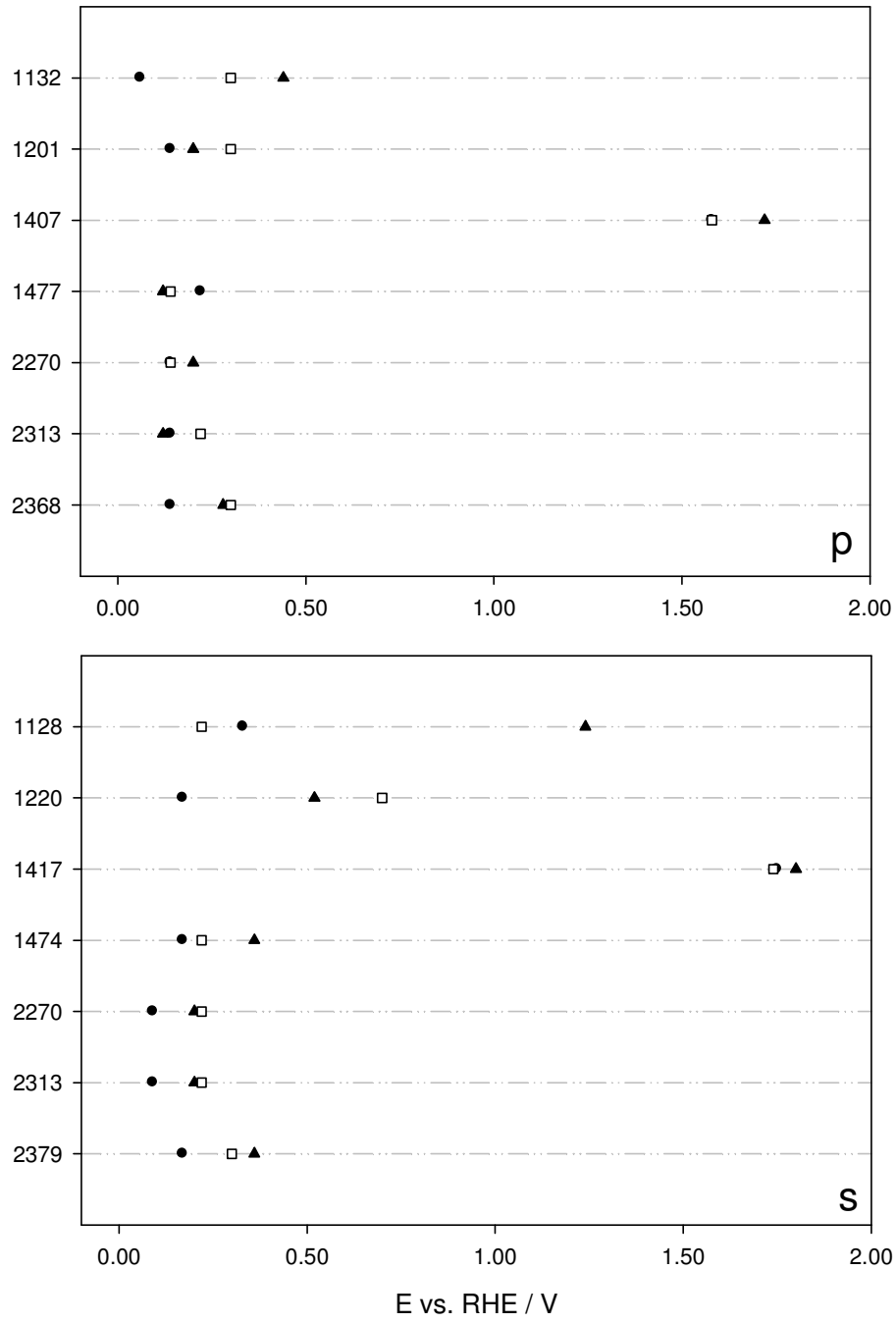

Figure 77. Potentials at which the different IR signals first appear on Au (111) (triangles), Au (110) (circles) and Au (100) (squares), using p- and s-polarised light (top and bottom, respectively).

Three bands going down can be seen in Figure 76b, indicating the production of new species in the system. These bands appear at approximately 1417, 1220 and 1128 cm^{-1} in s-polarised light. In p-polarised light the first and last bands move to 1407 and 1132 cm^{-1}, respectively, with the band in the middle progressively shifting down to 1201 cm^{-1} with applied potential; this behaviour can be seen in Figure 78. The band close to 1400 cm^{-1} is assigned to the asymmetric stretching of B-O bonds and appears only at highly positive potentials (above 1.60 V in all cases). Figure 77 shows that the potentials at which this band is seen on

the three gold surfaces follow the trend described in Section 5.1.1 for the reactivation peak. The other two spectroscopic signals appear during the first oxidation wave and correspond to the in-plane bending of B-O-H bonds. These types of bonds are likely to be found in intermediates and products of the DMAB oxidation, which is expected to occur by the uptake of hydroxyl ions and removal of hydrogen and electrons, as discussed in Section 1.2.[78,139,140]

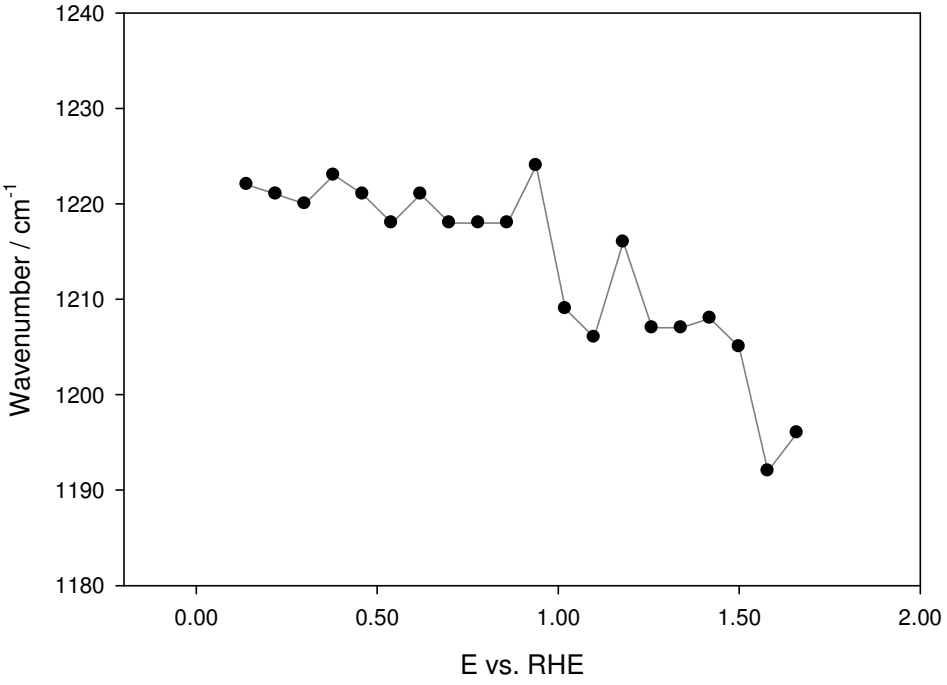

Figure 78. Potential dependence of one of the intermediate/product species on Au (110).

The signal in Figure 78 appears at similar potentials to those of the disappearance of the B-H bonds and follows the trend of the oxidation onset; it is, however, only present on the "s" spectra of Au (111) and Au (100) at more positive potentials. On Au (111), the signal observed around 1130 cm^{-1} also appears at particularly positive potentials on the "s" spectra in comparison to "p" spectra; this behaviour could indicate that the species forms on the surface at low potentials, yet does not go into solution until higher potentials are applied. This, added to the shift of wavenumber with applied potential (see Figure 78), confirms that some of the intermediates/products of the reaction are adsorbed on the electrode surface, possibly desorbing at higher potentials. An adsorbed intermediate, thought to be boron-containing, which is later removed from the surface through interaction with the gold oxide, has been proposed before, through EQCM studies.[26,77]

The spectroscopic results indicate that the two products associated with the bands seen around 1220 and 1130 cm^{-1} are formed early in the oxidation mechanism and interact strongly with the gold substrate; the molecule associated with the signal at ~1130 cm^{-1} has particularly strong adsorption on the Au (111) surface. These molecules could be of the form $BH_2(OH)_2^-$, $BH(OH)_3^-$ or $B(OH)_4^-$. The last signal observed, close to 1400 cm^{-1}, shows that a more oxidised product is reached only at very high potentials, possibly due to the chemical interaction between DMAB, or one of its intermediates, with the electrode surface; molecules of the form BO_2^- or $B_4O_7^-$ are likely, in this case.[69] The potential onset for this band follows the trend of the reactivation peak, again suggesting a chemical interaction between the electro-active species and the surface oxide/hydroxide. This interaction with the gold substrate at high potentials is consistent with the catalysis observed on the polycrystalline gold electrodes in Chapter 4.

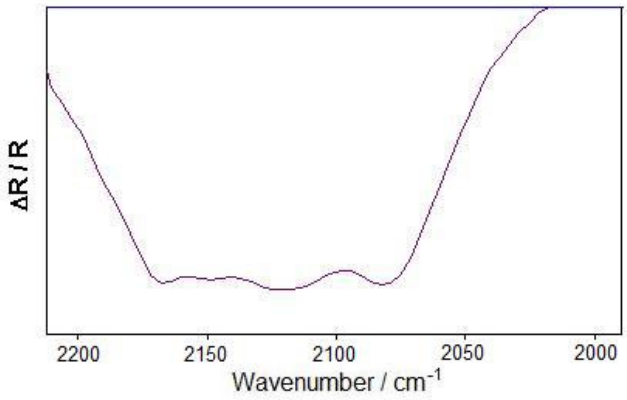

Figure 79. Magnification of the FTIR bands associated with the oxidation of dimethylamine.

Several additional bands appear, between 2170 and 2079 cm^{-1}, at potentials above 1.00 V vs. RHE (see Figure 79); they are associated with C-O and N-O bonds, indicating that in the region of gold oxide formation, dimethylamine is oxidised. As previously mentioned, the focus of previous studies of DMAB oxidation has always been the boron-containing reactions; it has been assumed that once the dissociation occurs, the amine is no longer involved in the electrochemistry; a few more recent studies have reported an influence of the amine on the second oxidation wave, although the assumption was that the adsorption of the dimethylamine had a negative effect on the oxidation.[45] The spectroscopic evidence obtained here is consistent with the voltammetric

behaviour observed in Section 4.3.5, confirming the oxidation of the amine as part of the overall electro-oxidation process.

5.3 DMAB Oxidation at pH 11

The voltammetric behaviour of DMAB was studied at pH 11, on the three gold surfaces described in the previous sections; 0.1 M potassium perchlorate was used as supporting electrolyte in all cases. Figure 80 illustrates typical voltammograms obtained on each gold electrode.

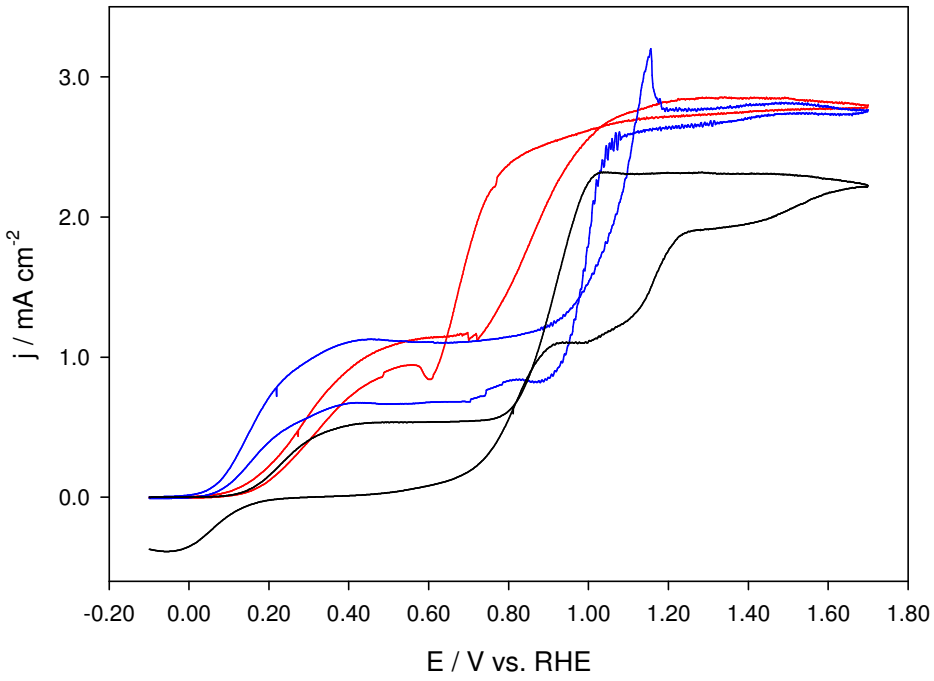

Figure 80. Cyclic voltammograms of 2.0 mM DMAB (pH 11), at 50 mV s^{-1}, on Au (111) (black), Au (110) (blue) and Au (100) (red) surfaces.

Two distinct plateaus are observed on all three surfaces, with the forward and reverse scans showing similar behaviour, particularly in the case of Au (110) and Au (100); the small peak observed at ~1.20 V vs. RHE on the forward scan, on Au (110), is present in the blank, and thus not linked to DMAB processes. On Au (111), an additional cathodic current is present at potentials close to zero. This latter feature was particularly unexpected, as DMAB has shown throughout this work to have an irreversible oxidation.

Unlike at pH 13, the current did not drop at highly positive potentials, and consequently no reactivation peak is present. At potentials higher than those of Figure 80, the current drastically increases as the evolution of oxygen is observed. The absence of the drop in current implies that a full monolayer of gold oxide is not formed; the blanks at pH 11, however, are fairly similar to those at pH 13, and gold oxide formation is observed in the absence of DMAB. It is likely that the difference in behaviour in the presence of DMAB is due to the much higher ratio of DMAB to hydroxide molecules at pH 11; at pH 13 there are approximately 50 molecules of hydroxide per every molecule of DMAB, while at pH 11 there is more DMAB than hydroxide in solution (~ 2:1). The oxidation of each DMAB molecule requires the intake of several hydroxides, lowering the local pH near the electrode thus inhibiting the formation of the gold oxide at the potential range studied.

Direct comparison between the voltammetric behaviour of DMAB at pH 13 and pH 11, on each gold surface, is presented in Figure 81. The forward, as well as the reverse scans, present differences in all cases. Although the oxidation onset potentials are similar for each surface, at both pH values, for example, the second oxidation wave occurs at higher potentials in less alkaline media. The current, on the other hand, is lower at all times at pH 11. These observations indicate that the lower hydroxide concentration has a limiting effect on the oxidation process of the DMAB molecule.

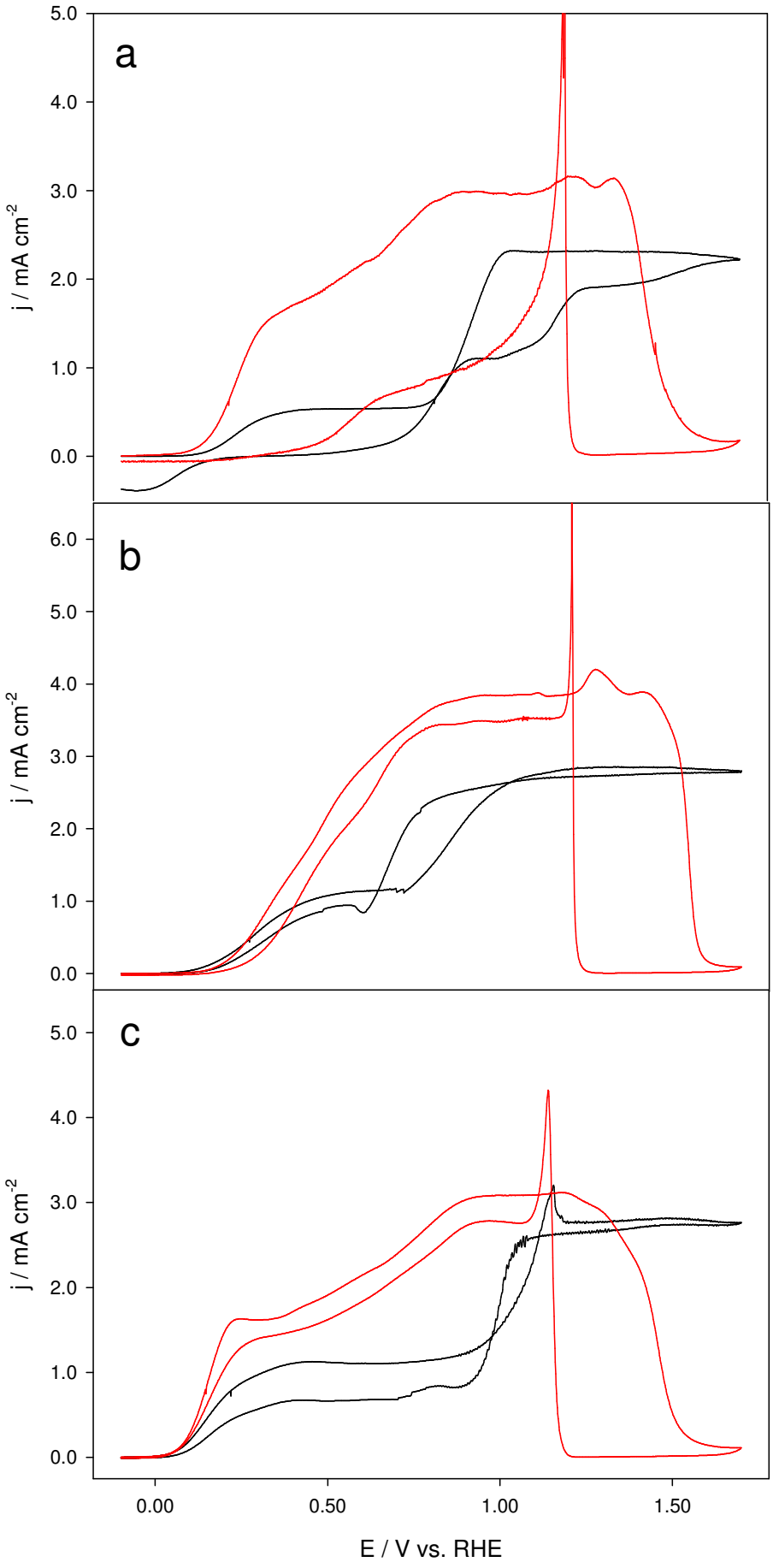

Figure 81. Cyclic voltammograms of 2.0 mM DMAB at pH 13 (red) and pH 11 (black), on Au (111) (a), Au (100) (b) and Au (110) (c) surfaces.

5.3.1 Consecutive Voltammetry

In order to further study the new behaviour, and in particular the cathodic current observed during the reverse scan on Au (111), consecutive voltammetry was performed. Figure 82 presents two consecutive cycles on each surface. The change from the first to the second scan is very marked; much more so than at pH 13 (see Figure 72). On the Au (110) surface the first oxidation signal decreases on the second cycle, as was the case at pH 13, but on the other two surfaces, it practically disappears. The second oxidation wave, although present in all three cases, is no longer a plateau; on the second scan, it becomes a diffusion limited signal.

The cathodic current observed in Figure 80, on Au (111), is observed on all three surfaces on the second cycle. As this current is evidently dependent on the history of the electrode, consecutive cycles were performed, with progressively higher turning potentials. This test was done in order to determine which of the oxidation waves is responsible for the subsequent production of the negative current in the reverse scan; Figure 83 shows the results obtained on Au (111). From the voltammograms, it is clear that the cathodic current is linked to the reduction of species produced during the second oxidation wave; the peak near zero volts is not noticeably present until the turning point is set well into the second oxidation signal in the forward scan.

The disappearance of the first oxidation wave is also linked to processes occurring during the second anodic signal; although the current decreases from one cycle to the next in Figure 83, the first oxidation process is evident until highly positive potentials are reached in the previous scan. This behaviour, added to the cathodic currents produced, indicates the likely production of adsorbed species on the electrode surface which can be reduced and/or inhibit further DMAB oxidation.

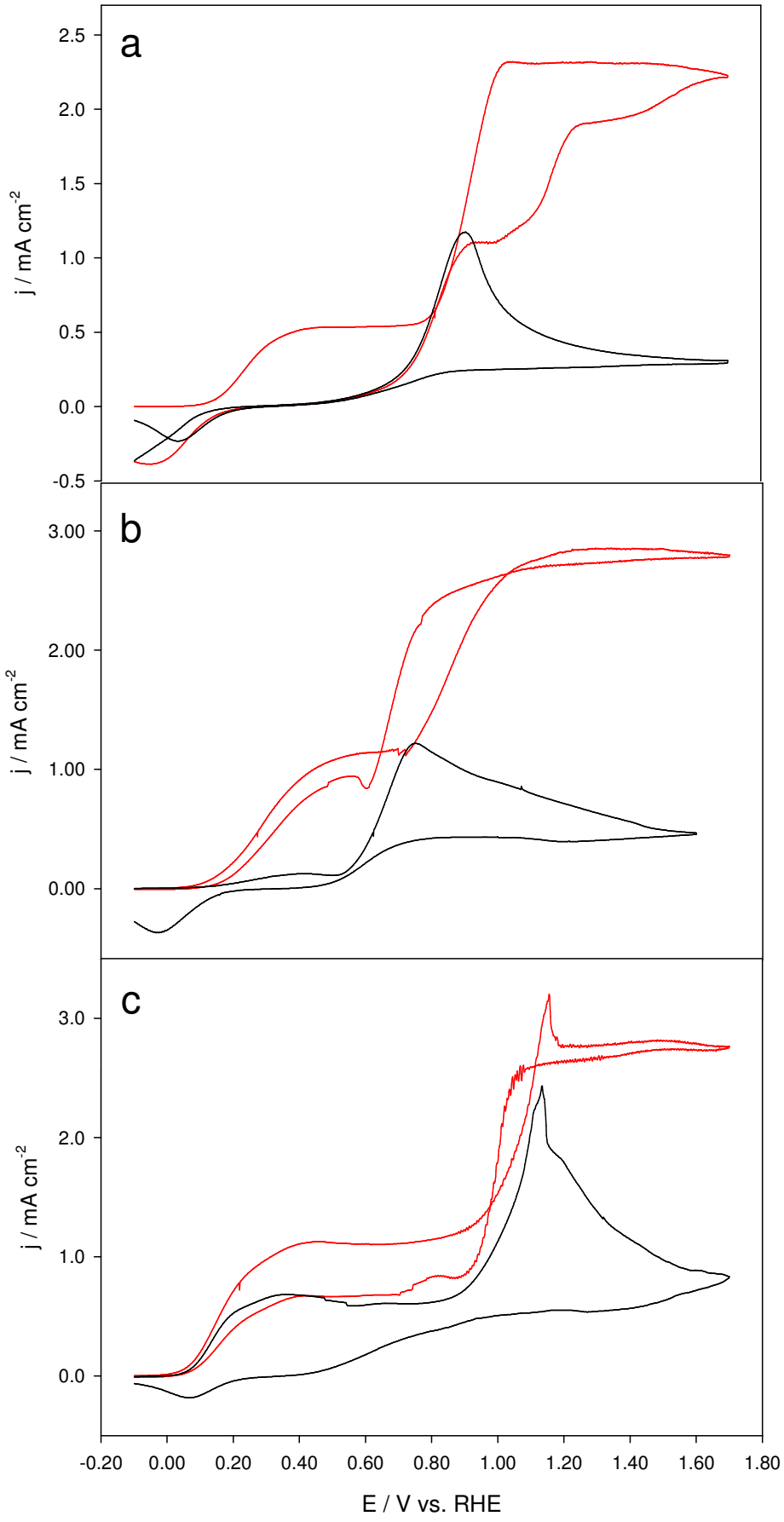

Figure 82. Consecutive CVs of 2.0 mM DMAB at pH 11 (50 mV s^{-1}), on Au (111) (a), Au (100) (b) and Au (110) (c) surfaces; the first scan is marked in red.

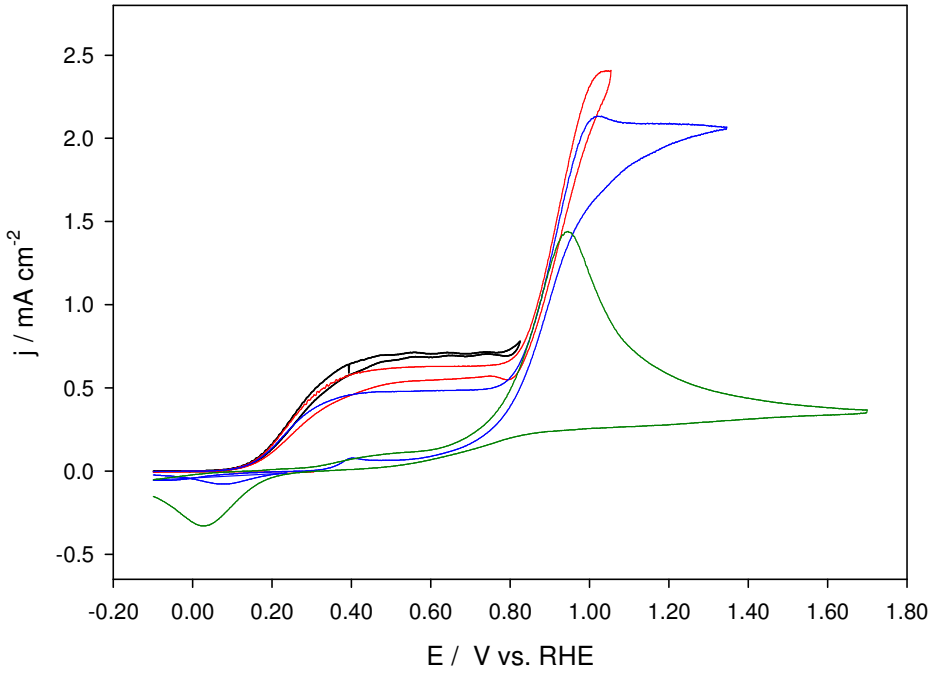

Figure 83. Consecutive DMAB CVs at pH 11, on Au (111), with progressively higher turning potentials: 0.82 (black), 1.05 (red), 1.35 (blue) and 1.70 (green)

5.3.2 Transfer Experiments

In order to confirm whether adsorbed species are produced during the second plateau of the forward voltammetric scan, transfer experiments were performed. These consisted of doing several cycles in a DMAB-containing solution and then removing the electrode, while holding the potential at ~1.20 V vs. RHE (see Figure 84a). The electrode was then introduced in a blank electrolytic solution, at similar pH, and voltammetry was once again performed, starting at positive potentials and initially going in a negative direction, as seen in Figure 84b.

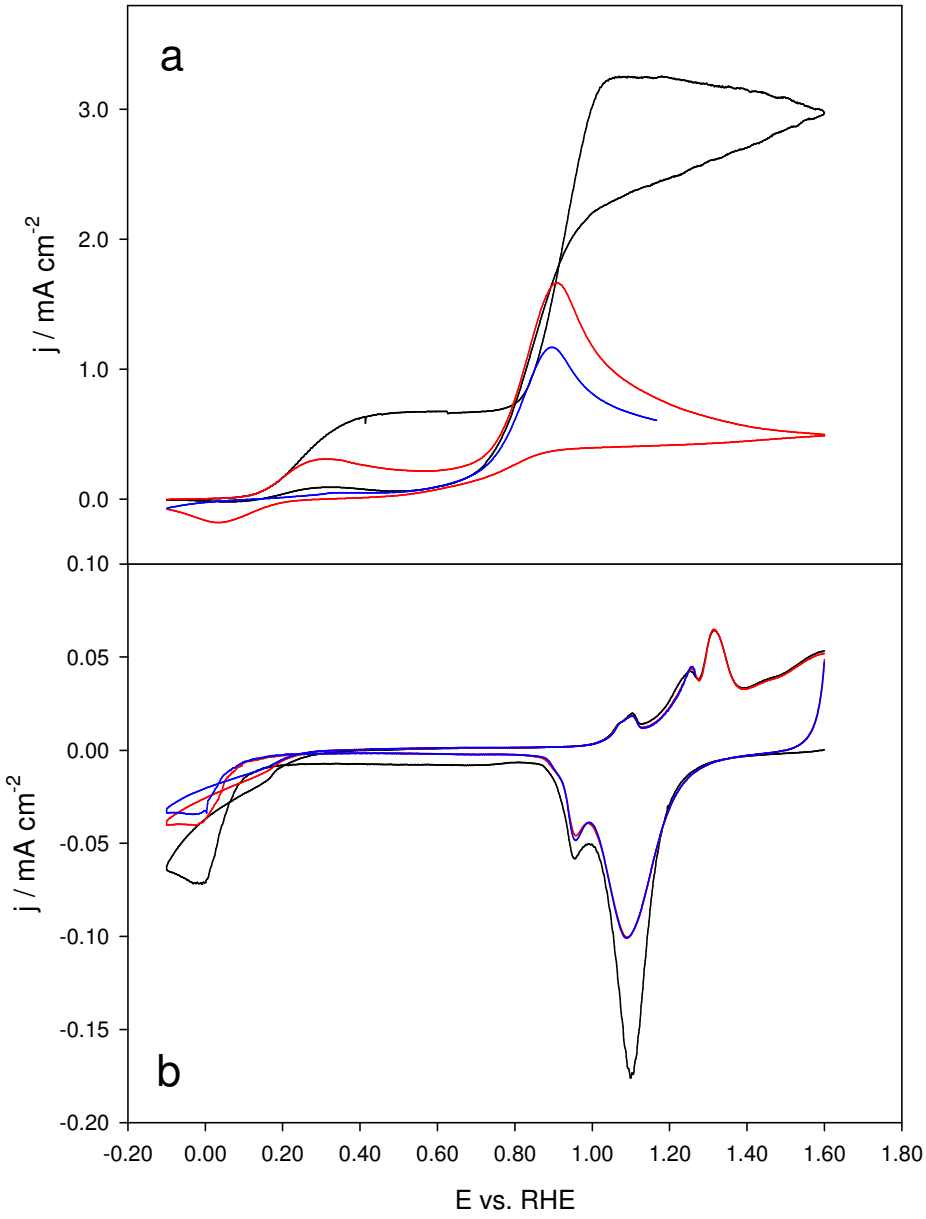

Figure 84. Consecutive CVs at pH 11, on Au (111), in 2.0 mM DMAB (a) and after transferring the electrode to a cell containing only 0.1 M $KClO_4$ at pH 11 (b). In each case: first (black), second (red) and third (blue) scans are shown.

In addition to the signals expected from a Au (111) electrode in the blank solution, Figure 84b shows cathodic currents near zero volts (vs. RHE), which decrease with consecutive scans. This behaviour confirms that adsorbed species, produced during the voltammetry in the DMAB solution, remained on the electrode surface and were reduced in the second part of the experiment. As the adsorbed species are not formed in the blank, they are undoubtedly DMAB related; however, as they form during the second anodic wave, it is unclear from these experiments whether they are boron-containing species or they are generated from the amine fragment.

5.3.3 FTIR Spectroscopy

In-situ FTIR was employed to shed further light on the different species produced at pH 11 during the oxidation process. The three model gold surfaces were studied through both p-polarised light and, as in the case of pH 13, no differences were found, other than the potentials at which the bands initially appeared in the spectra. Figure 85 shows the spectra obtained during a CV on the Au (111) surface. At first glance, the spectra are similar to those obtained at pH 13 (see Figure 75), with the main features being the signals due to O-H and N-H bonds.

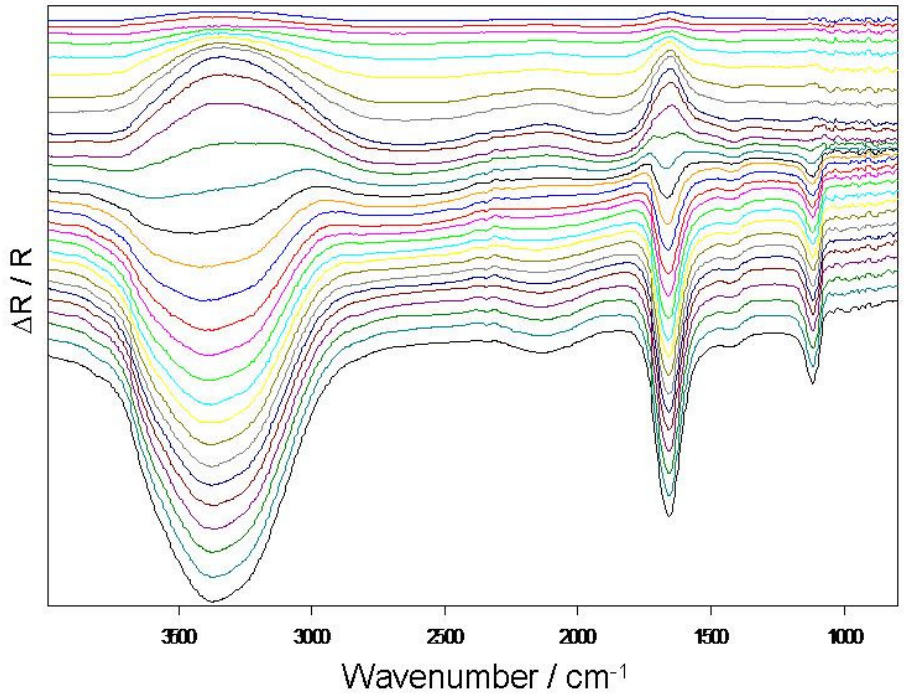

Figure 85. Consecutive spectra obtained every 80 mV, using p-polarised light, during 10 mV s^{-1} CV, from -0.20 to 1.80 V vs. RHE, on a Au (111) electrode, at pH 11. Reference: -0.20 V.

Further inspection of the regions of the spectra related to boron-containing bonds reveals the presence of the same bands previously seen. The only noticeable difference is the absence of the signal near 1200 cm^{-1}; the signal at lower wavelengths (~1120 cm^{-1}) is, on the other hand, much more prominent.

Another important difference is in the region of the C-O and N-O bonds, where no bands are seen, even at highly positive potentials. This indicates that at this lower pH the amine does not oxidise, or at least not to the extent of forming

these types of bonds. If the cathodic currents seen in Figure 82 are due to products of the dimethylamine oxidation, the IR signals of the adsorbed species are likely hidden within the O-H and N-H regions. This would also be in agreement with the lower currents and higher potential needed for the second oxidation wave in the cyclic voltammograms, at pH 11.

As no new boron-related bands are seen in the spectra, it seems unlikely that a new boron-containing species is produced at pH 11 which could produce the negative currents in the reverse scans.

5.4 Conclusions

The use of single-crystal gold electrodes confirmed the importance of the surface interaction during DMAB oxidation, while *in-situ* FTIR allowed the clarification of certain steps of the mechanism and the identification of different intermediates/products.

The spectroelectrochemical studies performed here allowed the determination that the initial dissociation step, which has been thought to be a simple chemical step, is catalysed not only by a metallic surface, but more importantly by the applied potential. It appears that the two oxidation waves observed in highly alkaline media correspond to two three-electron transfers; this possibly implies the oxidation of hydrogen to water during the second wave rather than further oxidation of the DMAB molecule, as new products are not observed spectroscopically in the region of the second wave. RDE experiments produced diffusion coefficients between 1.6 and 2.3 x 10^{-5} cm^2 s^{-1} for the DMAB molecule; these values are comparable to those obtained at polycrystalline electrodes when assuming an initial irreversible three-electron step.

The marked difference in electrochemical behaviour with consecutive scans, as well as with surface structure, confirms the suspected adsorption phenomena, by indicating that the interaction with the surface has an important effect on the oxidation. The variation in the capacity of each gold surface to oxidise the DMAB

molecule appears to be linked to its own oxidation (and reduction of its oxide) ability. An additional product is formed in the region of gold oxide formation, possibly of the form BO_2^- or $B_4O_7^-$.

The *in-situ* FTIR established that above 1.00 V vs. RHE, the amine fragment (dimethylamine) is also oxidised, further complicating any analysis made using only electrochemical methods. From the different results obtained at the lower pH, it seems that in highly alkaline media, the amine is extensively oxidised, whereas at pH 11, a strongly adsorbed species is produced which hinders other oxidation processes and can be reduced at potentials close to zero volts.

6 Copper Voltammetry

This chapter describes a limited voltammetric investigation of the electrochemical behaviour of the Cu(II) complex; as mentioned in the introduction 1,5,8,12-tetraazadodecane is used in order to provide a more stable plating bath.[9] The redox properties of the complex were studied on different electrode surfaces and solution pH values, as well as in the presence and absence of other electroless bath components, such as triethanolamine (TEA).

6.1 Copper Voltammetry on Glassy Carbon

The electrochemical behaviour of the copper(II)-1,5,8,12-tetraazadodecane complex was first studied by cyclic voltammetry in a 0.1 M Na_2SO_4 solution, on a GC electrode; concentrations of 0.50 mM $CuSO_4$ and 0.75 mM 1,5,8,12-tetraazadodecane were used. The ratio of 1:1.5 of copper ions to complexing agent was used in order to ensure complete formation of the 1:1 complex. The formation of this complex has a favourable Gibbs energy value (-123.8 kJ mol^{-1}), with a log (K) value of 21.69, at room temperature in aqueous solutions.[141] Figure 86 shows a series of CVs at different scan rates, where an apparently reversible process is visible near -0.70 V vs. Ag/AgCl.

A linear relationship was found between the cathodic peak current and the square root of the scan rate. If reversibility is assumed, and the Randles-Ševčik equation is applied, a diffusion coefficient of 4.7 x 10^{-6} cm^2 s^{-1} is obtained, for a single electron transfer. This value, obtained for a single electron process, is in line with similar Cu(II) complexes in aqueous solutions, such as those formed with quadrol, ethylenediaminetetraacetic acid or diethylenetetraaminepentaacetic acid which are in a range between 3 and 6 x 10^{-6} cm^2 s^{-1}.[142] A diffusion coefficient of the complex studied here has not been reported in the literature. The value of D, as well as the apparent reversibility of the process, indicate that under these conditions the complex is reduced to Cu(I) and does not form metallic copper on

the surface. The widening of the voltammetric window to lower potentials did not produce additional cathodic signals before the end of the window, nor did it significantly change the waveshape of the suspected Cu(I)/Cu(II) complex redox couple.

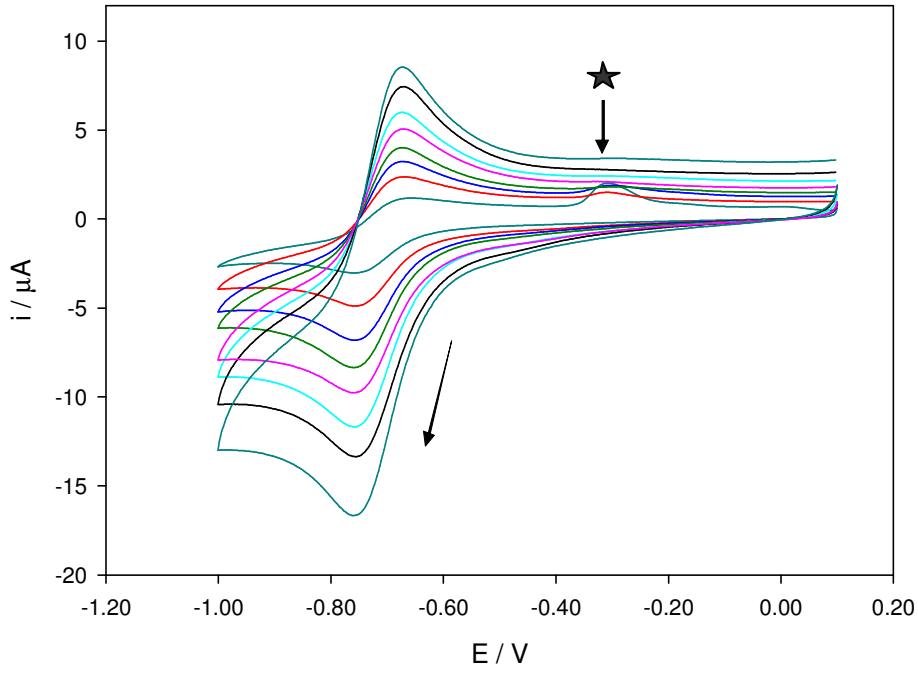

Figure 86. Cyclic voltammograms of copper(II)-1,5,8,12-tetraazadodecane in 0.1 M Na_2SO_4, on GC. The arrow indicates increasing scan rate: a range from 10 to 500 mV s^{-1} is shown.

An additional anodic signal was observed at approximately -0.30 V (marked with a star in Figure 86), at slow scan rates. If the redox process at -0.70 V is the reduction of the Cu(II) to Cu(I) in the complex, on the negative scan, the additional oxidation could involve the disintegration of the Cu(I) complex to produce free Cu^{+} ions in solution; their oxidation to Cu^{2+} would be observed at a somewhat different potential from the complex, generating the second anodic peak. Although the Cu(II) complex is very stable solution, above pH 3, the Cu(I) equivalent is considerably less so.[141,143,144] The widening of the potential window, mentioned above, produced an increase in the size of the second oxidation peak, making it visible at higher scan rates; this is consistent with a time-dependent process at the lower potential region producing the species that oxidises near -0.30 V.

6.1.1 Effect of Alkaline Media

As the interest lies mainly in the deposition of metallic copper from the Cu(II) complex in alkaline media, the voltammetric behaviour was studied in 0.7 M KOH *in lieu* of the 0.1 M sulfate solutions presented above. Figure 87 shows a series of voltammograms of the copper(II)-1,5,8,12-tetraazadodecane complex in alkali. Again a single cathodic process can be seen, in this case just negative of -0.60 V vs. Ag/AgCl. At slow scan rates, however, the cathodic signal splits into two individual peaks (see inset of Figure 87), indicating that, under these conditions, the Cu(II) complex is fully reduced over this potential region; two electrons are transferred to form metallic copper. A single two-electron transfer step has been reported previously for the reduction of this complex in acetonitrile, with the presence of metallic copper detected.[145] In aqueous alkaline solution, a single two-electron process was previously detected at approximately -0.5 V vs. Ag/AgCl.[143] The more negative potential observed here could be due to the electrode surface; GC has a higher overpotential for copper electrodeposition than noble metal surfaces.[146]

A diffusion coefficient cannot be determined under these conditions using simple voltammetric methods; the process is more complex than a simple redox reaction, as beside the multiple electron transfer, it involves the nucleation and growth of copper on the electrode surface.

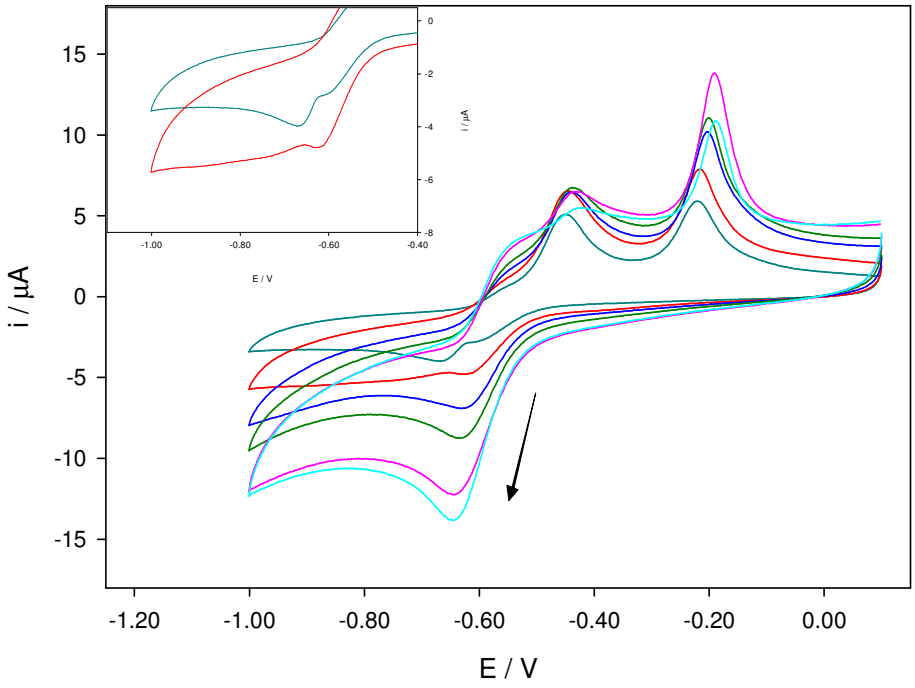

Figure 87. Cyclic voltammograms of copper(II)-1,5,8,12-tetraazadodecane in 0.7 M KOH, on GC. The arrow indicates increasing scan rate: 10, 25, 50, 75, 175 and 200 mV s^{-1} are shown. The inset amplifies the cathodic behaviour at slow scan rates.

The anodic behaviour of the complex in alkaline media is more complicated than that observed in sulfate. Two prominent peaks are observed at approximately -0.45 and -0.21 V, with a peak current ratio which changes with scan rate. The magnitude of the more negative oxidation peak does not greatly vary with scan rate, while that of the more positive peak does. Additionally the first peak appears to have a pre-peak. This latter feature indicates that the re-oxidation process occurs via two separate electron transfers, with the formation of the Cu(I) complex.

The peak near -0.21 V could be due to the direct oxidation of the metallic copper to Cu^{2+} ions, which once produced would then reform the complex. This oxidation process would be expected to occur at more positive potentials than that of oxidation of the complex, due to the stability of the Cu(II) in the complexed form, consistent with the observed behaviour.

6.2 Copper Voltammetry on Gold

As the catalytic surface plays a major role in a typical electroless bath, and DMAB oxidation was found particularly dependent on it, the behaviour of the copper complex was studied on gold. Figure 88 presents the resulting set of CVs at different scan rates, using a Au electrode. Although the general waveshape obtained changes again, a single cathodic process is still present; in this case the peak potential is approximately -0.50 V vs. Ag/AgCl, coinciding with that cited in the literature.[143] As mentioned above, the shift towards lower overpotentials is expected on a metallic surface, which is more catalytic towards copper deposition. At slow scan rates, however, the cathodic signal again splits into two, as seen in the inset of Figure 88, confirming the two-electron process.

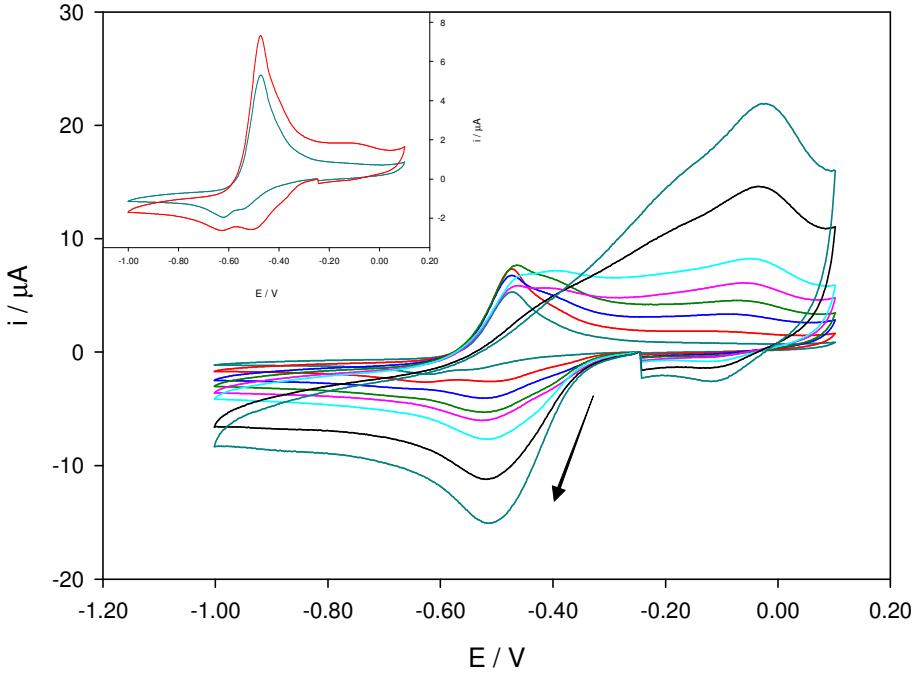

Figure 88. CVs of copper(II)-1,5,8,12-tetraazadodecane in 0.7 M KOH, on Au. The arrow indicates increasing scan rate: 10, 25, 50, 75, 100, 175, 300 and 500 mV s^{-1} are shown. The inset amplifies the slowest scan rates.

Although the reverse scan shows mainly two peaks, as it did on GC, the signals on gold are entirely different (see Figure 87). The lower scan rates tend to a single re-oxidation peak, centred just positive of -0.50 V; this signal is most likely due to the re-oxidation of the copper back to the complexed Cu(II) species, in a two-electron process.

The second peak appears close to 0.00 V and is more prominent at higher scan rates. Although this could be evidence of the oxidation to free Cu^{2+} ions, as observed on glassy carbon, it could also be due to the oxidation of the Cu(II) complex to form a Cu(III) species. This latter complex, although very unstable, has been previously reported to form in acetonitrile solutions.[145] A small cathodic signal is observed upon reversing the scan direction after this peak, at high scan rates, which would be consistent with the reduction back to the Cu(II) complex.

6.2.1 Mimicking Electroless Bath Conditions

In order to better reproduce the conditions of an electroless bath, the pH was lowered to 11.6 and the concentrations were changed to 3.0 mM and 4.5 mM 1,5,8,12-tetraazadodecane (see Chapter 8); 0.1 M Na_2SO_4 was added as supporting electrolyte. Figure 89 shows a series of voltammograms, with increasingly wide potential windows; as the currents are high at very negative potentials, the inset magnifies the reduction and oxidation peaks observed. The main difference between the cathodic behaviour in this case and that observed in highly alkaline media (Figure 88), is the potential at which the reduction peak appears. No negative currents are observed before -0.90 V, with a cathodic peak present around -1.10 V; immediately after the peak (at approximately -1.20 V), a large negative current appears, indicating the end of the potential window; this large cathodic current is also present in the absence of copper.

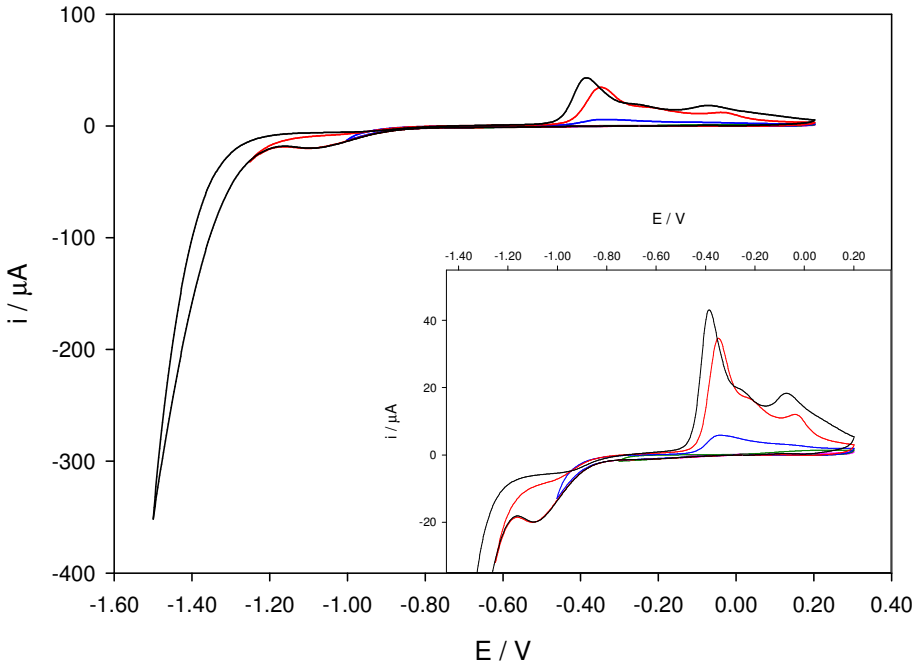

Figure 89. Voltammograms of copper(II)-1,5,8,12-tetraazadodecane, at pH 11.6 and 50 mV s^{-1}, with increasingly negative turning potentials. The redox behaviour is amplified in the inset.

The anodic scan is similar to those observed before, although an additional peak is seen between the peaks seen under other conditions. The first peak near -0.40 V is predominant, and as in highly alkaline media, it is thought to be due to the re-oxidation of the copper; as the new peak is very close to it, basically a shoulder, one interpretation is that the anodic process occurs via two single electron transfers, first to the Cu(I) and then to Cu(II) complexed species.

The effect of the scan rate was studied and the results are presented in Figure 90, where the behaviour in the reverse scan is more clearly observed. Although the last oxidation peak (~ 0.0 V) is present even at slow scan rates, it produces a small cathodic current only at high scan rates, as in the case of Figure 88; as they also appear at similar potentials it is reasonable to assume that they are due to the same process. Again the oxidation of the complex to the Cu(III) species is a plausible explanation, based on previous literature.

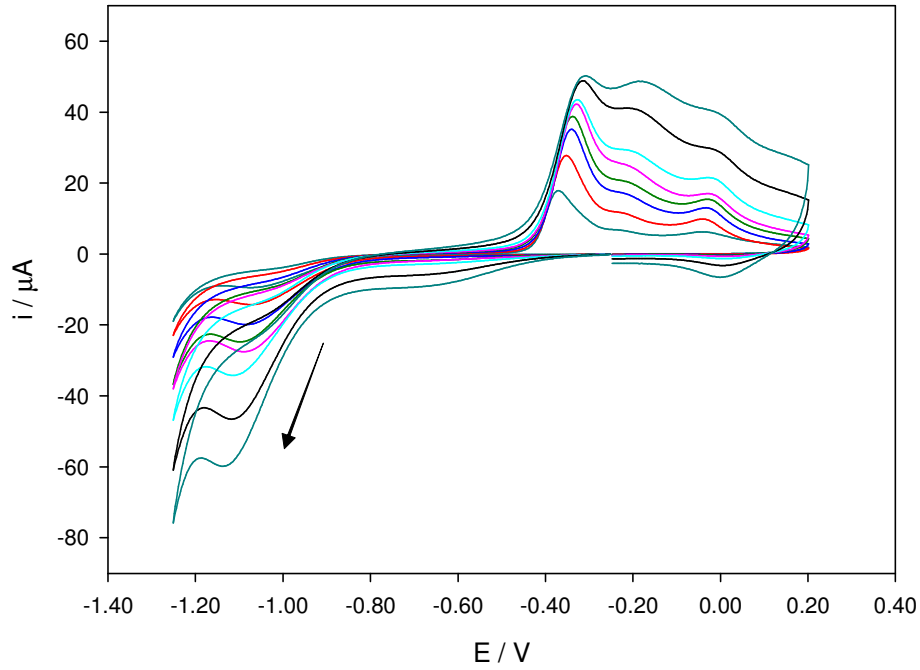

Figure 90. CVs of the Cu (II) complex at pH 11.6, on Au. The arrow indicates increasing scan rate: 10, 25, 50, 75, 100, 175, 300 and 500 mV s^{-1} are shown.

Triethanolamine is a common additive in electroless baths, as it helps to control the solution pH, to complex the copper ions and to catalyse the oxidation of the reducing agent.[9,147] The effect of TEA on the voltammetric behaviour of the copper complex was studied; Figure 91 shows the voltammograms in the presence and absence of TEA in solution. The main change observed is a small shift of the reduction peak towards more negative potentials in the presence of TEA, which is reasonable given the known ability of TEA to complex the Cu(II) ions.[9] On the anodic scan, the oxidation peak previously assigned to the re-oxidation of the copper is smaller in the presence of TEA; that is simply an immediate consequence of less of the complex being reduced in the cathodic scan.

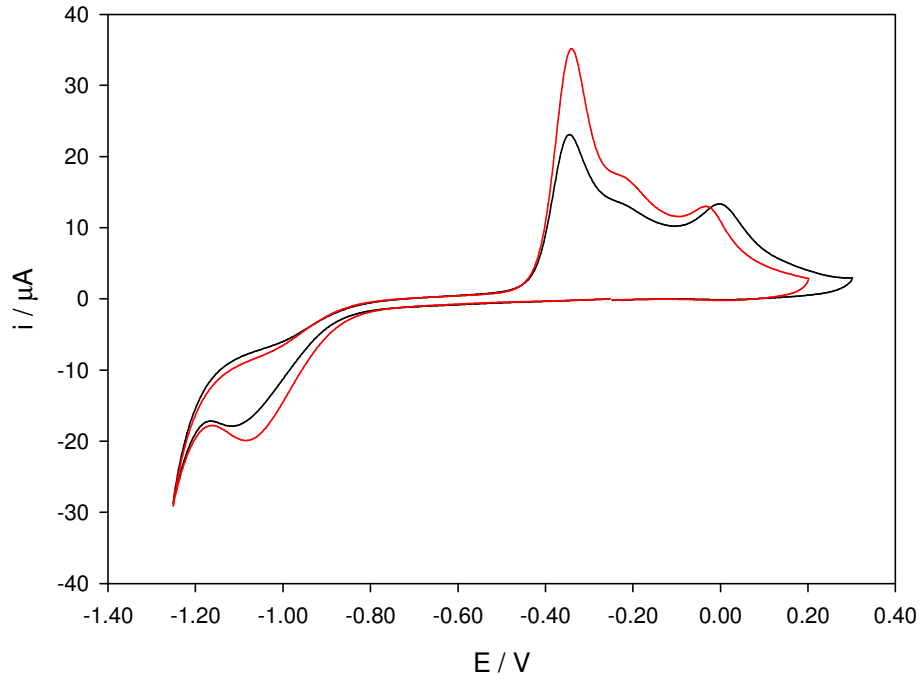

Figure 91. CVs of copper(II)-1,5,8,12-tetraazadodecane at pH 11.6, at 50 mV s^{-1}. Black: with 0.3 M TEA; red: without TEA.

A small shift in the potential of the last oxidation peak can also be observed. This behaviour could also be explained by further stabilisation or complexation of the Cu(II) species in the presence of TEA; this means that the reduction and the oxidation both require higher overpotentials to occur.

6.3 Conclusions

The effect of pH and electrode material on the voltammetric behaviour of the copper(II)-1,5,8,12-tetraazadodecane complex were studied. The electrochemical behaviour was noted to be heavily dependent both on the pH of the solution and the electrode surface, with particularly convoluted anodic behaviour in alkaline media. The presence of the TEA, on the other hand, had little effect on the voltammetric behaviour of the copper complex, with a small increase of the reduction overpotential being the main difference found.

From the results obtained it can be concluded that in sulfate on a glassy carbon electrode, the complex undergoes a reversible, one electron transfer, from

Cu(II) to Cu(I) and back. An additional signal can be seen if the Cu(I) complex is allowed to decomplex and the resulting Cu^{+} ions can be oxidised to Cu^{2+}.

In alkali media, on GC surfaces, the electrochemical behaviour of the copper complex becomes more intricate. First, the complex undergoes a two electron transfer to completely reduce the copper, then the metallic copper can be re-oxidised to the Cu(I) and subsequently the Cu(II) complex species or it can be directly oxidised to Cu^{2+}, as shown in Figure 92.

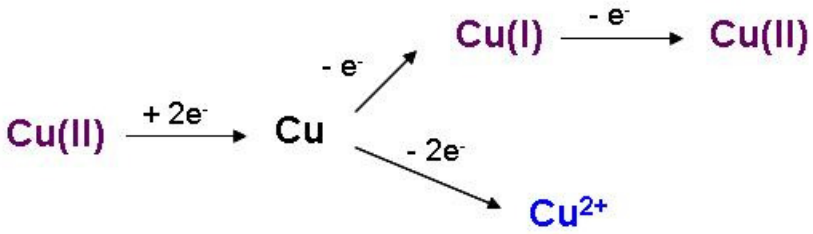

Figure 92. Scheme of the electrochemical behaviour of the copper complex on GC, in alkaline media. The purple colour denotes complexed species, while the blue are free ions in solution.

Gold surfaces catalyse the deposition of copper, so the two-electron reduction in alkali media occurs at less negative potentials than on GC. The anodic behaviour on this surface is again somewhat convoluted, with a Cu(III) complex possibly being formed, according to Figure 93.

Figure 93. Scheme of the electrochemical behaviour of the copper complex on GC, in alkaline media. The purple colour denotes complexed species.

In conditions mimicking the electroless bath, the electrochemical behaviour is similar to that of Figure 93, though the potential of deposition is far more negative and on the anodic scan, the re-oxidation possibly occurs via two single-electron transfers, with the formation of the Cu(I) complex. The presence of TEA in solution simply shifted the reduction potential of the Cu(II) complex towards more negative values.

7 The Voltammetric Response of Bipolar Cells

The bipolar cell configuration was chosen as an ideal way of probing the electroless deposition mechanism, as it provides access to *in-situ* measurements of the process. This set-up allows electrochemical control of the system and, while the cathodic and anodic reactions remain electronically connected, the bipolar cell physically separates the two half-reactions.

This chapter describes the use of bipolar cells as a tool to investigate the voltammetric behaviour of a reversible electrochemical system.[ix] Although similar experimental configurations to the bipolar cell discussed here have been used before, particularly in liquid/liquid applications,[115,117] a complete study of the cell has not been reported. Conditions were varied to evaluate the effect of mass transport in either or both half-cells on the overall process and numerical simulation is compared to the experimental data obtained. Preliminary work on more complex systems, including kinetically hindered redox couples and copper deposition, was also carried out and is described here.[x]

7.1 Reversible Electron Transfer

7.1.1 Preliminary Three Electrode Cell Studies

In order to study the voltammetric response of bipolar cells to reversible electron transfer, two model reversible redox couples were selected and studied separately in conventional (*i.e.* three electrode) cells. This was done to obtain the

[ix] Part of this work has been accepted for publication in the Journal of Electroanalytical Chemistry and is partly copyright of Elsevier B.V. (in particular some of the figures). See Appendix A for more details.

[x] Some of the work on the investigation of the copper-DMAB electroless system, using the bipolar cell, was published in Electrochemistry Communications and is, in part, copyright of Elsevier B.V. (in particular some of the figures). See Appendix A for more details.

necessary information to study the response of these couples in the bipolar cell, specifically reduction potentials and diffusion coefficients, but also to establish the best experimental conditions for each redox couple (supporting electrolytes and electrodes, for example).

Hexacyanoferrate and hexaammineruthenium complexes were selected as model redox couples. Potassium chloride (0.5 M) was chosen as the electrolyte for both, and hydrochloric acid (0.05 M) was added in the case of ferro- and ferricyanide solutions to lower the pH and improve the kinetics (at higher pH, peak separations were dependent on scan rate and always larger than 60 mV). Glassy carbon disk electrodes were used as WE, Ag/AgCl as references and platinum and gold were used as CE in the hexaammineruthenium and hexacyanoferrate solutions, respectively.

Hexaammineruthenium(III) was studied through voltammetry in a three electrode cell in order to determine the reduction potential and the diffusion coefficient of the complex. The use of its counterpart, hexaammineruthenium(II) was avoided in the subsequent studies in the bipolar cell, as it was found to be unstable in solution even when thoroughly de-oxygenated. Figure 121 shows cyclic voltammograms performed at different scan rates; as discussed in Section 2.2, the Randles-Ševčik equation (Equation 50) allows the determination of the diffusion coefficients, if the peak currents are plotted versus the square root of the scan rates and all other values are known. Such a plot can be seen in Figure 95.

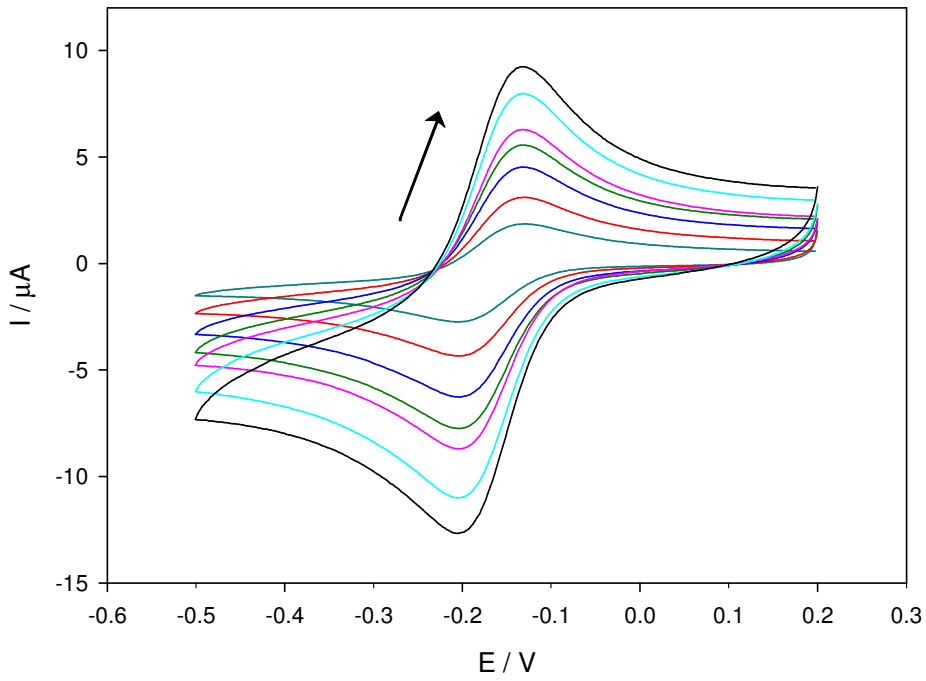

Figure 94. Cyclic voltammograms of 0.5 mM hexaammineruthenium(III), in 0.5 M KCl, obtained at 10, 25, 50, 75, 100, 150 and 200 mV s^{-1} (the arrow indicates increasing scan rate).

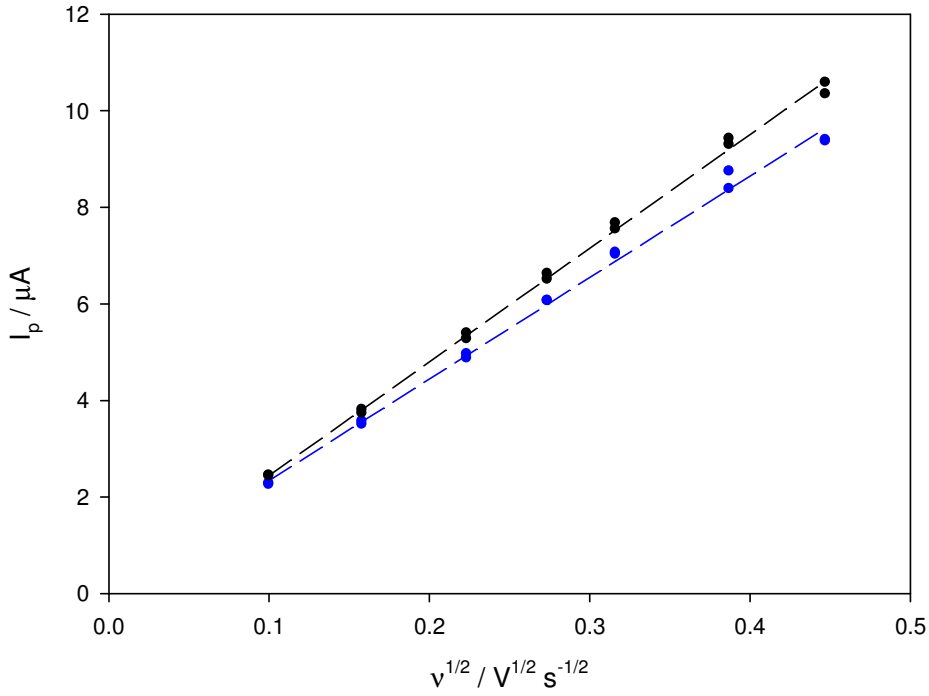

Figure 95. Peak current as a function of the square root of the scan rate for hexaammineruthenium(III) reduction (black) and hexaammineruthenium(II) oxidation (blue).

From the slope of the graphs in Figure 95, the diffusion coefficients were determined to be 6.0 x 10^{-6} and 4.8 x 10^{-6} cm^2 s^{-1} for $Ru(NH_3)_6^{3+}$ and $Ru(NH_3)_6^{2+}$, respectively (for the corresponding treatment of errors see Appendix B). Similar

procedures were followed for ferro- and ferricyanide, obtaining values of 5.2×10^{-6} and 5.4×10^{-6} cm^2 s^{-1}, respectively.

The standard reduction potentials of the two couples were also determined through the above voltammetry in three electrode cells. A value of -0.169 V vs. Ag/AgCl was obtained for the $Ru(NH_3)_6^{3+}/Ru(NH_3)_6^{2+}$ couple. For the $Fe(CN)_6^{4-}/Fe(CN)_6^{3-}$ couple, however, it was found that the redox potential at high concentrations varies from that at lower concentrations by approximately 30 mV, as can be seen in Figure 96. This observation could be attributed to a side reaction between both iron species to form Prussian blue, Berlin Green, or a similar mixed valence complex compound, as a colour change in the solution was easily observed over the course of a few hours. These types of compounds have been reported to form in moderately concentrated solutions.[148] Two formal potential values were consequently used: -0.305 V where 25 mM of both species were present and -0.336 V in all other cases.

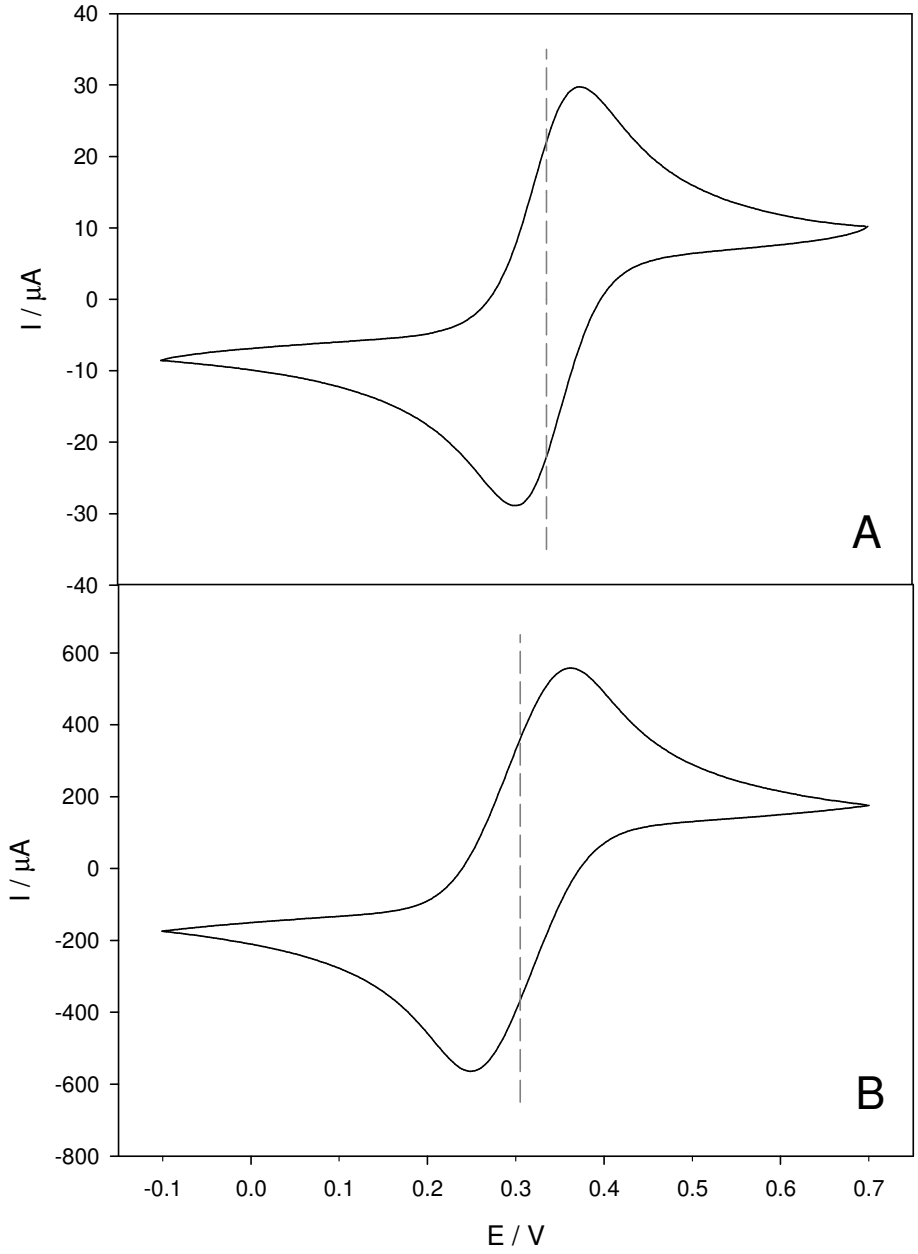

Figure 96. Cyclic voltammograms at 100 mV s^{-1} when both $Fe(CN)_6^{4-}$ and $Fe(CN)_6^{3-}$ are present in solution in equal concentrations: 1 mM (A) and 25 mM (B). 0.5 M KCl and 0.05 M HCl were used as electrolyte. The grey dashed lines indicate the redox potential in each case.

7.1.2 Voltammetric Comparison: Three Electrode Cell, Bipolar Cell and Numerical Simulation

Operating the bipolar cell in potentiostatic mode, as described in Section 3.3.5, controls the potential difference between the two half-cells. For Cell 1, the typical cell used in the study of reversible electron transfer in the bipolar cell, as the potential is swept towards negative potentials, the hexaammineruthenium

complex is reduced in half-cell (a), as the ferrocyanide is oxidised in half-cell (b) (see Figure 97A). Clearly as the direction of the scan is reversed, the opposite reactions occur; the ruthenium complex is oxidised, reducing the ferricyanide in the other cell, as seen in Figure 97B. The bipolar cell was connected to the potentiostat in such a way that negative currents were observed when the ruthenium complex was reduced; positive currents thus implied oxidation of the ruthenium complex.

Ag/AgCl	x mM $Ru(NH_3)_6Cl_3$ 0.5 M $KCl_{(aq)}$	‖	y mM $K_3Fe(CN)_6$ y mM $K_4Fe(CN)_6$ 0.5 M KCl, 0.05 M $HCl_{(aq)}$	Ag/AgCl

Cell 1. Electrochemical cell used for the study of reversible electron transfer in the bipolar cell.

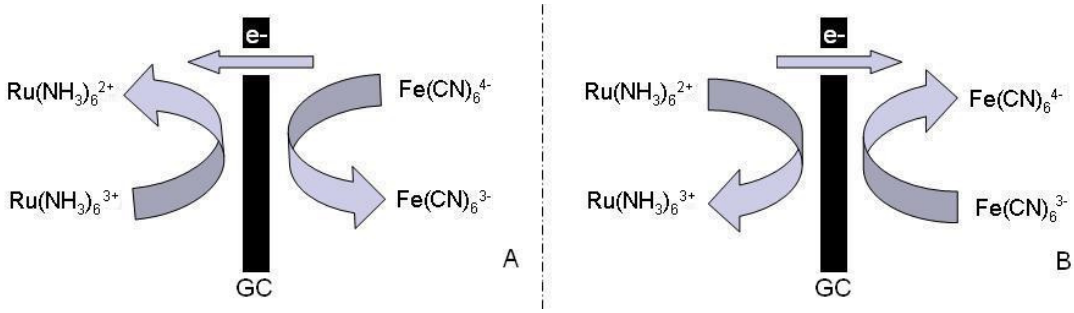

Figure 97. Reactions that occur during a cyclic voltammetry in Cell 1; A – forward scan, B – reverse scan.

As discussed in Section 2.4, when the iron-containing species are in equal concentrations and in sufficient excess with respect to the ruthenium complex, the ferrocyanide and ferricyanide solution acts as a metallic conductor and the system behaves as a conventional three electrode cell. This has been previously demonstrated for liquid/liquid systems by Stewart *et al*. using numerical simulation and experimentally by Geblewicz *et al*.[113,114] Figure 98 shows this type of behaviour in the bipolar cell: Figure 98A shows the results from the three electrode cell (same data as shown in Figure 121), while Figure 98B shows the corresponding system in the bipolar cell, containing an excess of ferrocyanide and ferricyanide ions.

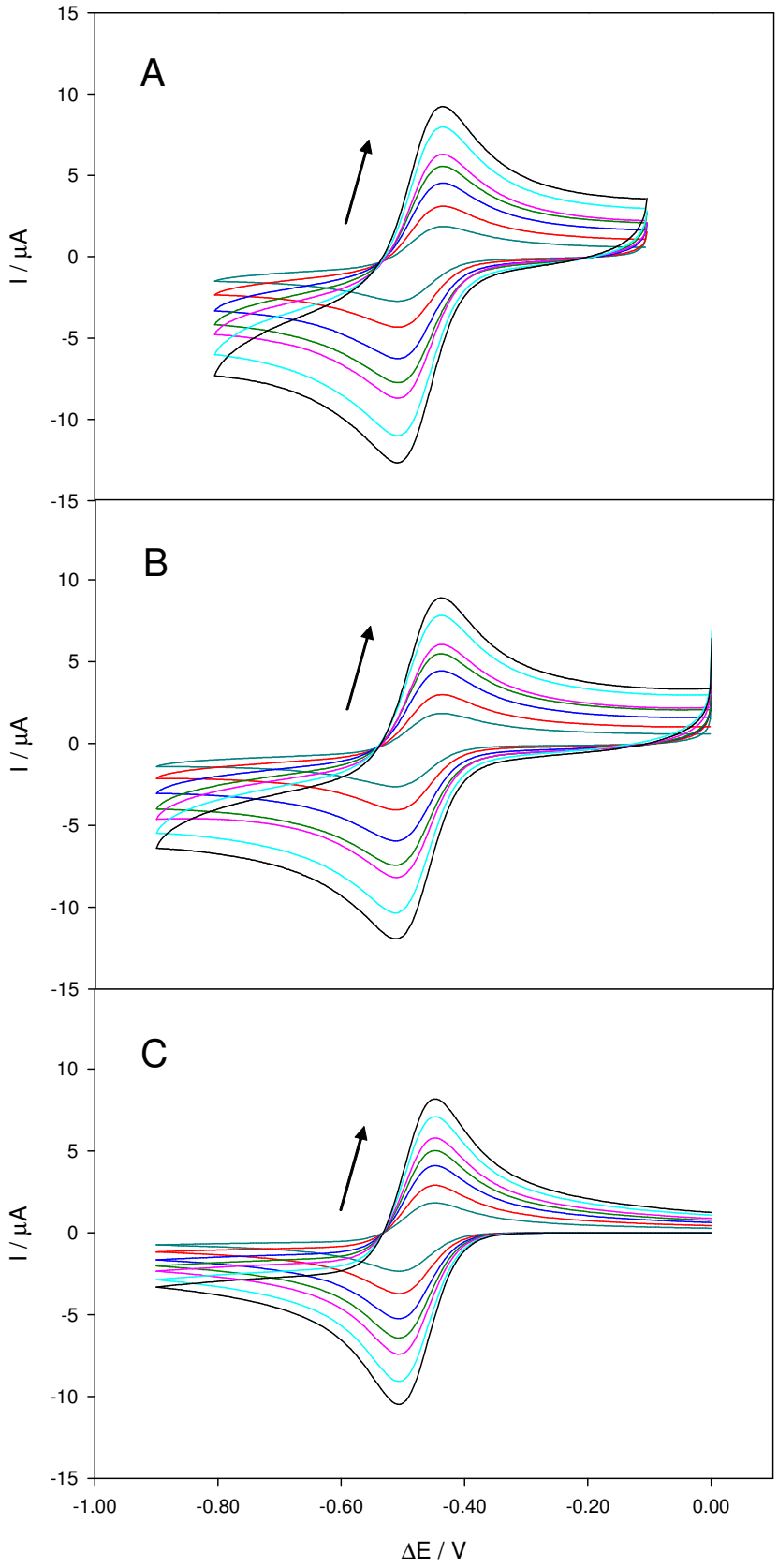

Figure 98. Cyclic voltammograms of a 0.5 mM Hexaammineruthenium(III) Chloride solution (arrow indicates increasing scan rate) in the three electrode cell (A) and the bipolar cell (B), where x = 0.5 and y = 25 for Cell 1. Numerically simulated voltammograms, for conditions corresponding to those of (B), are also shown (C).

The mid-point between the peaks seen in voltammograms of the bipolar cell (Figure 98B) should be at an applied potential difference equal to ΔE^0, the difference in the standard potentials of the two couples. In order for direct comparison to be made with the three-electrode experiment (Figure 98A), the response of the three electrode cell was plotted with respect to the standard potential of the ferrocyanide/ferricyanide couple. Consequently, the redox potentials obtained experimentally in the bipolar cell, and those calculated from the redox potentials of both couples found in three electrode cells should agree. It can be seen in Table 19 that the difference between these values is small. As stated above (see Section 7.1.1), two apparent values of E^0 were used for the ferrocyanide/ferricyanide couple.

Table 19. Literature and experimental redox potentials for the ruthenium and iron containing complexes, quoted vs. Ag/AgCl.[98,130]

	$Ru(NH_3)_6^{2+}/Ru(NH_3)_6^{3+}$	**$Fe(CN)_6^{4-}/Fe(CN)_6^{3-}$**
E^0 (Literature) / V	-0.10	0.363 (in 0.1 M HCl)
E^0 (Experimental) / V	-0.169	0.305 (25 mM, in 0.05 M HCl)
		0.336 (1 mM, in 0.05 M HCl)
ΔE^0 (Literature) / V	-0.463	
ΔE^0 (Experimental) / V	-0.474 (for 25 mM); -0.505 (for 1 mM)	
ΔE^0 (Bipolar, Experimental) / V	-0.478 (for 25 mM)	

Note that Figure 98C shows the simulated voltammograms obtained using the experimental conditions of Figure 98B. The diffusion coefficients and redox potentials used in the simulation were those determined in Section 7.1.1. The difference between the standard potentials of each redox couple was -0.474 V (see Table 19). The current convention was defined as negative for a reduction of the ruthenium complex, for comparison with experimental values. It can be seen, through the graph and the calculated values of ΔE^0, that the tendencies observed are similar in all three cases: the three electrode cell, the bipolar cell and the numerical simulation of the bipolar cell; This confirms that in the bipolar configuration under these conditions, half-cell (b) acts simply as a conductor, and thus the overall system mimics a conventional three-electrode set-up.

7.1.3 Effect of the Concentration Ratios on the Voltammetric Response of the Bipolar Cell

When the concentration ratios between the two half-cells are varied, the voltammetric behaviour of the bipolar cell changes; it no longer mirrors that of the typical three electrode cell. While equimolar concentrations of the ferrocyanide and ferricyanide were maintained, the ratio between them and that of the ruthenium complex was varied: the resulting voltammograms can be seen in Figure 99. The wave shape of the voltammograms is affected, as it now responds to the diffusion of all four participating species to and from the electrode surface, as well as their respective concentrations (see Section 3.4.4, Equation 65); the peak currents and positions change as the solution concentrations shift the equilibrium expressed through the above-mentioned equation.

In Figure 99, curves (a) and (d) represent the limiting cases of excess concentrations of the iron-containing species and the ruthenium complex with respect to the other half-cell, respectively; curves (b) and (c), on the other hand, have similar concentrations in each side of the cell. Comparison between the curves clearly indicate deviations from a standard reversible wave shape; as the concentrations between half-cells become comparable, the peak separations increase and the relative size and shape of the forward and back peaks change.

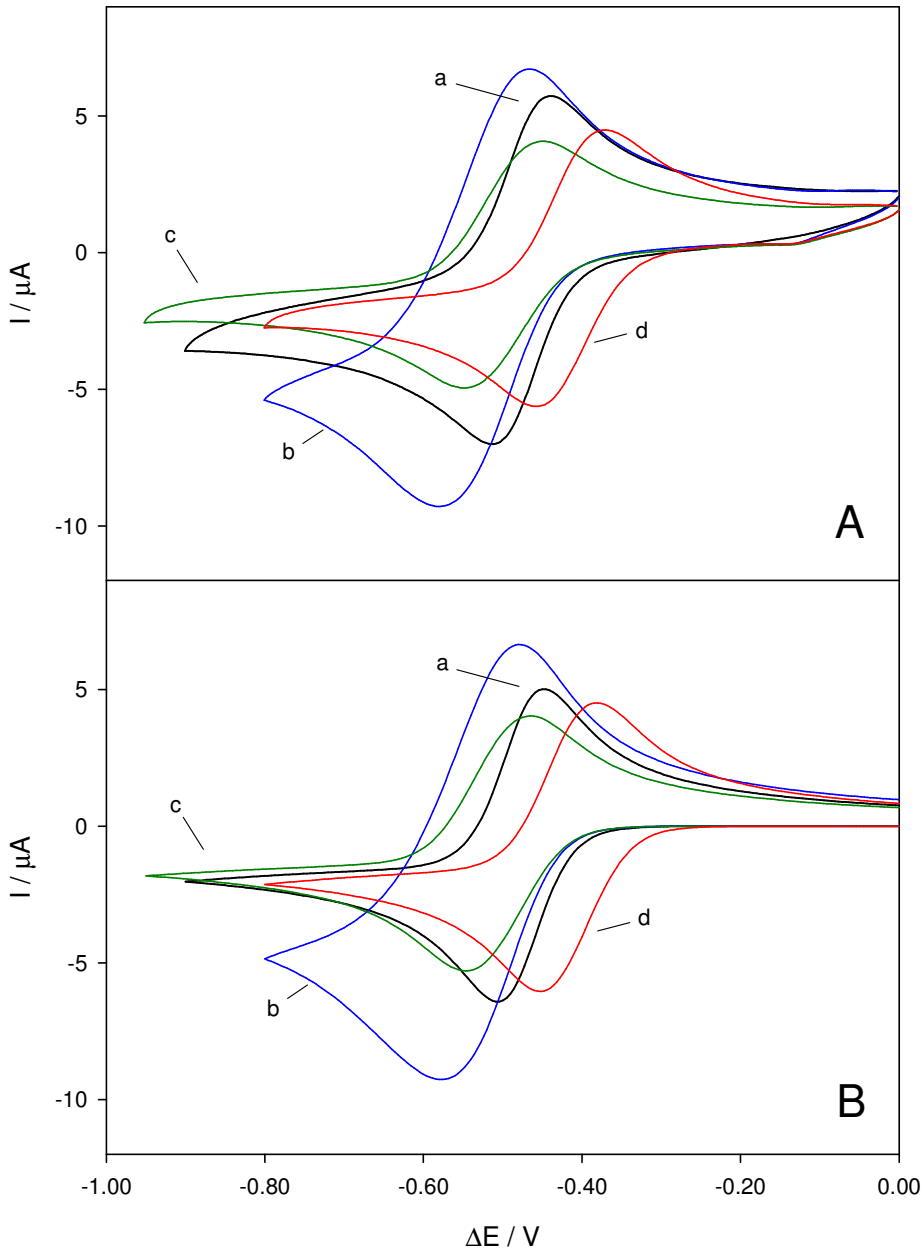

Figure 99. Cyclic voltammograms obtained experimentally (A) and through simulation (B) at 75 mV/s for different values of x and y in Cell 1. a: x = 0.5, y = 25.0; b: x = 1.0, y = 1.0; c: x = 1.0, y = 0.5; d: x = 25.0, y = 0.5.

Figure 99B shows the simulated curves for the conditions presented in Figure 99A. As will be discussed in detail in this section, similar tendencies are observed in both experimental and simulated curves, confirming that the effects observed on the wave shape are indeed due to the concentrations ratios. The different concentrations used throughout the study are presented in Table 20. These values were used in the calculation of the term which serves as the ordinate in Figure 100 to Figure 103: $\ln\{[Ru(NH_3)_6^{3+}]/([Fe(CN)_6^{4-}]+[Fe(CN)_6^{3-}])\}$. In this set of figures, the effect of the relative concentrations of the different redox

species is revealed more clearly by extracting parameters such as the current function and the peak potentials.

Table 20. Concentrations of each species used to vary the concentration ratios in the bipolar cell.

$\ln\{([Ru(NH_3)_6^{3+}]/[Fe(CN)_6^{4-}]+[Fe(CN)_6^{3-}])\}$	$Ru(NH_3)_6^{3+}$ / M	$Fe(CN)_6^{4-}$ / M	$Fe(CN)_6^{3-}$ / M
-4.59	5.06×10^{-4}	2.50×10^{-2}	2.50×10^{-2}
-3.00	9.94×10^{-4}	1.00×10^{-2}	1.00×10^{-2}
-2.32	9.94×10^{-4}	5.01×10^{-3}	5.07×10^{-3}
-0.74	2.00×10^{-3}	2.11×10^{-3}	2.07×10^{-3}
-0.69	9.88×10^{-4}	9.94×10^{-4}	9.84×10^{-4}
-0.01	1.01×10^{-3}	4.97×10^{-4}	5.28×10^{-4}
-0.01	1.99×10^{-3}	1.03×10^{-3}	9.72×10^{-4}
0.66	1.98×10^{-3}	5.19×10^{-4}	5.04×10^{-4}
2.31	1.00×10^{-2}	4.97×10^{-4}	4.98×10^{-4}
3.18	2.50×10^{-2}	5.40×10^{-4}	5.04×10^{-4}

Figure 100 shows how the dimensionless current function, χ, varies with the concentration ratio. The dimensionless current is related to the peak current by Equation 66, where the concentration and diffusion coefficient were defined in terms of the hexaammineruthenium(III) complex.[98]

$$\chi = \frac{i_p}{nFA\left(\frac{\pi nF}{RT}\right)^{1/2} CD^{1/2}\upsilon^{1/2}} \qquad \text{Equation 66}$$

For a three electrode cell, operating under standard conditions, χ has a fixed value of 0.252.[104] In the bipolar cell, that value is obtained for the limiting case of a clear excess of both of the iron-containing species. The value of χ decreases, however, as the concentration of those complexes is lowered. Figure 100 shows two experimental series, as well as the corresponding simulations. Each data point shown is the average resulting from seven voltammograms (experimental or simulated) under the same conditions, but at different scan rates; the scan rates used were: 10, 25, 75, 100, 150 and 200 mV s^{-1}.

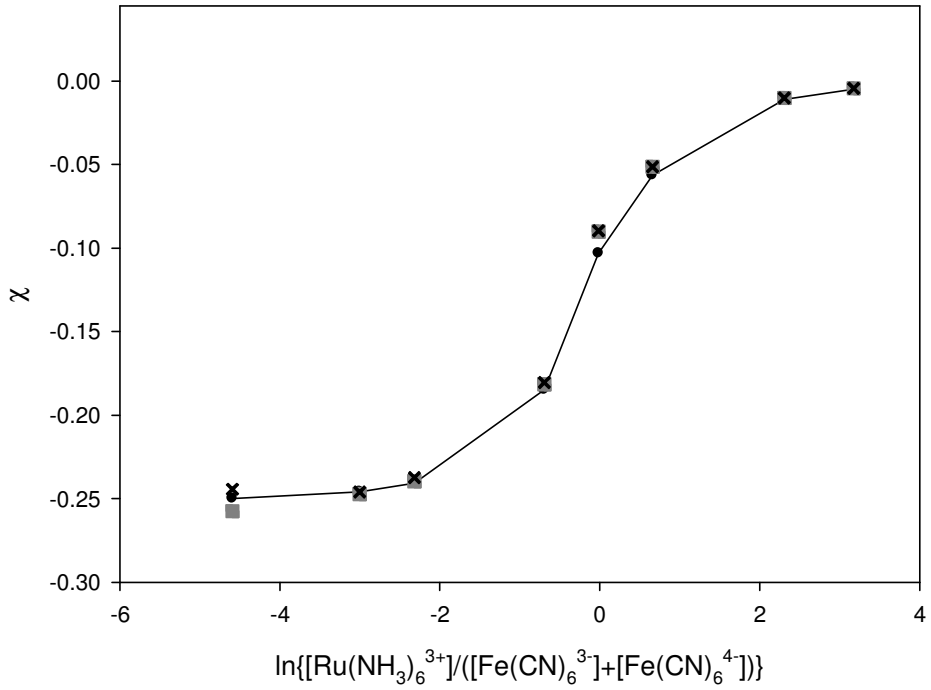

Figure 100. The dimensionless current as a function of the concentration ratio in the bipolar cell. The grey squares and black crosses represent two independent experimental values. The continuous line, with dots, is the numerical simulation corresponding to the experimental conditions used.

The trend observed shows the current function decreasing asymptotically towards zero as the excess of the ferro- and ferricyanide decreases. This behaviour agrees with the numerical integration approach of Stewart *et al*, who reported a decrease from 0.251, with an equimolar excess of one phase, to 0.111 when the concentrations in each phase were equal (equivalent to x = 1 and y = 0.5 in Cell 1, while the corresponding logarithmic term would be equal to zero in Figure 100).[113]

As stated above, the peaks change not only in magnitude, but also in position, with the concentration ratios. These changes in potential, for the forward and back peaks, can be seen in Figure 101A and B, respectively. As in Figure 100, two series of experimental values are depicted, along with their simulated counterparts, all averaged over a range of scan rates.

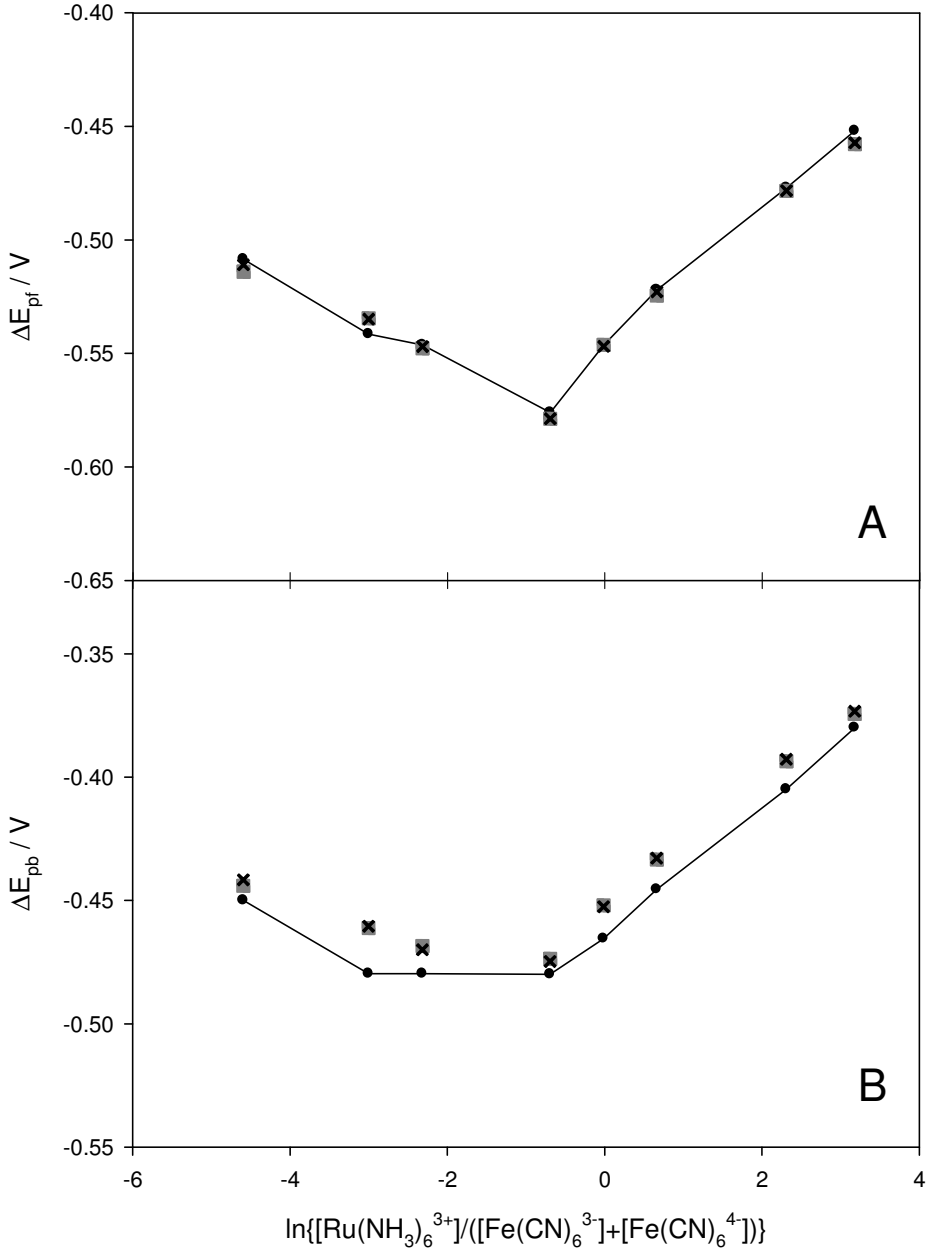

Figure 101. Peak potential as a function of concentration ratios. Conditions are as in Figure 100. A – forward scan, B – reverse scan.

The trends observed are different for the back and forward peaks. In the case of the forward scan a V-shaped plot is obtained, with a minimum when the $\ln\{[Ru(NH_3)_6^{3+}]/([Fe(CN)_6^{4-}]+[Fe(CN)_6^{3-}])\}$ term is just negative of zero, where a more extreme potential difference is required for the current function to reach its maximum value due to the active species in both half cells being depleted. The forward scan is mainly limited by ferrocyanide oxidation, when the logarithmic term exceeds zero, and by hexaammineruthenium(III) reduction when the logarithmic term is negative.

The potential of the back peak also has a linear increase when the logarithm term exceeds zero, where it is mainly limited by the ferricyanide reduction. On the negative region of the graph, however, the decrease in potential is less pronounced. In this region, the oxidation of the hexaammineruthenium(II) is the dominant factor and the initial absence of this species from solution produces the asymmetry observed; a gradient of zero would be expected if the standard potential of the ferrocyanide/ferricyanide couple were truly a constant over that concentration range (see Table 19).

As the trends in the change of peak potentials differ for the forward and back scans, the peak separation also changes with the logarithmic term, as can be seen in Figure 102. When there is an excess of concentration on either side of the cell, the peak separation approaches that expected for a reversible system, while as the concentrations become similar, the peak separation increases, producing a maximum in the graph. The only semi-analytical description for the non-excess case arises when the initial concentration of ferrocyanide equals that of the hexaammineruthenium(III) and the other species are absent. In that case, the system would correspond to a charge transfer equivalent to half an electron and a peak separation of 0.118 V would be expected.[104] A numerical simulation of these conditions produced a peak separation of 0.117 V; the difference of 1 mV can be attributed to the unequal diffusion coefficients of the solutes, as the theoretical value quoted assumes that the diffusion coefficients are equal.

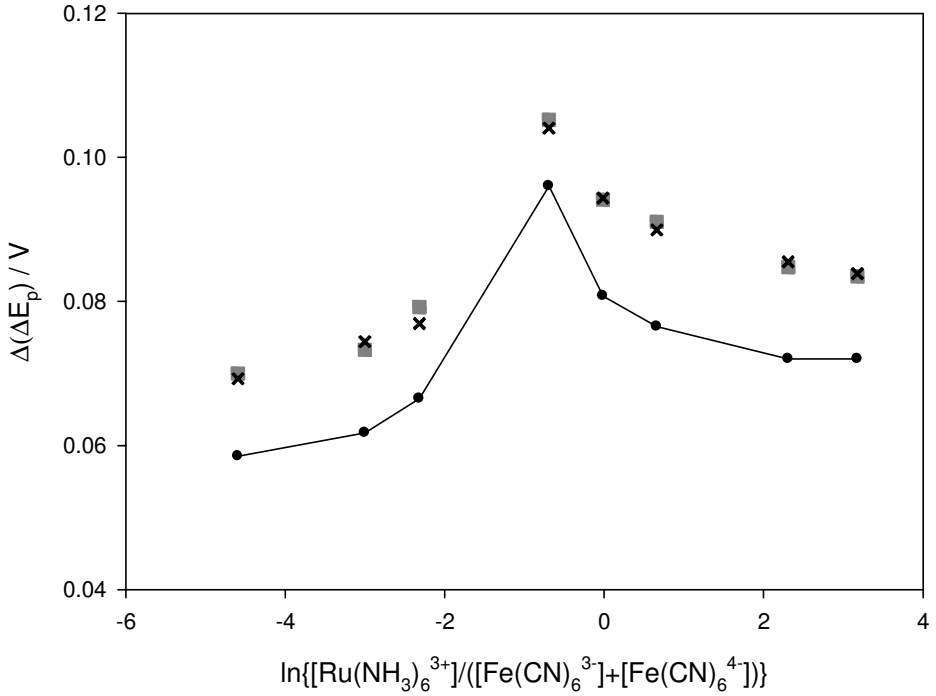

Figure 102. Peak separation as a function of concentration ratio in the bipolar cell. Conditions equal to Figure 100.

Although the trend for experimental and simulated peak separation values is the same, the experimental peak separation is higher than that predicted by the simulation in all cases. Experiments performed with the hexaammineruthenium(III) complex, in the three electrode cell, also exhibited a peak separation approximately 10 mV higher than the ideal 59 mV separation expected at room temperature (see Figure 121).[104] As the peak separation was independent of scan rate, kinetic influence was ruled out as an explanation for this behaviour; it is possibly due to surface heterogeneity of the glassy carbon or Ohmic losses.

In order to confirm the trends observed, further experiments were performed using different absolute concentrations but maintaining the concentration ratios. Figure 103 shows the simulated data presented before, for the dimensionless current and the forward peak potential, along with experiments using identical concentration ratios but with the concentrations of all electroactive species doubled. The figure shows that the trends seen in Figure 100 and Figure 101A are maintained.

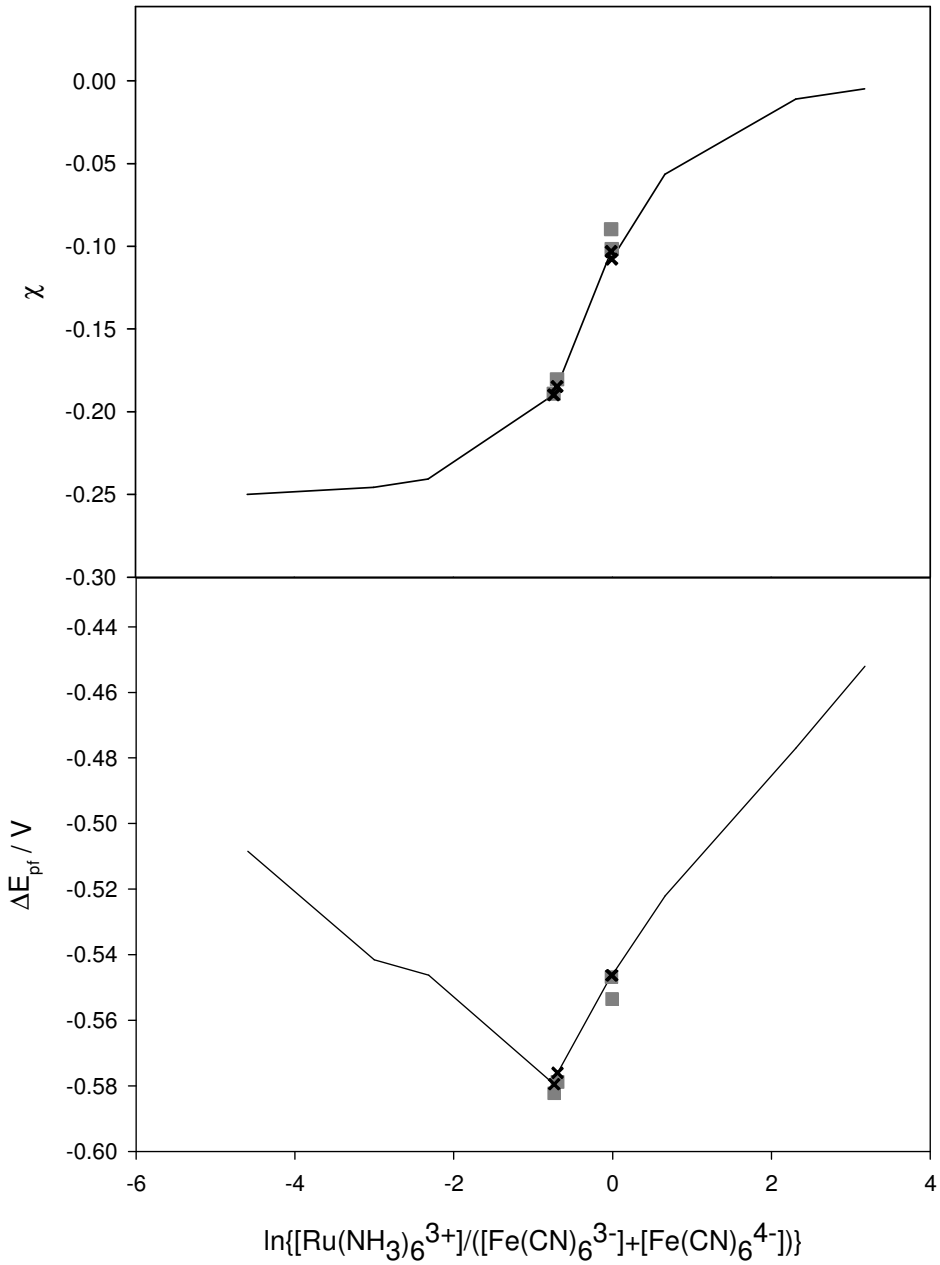

Figure 103. Dimensionless current (top) and forward peak potential (bottom) as a function of concentration ratios. Conditions are as in Figure 100; the data points shown have similar ratios, with doubled concentrations.

7.1.4 Additional Numerical Simulation Studies

As the numerical simulation consistently reproduced the voltammetric response of the bipolar cell, final simulations of the reversible system were performed in order to gain further understanding. In Figure 104, the case of an excess concentration of ferrocyanide and ferricyanide is presented, accompanied by the same case, with the diffusion coefficients of these species decreased by a

factor of 100. It can be seen that a slightly different voltammogram is obtained in the latter case: the peak currents decrease slightly and the peak separation increases marginally. This result would be expected for a decrease in mass transport, even for such an excess of concentrations.

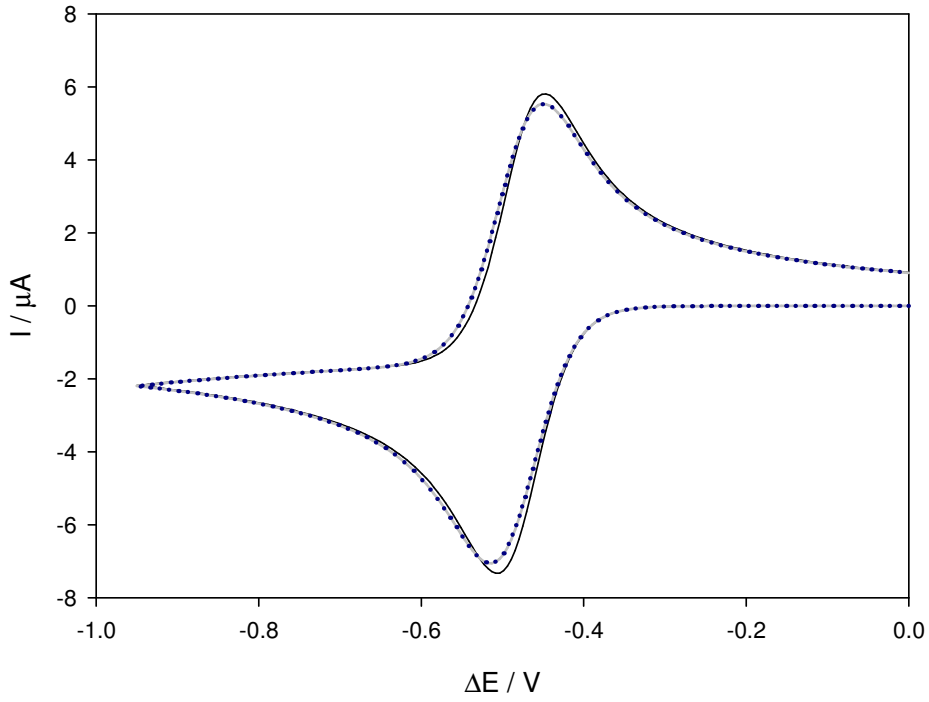

Figure 104. Numerically simulated cyclic voltammograms for the case of excess ferrocyanide and ferricyanide. Continuous black line – concentrations: 0.5 mM $Ru(NH_3)_6^{3+}$ and 25 mM $Fe(CN)_6^{4-}$/$Fe(CN)_6^{3-}$, diffusion coefficients: determined experimentally (see Section 7.1.1). Dotted blue line - diffusion coefficients: decreased 100 times for $Fe(CN)_6^{4-}$ and $Fe(CN)_6^{3-}$. Continuous grey line – concentrations: decreased 10 times for $Fe(CN)_6^{4-}$ and $Fe(CN)_6^{3-}$.

The two cases described above are also compared to a case with lower concentrations of the iron-containing species (10 times less), with the experimentally determined diffusion coefficients. This voltammogram agrees perfectly with the case of the decreased diffusion coefficients, demonstrating that the normalized current function (Equation 66) holds for conditions where mass transport in both half-cells has to be considered.

The excess of hexaammineruthenium(III) did not produce the same results as the excess of the ferrocyanide and ferricyanide, in terms of peak separation and position, presumably due to the initial presence of only one form of the redox couple involved. As equimolar concentrations of the iron-containing species were used in all experiments, the effect of having only ferrocyanide in solution was

investigated. Two cases were considered: having ferrocyanide at concentrations of 25 and 50 mM, *i.e.* the original concentration of ferrocyanide and the total concentration of iron-containing species in the default excess Fe case. The resulting simulated linear voltammograms are presented in Figure 105, along with the original simulated and experimental cases.

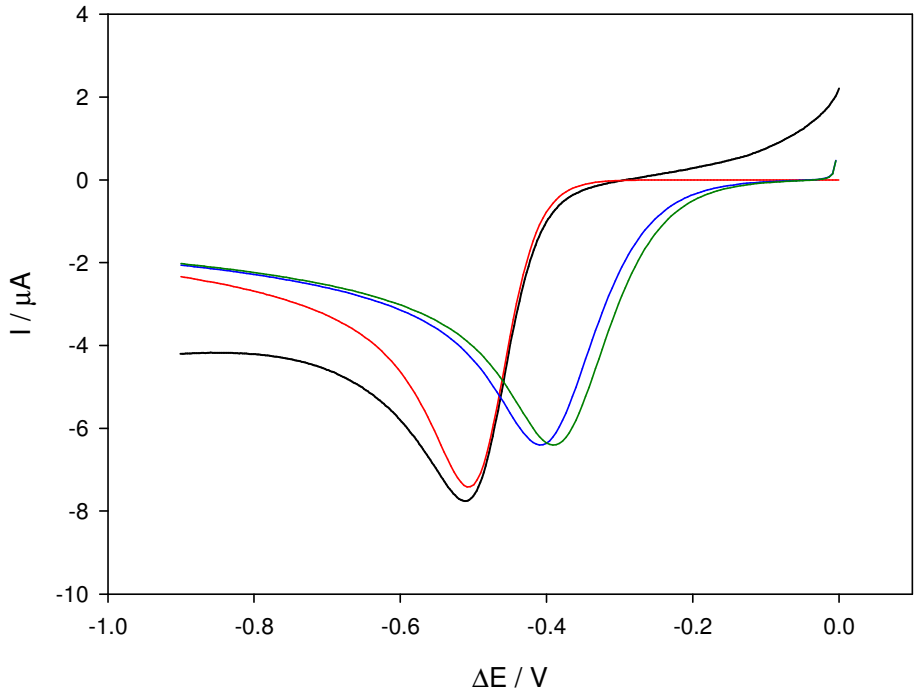

Figure 105. Linear sweep voltammetry of 0.5 mM $Ru(NH_3)_6^{3+}$ in the bipolar cell. Black – experimental result with 25 mM $Fe(CN)_6^{4-}$/$Fe(CN)_6^{3-}$, red – corresponding simulation. The blue and green lines were simulated with no ferricyanide present and 25 mM and 50 mM of ferrocyanide, respectively.

The difference between having both redox species in solution and only one of them is apparent, even at higher concentrations of ferrocyanide; in both ferrocyanide-only cases the peak appears at less negative potential differences, but with lower currents. The shift in potential can be explained by the fact that, in these cases, the midpoint in the voltammograms is no longer simply due to the difference in redox potentials between the two couples; the concentrations of the iron-containing species play an important role in the Nernstian equilibrium, rather than cancelling out by being equal, leading to the shifts observed in Figure 105.

7.2 Kinetic Studies

In order to gain further understanding of the voltammetric behaviour of the bipolar cell, kinetically hindered systems were studied; cerium(III/IV) sulfate was chosen as the model redox couple for this purpose. As in the case of reversible electron transfer, preliminary studies were carried out in the three electrode cell.

7.2.1 Voltammetric Comparison: Three Electrode Cell, Bipolar Cell and Numerical Simulation

The cerium(III/IV) sulfate redox couple was initially studied in the three electrode cell and numerical simulation was used in order to extract kinetic and mass transport information. Figure 106 shows some typical voltammograms obtained using a glassy carbon working electrode, with a platinum counter and a Ag/AgCl reference. The figure also contains the corresponding simulated response.

The numerical simulations were performed using a costum-written C program,[xi] which solved the Butler-Volmer equation (Equation 55) for each point of the voltammogram. Experimental parameters such as initial solution concentration, scan rate and potential range were fixed, while kinetic parameters and diffusion coefficients were obtained from the literature and used as initial values in the simulations.[149,150] The k^0, D and α values were then systematically changed until good agreement between experiment and simulation was obtained.

[xi] The program was written by Dr Fran G.E. Jones, former Postdoctoral Research Associate of the Manchester Electrochemistry Group.

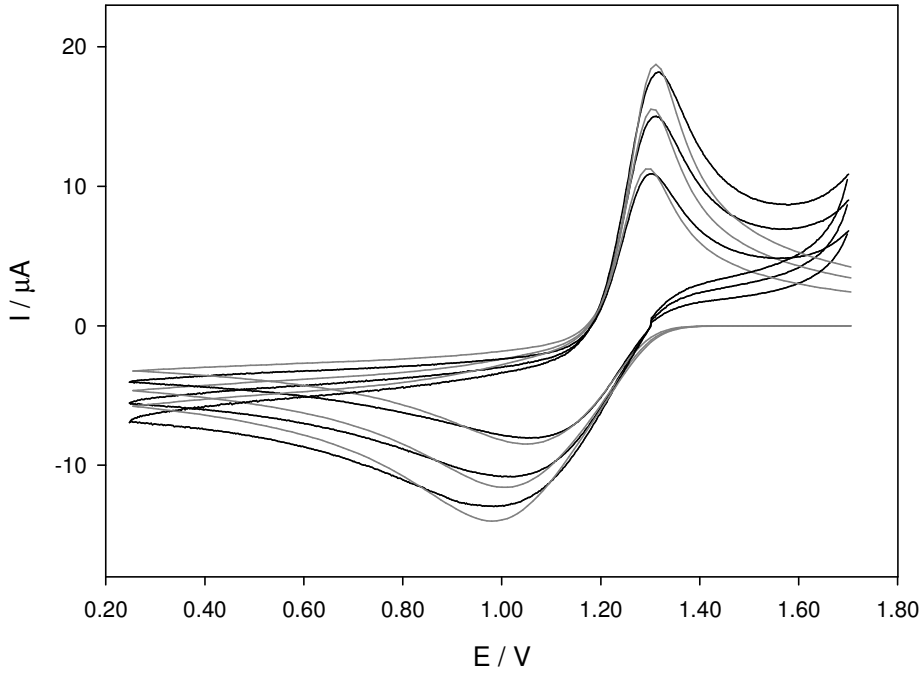

Figure 106. Cyclic voltammograms of 2.52 mM $Ce(SO_4)_2$ in 0.5 M H_2SO_4 (black) with the corresponding numerical simulation (grey). Scan rates of 25, 50 and 75 mV s^{-1} are shown.

A range of scan rates (10, 25, 50, 75, 100, 150 and 200 mV s^{-1}) and two concentrations (2.52 and 3.50 mM) were studied. Table 21 shows the literature values initially used and the experimental values extracted from the simulations. The standard reduction potential was found to be 1.205 V vs. Ag/AgCl. Since good agreement between experimental and simulated voltammograms was found, and values close to those found in the literature were obtained, the system was consequently used to study the behaviour of the bipolar cell. The first case studied consisted of using a reversible couple in half-cell (b), while cerium(IV) sulfate was placed in half-cell (a); ferro- and ferricyanide were again used, as can be seen in Cell 2.

Table 21. Literature and experimental values for kinetic parameters and diffusion coefficients of the cerium sulfate redox couple.[149,150]

	Literature	**Experimental**
$\mathbf{D_{Ce(III)}}$ / **cm^2 s^{-1}**	1.05 x 10^{-5}	1.05 x 10^{-5}
$\mathbf{D_{Ce(IV)}}$ / **cm^2 s^{-1}**	3.6 x 10^{-6}	3.7 x 10^{-6}
$\mathbf{k_0}$ / **cm s^{-1}**	3.8 x 10^{-4}	4.5 x 10^{-4}
α	0.28	0.23

Ag/AgCl	0.53 mM $Ce(SO_4)_2$ 0.5 M $H_2SO_{4(aq)}$	25 mM $K_3Fe(CN)_6$ 25 mM $K_4Fe(CN)_6$ 0.5 M KCl, 0.05 M $HCl_{(aq)}$	Ag/AgCl

Cell 2. Cell used for the study of the kinetic behaviour of the bipolar cell, with an excess of a reversible couple in half-cell (b).

As was discussed for the case of the reversible electron transfer, the relative excess of $Fe(CN)_6^{4-}$ and $Fe(CN)_6^{3-}$ in one half-cell ensured that this compartment acted as a conductor, producing a voltammetric response in the bipolar cell quite similar to that obtained in the conventional three electrode configuration. Figure 107 shows a typical voltammogram obtained in Cell 2, along with the corresponding numerical simulations. Simulations performed assuming a three electrode cell, using the conditions of half-cell (a), are almost identical to that obtained from a bipolar simulation and agree fairly well with the experimental values. The bipolar simulation was performed using a costum-written C program,[xii] similar to that described in Section 3.4.4, for the reversible system, with the incorporation of kinetic parameters to the equations solved.

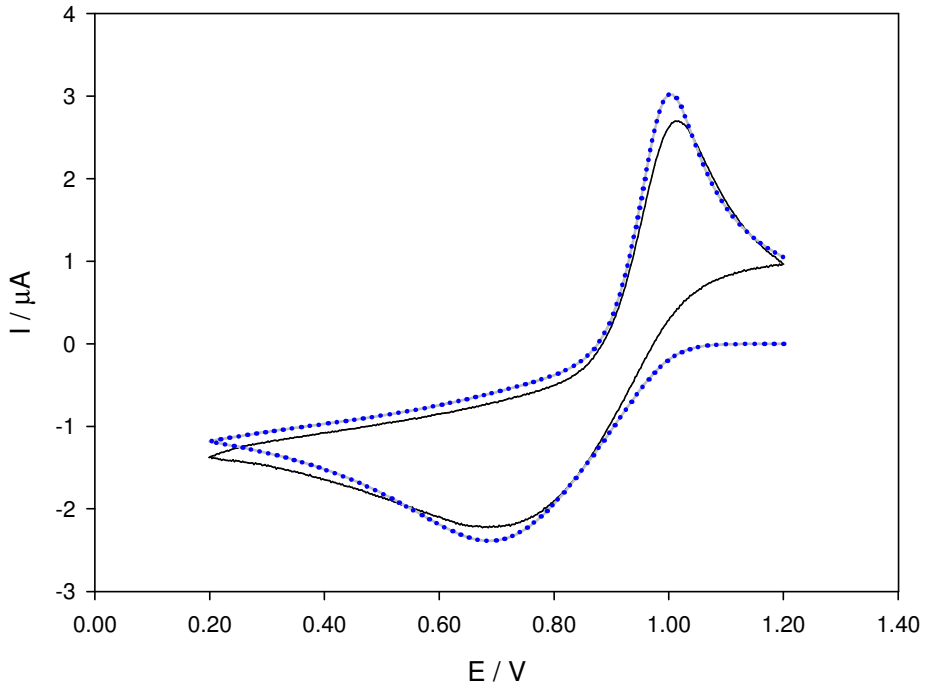

Figure 107. Cyclic voltammogram obtained in Cell 2 (black) at 50 mV s^{-1}. Corresponding three electrode (grey) and bipolar (dotted blue) simulations are also shown.

[xii] The program was written by Dr Fran G.E. Jones, former Postdoctoral Research Associate of the Manchester Electrochemistry Group.

A slightly lower value of the heterogeneous rate constant was obtained in this case (4.0 x 10^{-4} cm s^{-1}), but all other values remained constant. The reduction potential extracted was 0.90 V, which, as expected, corresponds to the algebraic difference between the two redox couples (1.205 and 0.305 V for the cerium and iron species, respectively).

Kinetically hindered redox systems present widening voltammograms as the scan rate is increased.[98] Figure 108 shows the peak separation as a function of the inverse of the square root of the scan rate. A wider range of scan rates was evaluated in the bipolar cell, than in its three electrode counterpart: 5, 10, 25, 50, 75, 100, 125, 150, 175 and 200 mV s^{-1}. Although both numerical simulations slightly under estimate peak separations, they describe the overall trends of the experimental values. The dashed line in Figure 108 represents the simulated values obtained assuming reversibility for the system; the difference between the reversible case and the kinetically-hindered one is evident, ranging between 100 and 400 mV, approximately.

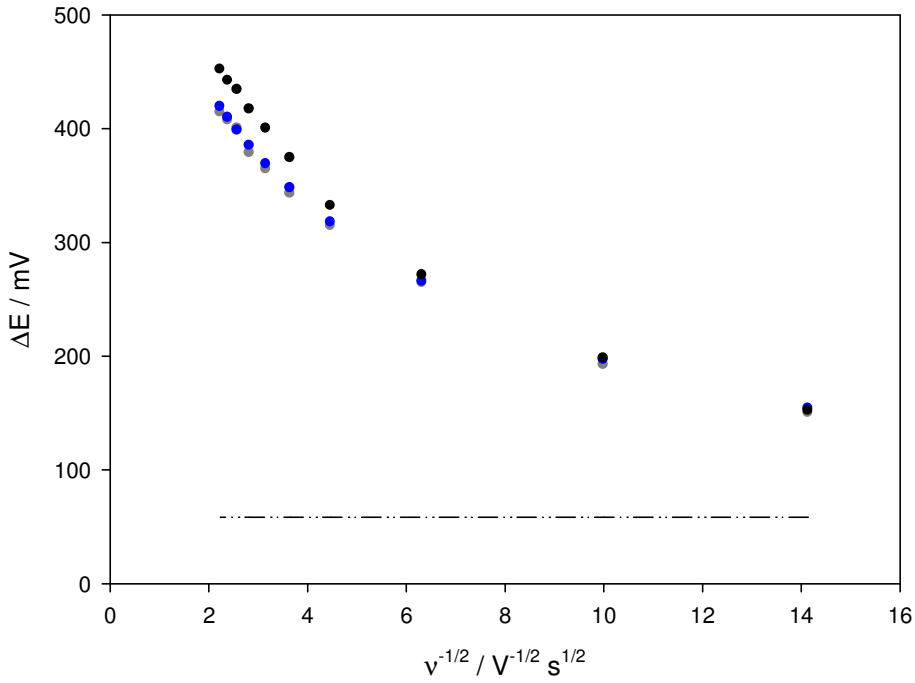

Figure 108. Effect of the scan rate on the peak separation in Cell 2. Experimental (black), three electrode (grey) and bipolar (blue) simulated values are shown. The dashed lines represent the corresponding reversible case, for comparison.

7.2.2 Effect of the Concentration Ratios and the Redox Couples

In Cell 2, half-cell (a) is expected to dominate the voltammetric behaviour of the bipolar cell, as both the mass transport (solute concentrations) and kinetic limitations lie within it. An interesting case is presented in Cell 3, where the concentration ratio between the half-cells approaches unity, while the kinetic limitation remains within half-cell (a).

Ag/AgCl	1.0 mM $Ce(SO_4)_2$ 0.5 M $H_2SO_{4(aq)}$	‖	0.51 mM $K_3Fe(CN)_6$ 0.51 mM $K_4Fe(CN)_6$ 0.5 M KCl, 0.05 M $HCl_{(aq)}$	Ag/AgCl

Cell 3. Cell used for the study of the kinetic behaviour of the bipolar cell, with comparable concentrations of a reversible couple in half-cell (b).

Figure 109 shows the voltammetric response of Cell 3 at 50 mV s^{-1}. The voltammogram appears more "reversible" in this case than in that of Cell 2, with the peaks closer together (see Figure 110), with similar shapes and sizes. Although this behaviour is the opposite of the effect seen in the reversible transfer case (Section 7.1.3), it is also explained by a bigger influence of the reversible couple in half-cell (b) on the overall process.

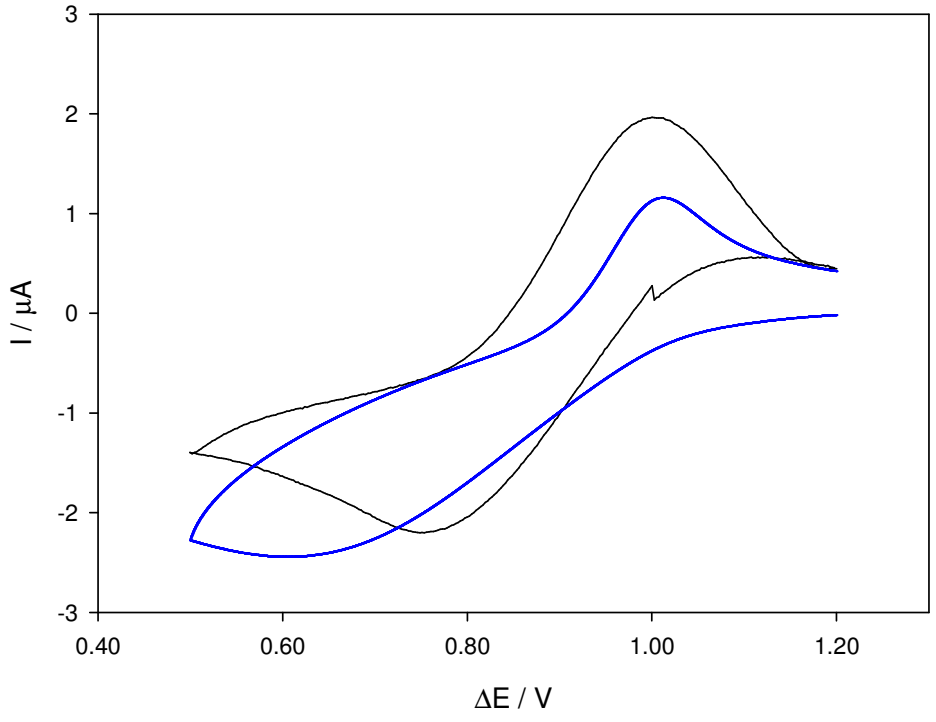

Figure 109. Cyclic voltammogram obtained at 50 mV s^{-1} in Cell 3 (black) with the corresponding simulation (blue).

An attempt was made to simulate the bipolar behaviour using the same parameters obtained in Section 7.2.1, but the prediction did not agree with the experimental observation, as can be seen in Figure 109. This is believed to be due to the fact that the program used to perform the numerical simulations used the kinetic parameters for the overall process, rather than for the couple in half-cell (a). In other words, the unequal transfer coefficient and k^0 values were not applied to the electron transfer of the cerium(III)/cerium(IV) couple to and from the electronic conductor, but to the bipolar reaction as a whole. The fact that the effect of wrongly applying the kinetic parameters to the overall process was not observed in the comparison between simulations and experiments for Cell 2, confirms once more that in the case of such excess of concentrations in half-cell (b) the behaviour is completely dominated by half-cell (a); although the kinetic parameters were applied to the overall process in the simulation, the resulting voltammograms coincided with the experimental ones.

A look at the effect of the scan rate on the peak separation (see Figure 110) clearly indicates a less pronounced increase in the range of scan rates studied, than in Cell 2 (Figure 108). The inadequacy of the model used to perform the numerical simulations is highlighted here by the much higher peak separations predicted throughout all the scan rates studied.

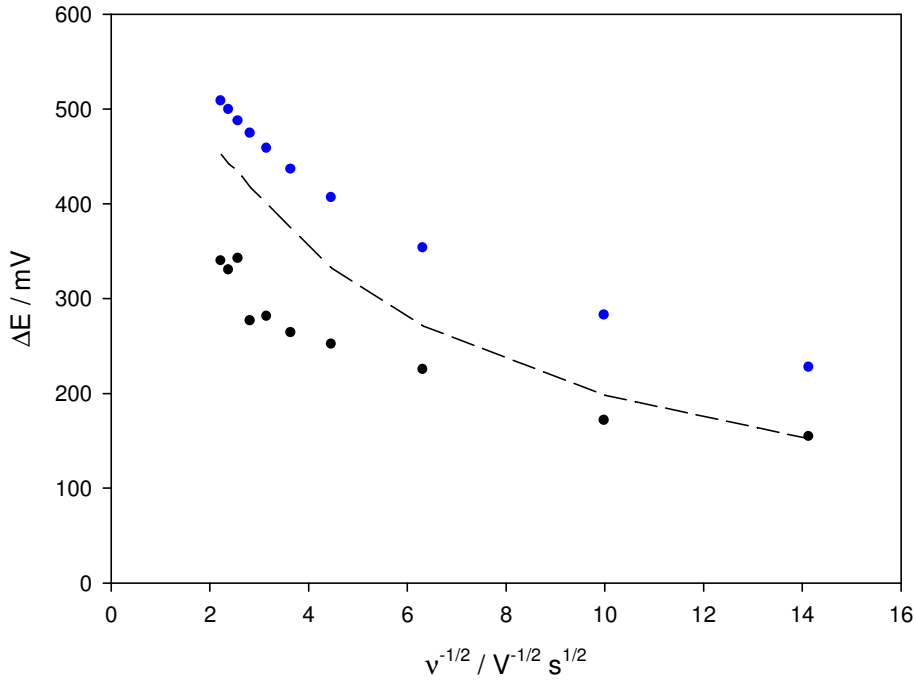

Figure 110. Effect of the scan rate on the peak separation in Cell 3. Experimental (black) and simulated (blue) values are shown. Dashed line: experimental results using Cell 2.

Although it is evident that a better model is needed to predict the kinetic voltammetric behaviour of the bipolar cell, these preliminary studies demonstrate that it can be a useful tool in the study of kinetic systems. It could have advantages over the three electrode configuration, such as the widened potential window; in some cases, such as the cerium compound studied, the redox potentials are very close to the edge of the experimental potential window in the conventional cell, yet the voltammograms are much less susceptible to the influence of the electrolyte solution in the bipolar case.

The effect of k^0 and α might be more easily resolved by using the bipolar cell. The possibility of studying the kinetic system versus different redox systems, such as reversible couples or even the same quasi-reversible system, for example, might facilitate the extraction of each kinetic parameter separately. Figure 111 shows the difference between an excess of the cerium(III/IV) couple and the ferro- and ferricyanide couple in half-cell (b), while maintaining a low concentration of cerium(III) sulfate in half-cell (a). The effect of kinetics in half-cell (b) is seen through small changes in the voltammetric behaviour, even for relatively high concentrations; lowering the concentrations in half-cell (b) would

likely lead to more significant changes between the use of ferro/ferricyanide or the cerium system in said half-cell.

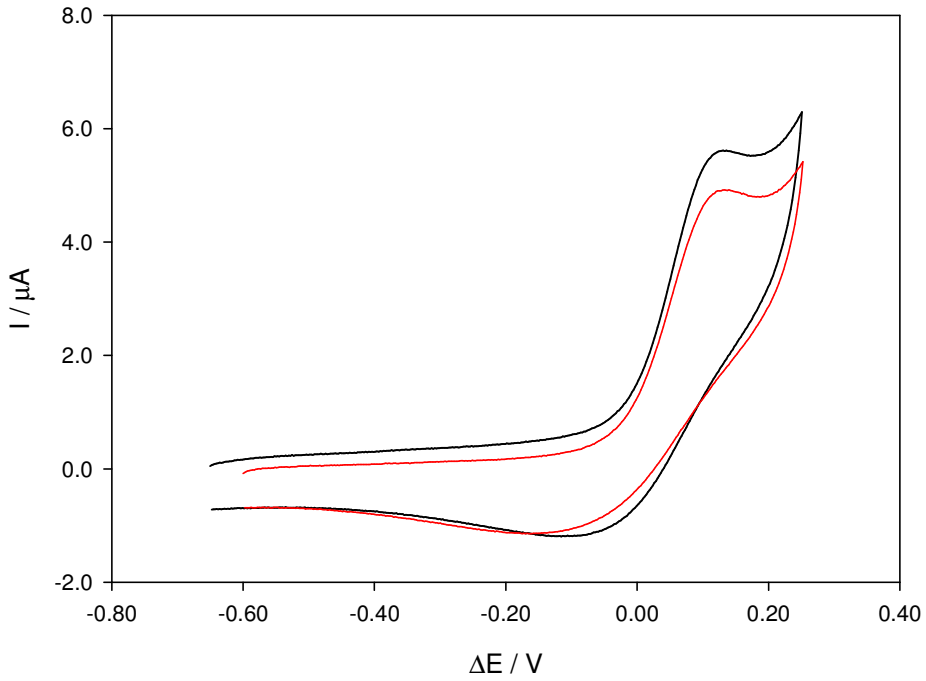

Figure 111. Cyclic voltammograms of 0.5 mM $Ce_2(SO_4)_3$ at 50 mV s^{-1} in the bipolar cell with an excess of ferrocyanide/ferricyanide (black) and cerium(III/IV) (red) in the other half-cell. The potentials for the black curve were corrected by subtracting the difference in standard potentials for comparison purposes.

7.3 Electroless System

Having characterized the bipolar cell using chemically simple systems, it was then used to study the Copper-DMAB electroless system. In order to do this, each half reaction (copper deposition and DMAB oxidation) was first studied using a reversible couple (ferrocyanide and ferricyanide) in the opposite half-cell. The full electroless system was then studied, taking into account the effect of the potential range studied, the deposition surface and the effect of other components of the electroless bath.

7.3.1 Copper Deposition

Copper deposition was studied using Cell 4, the electrodes and connections were as described in Sections 7.1.1 and 7.1.2. In contrast with usual electroless baths, a low pH was initially used in order to simplify the system, by avoiding the use of buffers and complexing agents; a typical copper electrodeposition solution was used instead.[151] Figure 112 shows the comparison between the behaviour observed in equivalent three electrode and bipolar cells, with an excess of the iron-containing species (x = 25); the corresponding three electrode cell conditions were those of the left-hand side of Cell 4. In the figure, the reduction of the Cu(II) ions can be seen as a peak with negative currents in the forward scan, while copper oxidation is evident through the stripping peak observed at potentials just negative of -0.20 V.

Ag/AgCl	0.55 mM $CuSO_4$ 0.5 M Na_2SO_4, 0.05 M $H_2SO_{4(aq)}$	‖	x mM $K_3Fe(CN)_6$ x mM $K_4Fe(CN)_6$ 0.5 M KCl, 0.05 M $HCl_{(aq)}$	Ag/AgCl

Cell 4. Electrochemical cell used for the study of copper deposition in the bipolar cell.

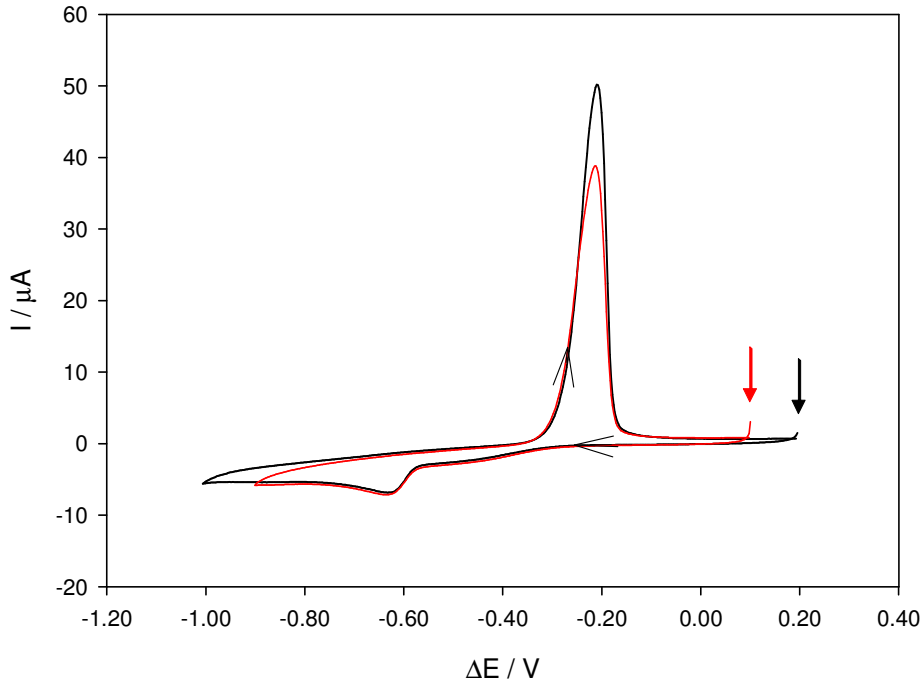

Figure 112. Cyclic voltammograms of copper deposition at 50 mV/s in Cell 4, with x = 25 (black), and the corresponding three electrode cell (red). The initial sweep direction was negative; the arrows indicate the starting point.

The potential for the three electrode cell was modified by subtracting the standard potential of the ferrocyanide/ferricyanide couple (see Table 19). Although copper electrodeposition is not a diffusion-limited, reversible system, it still presents similar behaviour in both the conventional and bipolar configurations. The only difference observed between the two voltammograms in Figure 112 is a smaller stripping peak in the three electrode cell, simply due to a less negative vertex potential on the forward scan.

Although the results obtained as the concentration ratio is varied cannot be predicted with the numerical simulations available at present, preliminary experiments for the case of similar concentrations of the three reactants were performed and are presented in Figure 113. In this case the concentration of the iron-containing species was lowered to 1.0 mM.

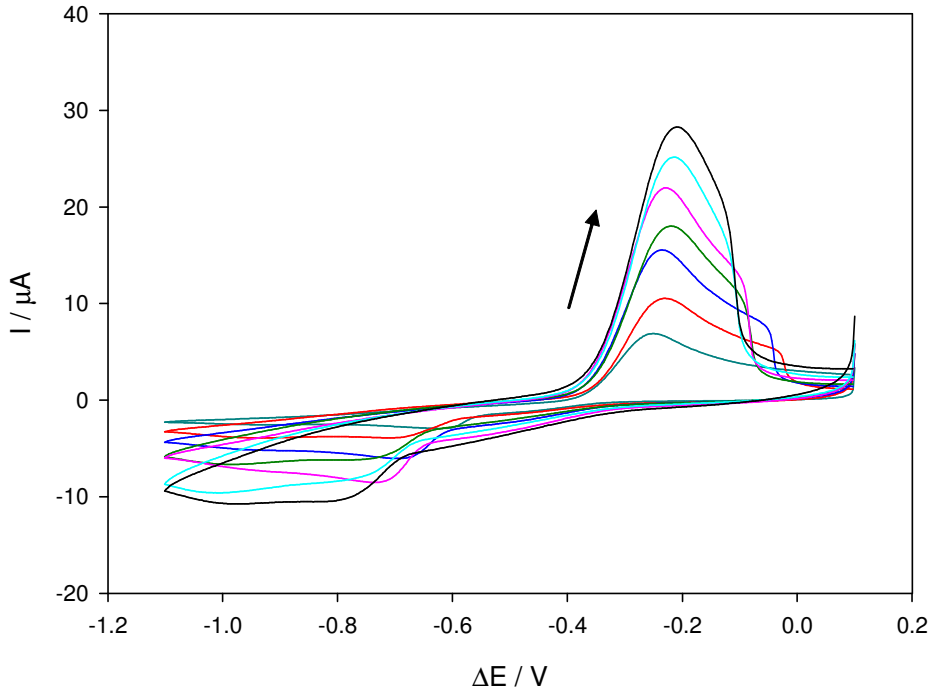

Figure 113. Cyclic voltammograms obtained in Cell 4, with the concentrations of ferrocyanide and ferricyanide (x) lowered to 1.0 mM. The scan was initially in the negative direction, starting at 0.10 V. The arrow indicates increasing scan rate.

In Figure 113, the stripping peak is broader than in Figure 112; it presents a shoulder which can usually be seen in copper electrodeposition systems that stabilize the Cu(I) ion.[151] The pre-peak observed before the Cu(II) reduction can also be explained by stabilization of Cu(I). Although the solution in the copper

half-cell does not stabilize the Cu(I) ion under conventional conditions,[151] the relative amount of reactants in the other half-cell, combined with the fact that the copper reaction involves two electrons, can explain this behaviour. As the reaction is partially limited by the mass transport of the iron-containing species, enough electrons are not immediately available for a two-electron transfer, making the voltammetric features of two one-electron reactions apparent.

The system is interesting because of its apparent ability to stabilise Cu(I). It could also be used in aiding the understanding of metal deposition on semiconductors; similarities arise from the unavailability of a sufficient charge carrier density, under certain conditions, for a multi-electron reaction. On semiconductors, this can result in the stepwise reduction of metal ions, or the deposition on sites with different energy.[97,152]

7.3.2 DMAB Oxidation

DMAB oxidation was studied in the bipolar cell using Cell 5, with electrodes and connections as described in Sections 7.1.1 and 7.1.2. A gold working electrode was used in the DMAB compartment (half-cell (a)), however, as the glassy carbon surfaces used in the foregoing bipolar cells are known to be non-catalytic towards DMAB oxidation (see Section 4.2.1).

Ag/AgCl	x mM DMAB 0.7 M $KOH_{(aq)}$	||	25 mM $K_3Fe(CN)_6$ 25 mM $K_4Fe(CN)_6$ 0.5 M KCl, 0.05 M $HCl_{(aq)}$	Ag/AgCl

Cell 5. Typical electrochemical cell used for the study of DMAB oxidation in the bipolar cell.

A comparison between the voltammetric response using gold and glassy carbon WE in half-cell (a), the DMAB compartment of Cell 5, can be seen in Figure 114. The prominent features observed in the voltammogram obtained with a gold electrode (black solid line) disappear when a GC electrode is used (dashed gray line). These peaks were assigned as gold oxidation (O), on the positive scan, and gold oxide reduction (R), in the reverse scan, hence their disappearance with the use of a glassy carbon electrode. This assignation was confirmed by removing

DMAB from the cell (dashed blue line); in this case, although the potentials shifted slightly, the same main peaks are observed.

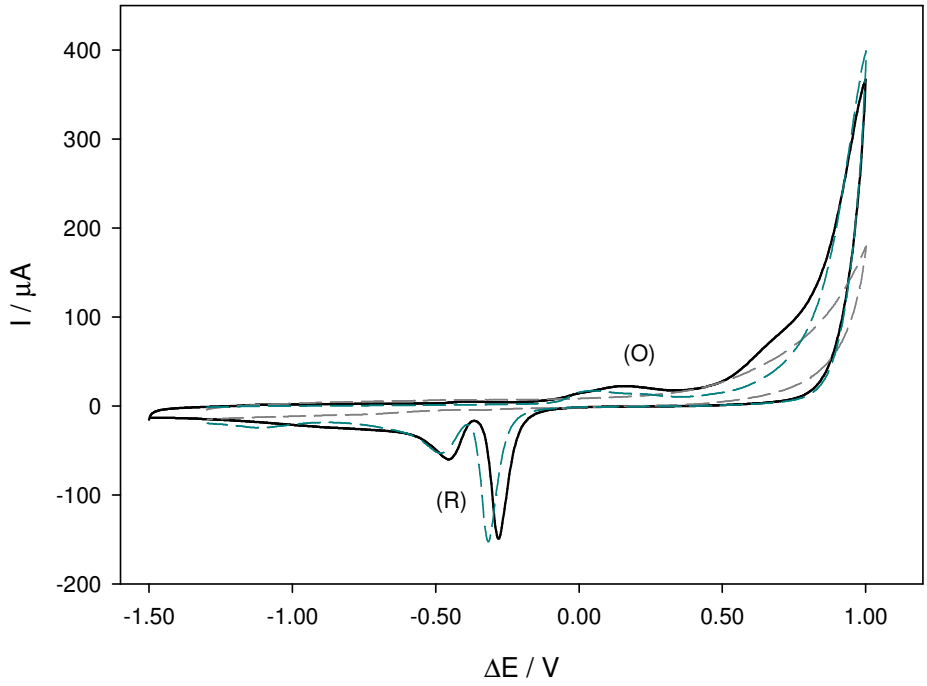

Figure 114. Voltammograms obtained in Cell 5 at 200 mV s^{-1}. Black solid line: x = 0.3, dashed blue line: x = 0, and dashed gray line: x = 0.3 (glassy carbon WE). (O) and (R) denote the formation and reduction of gold oxide.

In order to study the oxidation of DMAB, the potential window was restricted to the negative potential region, where the gold oxide formation was avoided; Figure 115 shows the voltammetric behaviour obtained. The characteristic irreversible oxidation of DMAB on gold is observed in the bipolar cell, with a prominent peak at -1.1 V, followed by non-zero “steady” current. Consecutive scans have similar shapes, but lower currents, as seen in the conventional three electrode cell (Section 4.3.1).

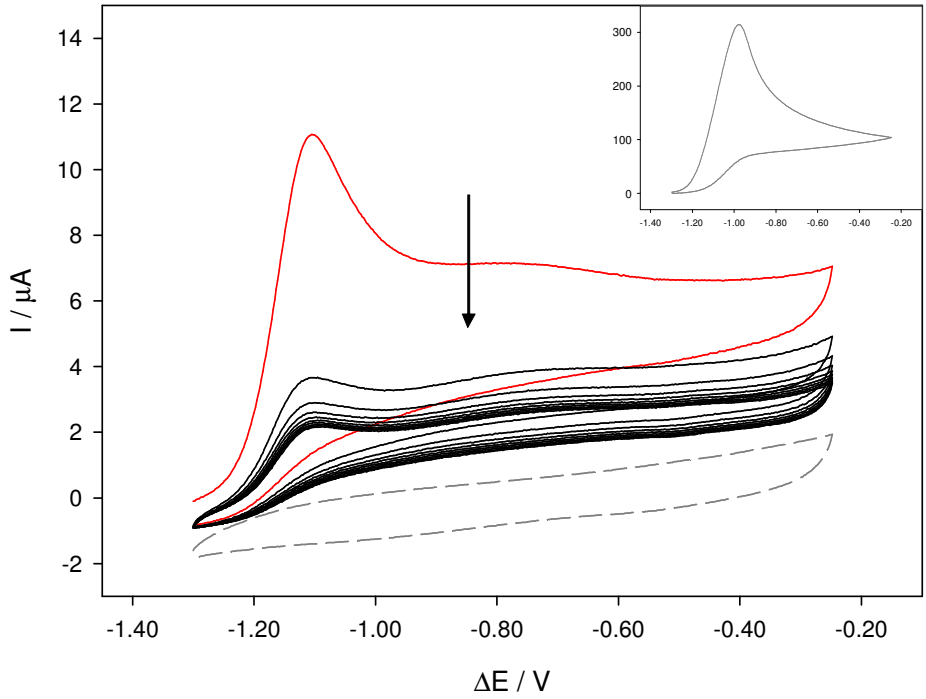

Figure 115. DMAB oxidation in the bipolar cell (Cell 5, x = 0.3). Consecutive scans, at 200 mV s^{-1}, are shown, with the first one marked in red. The sweep direction was initially positive, starting at -1.30 V. Dashed grey line: x = 0. Inset: x ~ 8.0.

The assignation of the peak at -1.1 V as DMAB oxidation was confirmed by removing DMAB from the cell (x = 0 in Cell 5); the voltammogram obtained in this case was basically featureless (dashed gray line). The inset of Figure 115 shows the voltammetric behaviour at higher concentrations of DMAB, which shows the expected proportional increase in peak current due to the increase in concentration. The current magnitudes observed in Figure 115 are also in agreement with those obtained in the conventional three electrode cell (see Section 4.3), as expected for the excess concentration of ferro- and ferricyanide used in Cell 5.

The peak potential observed corresponds to approximately -0.8 V vs. Ag/AgCl in the three electrode cell, once the correction for the ferrocyanide/ferricyanide redox potential is made; this potential is consistent with that observed in the three electrode cell (see Figure 18, for example).

7.3.3 The Copper-DMAB System

In order to study the copper-DMAB system, typical of an electroless plating bath, Cell 6 was used. Electrodes and connections were as previously described, with the DMAB solution placed in half-cell (b). In this case, all additives were avoided, to simplify the system. Potassium hydroxide was used in both half-cells, both to produce the necessary pH and to act as supporting electrolyte. In the copper-containing half-cell, 1,5,8,12-tetraazadodecane was added in order to complex the copper ions, which are otherwise unstable at high pH.[9]

Ag/AgCl	x mM $CuSO_4$ 1.5 mM 1,5,8,12-tetraazadodecane 0.7 M $KOH_{(aq)}$	||	10.0 mM DMAB 0.7 M $KOH_{(aq)}$	Ag/AgCl

Cell 6. Electrochemical cell used for the study of the Copper-DMAB system in the bipolar cell.

Ten consecutive voltammograms obtained in Cell 6, at 50 mV s^{-1}, can be seen in Figure 116, where the first one is marked in red and the arrow indicates the decrease in current with continuous cycling. A negative peak due to copper reduction is present just positive of 0.2 V. A voltammogram in the absence of copper in half-cell (a) is also shown (dashed grey), and confirms the assignation of the peak, as it is not present in this case.

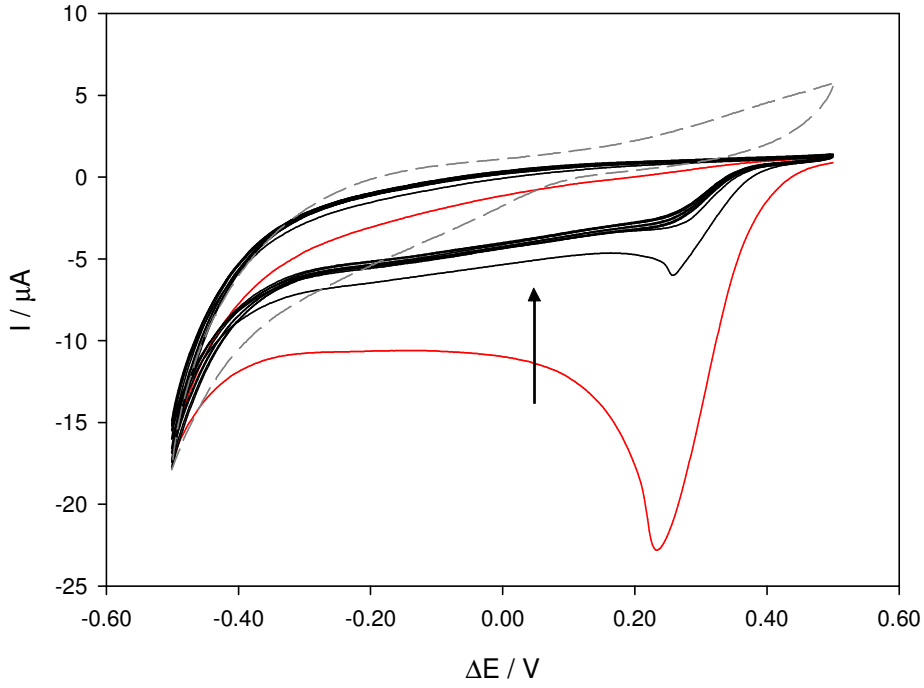

Figure 116. Consecutive cyclic voltammograms obtained at 50 mV s^{-1} in Cell 6 (x = 1.0); the first scan is marked in red and the arrow shows the trend observed. The potential was swept in a negative direction first, starting at 0.50 V. The dashed grey line corresponds to x = 0.

The reduction of the copper complex is driven by the oxidation of DMAB in the other half-cell, producing the typical decrease of current in consecutive scans expected from the DMAB voltammetric behaviour (see Section 7.3.2). The potential of the peak is also in agreement with that expected from the algebraic sum of the redox potentials of DMAB and the copper complex in highly alkaline conditions; as stated in Section 7.3.2, the peak potential of DMAB is approximately -0.8 V vs. Ag/AgCl, while the copper complex peak appears just negative of -0.60 V vs. Ag/AgCl in a conventional three electrode cell (see Section 6.1). The positive potential of the DMAB-induced copper reduction indicates it is a spontaneous process, which is consistent with the use of the system as an electroless plating bath.

Extending the potential window towards more positive potentials produces the voltammograms seen in Figure 117. In this case the arrow indicates the starting potential. The potential was initially swept in the positive direction, producing a featureless voltammogram until copper reduction potentials were achieved, below 0.50 V. In the second scan, however, a positive current is observed which is attributed to the re-oxidation of the copper deposited in the first

scan. As the oxidation of DMAB is irreversible,[33] this process is thought to be coupled to hydrogen evolution in half-cell (b).

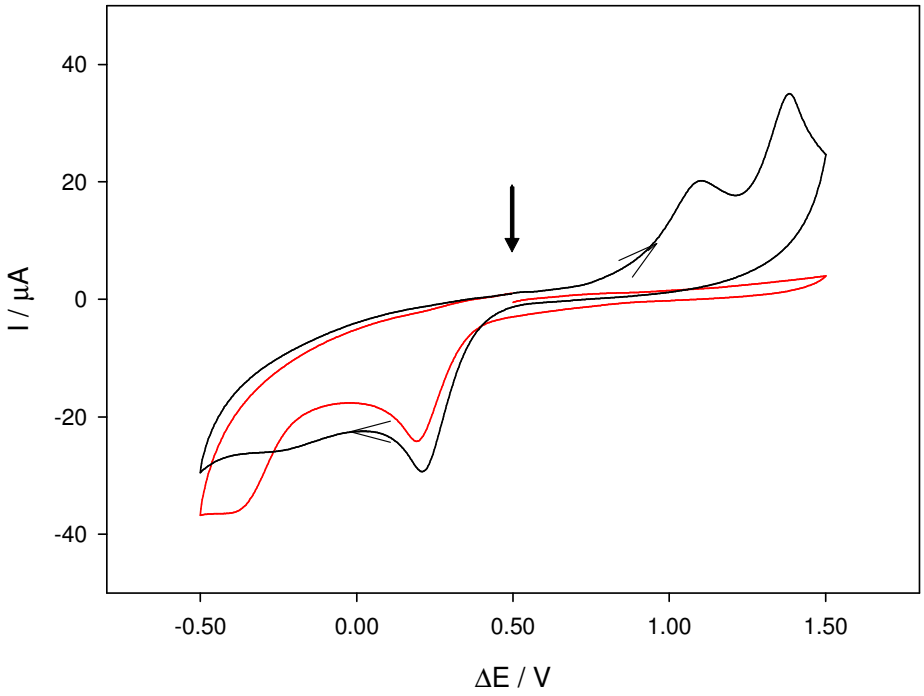

Figure 117. Cyclic voltammograms obtained in Cell 6 (x = 1.0), at 200 mV s^{-1}. The first scan is marked in red. The bold arrow indicates the starting potential; the initial direction was positive in potential.

Further widening of the potential window, towards more negative values in this case, can be seen in Figure 118. In addition to the peaks seen in Figure 117, the characteristic voltammetric behaviour of DMAB oxidation is clearly observed at potentials below -0.50 V; the only marked difference with respect to the three electrode cell behaviour is the potential of the reactivation peak with respect to the rest of the voltammogram (see Section 4.3). This, however, is probably due to the coupling to different reactions in the other half-cell.

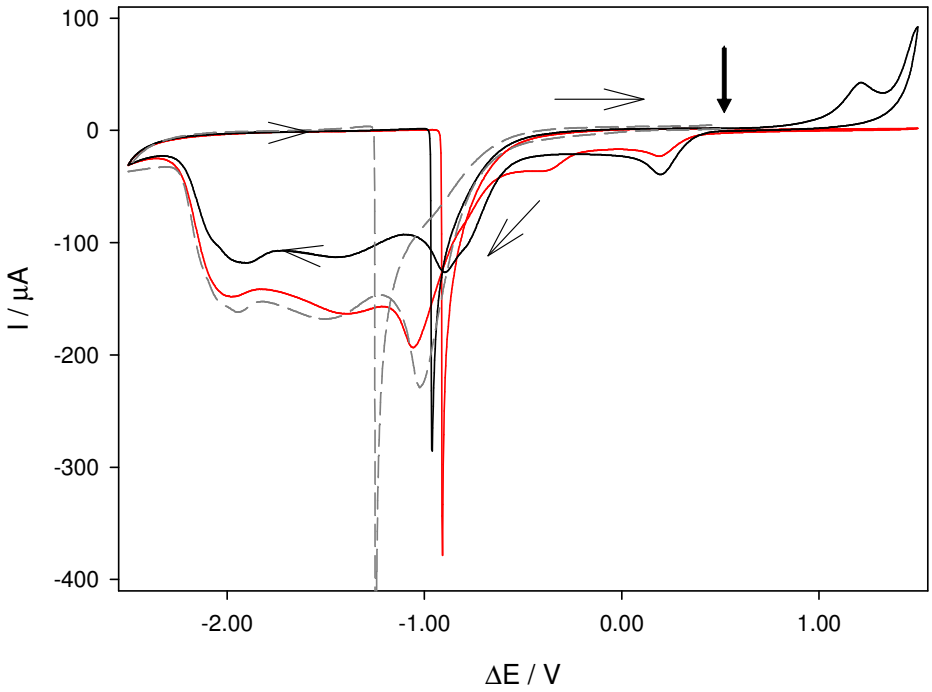

Figure 118. As in Figure 117, with a wider potential window. The dashed grey line was obtained in the absence of $CuSO_4$ (x = 0).

The further appearance of the DMAB voltammetric features is most likely driven by hydrogen evolution in the copper-containing half-cell; this was studied by removing $CuSO_4$ from Cell 6. The voltammogram obtained (dashed grey line) is similar to that seen in the presence of copper, but without the peaks due to the copper reduction and oxidation, at approximately 0.20 and 1.20 V, respectively. Again the only clear difference is the position of the reactivation peak, which confirms that its position is dependent on the coupling with reduction reactions in half-cell (a).

Further confirmation of the hydrogen evolution reaction driving the DMAB oxidation was obtained by substituting half-cell (a) of Cell 6 with a 0.5 M solution of sulfuric acid. As expected for acidic conditions, the potentials shifted towards less negative values, *i.e.* the reaction is more favourable, and the currents increased in comparison to the alkaline case.

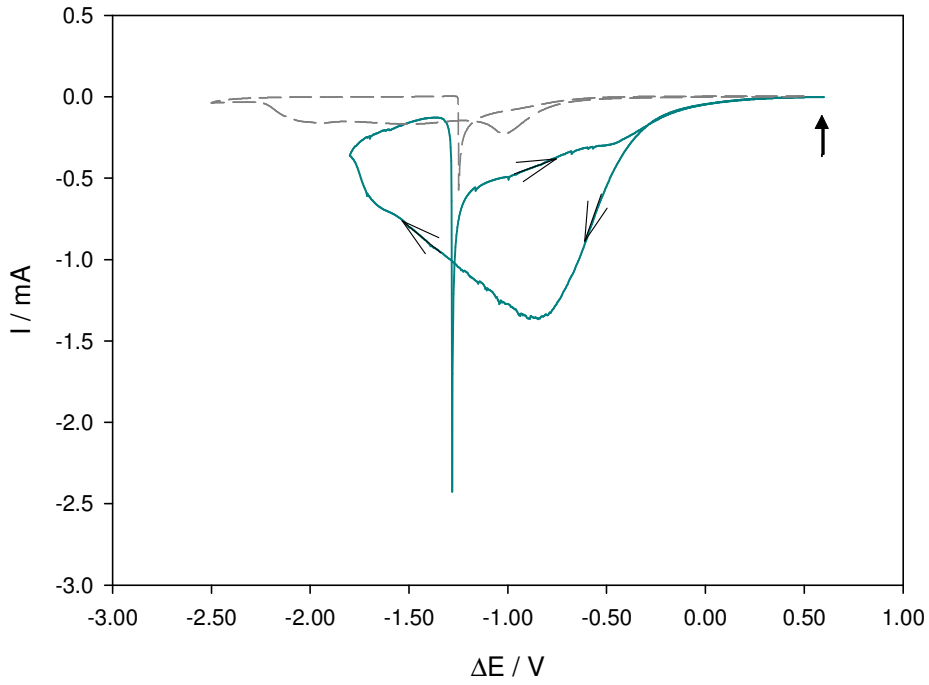

Figure 119. Comparison between acidic (solid blue) and alkaline (dashed gray) conditions in half-cell (a) of Cell 6, at 200 mV s^{-1} and x = 0. The bold arrow indicates the start potential; the scan is initially in the negative direction.

In a typical electroless bath, the reduction of the copper complex and the oxidation of DMAB occur on the same surface, thus a gold WE was introduced in the copper-containing half cell *in lieu* of the GC. Figure 120 shows a comparison between the voltammograms obtained in Cell 6, in the presence of copper, with glassy carbon and gold working electrodes in half-cell (a). The overall behaviour is similar in both cases, with only a few differences observed. The potential of the copper reduction peak is more positive on the gold surface, in agreement with the behaviour of the corresponding three electrode cells. This is not surprising as the overpotential needed for metallic nucleation on GC is usually higher than on metallic substrates.[146]

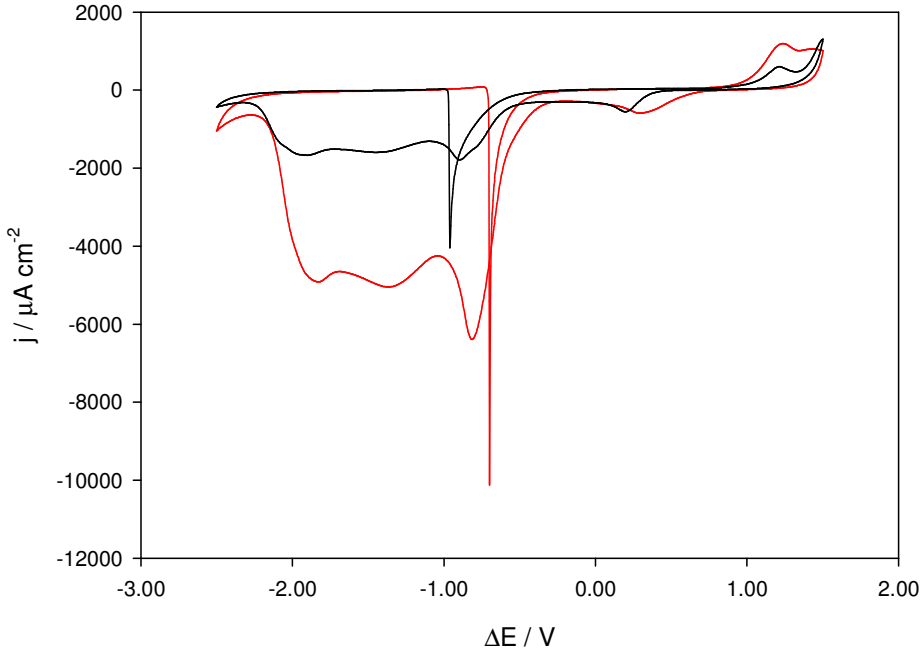

Figure 120. Cyclic voltammograms obtained in Cell 6 (x = 1.0), at 200 mV s^{-1}, with gold (red) and glassy carbon (black) electrodes in the copper-containing half-cell.

The currents densities are higher on the gold surface than on the glassy carbon, particularly in the potential region corresponding to the DMAB related features. This can be explained by gold being more catalytic toward hydrogen evolution, the corresponding reaction in half-cell (a), than carbon surfaces; glassy carbon electrodes being particularly poor catalysts for the hydrogen evolution reaction.[153,154]

7.4 Conclusions

The use of the bipolar cell allows the investigation of bimolecular electron transfer. The behaviour of excess concentrations of both forms of a reversible redox couple in one half-cell, as a perfect conductor was confirmed not only when coupled with reversible electron transfer, but also with kinetically hindered systems and metal deposition systems. Comparison with the corresponding three electrode cells showed almost identical wave shapes in all cases: the potentials could be easily converted by the algebraic sum of the redox potentials of the individual couples. These cells therefore correspond to the relevant three-

electrode cell with the fero/ferricyanide redox couple acting as a solution phase reference electrode.

The changes observed in the wave-shape and potentials with the relative concentration ratios of reversible couples on both half-cells, which at first glance would indicate kinetic influences, are simply due to the effect of the mass transport and bulk concentrations of each of the different species involved. The relative importance of their concentrations and mass transport changes the voltammetric behaviour, while the kinetics of the electron transfer remains unchanged.

The two-phase numerical model yielded good agreement with experimental data, in the case of reversible systems; this agreement proved, amongst other things that cell resistance does not have a significant influence on the voltammetric behaviour observed. A more complex model is needed for the kinetically hindered systems, however; a model that allows for different kinetic constants and transfer coefficients for each half-cell would represent more faithfully the systems studied.

The bipolar cell has potential not only as a tool for investigating the kinetics of different redox reactions, but also multi-electron transfer reactions. The study of the deposition of copper by reduction of Cu^{2+} ions, indicates the possibility of separating the transfer of each individual electron by changing the relative concentrations of the other half-cell.

A first approximation to the study of electroless deposition systems was made. The usefulness of the bipolar cell in studying the “coupling” effects between the half-reactions, as well as the effect of the substrate on the separate oxidative and reductive processes, was shown. The possibility of identifying side reactions of the process was also demonstrated. This last point is important as such reactions might influence the efficiency of the plating process.

8 Electroless Copper Deposition

This chapter describes a comprehensive study of the electroless deposition of copper, on gold substrates, using DMAB as a reducing agent.[xiii] The typical electroless bath composition is described by Bath 1, although throughout the study certain conditions were changed and will be detailed accordingly. The 1,5,8,12-tetraazadodecane was employed as a complexing agent for the copper(II) ions and triethanolamine (TEA) was added to control the pH, which was adjusted to 11.6 using potassium hydroxide and sulphuric acid as needed.[9,147] The temperature was kept constant at 55.0 ºC (±0.5 ºC), using a thermostatic water bath. Unless otherwise stated, the pH and temperature were unchanged through the study.

0.065 M DMAB 0.030 M Copper Sulfate 0.3 M Triethanolamine 0.045 M 1,5,8,12-Tetraazadodecane	Au

Bath 1. Typical electroless bath used for copper deposition.

The deposition kinetics of the bath were studied, through the measurement of deposit thicknesses at varying deposition times. A simple and effective way of measuring the thickness of the deposits was found in electrochemical anodic stripping. The influence of bath composition and mass transport on the kinetics was investigated.

A galvanic cell configuration (described in Section 3.3.4) was used to study the interdependence of the anodic and cathodic processes and the resulting influence on deposition kinetics. The effect of the catalytic substrate was examined using this set-up, while it also allowed the open circuit potential and faradaic efficiency to be investigated. A study of the effect of TEA on the half-reactions constituting the electroless deposition system was also performed.

[xiii] Some of this work has been published in Langmuir and is partly copyright of the American Chemical Society (in particular some of the figures). See Appendix A for more details.

The morphology, crystal structure and purity of deposits obtained through the variations of the plating conditions were characterized using surface techniques such as AFM and XRD, as well as micro analytical methods.

8.1 Thickness Measurements

In order to study the kinetics of the copper-DMAB electroless system, copper was deposited onto gold and the thickness of the deposits were measured. The plating rates were then determined through the study of the thickness as a function of deposition time.

Traditionally electroless deposition rates and/or thicknesses have been measured using gravimetric methods (comparing the weight before and after deposition) or calculated using the mixed potential theory.[10,25,32,89] Although these approaches are still widely used, other methods have been employed more recently such as profilometry, QCM and electrochemical impedance.[19,38-40] In the present work, two different methods were used to measure the deposit thicknesses: electrochemical stripping and atomic force microscopy.

8.1.1 Electrochemical Stripping

The copper-covered electrodes were transferred from the deposition bath to a three-electrode cell filled with 0.1 M H_2SO_4. The copper was completely removed from the surface by applying a potential of 0.45 V vs. Ag/AgCl for 180 s (60 s were used on samples deposited for less than one minute).[155] Typical chronoamperometric responses obtained during the anodic stripping process can be seen in Figure 121.

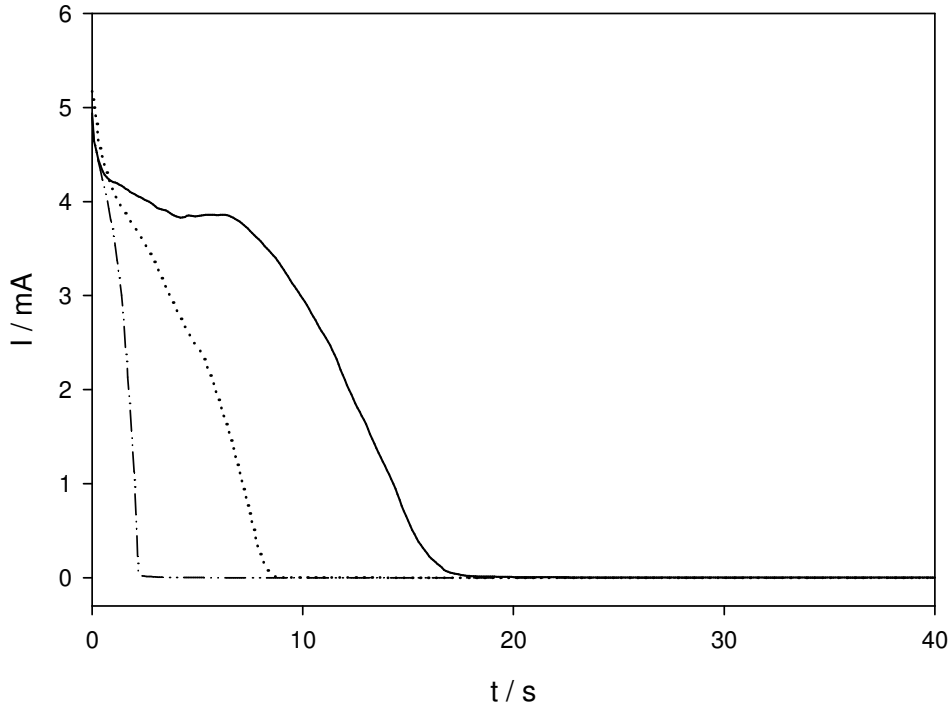

Figure 121. Representative anodic stripping chronoamperograms for deposits obtained from immersion in Bath 1 for 2, 5 and 10 minutes (dashed, dotted and solid lines, respectively).

The charge transferred during each potential step was obtained directly from the Autolab potentiostat software (GPES) and was used to calculate the number of moles of copper deposited, using the Faraday equation (Equation 44). The thickness of the deposits was obtained knowing the number of moles and the area of the electrode, assuming homogeneous films with the properties of metallic copper.[130] The volume of the deposit was obtained by multiplying the number of moles by the copper atomic mass and dividing that by its density. The result was then divided by the electrode area to obtain the thickness of the copper film.

8.1.2 Atomic Force Microscopy (AFM)

Samples for AFM measurements were prepared on gold foils, previously cleaned by submersion in dilute nitric acid and mechanical polishing (as described for gold working electrodes in Section 3.2.3). The foils were partially covered with nail varnish so deposition only took place on part of the surface. A step edge was produced between the gold and the copper surfaces, once the varnish was removed with acetone after electroless copper deposition (see Figure 122). The film thicknesses were measured with the atomic force microscope across the

gold/copper interface for at least five points of each sample and average values were taken.[xiv] Figure 122 shows a representive AFM image of a two minute copper deposit on a gold substrate, using Bath 1.

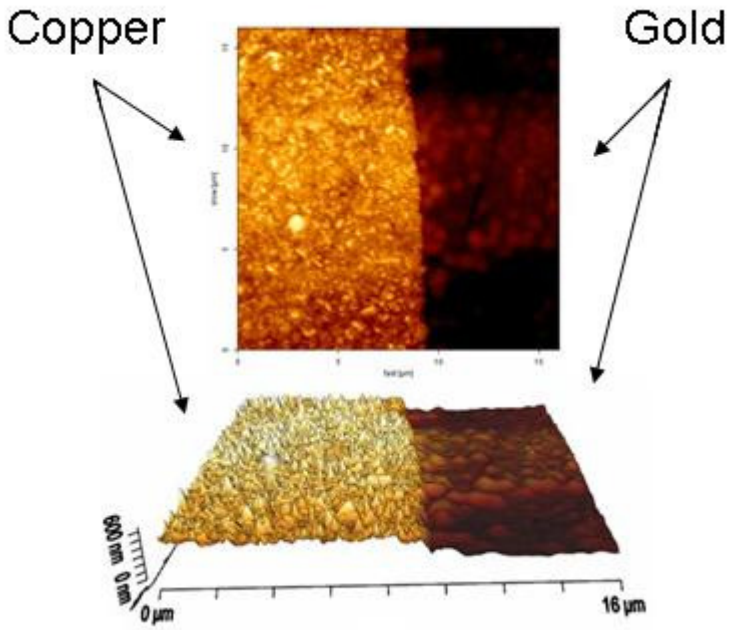

Figure 122. AFM image of a copper deposit (left) on a gold surface (right) obtained using Bath 1 for two minutes. Both a top view (upper) and a cross section (lower) are shown.

8.2 Electroless Bath Kinetics

The kinetics of the electroless deposition of copper were firstly studied by the deposition of copper onto gold electrodes by immersion in Bath 1, for varying amounts of time, ranging from ten seconds to half an hour. Once deposits were obtained, anodic stripping was performed and the amount of copper deposited was calculated. Figure 123 shows the number of moles of copper deposited for immersions between ten seconds and two minutes in Bath 1; in this case the thicknesses were not calculated as detailed in Section 8.1.1, as a homogeneous coverage cannot be easily assumed at such short times. Although the values obtained could indicate up to 2 or 3 monolayers of copper atoms on the gold surface, due to the nature of the nucleation process occurring, it is likely that

[xiv] AFM measurements were made by Dr Samson N. Patole, former Postdoctoral Research Associate of the Manchester Electrochemistry Group.

initially small copper clusters are formed that eventually grow and coalesce to form a continuous film; copper is known to initially form multiple three-dimensional clusters even on perfectly smooth single crystal surfaces.[30] The use of *in-situ* scanning tunnelling microscopy has proven, for example, that the electrodeposition of copper on polycrystalline and single-crystal gold surfaces occurs via instantaneous nucleation with 3D growth, forming islands on the surface.[156,157] To avoid making unsupported assumptions of homogeneity, the number of moles was used at short times *in lieu* of the deposit thickness.

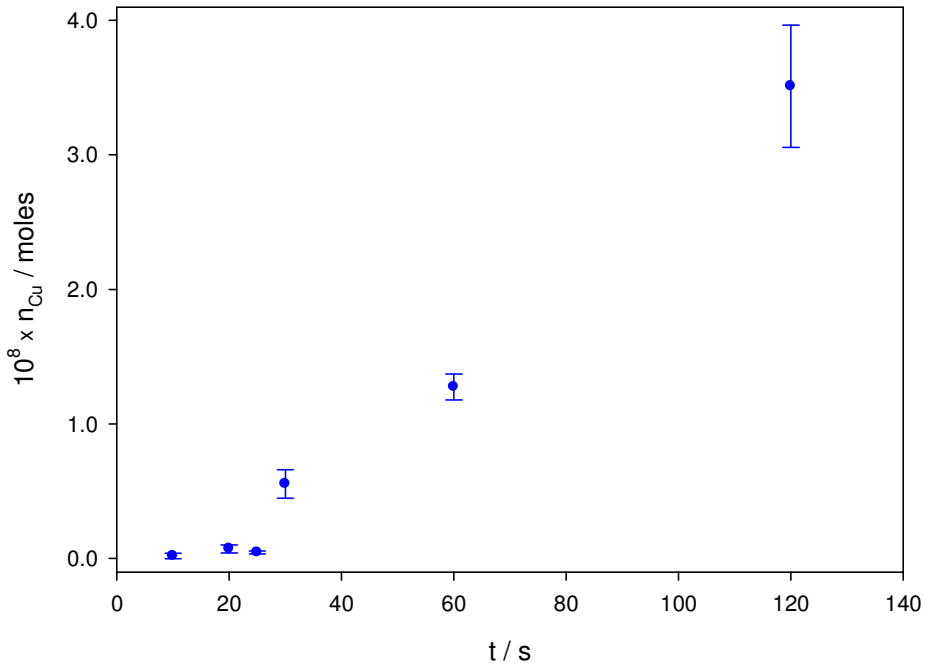

Figure 123. Moles of copper deposited from Bath 1 at short times.

Deposition at short times was not very reproducible and an average of six experiments is represented by each data point in the graph (with the standard deviations shown through error bars). A clear break between 25 and 30 seconds can be seen in Figure 123, however, which indicates that an induction time of approximately 30 s exists. The sharp increase in deposition after this time can be explained by an initially slow and random nucleation of copper on the gold substrate. Initial kinetic difficulties in the formation of a new phase on the substrate, as well as lower catalytic activity of the initial substrate in comparison to the metal being deposited, have been suggested as possible explanations for the induction times seen in electroless deposition.[10,86] It is also possible that the change in deposition rate is partly due to the change in mass transfer regime, as

natural convection and that produced by gas evolution start to play an important role in the system; the effect of convection will be discussed further on.

After the induction period, a linear trend is seen, which was investigated further by examining deposits at longer immersion times; a range from one minute to half an hour was studied and in this case deposit thicknesses were calculated. The results can be seen in Figure 124, where again each data point represents the average of six individual experiments and reproducibility greatly improved over that seen at shorter times; the standard deviations of the measurements are presented as error bars in the graph. A linear trend was confirmed (blue dashed line in the graph) and a steady deposition rate of 0.052 ± 0.003 µm min^{-1} was calculated. This value is comparable to values reported in the literature for different copper plating baths. Values from 0.02 to 0.12 µm min^{-1} have been quoted for typical electroless copper baths, using formaldehyde as a reducing agent, a number of which report rates close to 0.06 µm min^{-1}.[23,28,30,158] Baths that use DMAB as a reducing agent, on the other hand, have been reported to plate at rates between 0.01 and 0.7 µm min^{-1}, with values mainly centred around 0.04 µm min^{-1}.[9,19,92]

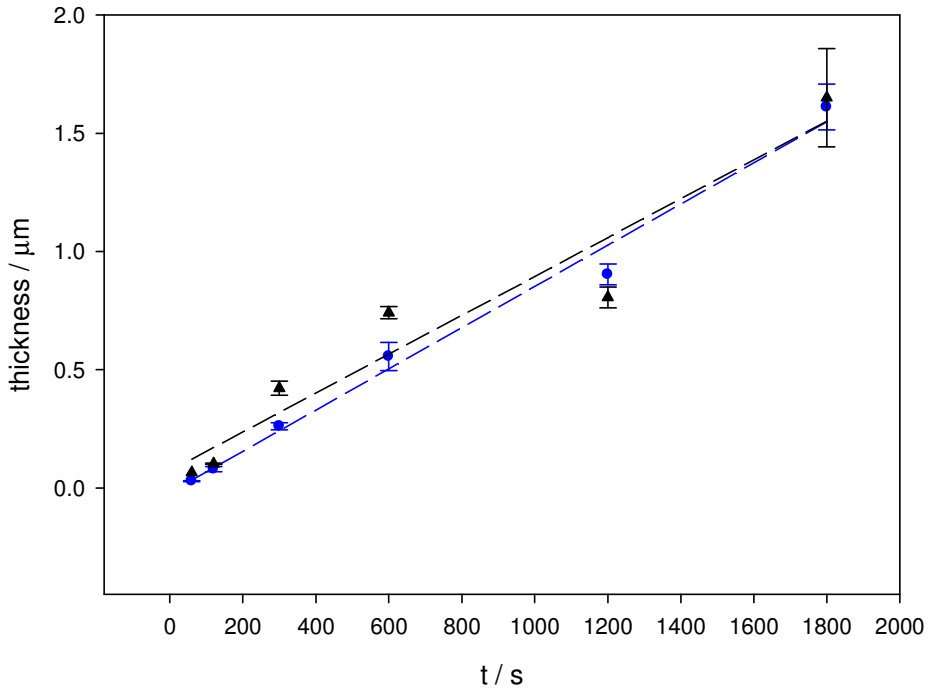

Figure 124. Thickness of the copper deposits as a function of plating time in Bath 1, measured through anodic stripping (●) and AFM (▲). Lines of best fit are shown.

Figure 124 also shows the results of thickness measurements performed using AFM. The rate obtained through this method (0.049 ± 0.007 μm min^{-1}) coincided with that observed through electrochemical stripping, confirming that the latter is a simple, yet effective, technique to evaluate the kinetics of the electroless process. It was consequently used throughout the rest of the study. Extrapolation from the graph also showed an induction time of approximately 30 seconds.

The steady deposition rate observed could indicate a surface limited reaction rather than mass transport control exerted by one (or more) of the reactants over the electroless process. Experiments were performed doubling the concentration of all the reactants in Bath 1, while maintaining identical plating conditions of pH and temperature. These tests produced a plating rate twice as high as that observed in Figure 124, indicating a clear influence of solution concentration on the kinetics of the system. After five minutes in Bath 1, for example, films of 0.26 μm were obtained, while the deposits obtained for the same time in baths of doubled concentrations had thicknesses of 0.51 μm; immersion times of 10 min produced 0.56 μm thicknesses in the first case and 0.99 μm in the latter bath. The effect observed could imply that the limiting step of the deposition kinetics is a surface adsorption process, which would be greatly dependent on the concentration in solution of the adsorbate. Control of the electroless process by adsorption of the reducing agents has recently been suggested in a study using DMAB, amongst other reductants.[11]

0.033 M DMAB 0.030 M Copper Sulfate 0.3 M Triethanolamine 0.045 M 1,5,8,12-Tetraazadodecane	Au

Bath 2. Electroless bath with half the DMAB concentration (as compared to Bath 1).

Bath 1 is stoichiometrically limited by the copper complex, having in comparison a large excess of DMAB; not only is the concentration of DMAB more than twice that of the copper, but full oxidation of the molecule provides six electrons, three times those needed to reduce copper(II). Here the effective stoichiometric excess is 6:1, if complete oxidation of DMAB is assumed.[44,76] If the deposition process were mass transport limited, halving the concentration of

DMAB should have little effect on the rate of reaction, as the copper would continue to be the limiting reactant. The use of the numerical simulation of the bipolar cell, assuming reversibility of the cathodic and anodic processes, for example, predicts a shift of only 10 mV for the copper reduction peak, with a change in the peak current of less than 1%, for the difference in DMAB concentrations in Bath 1 and Bath 2. Both cases, however, present a ~15% decrease in the peak current predicted by the Randles-Ševčik equation for the copper complex in the conditions of the baths. These limited approximations imply that although the use of DMAB to reduce the copper complex has a significant effect on the deposition rate, the change in DMAB concentration should not significantly affect the behaviour if the reaction rate is solely dependent on mass transport.

Bath 2 was used to test this statement and the results obtained can be seen in Figure 125. The rate of reaction was not equal to that of Bath 1, decreasing by approximately 20% to 0.04 μm min^{-1}, while also remaining constant throughout the time range studied. It seems unlikely that mass transport is controlling the system's kinetics, a more likely explanation for the decrease in rate is that the DMAB oxidation reaction is limited by its adsorption and dissociation on the surface or simply that there is an overall mix of surface and mass transport control on the kinetics; the important influence of adsorption and surface reactions on DMAB oxidation was seen in Chapters 4 and 5.

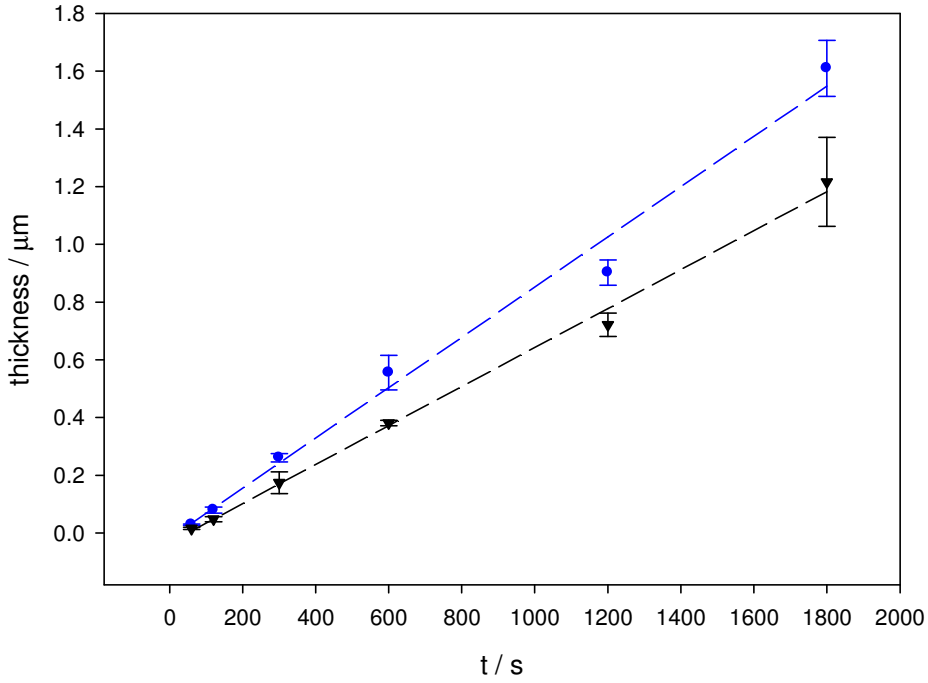

Figure 125. Thickness of copper deposits obtained from Bath 1 (●) and Bath 2 (▼) as a function of time.

The constant plating rate could be due, in part, to local convection created by the evolution of gas during the process; Equation 41 in Section 1.2.2, for example, provides a possible reaction scheme for copper deposition with DMAB, which includes the production of hydrogen as a side-product. The important effect on mass transport, by microconvection created by hydrogen evolution in unstirred copper baths has been previously noted.[25,88] In order to further understand the effect of mass transport, and particularly convection, on the electroless deposition, a rotating disk electrode was used as a plating surface. The deposit thicknesses obtained at the RDE, for an immersion time of five minutes, are shown as a function of rotation frequency in Figure 126.

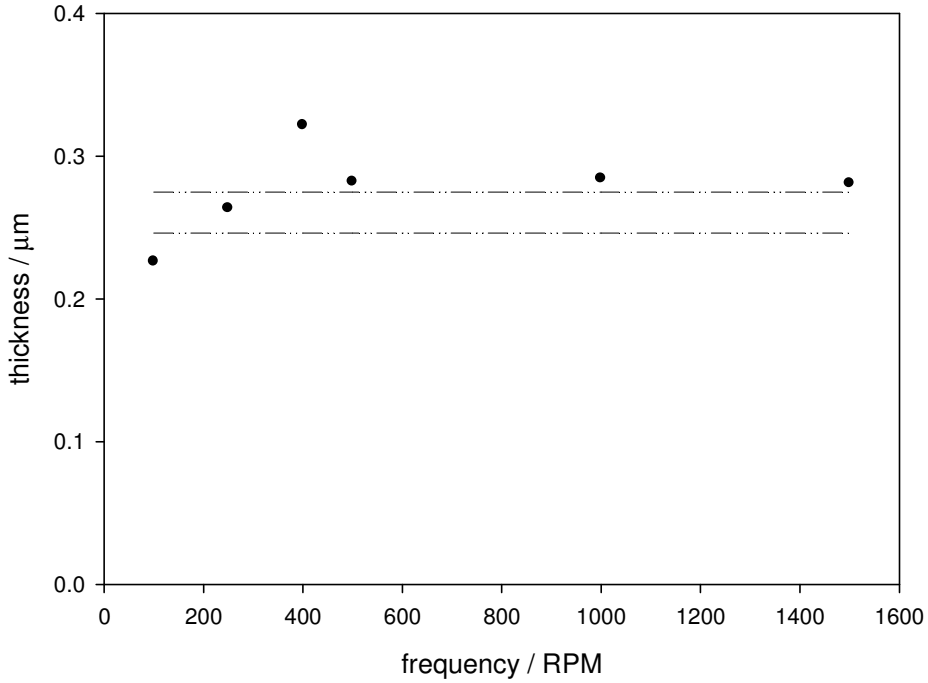

Figure 126. Thickness of copper deposits as a function of electrode rotation speed (bath immersion time: 5 min). The spread of thicknesses achieved under static conditions, for the same immersion time, is represented by the dashed lines.

As stated in Section 2.6, increasing the rotation speed increases the mass transport towards the surface; if the limiting factor in the system's kinetics was mass transport, an increase in the deposit thicknesses would be observed. From the graph, it can be inferred that the increase in mass transport due to rotation of the plating surface has little or no influence on the deposition kinetics; this again points to surface reactions controlling the process' kinetics.

8.3 Galvanic Cell Configuration

In order to probe the electroless Copper-DMAB system in more detail, a galvanic cell configuration was used. As this set-up physically separates the copper complex and the reducing agent into two half-cells, while allowing the spontaneous reaction to occur through electronic and ionic conductors, it enabled the study of the interdependence of the anodic and cathodic processes, and the resultant effect on the electroless deposition kinetics.

8.3.1 Kinetics

The galvanic cell configuration was firstly used in circumstances that mimicked those of Bath 1, maintaining the same chemical composition and plating conditions (see Cell 7). In this set-up measurements were more reproducible than in the electroless bath, possibly due to a better control on the immersion times through the switch placed between the WE (see Figure 15 in Section 3.3.4), added to factors commented on below, such as more evenly distributed currents and avoidance of violent hydrogen evolution. At least three independent experiments were made in each case, however, and average values are presented, along with their corresponding standard deviations. Figure 127 shows the deposit thicknesses obtained in Cell 7 for a time frame between one minute and half an hour.

Au	0.065 M DMAB 0.3 M Triethanolamine	0.030 M Copper Sulfate 0.3 M Triethanolamine 0.045 M 1,5,8,12-Tetraazadodecane	Au

Cell 7. Galvanic cell equivalent to the typical electroless used (Bath 1).

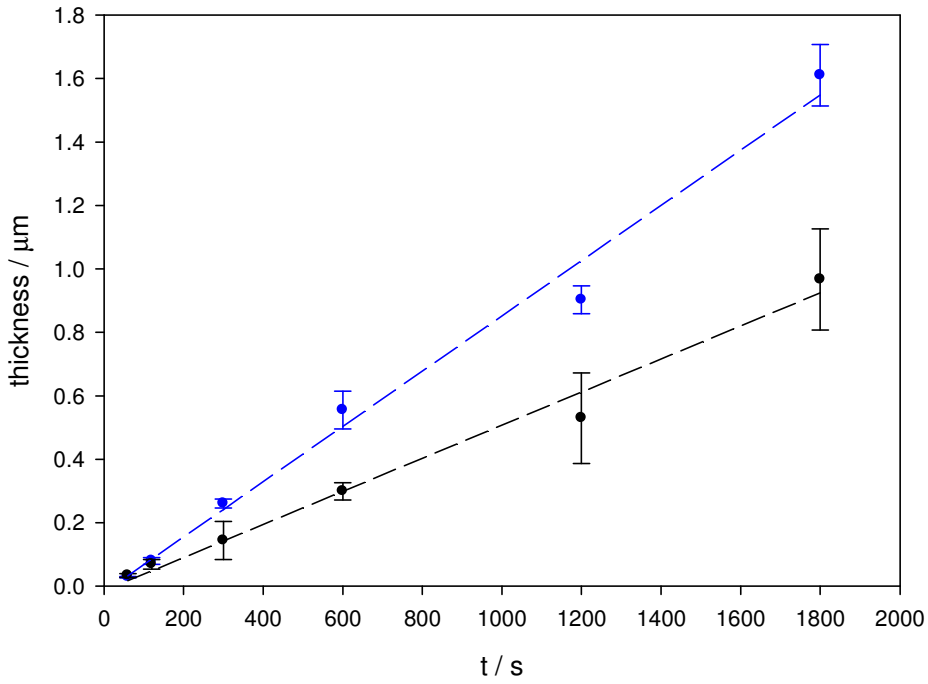

Figure 127. Thickness of copper deposits obtained in Bath 1 (●) and Cell 7 (●).

A constant deposition rate was once again observed, with a calculated value of 0.031 ± 0.002 µm min^{-1}. This is approximately 1.7 times slower than that of

Bath 1. This shows that the physical separation of the anodic and cathodic processes has a marked effect on the system's kinetics, showing the inadequacy of the mixed potential theory in describing the electroless deposition process.[35] The use of the Arrhenius equation allowed the determination of the difference in activation energies between the two systems, through the ratio of their rate constants; a value of 1.6 kJ mol^{-1} was obtained. In view of the reported activation energies for other electroless copper baths (see Section 1.3.1), this difference appears not be significant; the energy barrier in the bath and the galvanic cell configuration is not significantly different.

Through an extrapolation on the graph, an induction time of close to 30 seconds can be determined for Cell 7. This shows that although the kinetics of the plating process are faster in Bath 1, the initial stages appear to have the same limiting factors in both configurations, independently of the concomitance of DMAB and the copper complex.

Au	0.065 M DMAB 0.3 M Triethanolamine	||	0.015 M Copper Sulfate 0.3 M Triethanolamine 0.023 M 1,5,8,12-Tetraazadodecane	Au

Cell 8. Galvanic cell with half the copper concentration of that in Cell 7.

As was discussed in Section 8.2, the stoichiometry of the electroless system used would lead to the assumption that the copper complex is the limiting reactant, so it should have an important effect on the deposition kinetics. In order to probe this, the copper salt and complexing agent concentrations were lowered in the corresponding half-cell, while maintaining the DMAB-containing half cell composition (see Cell 8). Figure 128 presents the thickness of the deposits obtained using Cell 8 as a function of time. Although the rate of reaction decreases in comparison to Cell 7, it does so by approximately 35%, showing that the deposition rate is not directly proportional to the concentration of the copper complex, in spite of its significant stoichiometric limitation; this confirms the important influence of the DMAB oxidation reaction on the overall kinetics.

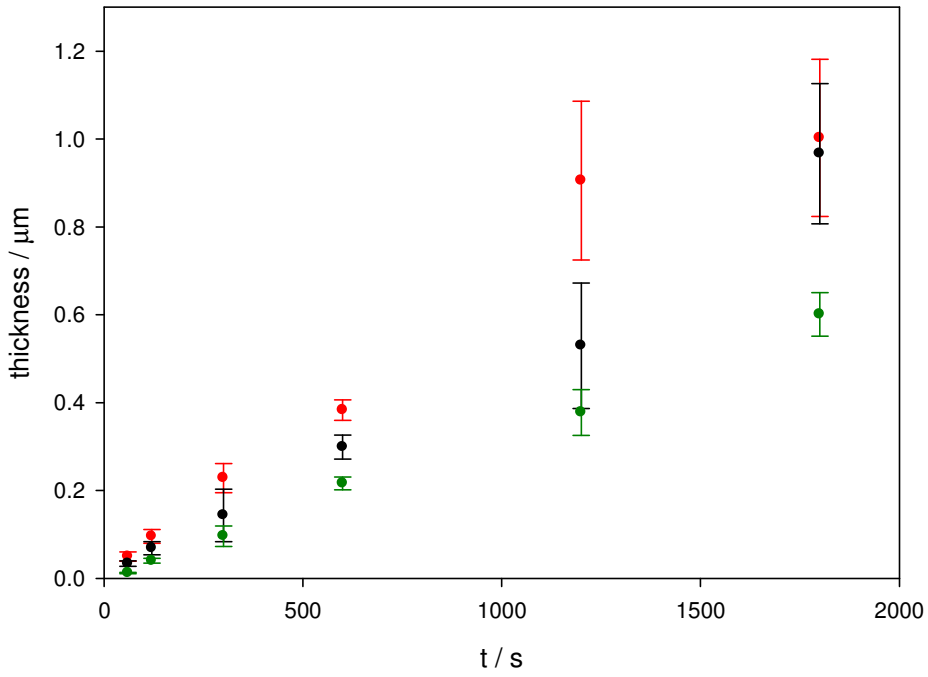

Figure 128. Thickness of the copper deposits obtained in Cell 7 (●), Cell 8 (●) and Cell 9 (●) as a function of time.

In addition to the separation of the anodic and cathodic reactions in the galvanic cell configuration, an important difference between it and the electroless bath is that, in the latter, the substrate on which the reaction takes place changes over time. In the conventional electroless bath, the DMAB oxidation occurs initially on a gold surface, but within a minute, the reaction takes place on a copper substrate (see Figure 124). In the galvanic cell set-up, on the other hand, this compositional change of the catalytic surface only occurs in the cathodic compartment. A copper electrode was introduced to the anodic half-cell, in order to investigate the effect of the copper substrate on the DMAB oxidation reaction (see Cell 9).

Cu	0.065 M DMAB 0.3 M Triethanolamine	‖	0.030 M Copper Sulfate 0.3 M Triethanolamine 0.045 M 1,5,8,12-Tetraazadodecane	Au

Cell 9. Galvanic cell with a copper electrode in the DMAB-containing half-cell and identical chemical composition to Cell 7.

The effect of introducing the copper electrode on the overall deposition rate can be seen in Figure 128, where a higher deposition rate relative to that of Cell 7 is observed. As the copper-containing half-cell was not changed, this result indicates that DMAB oxidation is faster on copper than on gold substrates. This

result is consistent with suggestions, made in previous work using DMAB as a reducing agent, that DMAB presents faster oxidation kinetics on copper than on gold,[41] as well as the interpretation of the induction times observed in the electroless bath and galvanic cell configurations. Earlier work has also demonstrated that formaldehyde oxidation is catalyzed by the formation of fresh copper layers during electroless deposition of copper.[37]

A first glance at the data in Figure 128 might indicate that the deposition rate of Bath 1 is regained on introduction of the copper electrode. A closer look, however, reveals that the initial deposition rate is actually higher in Cell 9 (Figure 129). A non-linear trend is observed, with the subsequent deposition rate dropping below that of the electroless bath. This implies that, although the catalytic properties of the substrate for the oxidation of the reducing agent play a major role on the kinetics of the overall process, there is a further interaction between the two half reactions.

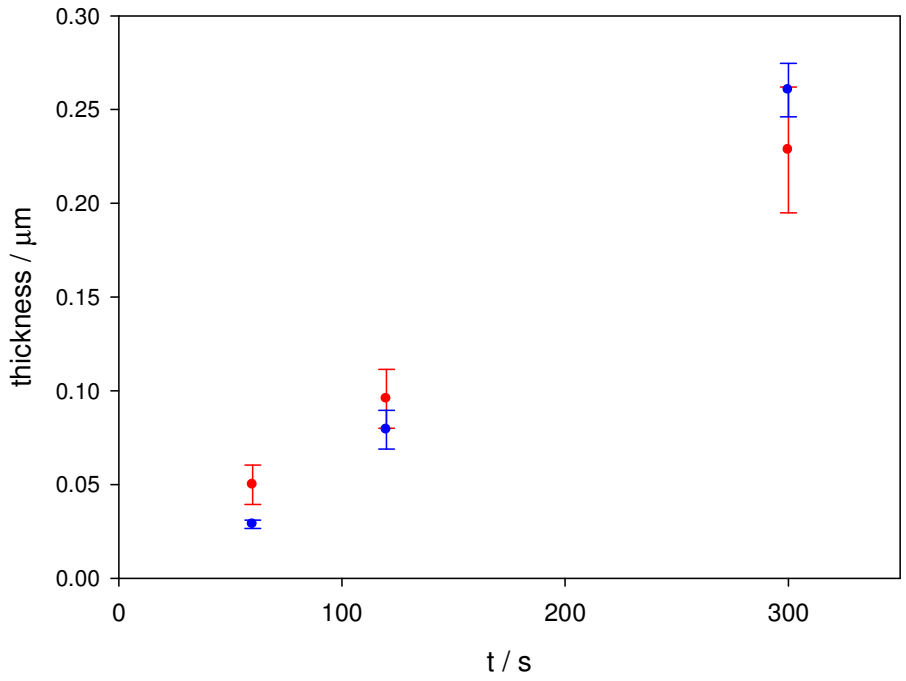

Figure 129. Deposit thicknesses obtained in Bath 1 (●) and Cell 9 (●) in the first five minutes.

The use of the galvanic cell configuration allowed the measurement of the open circuit potential (OCP). The OCP is simply the potential difference between the two half-cells and provides information about the driving force of the process. Figure 130 shows the OCP values for Cell 7, Cell 8 and Cell 9; although the

accuracy of the multimeter is high, the measured values varied between experiments under nominally identical conditions, so averages of at least 18 tests are presented, with their corresponding standard deviations shown as error bars. Decreasing the concentration of the copper complex has little effect on the OCP, while replacing the gold electrode in the anodic half-cell by a copper one increases the potential difference by approximately 250 mV. The higher rate observed in Cell 9 is consistent with the increase in driving force measured here.

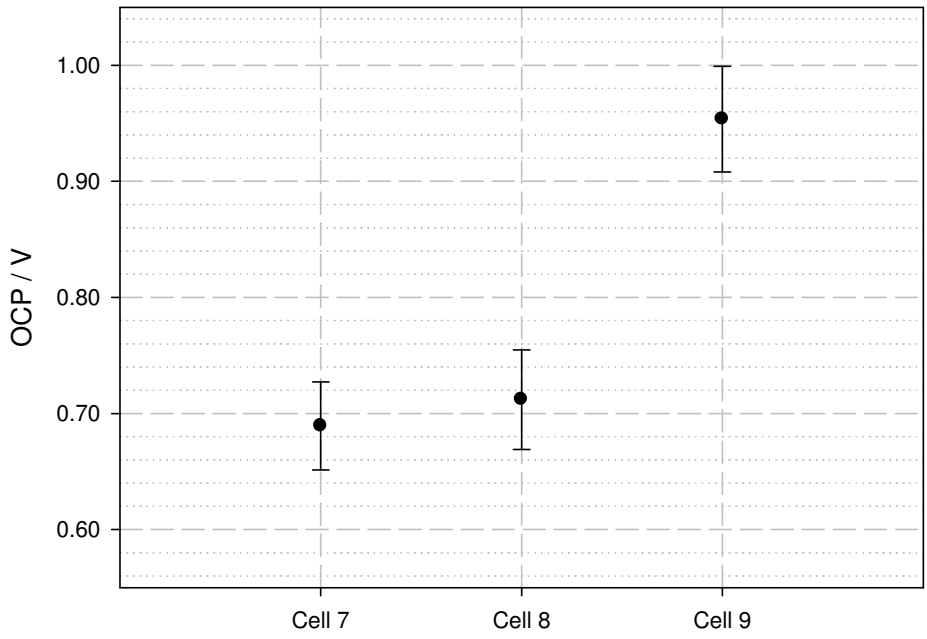

Figure 130. Open circuit potential measured for Cell 7, Cell 8 and Cell 9.

8.3.2 Faradaic Efficiency

As well as allowing the measurement of the OCP, the galvanic cell configuration also allows the current transferred from one half-cell to the other to be recorded, while the deposition process occurs. Examples of such current transients can be seen in Figure 131, where absolute current magnitudes are shown. These are a direct measure of the flow of electrons produced by DMAB oxidation and transferred to the cathodic half-cell.

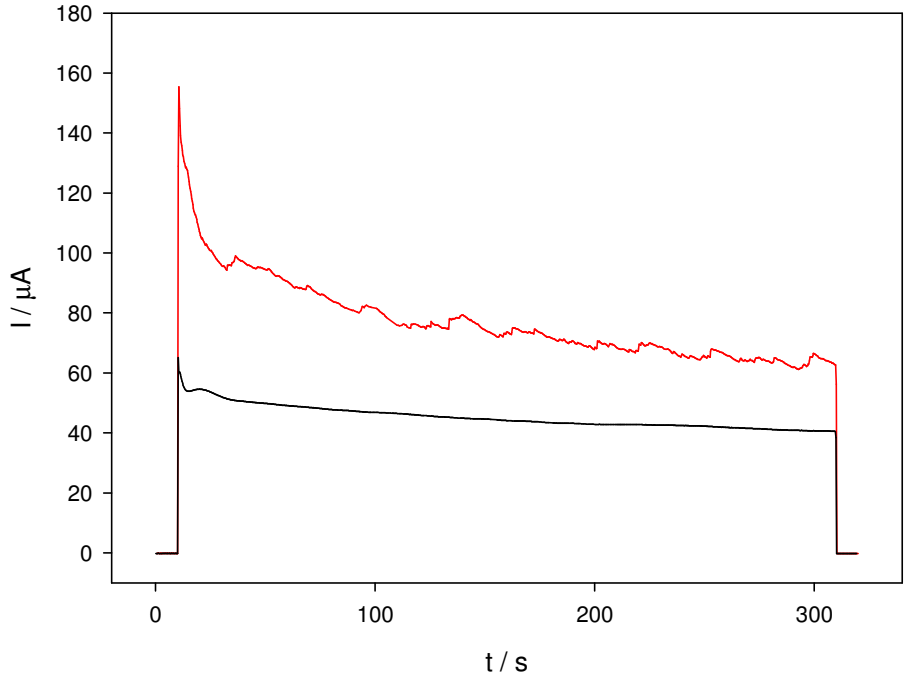

Figure 131. Current transients of five minute depositions in Cell 7 (black) and Cell 9 (red). Absolute values are presented.

The magnitude of the current increases when a copper electrode is used (Cell 9), *in lieu* of a gold electrode (Cell 7); this again shows that copper is a more efficient catalyst for DMAB electro-oxidation than gold. The transient produced is also noisier, which implies that gas evolution accompanies the process. Gas evolution could be attributed to a number of processes in the anodic half-cell, or a combination of them: hydrogen produced by hydrolysis of DMAB catalysed by the copper substrate, hydrogen evolved as a side-product of the DMAB oxidation and/or the evolution of the dimethylamine (a gas at the conditions used)[130] produced by the rupture of boron-nitrogen bond in the DMAB molecule. Hydrogen evolution is the most likely process if the gas is derived from a cathodic reaction.

The overall deposition charge (Q_{od}) can be calculated through integration of transients such as those presented in Figure 131. A measure of the faradaic efficiency can be made by calculating the ratio between the stripping charge (Q_s) and the overall deposition charge, as this gives the fraction of the charge produced by DMAB oxidation that actually goes towards copper reduction. Figure 132 presents the results obtained from Cell 7, Cell 8, and Cell 9 as a function of time.

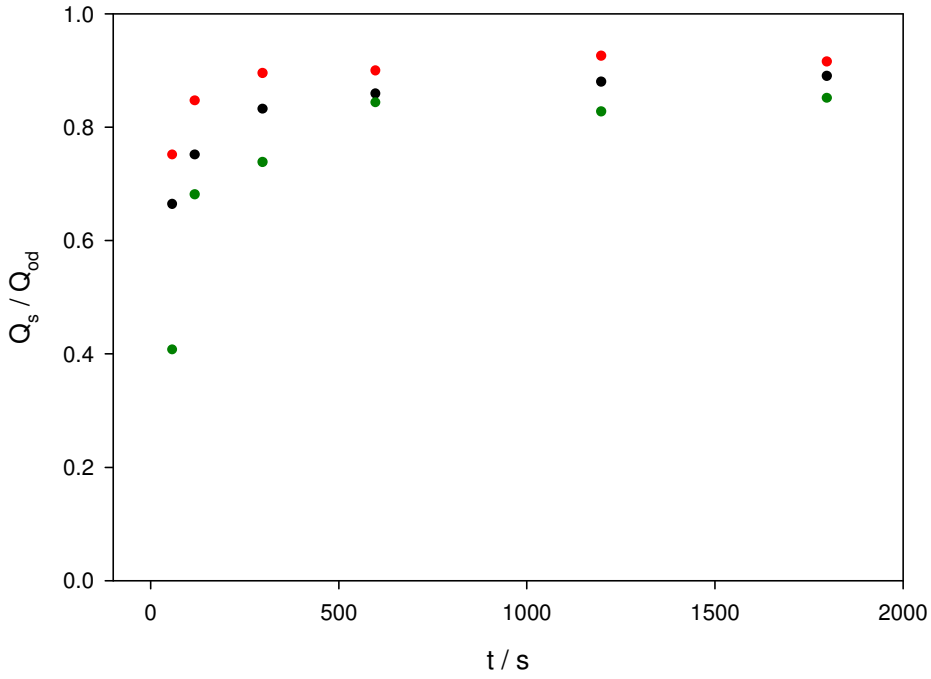

Figure 132. Ratio of the stripping and overall deposition charges as a function of time in Cell 7 (●), Cell 8 (●) and Cell 9 (●).

In all three cases the efficiency increases with time, reaching values close to unity at longer times. These results indicate that a side reaction (or reactions), takes place in the copper-containing half-cell which consumes a fraction of the charge produced by the anodic oxidation of DMAB. This “parasitic” process is probably hydrogen evolution, as shown in the bipolar experiments of Section 7.3, where it was demonstrated that in the absence of copper, hydrogen evolution drives the oxidation of DMAB. Further evidence of the overlap of copper reduction and hydrogen evolution in the relevant potential region will be discussed in Section 8.4.2, with additional bipolar voltammetric experiments.

The cathodic side-reaction is more pronounced during the initial stages of deposition. This might be due to copper reduction being less prominent at first, as the initial nucleation process is less favourable than hydrogen evolution. The effect of the side reaction is more important when the copper concentration is lowered (Cell 8); as the amount of copper reacting decreases, a larger fraction of the charge goes towards the parasitic process.

8.3.3 Effect of Triethanolamine

Triethanolamine has been used as an additive to electroless deposition baths for a number of reasons: it helps control the pH, aids in complexing the copper(II) ions, improves plating uniformity and has been reported as a catalyst for electroless deposition.[9,41,89,147] In order to study the effect of TEA on the process it was consecutively removed from each half-cell of the galvanic cell configuration (Cell 10 and Cell 11), and lastly from both (Cell 12).

Au	0.065 M DMAB 0.3 M Triethanolamine	‖	0.030 M Copper Sulfate 0.045 M 1,5,8,12-Tetraazadodecane	Au

Cell 10. Galvanic cell without TEA in the cathodic half-cell.

Au	0.065 M DMAB	‖	0.030 M Copper Sulfate 0.3 M Triethanolamine 0.045 M 1,5,8,12-Tetraazadodecane	Au

Cell 11. Galvanic cell without TEA in the anodic half-cell.

Au	0.065 M DMAB	‖	0.030 M Copper Sulfate 0.045 M 1,5,8,12-Tetraazadodecane	Au

Cell 12. Galvanic cell without TEA present.

The open circuit potentials of Cell 10, Cell 11 and Cell 12 were measured and are compared to that of Cell 7 in Figure 133. It can be seen that the presence or absence of TEA has little effect on the OCP, and thus on the initial driving force of the electroless process.

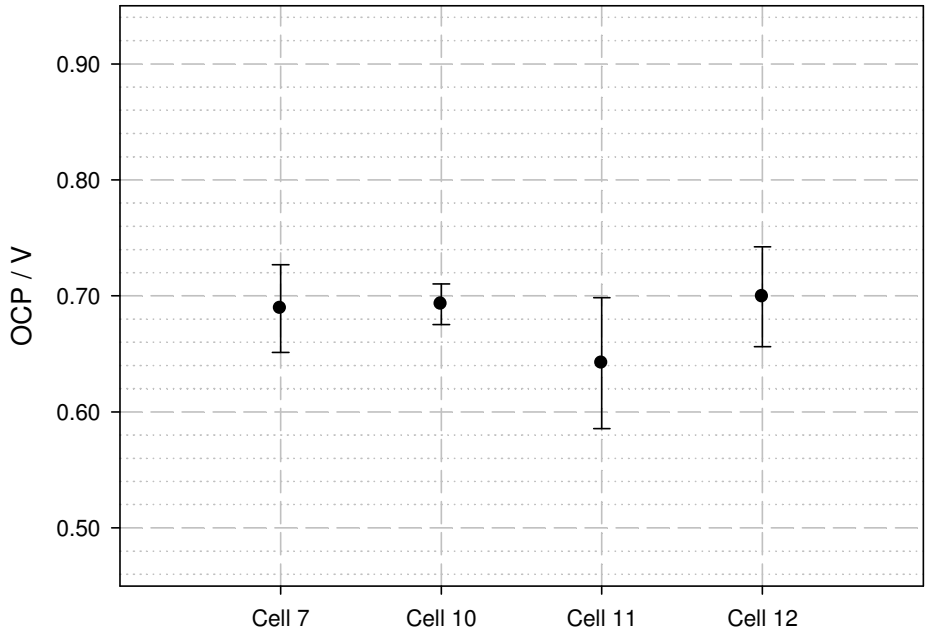

Figure 133. Open circuit potentials measured for Cell 7, Cell 10, Cell 11 and Cell 12.

Despite not changing the OCP of the system, the presence of TEA has a marked impact on the thickness of the copper deposits obtained. Figure 134 shows the thicknesses for two different immersion times (five and ten minutes) in all four cases studied. Assuming that a steady deposition rate is also attained in the absence of TEA (Cell 12), the decrease in rate is well above 50% in comparison to when it is present in both half-cells (Cell 7).

From the graph it can be see that having TEA in the copper compartment (Cell 11) has little or no effect in comparison to not having TEA in either half-cell (Cell 12); introducing TEA in the anodic half-cell (Cell 10), however, increases the thickness of the deposits obtained. This last indicates that the presence of TEA catalyses DMAB oxidation, in agreement with previous studies.[41,147]

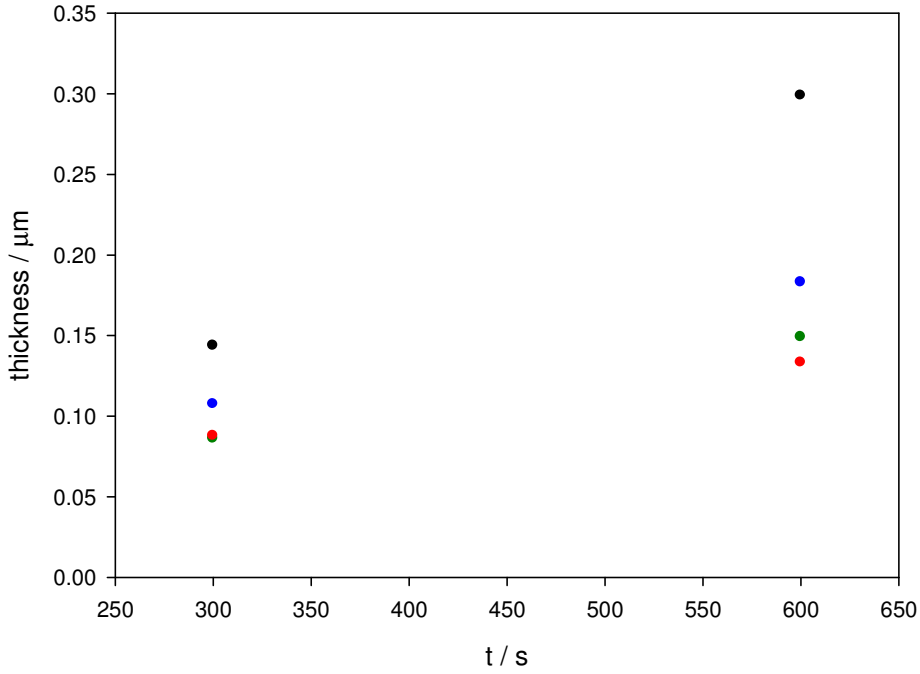

Figure 134. Deposit thicknesses obtained for immersions of 5 and 10 minutes in Cell 7 (black), Cell 10 (blue), Cell 11 (green) and Cell 12 (red).

The thicknesses achieved when TEA is only present in the DMAB compartment (Cell 10) are significantly lower than those obtained in the original galvanic cell (Cell 7); the effect of TEA on the system is consequently more complex than simply catalysing DMAB oxidation.

The faradaic efficiency, measured through the charge ratio as described in Section 8.3.2, was also studied as a function of the presence of TEA in the system (see Figure 135). The highest efficiencies are reached when TEA is present in both half-cells and the lowest when it is completely absent, with a difference between the two of 7-8% approximately; the values in all cases are above 75%.

The increased efficiency of the process when TEA is present in the copper compartment could contribute to the difference in thickness obtained between Cell 7 and Cell 10; the rate of DMAB oxidation would be similar in both cases, but the inclusion of TEA in the cathodic compartment of Cell 7 increases the efficiency and thus the deposition rate.

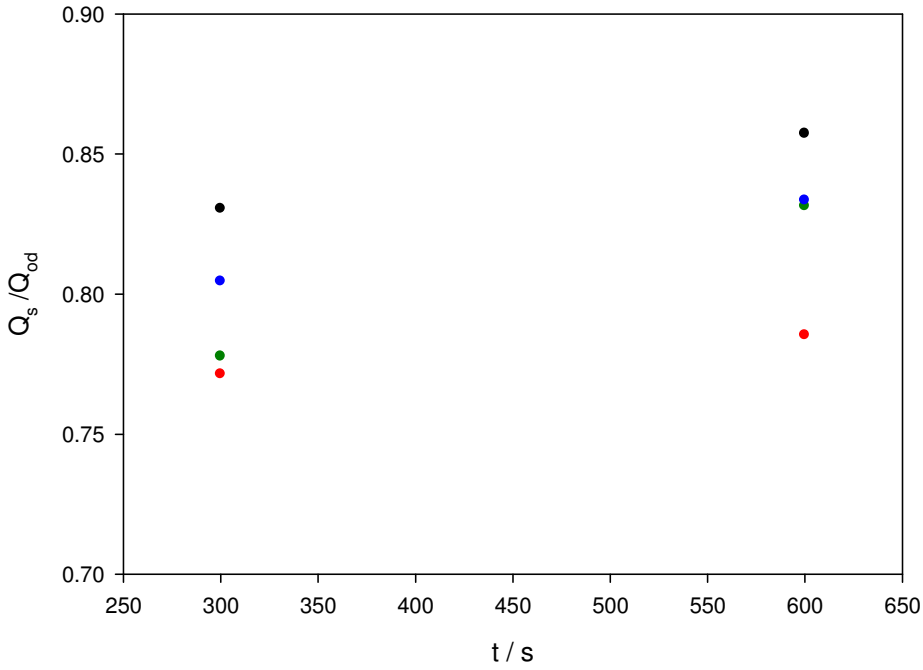

Figure 135. Ratio of the stripping and overall deposition charges in Cell 7 (black), Cell 10 (blue), Cell 11 (green) and Cell 12 (red).

8.4 Bipolar Cell

8.4.1 Deposit Thickness as a Function of Applied Potential

The bipolar cell was employed to study the electroless process under applied potential, rather than the spontaneous conditions used in the galvanic cell configuration. The conditions employed were equivalent to those of Cell 7, using platinum and graphite CEs in the copper and DMAB half-cells, respectively, to complete the circuit; graphite was used in the DMAB compartment, *in lieu* of platinum, in order to avoid the catalysis of the possible hydrolysis side-reactions mentioned in Section 1.2. Ag/AgCl reference electrodes were used in both half-cells, in order to adjust the applied potential difference (see Cell 13).

Ag/AgCl	0.030 M Copper Sulfate 0.3 M Triethanolamine 0.045 M 1,5,8,12-Tetraazadodecane	0.065 M DMAB 0.3 M Triethanolamine	Ag/AgCl

Cell 13. Electrochemical bipolar cell used for the study the copper-DMAB electroless system.

The bipolar cell was connected to the potentiostat in such a way that negative currents where observed when the copper was reduced: the copper half-cell was connected to the CE and RE leads on the potentiostat, while the DMAB-cell was connected to the WE and sense. Temperature and pH were kept constant at 55.0 ºC and 11.5, as with all experiments described above. Potential differences were applied for 10 minutes and the resulting deposits thicknesses can be seen in Figure 136.

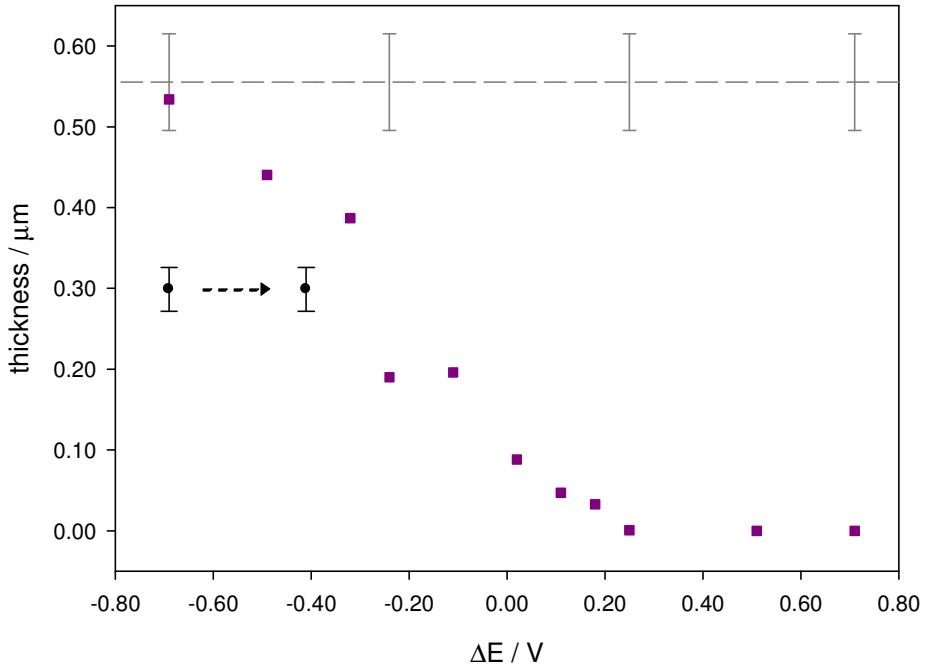

Figure 136. Deposit thickness as a function of applied potential difference in the bipolar cell (■); deposition time: 10 min. For reference: thickness obtained in Bath 1 (dashed line) and in Cell 7 (●).

From the figure, it can be seen that no deposition occurs at potential differences above 0.20 V. Below that point the deposit thickness increases until a potential difference of -0.69 V, where the deposit obtained has the same thickness as those obtained in Bath 1. This potential coincides with the OCP measured in Cell 7; in the latter case, however, the deposits obtained after 10 minutes were much thinner.

These results seem to indicate that the OCP of the galvanic cell configuration is a good indicator of the driving force of the electroless deposition process. An external input of energy is needed, however, in order to maintain the deposition rate when the two half-reactions are separated, as evidenced by the

difference in deposit thickness at the same potential in the galvanic and bipolar cells.

In order to better understand the difference obtained between Cell 7 and Cell 13, the OCP was studied at different deposition times in Cell 7. This was accomplished by interrupting deposition for a few seconds, while the potential was measured. As with all measurements in the galvanic cell configuration, experiments were performed three times, and average values are presented in Figure 137.

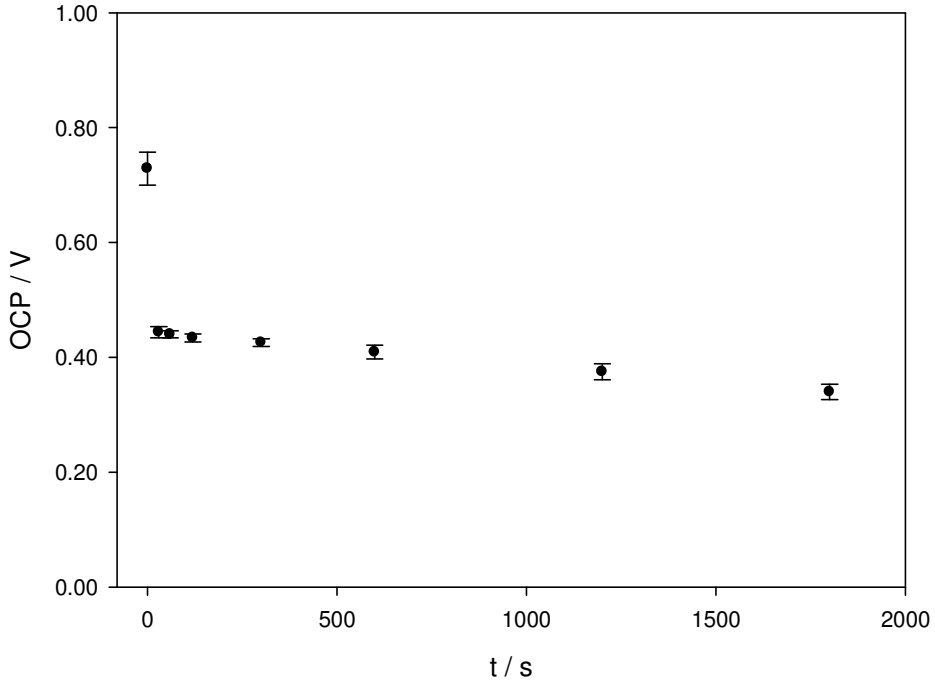

Figure 137. Open circuit potential of Cell 7, as a function of deposition time.

Figure 137 shows that the OCP of the galvanic cell drops considerably within the first 30 seconds of deposition (~ 300 mV). After 30 seconds, the decrease of the potential with time is considerably smaller. This time coincides with the induction time observed in Sections 8.2 and 8.3.1, possibly indicating the influence of the copper deposit, in the copper half-cell, on the OCP. If the OCP value obtained after ten minutes is used for comparison in Figure 136, instead of the initial value, the thickness obtained in Cell 7 is closer to the trend obtained in the bipolar cell configuration (Cell 13); the dashed arrow in the figure indicates the direction of the OCP shift.

In the bath, the decrease of the driving force observed here would be countered by the increase due to the catalytic nature of the copper surface towards DMAB oxidation seen in 8.3.1; Figure 130 shows an increase of ~ 250 mV by introducing a copper surface in the DMAB compartment.

The efficiency of the deposition in the bipolar cell was also studied and the results can be seen in Figure 138. Three distinct regions are present. Above 0.20 V, the ratio of the stripping and deposition charges is close to zero. The potential window between 0.20 and -0.20 V shows a sharp and steady increase in efficiency, which reaches values of approximately 0.9 below -0.20 V. The values of this last region agree with the efficiency values obtained in the galvanic cell for equivalent systems (Cell 7 and Cell 9, for example). The fact that the efficiencies of the galvanic and bipolar cells coincide in this potential region indicates that the efficiencies of the galvanic cell are a good approximation to that of the electroless bath; *i.e.* in this window, the bipolar cell produces films that match in thickness those of the bath.

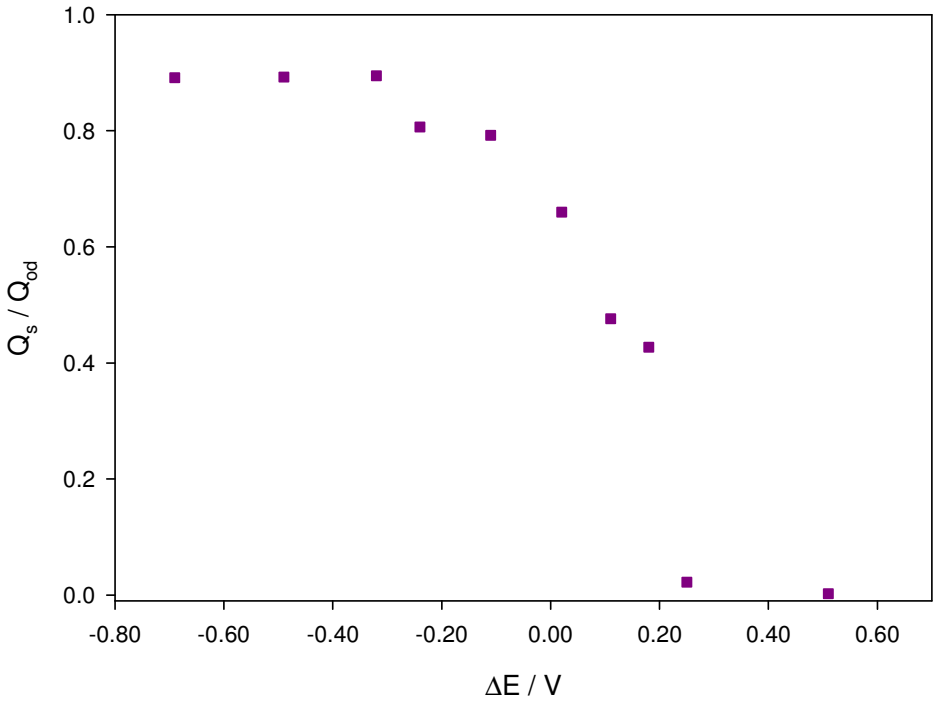

Figure 138. Ratio of the stripping and overall deposition charges in Cell 13.

8.4.2 Voltammetric Studies

The bipolar cell allows the voltammetric behaviour of the electroless system to be studied, as demonstrated in Chapter 7. In order to investigate the voltammetry of the electroless bath, Cell 14 was used; all concentrations were lowered by a factor of 10 and consequently a supporting electrolyte (sodium sulfate) was added. Although the pH was adjusted to 11.5, room temperature was used in these studies. Electrodes and connections were as described for Cell 13.

Ag/AgCl	3.0 mM Copper Sulfate 0.03 M Triethanolamine 4.5 M 1,5,8,12-Tetraazadodecane 0.1 M Na_2SO_4	6.5 M DMAB 0.03 M Triethanolamine 0.1 M Na_2SO_4	Ag/AgCl

Cell 14. Bipolar cell used for the study the voltammetric behaviour of the copper-DMAB electroless system.

The voltammetric response of Cell 14 is presented in Figure 139. The behaviour observed is similar to that seen in Figure 117; although the potentials vary due to the different pH, along with the presence of TEA and relative concentrations used in this case. The reduction of copper can be seen near -0.40 V, with the subsequent oxidation process visible on the second scan in the potential region between 0.50 and 1.50 V. The blanks show that no reactions take place in the absence of DMAB, while currents are produced in the absence of copper at either end of the potential range studied; the current at potential differences more negative than -0.50 V are likely due to DMAB oxidation coupled to hydrogen evolution in the other half-cell. This reaction occurs along with copper reduction when copper is present, accounting for the loss of efficiency observed in the system (see Figure 138, for example).

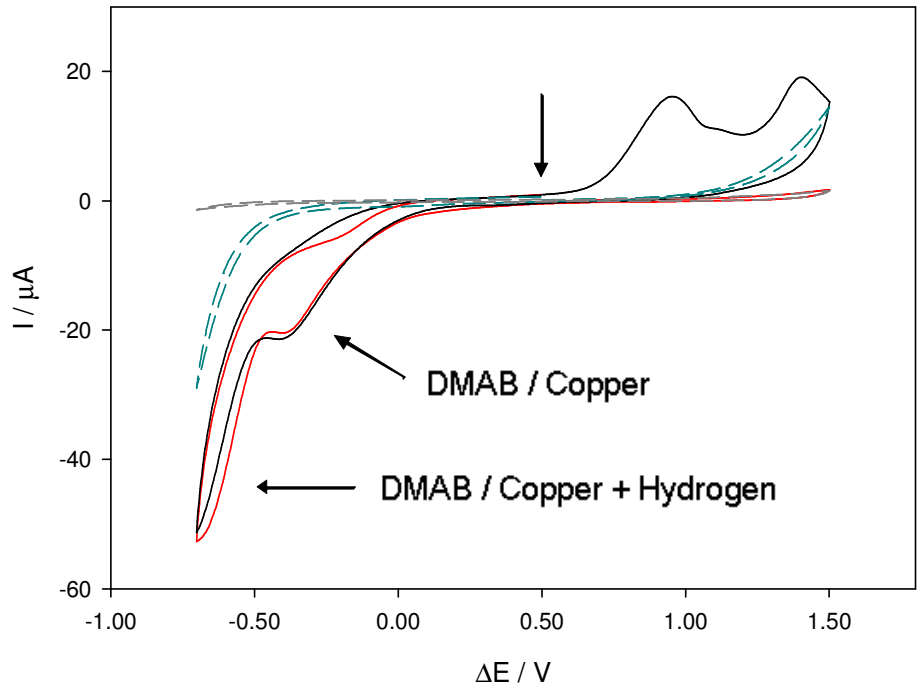

Figure 139. Voltammetric response of Cell 14. Two consecutive cycles are shown (first: red, second: black), along with scans in the absence of DMAB (dashed grey) and in the absence of copper (dashed blue). The arrow indicates the starting potential; the initial direction was positive.

The different potential regions observed in Section 8.4.1 can be easily identified in the voltammetric behaviour. The reduction currents due to copper begin close to 0.20 V, where deposition is initially observed in Figure 137; at potential differences more positive than this, there are no voltammetric features, in agreement with efficiencies close to zero and no deposition observed in the potential steps in Cell 13. The maximum efficiency observed in Figure 138 is achieved at potentials more negative than -0.40, which coincides with the peak observed in Figure 139.

The voltammetric behaviour observed is similar to that displayed by the three electrode cell, with similar conditions to that of the copper half-cell of Cell 14 (see Figure 91 in Chapter 6). The main difference is the larger potential difference between the negative and positive currents in the bipolar configuration, which is simply due to the copper reduction being coupled to DMAB oxidation, while its re-oxidation is probably linked to hydrogen evolution.

8.5 Characterization of the Copper Deposits

8.5.1 XRD Analysis

Due to the spontaneous nature of the electroless deposition process, any deviation from the controlled conditions can result in the homogenous decomposition of the solution or plating on the cell walls.[8,16] A deposit obtained in such a way from Bath 1 was analyzed through XRD: the resulting diffraction pattern can be seen in Figure 140. Although the sample was a black powder, typical signals metallic of copper are observed,[159] implying that small crystallites of copper are formed. The structural composition is that expected for polycrystalline copper, as can be deduced from the relative intensities of the peaks observed; the main contributions are those of Cu (111) ($2\theta = 43.3°$) and to a lesser extent Cu (200) ($2\theta = 50.4°$), while the three smaller signals correspond, from left to right, to Cu (220), Cu (311) and Cu (222).[15,159]

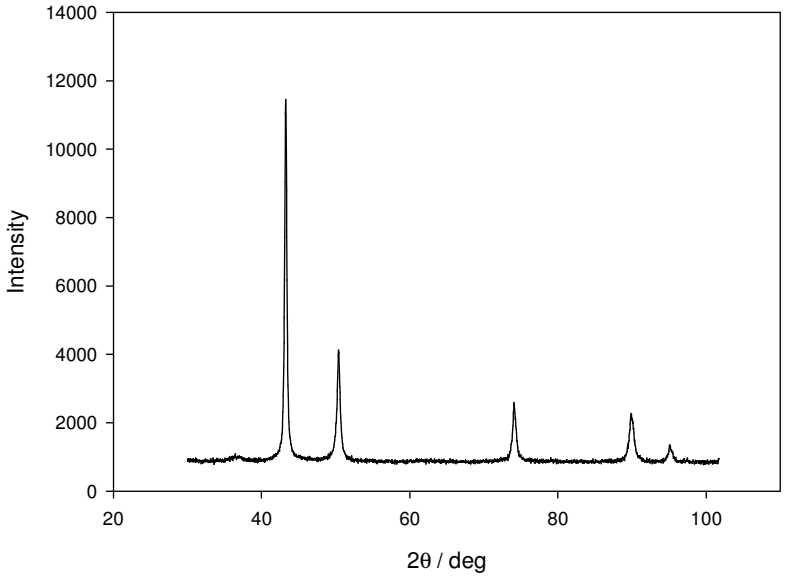

Figure 140. Diffraction pattern of the deposit obtained from spontaneous decomposition of Bath 1.

Copper deposits were obtained on gold foils from one hour immersions in Bath 1 and Bath 2. Diffraction patterns were obtained for each and are presented in Figure 141, which also shows the XRD pattern of the underlying gold substrate for comparison. The same signals attributed to metallic copper in Figure 140 can be seen, along with those due to the gold surface. Polycrystalline copper, with

very similar structural composition, is produced in both baths, irrespective of the DMAB concentration. However, it is slightly different from the deposits obtained from spontaneous decomposition (Figure 140); the same signals are obtained, but their relative intensities vary. The deposits obtained through controlled plating on gold surfaces present a higher ratio of Cu (111) than that expected in typical polycrystalline copper, as well as that obtained through spontaneous decomposition.[159] The ratio of the intensities of the Cu (111) to Cu (200) peaks in the later cases are 2.2 and 2.4, respectively, while on the electroless copper deposits examined the ratio ranged from 2.9 to 3.6. The difference in the ratios of Cu (111) peaks to the smaller copper peaks was found increasingly significant; for the case of the Cu (220) peaks, for example, the ratio increased from 5.0 in typical polycrystalline copper to between 7.5 and 10.8 in the electroless deposits on gold. Copper films with a high component of Cu (111) are desirable, for example in ultra-large scale integration and general interconnection technology, as they lower the oxidation rate and enhance electromigration resistivity due to the suppression of grain boundaries and interfacial diffusion of metal ions at highly textured microstructures.[85,89]

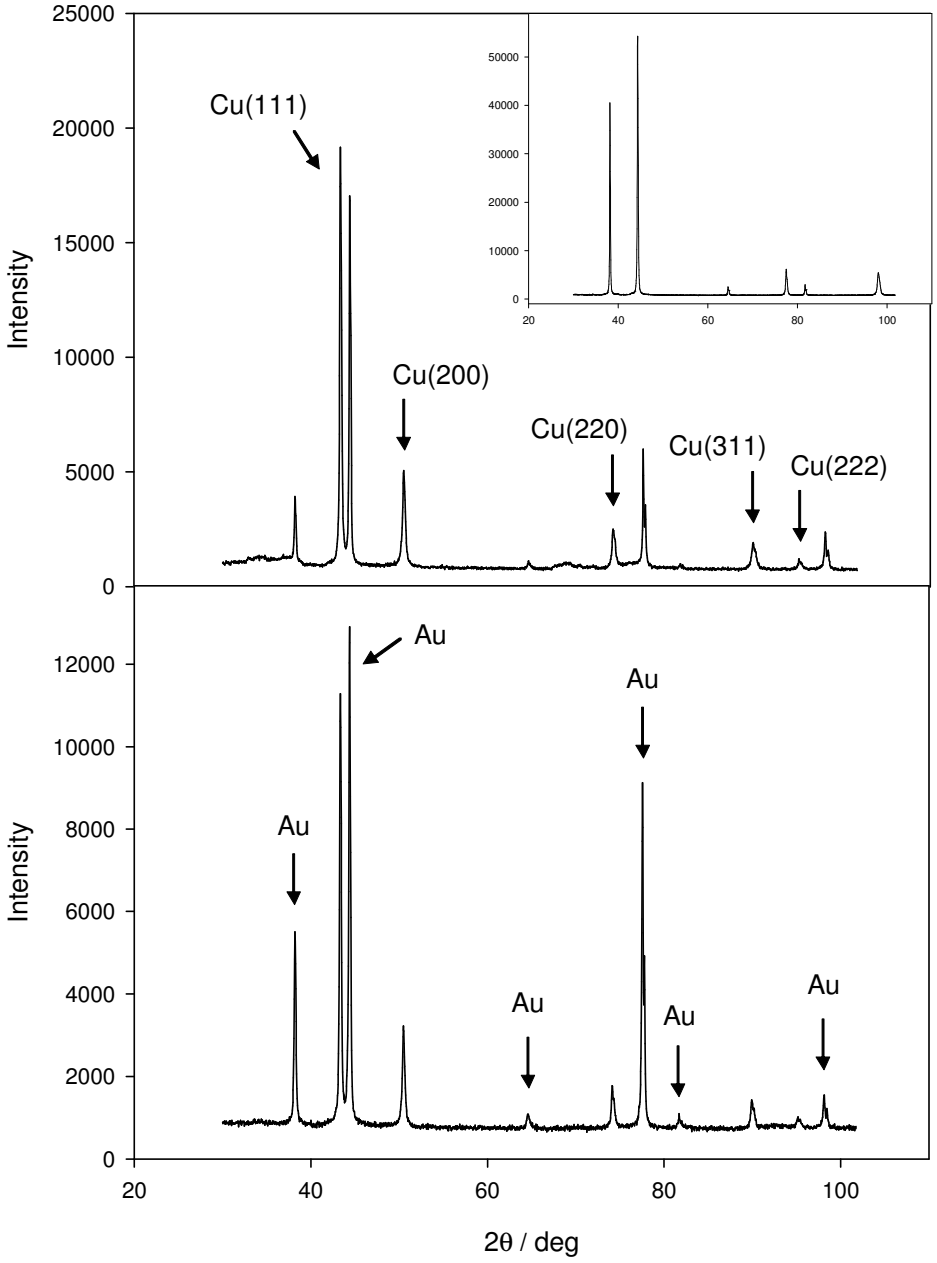

Figure 141. Diffraction patterns of copper deposits on gold, obtained from Bath 1 (top) and Bath 2 (bottom). The inset shows the diffraction pattern of the underlying gold surface.

From these studies, it can be seen that although changing the concentration of the reducing agent changes the kinetics of the process, the structural composition remains the same. On the other hand, whether the process occurs on a catalytic surface or not seems to have a small yet clear effect on the crystalline structure, the first case increasing the percentage of Cu (111) on the deposit. No traces of copper oxide were found in any of the deposits,[159-161] implying that the bulk of the deposit is in fact pure copper; a small layer of copper oxide (< 5 nm thick), expected due to the rapid reaction of copper with oxygen upon contact with air, might be present and go undetected in these tests.[24,162,163]

8.5.2 Elemental Analysis

Elemental analysis was also performed on deposits obtained from Bath 1, to determine whether pure copper was in fact obtained. A Carlo Erba EA1108 elemental analyser was used to detect carbon, hydrogen and nitrogen, while metal analysis was performed through a Fisons Horizon Inductively Coupled Plasma Optical Emission Spectrometer.[xv]

As with XRD, samples generated from spontaneous decomposition and through controlled electroless deposition, were studied; in the latter case, the substrates used to catalyse the deposition were thin copper films, rather than gold foils, in order to simplify the elemental analysis. The deposits were rinsed with deionised water three times and allowed to dry in air before testing. The results obtained are presented in Table 22.

Table 22. Weight percentages of elements present in samples obtained in Bath 1.

Element	Spontaneous Decomposition	Electroless Deposition
Cu	93.24	97.51
O[xvi]	6.60	2.32
C	0.16	0.17

Small traces of carbon were found, but the absence of hydrogen or nitrogen suggests that the complexing (1,5,8,12-tetraazadodecane) and buffering (TEA) agents are not co-deposited or irreversibly adsorbed on the copper surface.

Oxidation of the copper is likely after prolonged contact with air,[162,163] and appears confirmed by the elemental analysis performed. According to the results obtained, the oxidation is more prominent in samples obtained through

[xv] The elemental analysis was performed by the Microanalysis Laboratory of the School of Chemistry.

[xvi] The amount of oxygen is taken as the highest percentage that could be present in the sample, based on the other elements found. As the other elements present in the bath were not found in the deposits, oxygen is likely to account for most, if not all, of the percentages expressed in the table.

decomposition than those produced through controlled deposition. This could be explained by oxide layer forming on the surface of the deposits and the larger surface to volume ratio in the first case, due to the smaller particle size in comparison to the films obtained in the later case.

The maximum amount of oxygen for the deposits produced by electroless deposition, according to Table 22, implies that approximately 10% of the deposits would be copper oxide. If this copper oxide is produced as a layer on the surface once the deposits are in contact with air, as is suggested by XRD and elemental analysis, this percentage would be reduced by approximately 50% when the films are produced on templates and only one face of the films are exposed.

8.5.3 AFM Morphology Studies

The morphology of the deposits obtained in the electroless bath and galvanic cell configurations was studied using AFM to measure their average roughness;[xvii] this technique has been used on previous occasions to characterize electroless plating deposits.[29,40,85] Figure 142 shows the AFM images of copper deposits obtained from Bath 1, as a function of plating time. Small copper particles are observed at short times, which increase in size with time, eventually coalescing to form a film.

[xvii] All AFM measurements were made by Dr Samson N. Patole, former Postdoctoral Research Associate of the Manchester Electrochemistry Group.

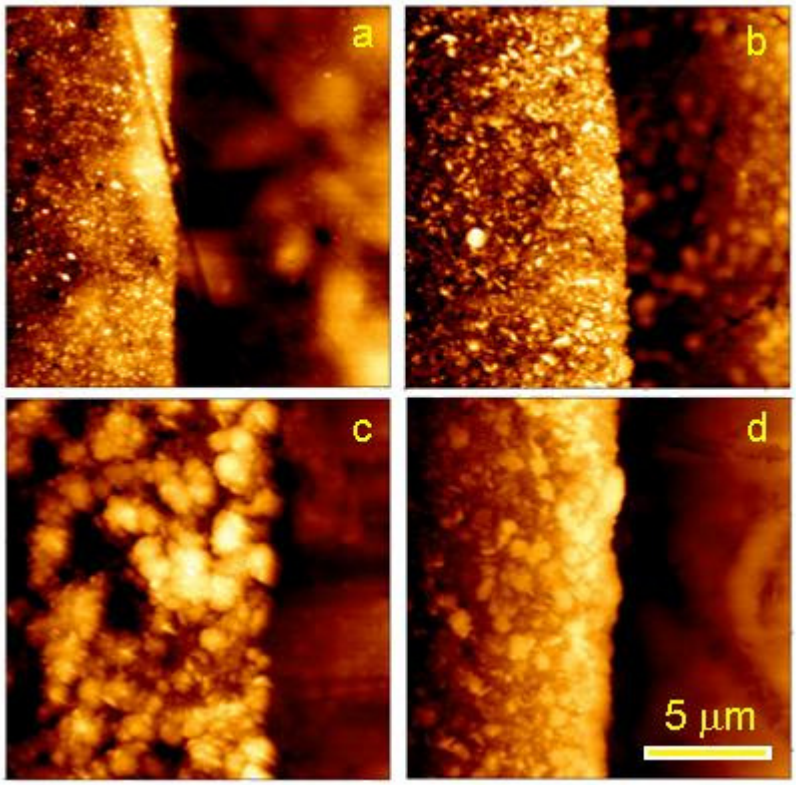

Figure 142. AFM images of copper deposits obtained using Bath 1 for 1 (a), 2 (b), 5 (c) and 30 (d) minutes (16 µm x 16 µm areas are shown). The underlying gold can be seen on the right-hand side of each image.

The evolution in the morphology of the copper deposits with time is more evident in Figure 143, which shows AFM images with a higher degree of magnification than that seen in Figure 142. The small particles observed after one minute of deposition (Figure 143a) can be seen to elongate after an additional minute of plating time (Figure 143b). Plateaux begin to form after longer plating times (Figure 143: c and d).

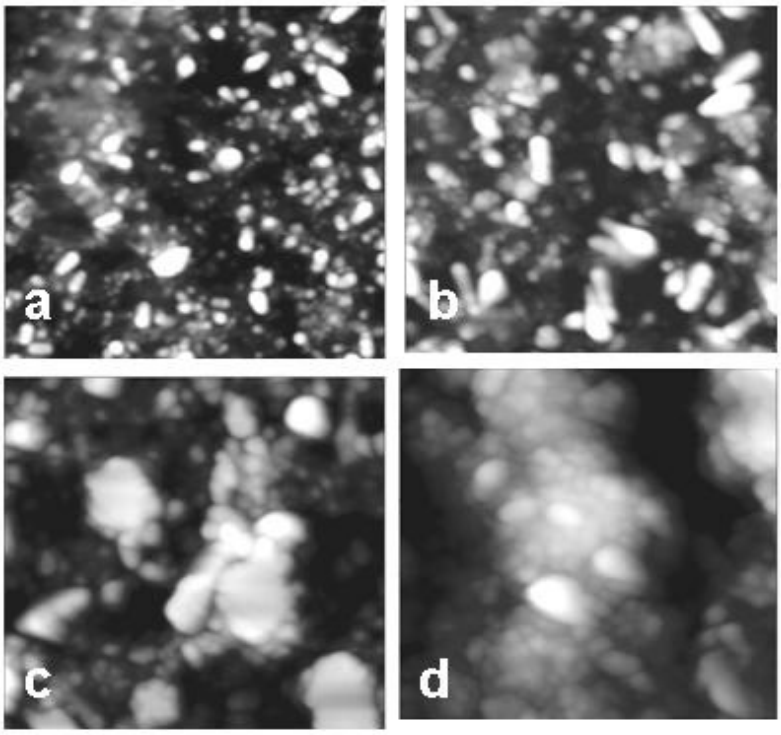

Figure 143. AFM images of copper deposits obtained using Bath 1 for 1 (a), 2 (b), 5 (c) and 30 (d) minutes (3 μm x 3 μm areas are shown).

Deposits obtained from Bath 1 and Cell 7 on gold foils were studied, with at least six measurements of the roughness taken on different areas across each surface. Average values are presented in Table 23, where the roughness of the underlying gold substrate was 4 nm. The roughness is seen to increase with deposition time, and thus with thickness, in both experimental set-ups.

Table 23. Roughness of the copper deposits obtained in the electroless bath and the galvanic cell.

Bath 1		**Cell 7**	
Time / min	**Roughness / nm (3 μm x 3 μm)**	**Time / min**	**Roughness / nm (3 μm x 3 μm)**
1	12	2	7
2	27	5	7
5	90	15	26
30	135	30	39

The roughness greatly decreases in the galvanic cell configuration in comparison to Bath 1. These results are not merely an effect of the deposit thickness as, for example, a 5 minutes deposit from Bath 1 is approximately three

times thinner than a 30 minutes deposit from Cell 7, and the roughness of the first is more than twice that of the latter case. The decrease in roughness in the galvanic cell can be attributed to the avoidance of the violent hydrogen evolution associated with DMAB oxidation, as well as to the fact that the electrons used to reduce the Cu(II) ions are evenly distributed as a current coming from the anodic half-cell and not produced *in-situ* by another electrochemical reaction on the same surface.

8.6 Conclusions

The electroless deposition of copper, using DMAB as a reducing agent, was studied. The deposition rate, determined using AFM thickness measurements and anodic stripping, was found to be 0.05 μm min^{-1}, with an induction time of ~30 seconds. The good agreement obtained between the two techniques, confirmed that the electrochemical method is a simple yet effective way of studying films obtained through electroless deposition.

Spontaneous decomposition of the electroless bath led to the production of small crystallites of polycrystalline copper, while controlled electroless deposition on gold produced metallic films with a slightly higher fraction of Cu (111) than expected. Changes in the concentration of the reducing agent (and thus the rate of deposition) had no effect on the crystalline structure obtained.

The rate decreased by 40% to 0.03 μm min^{-1} in the galvanic cell, which physically separates the two half-reactions. The deposition rate in the electroless bath was almost regained, when a copper electrode was immersed in the DMAB-containing half-cell. This indicates that the oxidation of the reducing agent is the limiting step of the process, even when DMAB is in stoichiometric excess compared to the copper complex; it also confirmed that copper is a better catalyst for DMAB oxidation than gold. The results obtained prove that the mixed potential theory is not valid for the case of the electroless copper deposition by DMAB, as the two half-reactions are interdependent; the rate of anodic oxidation of the

reducing agent is particularly sensitive to the substrate, which is continuously changing in a typical electroless bath.

The roughness of the deposits decreased in the galvanic cell, compared to the electroless bath. This is attributed the fact that the electrons used to reduce the Cu(II) ions are not produced *in-situ* by another molecule, but are evenly distributed as a current coming from the other half-cell, as well as to the avoidance of violent gas evolution linked to DMAB oxidation. This morphological change also points to an interdependence of the reactions when they are physically co-located.

The faradaic efficiency of the deposition process never reaches 100%, though it is above 80% after the first few minutes, demonstrating that side reactions occur in the copper-containing half-cell; these parasitic reactions are more prominent in the early stages of the deposition process.

The combination of galvanic and bipolar studies showed that a change in driving force occurs with time, under spontaneous conditions; the change was particularly significant during the first 30 s of deposition. These studies also confirm that hydrogen evolution is the most likely candidate for the parasitic reaction which decreases efficiency.

In addition to its intended role of pH control and complexing capabilities, triethanolamine was found to play an important role on the kinetics of the deposition process; TEA catalyses DMAB oxidation, while improving the faradaic efficiency of the Copper-DMAB system.

The galvanic set-up proved effective in the investigation of the electroless deposition process, providing information not only about the interaction between the cathodic and anodic processes, but also about the kinetics and efficiency of the system. This configuration could promote a better understanding of electroless deposition, by allowing the study of a wider range of concentrations and temperatures than the typical electroless bath is capable of, as it avoids the risk of homogeneous decomposition.

9 Conclusions and Further Work

9.1 Conclusions

An electrochemical study of copper electroless deposition, using DMAB as a reducing agent, was undertaken in order to gain further understanding of the electroless deposition process as a whole and more specifically of the Copper-DMAB system. The system's mechanism and kinetics were investigated using mainly voltammetric techniques, in combination with a number of other electrochemical and spectroscopic methods.

A thorough investigation of the electro-oxidation of DMAB was carried out as, despite its increasing relevance as a reductant in electroless deposition and fuel cell technology, the heterogeneous oxidation process is not well understood. It was determined that the initial dissociation step is not only catalysed by the presence of metallic surfaces, but more significantly by the applied potential.

Borohydride and DMAB have complicated, multiple step oxidation mechanisms, which while similar, do not appear to be identical. Both processes are greatly influenced by adsorption phenomena, which have more influence on DMAB than on borohydride. Adsorption is affected by time, potential and surface structure, being catalysed strongly by gold in comparison other surfaces. The use of single crystal gold electrodes demonstrated that the different crystal phases of gold have distinctive effects on the adsorption and oxidation of DMAB; more specifically, the Au (100) structure improves the oxidation kinetics, while adsorption is particularly prominent on Au (110) surfaces.

In highly alkaline media, on gold surfaces, DMAB oxidation occurs via two three-electron transfers; the second of these steps is probably attributed to the oxidation of hydrogen to water rather than further oxidation of the DMAB molecule. An additional oxidation product is formed in the region of gold oxide formation, likely of the form BO_2^- or $B_4O_7^-$. During the second oxidation wave, the

amine fragment of the DMAB molecule is also oxidised: in highly alkaline media, the amine is extensively oxidised; at lower pH, however, a strongly adsorbed species is produced, which can be reduced at certain potentials and hinders other oxidation processes.

Different experimental techniques produced a range of diffusion coefficients, for DMAB, between 0.9 and 2.3 x 10^{-5} cm^2 s^{-1}, under the assumption of an initial non-reversible three-electron transfer. An average value of 1.6 x 10^{-5} cm^2 s^{-1} was determined, which while higher than the values reported in the literature, agrees well with that of the borohydride anion.[44,67,73,77]

The use of the bipolar cell allowed the investigation of bimolecular electron transfer. Comparison with numerical models determined that the wave-shape changes observed with the relative concentration ratios are due to mass transport effects and not kinetic or resistive influences. On the other hand, using excess concentrations of both forms of a reversible redox couple in one half-cell produced the behaviour of a perfect conductor when coupled with reversible electron transfer, kinetically hindered systems and metal deposition systems.

The value of the bipolar cell in the investigation of “coupling” effects between the anodic and cathodic processes of electroless deposition were evidenced, and the effect of the substrate on each of the half-reactions was investigated. The possibility of identifying side reactions of the process, which influence the overall efficiency, was also shown; in the particular case of the Copper-DMAB electroless system, hydrogen evolution appears the most likely candidate.

The deposition kinetics of the Copper-DMAB system was studied using anodic stripping; the aptness and efficiency of this method was confirmed by comparison with AFM measurements. The plating rate of the bath was determined to be 0.05 μm min^{-1}, with an induction time of approximately 30 s. The rate decreased by 40%, to 0.03 μm min^{-1}, in the galvanic set-up, which separates the two half-reactions.

Controlled copper deposition on gold produced metallic films with a slightly higher fraction of Cu (111) than that of typical polycrystalline copper, while

spontaneous decomposition of the bath formed small copper crystallites. The roughness of the deposits increased with time (and consequently thickness), with equivalent deposits from the galvanic configuration being smoother than those of the bath.

The galvanic cell configuration proved to be an effective tool for the investigation of the electroless deposition process, as it provided information on the interaction between the two half-reactions, as well as on the kinetics and efficiency of the system. The results reported here prove that the mixed potential theory is not valid, at least for the specific system studied, as the cathodic and anodic reactions are interdependent; DMAB oxidation is particularly sensitive to the substrate, which is continuously changing as plating progresses.

The anodic reaction was found to be the limiting step of the deposition process, with DMAB oxidation being catalysed by the emerging copper substrate as well as the presence of TEA in the system. This bath component also improved the faradaic efficiency, which while never reaching 100% was generally above 80% after the first few minutes of deposition. The determination of the important effect of the DMAB oxidation reaction on the deposition kinetics only confirms the necessity of a clear understanding of its reaction mechanism.

9.2 Further Work

Although *in-situ* FTIR provided new information about the DMAB oxidation mechanism, further work is needed in the identification of the different species involved in the process. The speciation of the intermediates and products, and their dependence on solution pH, need to be determined through different spectroscopic techniques. Raman spectroscopy was attempted, but the gases produced during the oxidation made it impossible to obtain any significant results. Differential electrochemical mass spectroscopy (DEMS) could be used, for example, to identify the gaseous products such as hydrogen or dimethylamine; these gases could in theory be quantified through the use of DEMS. ^{11}BNMR, on the other hand, could be employed to identify final solution products.

As mentioned in Chapter 7, the kinetic model of the bipolar cell needs to be adjusted. A more realistic model that allows different kinetic parameters for each half-cell needs to be developed, in order to fully take advantage of the bipolar cell as a tool in the investigation of kinetically hindered electrochemical systems. Additionally the bipolar cell could be used to try to de-convolute the multi-electronic transfer of the DMAB oxidation mechanism, by using different concentration ratios of a completely reversible system in the other half-cell; the potential use of the bipolar cell in this type of system was demonstrated through the study of the copper voltammetry in Section 7.3.1.

The inclusion of common additives to the Copper-DMAB system, such as 2,2-dipyridyl, should be investigated; the effect of TEA on the system's kinetics and efficiency was shown here, and similar studies could be performed with other commercial additives in order to understand better their role in the mechanism of electroless deposition. The effect of these compounds on the deposit morphology is also of interest, and TEA is currently under investigation within the research group; preliminary results indicate that besides catalysing the anodic reaction (see Section 8.3.3), it plays a important role on the structure of the resulting deposit.

References

(1) Izumi, O., Osamu, W., and Shiro, H., *J. Electrochem. Soc.*, **1985**, *132* (10), 2323.

(2) Osaka, T., Misato, T., Sato, J., Akiya, H., Homma, T., Kato, M., Okinaka, Y., and Yoshioka, O., *Journal of The Electrochemical Society*, **2000**, *147* (3), 1059.

(3) Homma, T., Komatsu, I., Tamaki, A., Nakai, H., and Osaka, T., *Electrochimica Acta*, **2001**, *47* (1-2), 47.

(4) Balci, S., Bittner, A.M., Hahn, K., Scheu, C., Knez, M., Kadri, A., Wege, C., Jeske, H., and Kern, K., *Electrochimica Acta*, **2006**, *51* (28), 6251.

(5) Pavlov, M., Chalyt, G., Bratin, P., Kogan, A., and Perpich, M.J., *Measurement of the concentration of a reducing agent in an electroless plating bath*, in *UNITED STATES PATENT AND TRADEMARK OFFICE GRANTED PATENT*. 2004.

(6) Malel, E. and Mandler, D., *Journal of the Electrochemical Society*, **2008**, *155* (6), D459.

(7) Porter, L.A., Choi, H.C., Ribbe, A.E., and Buriak, J.M., *Nano Letters*, **2002**, *2* (10), 1067.

(8) O'Sullivan, E.J., *Fundamental and Practical Aspects of the Electroless Deposition Reaction*, in *Advances in Electrochemical Science and Engineering*, R.C. Alkire and D.M. Kolb, Wiley - VCH, p. 225, (2002).

(9) Jagannathan, R. and Krishnan, M., *IBM. Journal of Research and Development*, **1993**, *37* (2), 117.

(10) Sverdlov, Y., Bogush, V., Einati, H., and Shacham-Diamand, Y., *J. Electrochem. Soc.*, **2005**, *152* (9), C631.

(11) Shacham-Diamand, Y., Sverdlov, Y., Bogush, V., and Ofek-Almog, R., *Journal of Solid State Electrochemistry*, **2007**, *11* (7), 929.

(12) Hofmann, U. and Weil, K.G., *Plating and Surface Finishing*, **1992**, *79* (3), 60.

(13) Zhongliang, S., Shanqiang, W., and Jerzy, A.S., *Nanotechnology*, **2006**, *17* (9), 2161.

(14) Shi, Z., Wu, S., and Szpunar, J.A., *Chemical Physics Letters*, **2006**, *422* (1-3), 147.

(15) Wang, F., Arai, S., and Endo, M., *Electrochemistry Communications*, **2004**, *6* (10), 1042.

(16) Djokic, S.S., *Electroless Deposition of Metals and Alloys*. Modern Aspects of Electrochemistry, ed. B.E. Conway and R.E. White. Vol. 35. 2002: Kluwer Academic/Plenum Publishers.

(17) Lelental, M., *Journal of Catalysis*, **1974**, *32* (3), 429.

(18) Yoshino, M., Nonaka, Y., Sasano, J., Matsuda, I., Shacham-Diamand, Y., and Osaka, T., *Electrochimica Acta*, **2005**, *51* (5), 916.

(19) Patterson, J.C., Dheasuna, C.N., Barrett, J., Spalding, T.R., O'Reilly, M., Jiang, X., and Crean, G.M., *Applied Surface Science*, **1995**, *91*, 124.

(20) Dubin, V.M., Shacham-Diamand, Y., Zhao, B., Vasudev, P.K., and Ting, C.H., *Journal of The Electrochemical Society*, **1997**, *144* (3), 898.

(21) Kubo, N., Homma, T., Hondo, Y., and Osaka, T., *Electrochimica Acta*, **2005**, *51* (5), 834.

(22) Abrantes, L.M. and Correia, J.P., *Journal of the Electrochemical Society*, **1994**, *141* (9), 2356.

(23) Henry, J.R., *Metal Finishing*, **2002**, *100*, 409.

(24) Shacham-Diamand, Y., Dubin, V., and Angyal, M., *Thin Solid Films*, **1995**, *262* (1), 93.
(25) Bindra, P. and White, J.R., *Fundamental Aspects of Electroless Copper Plating*, in *Electroless Plating - Fundamentals and Applications*, G.O. Mallory and J.B. Hajdu, William Andrew Publishing/Noyes, p. 289, (1990).
(26) Sargent, A. and Sadik, O.A., *Langmuir*, **2001**, *17* (9), 2760.
(27) Iacovangelo, C.D. and Zarnoch, K.P., *J. Electrochem. Soc.*, **1991**, *138* (4), 983.
(28) Ohtsuka, K., Okuno, K., Hattori, N., and Torikai, E., *Trans. Inst. Metal Finishing*, **1991**, *69* (1), 33.
(29) Patterson, J.C., O'Reilly, M., Crean, G.M., and Barrett, J., *Microelectronic Engineering*, **1997**, *33* (1-4), 65.
(30) Wanner, M., Wiese, H., and Weil, K.G., *Berichte Der Bunsen-Gesellschaft-Physical Chemistry Chemical Physics*, **1988**, *92* (6), 736.
(31) Sargent, A. and Sadik, O.A., *J. Electrochem. Soc.*, **2001**, *148* (6), C413.
(32) Hasegawa, M., Okinaka, Y., Shacham-Diamand, Y., and Osaka, T., *Electrochemical and Solid-State Letters*, **2006**, *9* (8), C138.
(33) Sadik, O.A., Xu, H., and Sargent, A., *Journal of Electroanalytical Chemistry*, **2005**, *583* (2), 167.
(34) Homma, T., Tamaki, A., Nakai, H., and Osaka, T., *Journal of Electroanalytical Chemistry*, **2003**, *559*, 131.
(35) Spiro, M., *A Critique of the Additivity Principle for Mixed Couples*. Modern Aspects of Electrochemistry, ed. J.O.M. Bockris, B.E. Conway, and R.E. White. Vol. 34. 2001, New York: Kluwer Academic/Plenum Publishers. 1.
(36) Mital, C.K., Shrivastava, P.B., and Dhaneshwar, R.G., *Metal Finishing*, **1987**, *85* (6), 87.
(37) Wiese, H. and Weil, K.G., *Berichte Der Bunsen-Gesellschaft-Physical Chemistry Chemical Physics*, **1987**, *91* (6), 619.
(38) Ohno, I., *Materials Science and Engineering a-Structural Materials Properties Microstructure and Processing*, **1991**, *146* (1-2), 33.
(39) Schumacher, R., Pesek, J.J., and Melroy, O.R., *Journal of Physical Chemistry*, **1985**, *89* (20), 4338.
(40) Sverdlov, Y. and Shacham-Diamand, Y., *Microelectronic Engineering*, **2003**, *70* (2), 512.
(41) Iacovangelo, C.D., *J. Electrochem. Soc.*, **1991**, *138* (4), 976.
(42) Meerakker, J.E.A.M., *Journal of Applied Electrochemistry*, **1981**, *11* (3), 395.
(43) D'Ulivo, A., *Spectrochimica Acta Part B: Atomic Spectroscopy*, **2004**, *59* (6), 793.
(44) Nagle, L.C. and Rohan, J.F., *Electrochemical and Solid-State Letters*, **2005**, *8* (5), C77.
(45) Nagle, L.C. and Rohan, J.F., *J. Electrochem. Soc.*, **2006**, *153* (11), C773.
(46) Chang, S.Y., Wan, C.C., Wang, Y.Y., Shih, C.H., Tsai, M.H., Shue, S.L., Yu, C.H., and Liang, M.S., *Thin Solid Films*, **2006**, *515* (3), 1107.
(47) Mirkin, M.V. and Bard, A.J., *Analytical Chemistry*, **1991**, *63* (5), 532.
(48) Davis, R.E., Bromels, E., and Kibby, C.L., *Journal of the American Chemical Society*, **1962**, *84* (6), 885.
(49) Atwan, M.H., Macdonald, C.L.B., Northwood, D.O., and Gyenge, E.L., *Journal of Power Sources*, **2006**, *158* (1), 36.
(50) Dong, H., Feng, R., Ai, X., Cao, Y., Yang, H., and Cha, C., *J. Phys. Chem. B*, **2005**, *109* (21), 10896.
(51) Gyenge, E., *Electrochimica Acta*, **2004**, *49* (6), 965.

(52) Chatenet, M., Micoud, F., Roche, I., and Chainet, E., *Electrochimica Acta*, **2006**, *51* (25), 5459.
(53) Krishnan, P., Yang, T.H., Advani, S.G., and Prasad, A.K., *Journal of Power Sources*, **2008**, *182* (1), 106.
(54) Amendola, S.C., Onnerud, P., Kelly, M.T., Petillo, P.J., Sharp-Goldman, S.L., and Binder, M., *Journal of Power Sources*, **1999**, *84* (1), 130.
(55) Morris, J.H., Gysling, H.J., and Reed, D., *Chemical Reviews*, **1985**, *85* (1), 51.
(56) Davis, R.E. and Gardner Swain, C., *Journal of the American Chemical Society*, **1960**, *82* (22), 5949.
(57) Cheng, H. and Scott, K., *Electrochimica Acta*, **2006**, *51* (17), 3429.
(58) Gardiner, J.A. and Collat, J.W., *Inorganic Chemistry*, **1965**, *4* (8), 1208.
(59) Finkelstein, D.A., Da Mota, N., Cohen, J.L., and Abruna, H.D., *Journal of Physical Chemistry C*, **2009**, *113* (45), 19700.
(60) Gardiner, J.A. and Collat, J.W., *Journal of the American Chemical Society*, **1964**, *86* (15), 3165.
(61) Gardiner, J.A. and Collat, J.W., *Journal of the American Chemical Society*, **1965**, *87* (8), 1692.
(62) Mesmer, R.E. and Jolly, W.L., *Inorganic Chemistry*, **1962**, *1* (3), 608.
(63) Ponce-de-Leon, C., Bavykin, D.V., and Walsh, F.C., *Electrochemistry Communications*, **2006**, *8* (10), 1655.
(64) Wang, K., Lu, J., and Zhuang, L., *Journal of Electroanalytical Chemistry*, **2005**, *585* (2), 191.
(65) Guella, G., Zanchetta, C., Patton, B., and Miotello, A., *J. Phys. Chem. B*, **2006**, *110* (34), 17024.
(66) Mirkin, M.V., Yang, H., and Bard, A.J., *J. Electrochem. Soc.*, **1992**, *139* (8), 2212.
(67) Denuault, G., Mirkin, M.V., and Bard, A.J., *Journal of Electroanalytical Chemistry*, **1991**, *308* (1), 27.
(68) Martins, J.I. and Nunes, M.C., *Journal of Power Sources*, **2008**, *175* (1), 244.
(69) Concha, B.M., Chatenet, M., Coutanceau, C., and Hahn, F., *Electrochemistry Communications*, **2009**, *11* (1), 223.
(70) Chatenet, M., Molina-Concha, M.B., and Diard, J.P., *Electrochimica Acta*, **2009**, *54* (6), 1687.
(71) Chandra, M. and Xu, Q., *Journal of Power Sources*, **2006**, *159* (2), 855.
(72) Rostamikia, G. and Janik, M.J., *Journal of the Electrochemical Society*, **2009**, *156* (1), B86.
(73) Chatenet, M., Molina-Concha, M.B., El-Kissi, N., Parrour, G., and Diard, J.P., *Electrochimica Acta*, **2009**, *54* (18), 4426.
(74) Iotov, P.I., Kalcheva, S.V., and Bond, A.M., *Electrochimica Acta*, **2009**, *54* (28), 7236.
(75) Vaskelis, A., Tarozaite, R., Jagminiene, A., Tamasiunaite, L.T., Juskenas, R., and Kurtinaitiene, M., *Electrochimica Acta*, **2007**, *53*, 407.
(76) Burke, L.D. and Lee, B.H., *Journal of Applied Electrochemistry*, **1992**, *V22* (1), 48.
(77) Sargent, A., Sadik, O.A., and Luis, J.M., *J. Electrochem. Soc.*, **2001**, *148* (4), C257.
(78) Homma, T., Nakai, H., Onishi, M., and Osaka, T., *Journal of Physical Chemistry B*, **1999**, *103* (10), 1774.
(79) Shimada, T., Nakai, H., and Homma, T., *Journal of the Electrochemical Society*, **2007**, *154* (4), D273.

(80) Watanabe, H., Abe, S., and Honma, H., *Journal of Applied Electrochemistry*, **1998**, *28* (5), 525.
(81) Saito, T., Sato, E., Matsuoka, M., and Iwakura, C., *Journal of Applied Electrochemistry*, **1998**, *V28* (5), 559.
(82) Burke, L.D. and Ryan, T.G., *Electrochimica Acta*, **1992**, *37* (8), 1363.
(83) Mishra, K.G. and Paramguru, R.K., *Journal of the Electrochemical Society*, **1996**, *143* (2), 510.
(84) Pittermann, U. and Weil, K.G., *Berichte Der Bunsen-Gesellschaft-Physical Chemistry Chemical Physics*, **1993**, *97* (3), 495.
(85) Aithal, R.K., Yenamandra, S., Gunasekaran, R.A., Coane, P., and Varahramyan, K., *Materials Chemistry and Physics*, **2006**, *98* (1), 95.
(86) Ramasubramanian, M., Popov, B.N., White, R.E., and Chen, K.S., *Journal of The Electrochemical Society*, **1999**, *146* (1), 111.
(87) Bittner, A., Wanner, M., and Weil, K.G., *Berichte Der Bunsen-Gesellschaft-Physical Chemistry Chemical Physics*, **1992**, *96* (5), 647.
(88) Donahue, F.M., *Journal of The Electrochemical Society*, **1980**, *127* (1), 51.
(89) Jiang, H.Y., Liu, Z.J., Wang, X.W., and Wang, Z.L., *Transactions of the Institute of Metal Finishing*, **2007**, *85* (2), 103.
(90) Vaskelis, A., Jaciauskiene, J., Stalnioniene, I., and Norkus, E., *Journal of Electroanalytical Chemistry*, **2007**, *600* (1), 6.
(91) Paunovic, M. and Vitkavage, D., *Journal of The Electrochemical Society*, **1979**, *126* (12), 2282.
(92) Hendricks, T.R. and Lee, I., *Thin Solid Films*, **2006**, *515* (4), 2347.
(93) Feldman, B.J. and Melroy, O.R., *Journal of The Electrochemical Society*, **1989**, *136* (3), 640.
(94) Elraghy, S.M. and Abosalama, A.A., *Journal of The Electrochemical Society*, **1979**, *126* (2), 171.
(95) Donahue, F.M., Wong, K.L.M., and Bhalla, R., *Journal of The Electrochemical Society*, **1980**, *127* (11), 2340.
(96) Bindra, P., Light, D., and Rath, D., *Ibm Journal of Research and Development*, **1984**, *28* (6), 668.
(97) Strubbe, K., Vereecken, P.M., and Gomes, W.P., *Journal of The Electrochemical Society*, **1999**, *146* (4), 1412.
(98) Bard, A.J. and Faulkner, L.R., *Electrochemical methods: fundamentals and applications.* Second ed. 2001, USA: John Wiley and Sons, Inc.
(99) Kissinger, P.T. and Heineman, W.R., *Laboratory techniques in electroanalytical chemistry*. Second ed. 1996, New York: Marcel Dekker, Inc.
(100) Monk, P., *Fundamentals of electroanalytical chemistry*. Analytical Techniques in the Sciences (AnTS), ed. D.J. Ando. 2001, Great Britain: John Wiley and Sons LTD.
(101) Vanbenschoten, J.J., Lewis, J.Y., Heineman, W.R., Roston, D.A., and Kissinger, P.T., *Journal of Chemical Education*, **1983**, *60* (9), 772.
(102) Mabbott, G.A., *Journal of Chemical Education*, **1983**, *60* (9), 697.
(103) Kissinger, P.T. and Heineman, W.R., *Journal of Chemical Education*, **1983**, *60* (9), 702.
(104) Girault, H.H., *Analytical and physical electrochemistry*. 2004, New York: Marcel Dekker.
(105) Nicholson, R.S., *Analytical Chemistry*, **1965**, *37* (11), 1351.
(106) Mirkin, M.V. and Bard, A.J., *Analytical Chemistry*, **1992**, *64* (19), 2293.
(107) Samec, Z., Marecek, V., and Weber, J., *Journal of Electroanalytical Chemistry*, **1979**, *96* (2), 245.

(108) Samec, Z., *Journal of Electroanalytical Chemistry*, **1979**, *99* (2), 197.
(109) Samec, Z., Marecek, V., and Weber, J., *Journal of Electroanalytical Chemistry*, **1979**, *100* (1-2), 841.
(110) Samec, Z., Marecek, V., Koryta, J., and Khalil, M.W., *Journal of Electroanalytical Chemistry*, **1977**, *83* (2), 393.
(111) Samec, Z., *Journal of Electroanalytical Chemistry*, **1979**, *103* (1), 1.
(112) Samec, Z., Marecek, V., and Weber, J., *Journal of Electroanalytical Chemistry*, **1979**, *103* (1), 11.
(113) Stewart, A.A., Campbell, J.A., Girault, H.H., and Edddowes, M., *Berichte Der Bunsen-Gesellschaft-Physical Chemistry Chemical Physics*, **1990**, *94* (1), 83.
(114) Geblewicz, G. and Schiffrin, D.J., *Journal of Electroanalytical Chemistry*, **1988**, *244* (1-2), 27.
(115) Hotta, H., Akagi, N., Sugihara, T., Ichikawa, S., and Osakai, T., *Electrochemistry Communications*, **2002**, *4* (5), 472.
(116) Hotta, H., Ichikawa, S., Sugihara, T., and Osakai, T., *Journal of Physical Chemistry B*, **2003**, *107* (36), 9717.
(117) Osakai, T., Ichikawa, S., Hotta, H., and Nagatani, H., *Analytical Sciences*, **2004**, *20* (11), 1567.
(118) Cattarin, S. and Musiani, M.M., *Journal of The Electrochemical Society*, **1995**, *142* (11), 3786.
(119) Park, J.H. and Bard, A.J., *Electrochemical and Solid State Letters*, **2005**, *8* (12), G371.
(120) Wang, E. and Sun, Z., *TrAC Trends in Analytical Chemistry*, **1988**, *7* (3), 99.
(121) Aoki, K., *Electroanalysis*, **1993**, *5* (8), 627.
(122) Atkins, P. and Jones, L., *Chemical Principles: The Quest for Insight*. Second ed. 2002, New York: W. H. Freeman and Company.
(123) Iwasita, T. and Nart, F.C., *Progress in Surface Science*, **1997**, *55* (4), 271.
(124) Borras, C., Laredo, T., Mostany, J., and Scharifker, B.R., *Electrochimica Acta*, **2004**, *49* (4), 641.
(125) Huerta, F., Morallon, E., Cases, F., Rodes, A., Vazquez, J.L., and Aldaz, A., *Journal of Electroanalytical Chemistry*, **1997**, *421* (1-2), 179.
(126) Viana, A.S., Jones, A.H., Abrantes, L.M., and Kalaji, M., *Journal of Electroanalytical Chemistry*, **2001**, *500* (1-2), 290.
(127) Garcia, G., Rodriguez, P., Rosca, V., and Koper, M.T.M., *Langmuir*, **2009**, *25* (23), 13661.
(128) Samec, Z., *Pure and Applied Chemistry. © IUPAC.*, **2004**, *76* (12), 2147.
(129) Britz, D., *Digital Simulation in Electrochemistry*. Second ed. 1988, Darmstadt: Springer-Verlag.
(130) *CRC Handbook of Chemistry and Physics*. 76th ed, ed. D.R. Lide. 1995: CRC Press, Inc.
(131) Masui, M., Sayo, H., and Tsuda, Y., *Journal of the Chemical Society B: Physical Organic*, **1968**, 973.
(132) Harada, S., Okada, H., Sano, T., Yamashita, T., and Yano, H., *The Journal of Physical Chemistry*, **1990**, *94* (19), 7648.
(133) Bénézeth, P., Palmer, D.A., and Wesolowski, D.J., *Journal of Chemical & Engineering Data*, **2001**, *46* (2), 202.
(134) Drazic, D.M., Tripkovic, A.V., Popovic, K.D., and Lovic, J.D., *Journal of Electroanalytical Chemistry*, **1999**, *466* (2), 155.
(135) Markovic, N.M., Schmidt, T.J., Grgur, B.N., Gasteiger, H.A., Behm, R.J., and Ross, P.N., *J. Phys. Chem. B*, **1999**, *103* (40), 8568.
(136) Ortmann, R. and Schlitzer, M., *Synthesis-Stuttgart*, **2009**, (10), 1757.

(137) Nöth, H. and Wrackmeyer, B., *Nuclear Magnetic Resonance Spectroscopy of Boron Compounds*. NMR Basic Principles and Progress, ed. P. Diehl, E. Fluck, and R. Kosfeld. Vol. 14. 1978: Springer-Verlag.
(138) Angersteinkozlowska, H., Conway, B.E., Hamelin, A., and Stoicoviciu, L., *Electrochimica Acta*, **1986**, *31* (8), 1051.
(139) Socrates, G., *Infrared Characteristic Group Frequencies*. 3rd ed. 2001, New York: John Wiley and Sons Ltd.
(140) White, R.G., *Handbook of Industrial Infrared Analysis.* 1964, New York: Plenum Press.
(141) Hedwig, G.R. and Powell, H.K.J., *Journal of the Chemical Society-Dalton Transactions*, **1973**, (8), 793.
(142) Norkus, E., *Journal of Applied Electrochemistry*, **2000**, *30* (10), 1163.
(143) Golub, G., Cohen, H., Paoletti, P., Bencini, A., Messori, L., Bertini, I., and Meyerstein, D., *Journal of the American Chemical Society*, **1995**, *117* (32), 8353.
(144) Paoletti, P., Fabbrizzi, L., and Barbucci, R., *Inorganic Chemistry*, **1973**, *12* (8), 1861.
(145) Fabbrizzi, L., Poggi, A., and Zanello, P., *Journal of the Chemical Society-Dalton Transactions*, **1984**, (8), 1495.
(146) Trejo, G., Gil, A.F., and Gonzalez, I., *Journal of Applied Electrochemistry*, **1996**, *26* (12), 1287.
(147) Masahiro, S., Hideyuki, T., Makoto, S., and Masayuki, K., *Electroless gold plating solution*, in *European Patent Office*. 1987.
(148) Pharr, C.M. and Griffiths, P.R., *Analytical Chemistry*, **1997**, *69* (22), 4673.
(149) Liu, Y., Xia, X., and Liu, H., *Journal of Power Sources*, **2004**, *130* (1-2), 299.
(150) Maeda, Y., Sato, K., Ramaraj, R., Rao, T.N., Tryk, D.A., and Fujishima, A., *Electrochimica Acta*, **1999**, *44* (20), 3441.
(151) Vazquez-Arenas, J., Vazquez, G., Melendez, A.M., and Gonzalez, I., *Journal of The Electrochemical Society*, **2007**, *154* (9), D473.
(152) Munoz, E.C., Schrebler, R.S., Cury, P.K., Suarez, C.A., Cordova, R.A., Gomez, C.H., Marotti, R.E., and Dalchiele, E.A., *J. Phys. Chem. B*, **2006**, *110* (42), 21109.
(153) Knoll, J. and Swavey, S., *Inorganica Chimica Acta*, **2009**, *362* (9), 2989.
(154) Chikae, M., Idegami, K., Kerman, K., Nagatani, N., Ishikawa, M., Takamura, Y., and Tamiya, E., *Electrochemistry Communications*, **2006**, *8* (8), 1375.
(155) Herranen, M. and Carlsson, J.O., *Corrosion Science*, **2001**, *43* (2), 365.
(156) Andersen, J.E.T., BechNielsen, G., Moller, P., and Reeve, J.C., *Journal of Applied Electrochemistry*, **1996**, *26* (2), 161.
(157) Nichols, R.J., Beckmann, W., Meyer, H., Batina, N., and Kolb, D.M., *Journal of Electroanalytical Chemistry*, **1992**, *330* (1-2), 381.
(158) Weber, C.J., Pickering, H.W., and Weil, K.G., *Journal of the Electrochemical Society*, **1997**, *144* (7), 2364.
(159) Swanson, H.E. and Tatge, E., *Standard X-Ray Diffraction Powder Patterns*. National Bureau of Standards Circular No. 539. Vol. I. 1953, Washington D.C.: U.S. Dept. of Commerce.
(160) Swanson, H.E. and Fuyat, R.K., *Standard X-Ray Diffraction Powder Patterns*. National Bureau of Standards Circular 539. Vol. II. 1953, Washington, D.C.: U.S. Dept. of Commerce.
(161) Hanawalt, J.D., Rinn, H.W., and Frevel, L.K., *Industrial & Engineering Chemistry Analytical Edition*, **1938**, *10* (9), 457.
(162) Ding, P.J., Lanford, W.A., Hymes, S., and Murarka, S.P., *Applied Physics Letters*, **1994**, *64* (21), 2897.

(163) Luechinger, N.A., Athanassiou, E.K., and Stark, W.J., *Nanotechnology*, **2008**, *19* (44).

Appendix A: Publications and Presentations

D. Plana, P. Rodríguez, M.T.M. Koper, R.A.W. Dryfe. *Oxidation of DMAB on Single Crystal Electrodes: Implications for Electroless Deposition and Borohydride Fuel Cells* (Oral Presentation). ECNW 2010. University of Bangor, UK. June 2010.

D. Plana, A.I. Campbell, S.N. Patole, G. Shul, R.A.W. Dryfe. *Kinetics of Electroless Deposition: the Copper-Dimethylamine Borane System*. Langmuir 26 (12), p 10334-10340, 2010.

D. Plana, F.G.E. Jones, R.A.W. Dryfe. *The Voltammetric Response of Bipolar Cells: Reversible Electron Transfer.* Journal of Electroanalytical Chemistry 646 (1-2), p 107-113, 2010.

D. Plana, S.N. Patole, G. Shul, R.A.W. Dryfe. *Electroless Deposition of Copper: Nano-scale Topography from Micro-scale Kinetics* (Oral Presentation). 216th ECS Meeting. Vienna, Austria. October 2009.

D. Plana, S.N. Patole, G. Shul, R.A.W. Dryfe. *Electroless Deposition of Copper: Morphology and Kinetics* (Poster presentation). Electrochem 09. University of Manchester, UK. September 2009.

D. Plana, G. Shul, M.J. Stephenson, R.A.W. Dryfe. *The Voltammetric Response of Bipolar Cells: Mechanistic Investigations of Electroless Deposition.* Electrochemistry Communications 11 (1), p 61-64, 2009.

D. Plana, F.G.E. Jones, R.A.W. Dryfe. *Bipolar Voltammetry as a Tool to Understand Deposition Processes* (Oral Presentation). Electrochem 2008. University of Liverpool, UK. September 2008.

D. Plana, R.A.W. Dryfe. *The Oxidation Mechanism of Borohydride and Dimethylamine Borane: Application to Fuel Cells and Electroless Deposition* (Poster presentation). The 59th Annual Meeting of the International Society of Electrochemistry. Seville, Spain. September 2008.

D. Plana, F.G.E. Jones, R.A.W. Dryfe. *Voltammetric Response of Bipolar Cells* (Oral Presentation). ECNW 2008. University of Manchester, UK. June 2008.

D. Plana, R.A.W. Dryfe. *Borohydride and DMAB Oxidation: Applications to Electroless Deposition and Fuel Cell Chemistry* (Poster presentation). Electrochem 07. Imperial College, London, UK. September 2007.

Appendix B: Treatment of Errors

Throughout this work diffusion coefficients (D) and number of electrons (n) were calculated repeatedly and the treatment of the errors associated with these calculations is described here.

Values of D and n were obtained for DMAB and borohydride through different experiments; the most common form was through voltammetric techniques and the use of linear regressions based on Equation 50 and/or Equation 53. The errors associated with these particular calculations are mainly due to the uncertainty in the linear regression and the errors associated with the determination of the area of the electrode and the concentration of the solutions. The relative error associated with the electrode area (A) was approximately 5%, while the error due to the concentrations (C) was always less than 2%; the concentration error was minimised by always weighting large amounts of DMAB or borohydride relative to the error of the balance, and preparing large volumes of solution in precise volumetric flasks. The relative error obtained from the linear regression was on average 3%, leading to an average value of the relative error associated with the diffusion coefficients found this way of ~12%. This value was obtained by taking an average of the relative error associated with each particular determination of D; individual values were obtained through the following equation:[xviii]

$$(\%error(D))^2 = (2\times\%error(m))^2 + (2\times\%error(A))^2 + (2\times\%error(C))^2$$

where %error(*x*) is the relative error associated with *x* and m is the slope obtained from the linear regression.

The Cottrell equation (Equation 46) was also used to determine values of D and n for DMAB and borohydride. The relative error in these calculations is due essentially to the same uncertainties as in the case described above and the same method can be used determine an average relative error. In this case a

[xviii] Steiner, E., *The Chemistry Maths Book*. 1996, Great Britain: Oxford University Press.

value of ~11% was obtained, as the uncertainties from the linear regressions were smaller (~1%). The use of the Levich and the Koutecký-Levich equations (Equation 61 and Equation 63, respectively), on the other hand, provided larger errors on the linear regressions (7 and 5%, respectively); this led to relative errors of 17 and 14% for the diffusion coefficients obtained through RDE methods.

Diffusion coefficients were also determined for the hexaammineruthenium and hexacyanoferrate complexes, using Equation 50. Following the procedure described above, an average relative error of ~11% was obtained, as the linear regressions provided an average relative error of approximately 2%.

The errors associated with the determination of deposit thicknesses and plating rates, the other type of repetitive calculations performed in this work, were included in the corresponding chapter. For these cases standard deviations were obtained, as multiple experiments were performed.